

**Damping of
Piezoelectric MEMS Oscillators**

–

**Fundamentals and
Applications**

Dissertation

zur Erlangung des Grades
des Doktors der Ingenieurwissenschaften
der Naturwissenschaftlichen-Technischen Fakultät
der Universität des Saarlandes

von

Tobias Zengerle

Saarbrücken

2022

Tag des Kolloquiums: 31.10.2022

Dekan: Univ.-Prof. Dr. Ludger Santen

Mitglieder des Prüfungsausschusses:

Vorsitzender: Univ.-Prof. Dr. Rolf Pelster

1. Gutachter: Univ.-Prof. Dr. Helmut Seidel

2. Gutachter: Univ.-Prof. Dr. José Luis Sánchez-Rojas

3. Gutachter: Univ.-Prof. Dr. Ulrich Schmid

Akademischer Mitarbeiter: Dr.-Ing. Christian Bur

Abstract

A limiting parameter for the performance of micromechanical oscillators is the damping induced by the surrounding medium. In this work, the damping losses of micromechanical oscillators with piezoelectric actuation and detection are investigated in nine different gas atmospheres over a pressure range of six decades. In addition, the influence of the distance to a spatial boundary is examined, covering a range from narrow gaps with squeeze film damping to an almost freely oscillating structure. This reveals a superposition of four different damping mechanisms, which occur in varying strength depending on pressure, distance and eigenmode. Using an analytical approach, the individual damping phenomena can be separated from each other and subsequently evaluated in a targeted manner. Based on these results, new insights are gained for the molecular flow regime as well as the transitional flow regime, which include the impact of the number of active degrees of freedom of the gas molecules as well as thermal resonance effects. In addition, an electrical equivalent circuit was designed for the entire measurement range, which shows very good agreement with the experimental data. Finally, the damping effects are exploited for applications in sensor technology and a wide range pressure sensor using the nonlinear regime of the oscillators as well as a concept for the measurement of the oxygen concentration are presented.

Kurzfassung

Eine für die Leistungsfähigkeit mikromechanischer Oszillatoren limitierende Größe stellt die Dämpfung durch das umgebende Medium dar. In dieser Arbeit werden daher die Dämpfungsverluste mikromechanischer Oszillatoren mit piezoelektrischer Anregung und Detektion in neun verschiedenen Gasatmosphären über einen Druckbereich von sechs Dekaden untersucht. Zusätzlich wird der Einfluss des Abstandes zu einer räumlichen Begrenzung betrachtet und dabei ein Bereich von engen Spalten mit Squeeze Film Dämpfung bis hin zu fast frei schwingenden Strukturen untersucht. Dabei ergibt sich eine Überlagerung von vier verschiedenen Dämpfungsmechanismen, welche in Abhängigkeit von Druck, Abstand und Eigenmode in unterschiedlich starker Ausprägung auftreten. Durch einen analytischen Ansatz lassen sich die einzelnen Dämpfungsphänomene voneinander separieren und in der Folge gezielt auswerten. Anhand dieser Ergebnisse wurden für den molekularen sowie den Übergangsbereich neue Erkenntnisse gewonnen, welche die Anzahl aktiver Freiheitsgrade der Gasmoleküle sowie thermische Resonanzeffekte miteinbeziehen. Darüber hinaus wurde für den gesamten Messbereich ein elektrisches Ersatzschaltbild konzipiert, das eine sehr gute Übereinstimmung mit den experimentellen Daten zeigt. Abschließend werden die Dämpfungseffekte für Anwendungen in der Sensorik erschlossen und ein Mehrbereichsdrucksensor mit Hilfe des nichtlinearen Bereichs der Oszillatoren sowie ein Konzept zur Messung des Sauerstoffgehaltes präsentiert.

Eidesstattliche Versicherung

Hiermit versichere ich an Eides statt, dass ich die vorliegende Arbeit selbstständig und ohne Benutzung anderer als der angegebenen Hilfsmittel angefertigt habe. Die aus anderen Quellen oder indirekt übernommenen Daten und Konzepte sind unter Angabe der Quelle gekennzeichnet. Die Arbeit wurde bisher weder im In- noch im Ausland in gleicher oder ähnlicher Form in einem Verfahren zur Erlangung eines akademischen Grades vorgelegt.

Datum, Ort

Unterschrift

Table of Contents

Abstract	III
Kurzfassung.....	IV
Eidesstattliche Versicherung	V
Table of Contents	VI
1 Introduction	9
2 Theoretical Background	11
2.1 Properties of Gases	11
2.1.1 Flow Regimes.....	11
2.1.2 Physical Properties	12
2.1.3 Thermal Properties	14
2.1.4 Magnetic Properties.....	15
2.2 Harmonic Oscillator	17
2.2.1 Linear Harmonic Oscillator.....	17
2.2.2 Nonlinear Harmonic Oscillator	22
2.3 Damping Mechanism.....	23
2.3.1 Intrinsic Damping.....	24
2.3.2 Molecular Damping.....	25
2.3.3 Viscous Damping	27
2.3.4 Damping in the Transitional Flow Regime	28
2.3.5 Squeeze Film Damping	29
2.3.6 Damping in Liquids.....	30
3 Simulations.....	32
3.1 Eigenfrequency Study.....	32
3.1.1 Micro-oscillator Design.....	32
3.2 Thermo-Viscous Damping	34
3.3 Fluid-Structure Interaction	37
3.4 Stationary Magnetic Field Simulation.....	39
4 Manufacturing	42
4.1 Process Flow	42
4.1.1 Mask Production	44

4.1.2	Lithography	45
4.1.3	Thin Film Deposition	46
4.1.4	Etching	46
4.2	Process Control.....	48
4.2.1	Thin Film Thickness.....	48
4.2.2	Membrane Thickness	49
4.2.3	Residual Stress	50
5	Measurement	52
5.1	Vacuum Chamber	52
5.2	Measurement Circuit	52
5.3	Experimental Setup.....	55
5.4	Magnetic Field Construction	56
6	Results	60
6.1	Summary of the Appended Publications	61
6.2	Influence of Polyatomic Degrees of Freedom	62
6.2.1	Introduction	62
6.2.2	Degrees of freedom	63
6.2.3	Addendum I.....	67
6.3	Damping Model for the Transitional Flow Regime	75
6.3.1	Thermal Wave Concept.....	75
6.3.2	Addendum II	77
6.3.3	Addendum III	84
6.4	Higher Modes	91
6.4.1	Introduction	91
6.4.2	Addendum IV	93
6.5	Lumped Element Model	111
6.5.1	Equivalent Circuit	111
6.5.2	Addendum V	112
6.6	Damping in Liquids (Unpublished Data)	122
6.6.1	Experimental Results in Liquids	122
6.6.2	Comparison between Liquid and Gases	125

6.7	Wide-Range Pressure Sensing Application	127
6.7.1	Linear Pressure Sensing	127
6.7.2	Addendum VI	129
6.8	Oxygen Concentration Sensor (Unpublished Data)	143
6.8.1	Numerical Investigation	143
6.8.2	Oxygen Concentration Detection	145
6.8.3	Paramagnetic Effect	148
7	Summary	150
8	Outlook	154
	Bibliography	155
	Publications	169
	Journal Publications	169
	Conference Publications	170
	List of Figures	171
	List of Tables	176
	List of Symbols	177
	Acknowledgement	180

1 Introduction

The continuous development and miniaturization of numerous sensor concepts is paving the way for the success of micromechanical oscillators, which can now be found in many technical applications. For example, micromechanical oscillators are used in basic research as the core of scanning probe microscopy (SPM) [1], as precise microbalances in many biological investigations [2], in inertial and pressure sensors [3] and as energy harvesters for operating autonomous systems [4]. In general, two actuation principles are widely used, electrostatic and piezoelectric [5]. The electrostatic micro-oscillators working with capacitive attraction forces possess a relatively high quality factor as well as a high frequency stability [6]. Therefore, this actuator principle has prevailed especially in timing applications. Disadvantages of the electrostatic actuation principle are the high operating voltage, occurring nonlinearities and a complex manufacturing technology due to the requirement of narrow gaps between the capacitive plates in the range of a few μm . Furthermore, the narrow gaps also lead to significant damping, the squeeze film damping, which requires the oscillators to be encapsulated under a good vacuum to increase the quality factor and thus the performance of the device [7]. Piezoelectric micro-oscillators, on the other hand, are characterized by low actuation voltages, high electromechanical coupling and by their compatibility to complementary metal-oxide-semiconductor (CMOS) process technology using aluminum nitride as piezoelectric material. A disadvantage is the relatively low quality factor due to the residual stress of the applied piezoelectric layer, which can be adjusted by the deposition parameters [8].

A primary aim of this dissertation is the investigation of the individual damping losses and their associated fundamental physical description. From this, conclusions can be drawn about the reduction of the damping effects. These findings lead to an optimization of the quality factor and consequently to an enhancement of the performance of the micro-oscillators. Furthermore, another point is the utilization of the damping effect to gain information about the properties of the surrounding fluid. This aspect has been largely studied in liquids, leading to applications for example in the monitoring of operating fuels [9]. For gases, this point has been mostly neglected, so far.

With respect to pressure, damping in gas atmospheres can basically be divided into three regions: the viscous flow regime, the molecular flow regime and the transitional flow regime in-between. The transitional flow regime is not fully described by either of the two theories and is only partially covered at the edges. The flow regimes are defined by the ambient pressure, which gives the number of gas molecules available for an interaction in a certain volume and by a geometrical boundary. Both influences are merged in the so-called Knudsen number, which is applied to distinguish the individual flow regimes [10]. In the scope of this dissertation, a range of six pressure decades from 10^{-3} to 900 mbar is covered as well as a range for the distance to a boundary from 150 μm up to 3500 μm . This results in a range of the Knudsen number from 100 (molecular flow regime) down to 10^{-4} (viscous flow regime). In addition, the damping is strongly influenced by the physical and thermal properties of the gas atmosphere, for which nine different gases are explored in the inves-

tigations. These are the noble gases helium (He), neon (Ne), argon (Ar), krypton (Kr) and the polyatomic gases hydrogen (H₂), nitrogen (N₂), carbon dioxide (CO₂), nitrous oxide (N₂O) and sulfur hexafluoride (SF₆).

The damping is experimentally measured via resonance curves. From these curves, the quality factor and the resonance frequency are extracted as a function of the ambient pressure and the distance to a geometrical boundary. These results are then analyzed regarding correlations with the type of gas and the pressure level. The data reveal an interesting interaction of four different types of damping losses, which have varying impact depending on the ambient conditions. According to the dominating effect, different parameters can be extracted from the damping phenomena: the viscous flow regime is suitable for the determination of macroscopic properties such as density and dynamic viscosity, whereas in the transitional flow regime, where thermal resonance effects prevail, thermal properties can be obtained. In the molecular flow regime, molecular properties such as the number of active degrees of freedom can be deduced. Based on these findings, innovative sensor principles are proposed, which are able to identify the physical and thermal properties of the environmental gas atmosphere by evaluating the damping losses. Additionally, a nonlinear effect of piezoelectric micro-oscillators is investigated in dependence of the ambient pressure, leading to a novel pressure sensing concept with a very wide measurement range, exceeding the mechanical sensors commercially available on the market. Finally, the micro-oscillators are studied in a mixture of nitrogen and oxygen to test the possibility of their use as sensors for the measurement of oxygen concentrations.

The dissertation is structured as follows and starts in chapter 2 with the theoretical fundamentals. First, the different flow regimes are illustrated and the basic physical, thermal and magnetic properties of gases are introduced. This is continued by the mathematical description of the micro-oscillators based on the model of a linear and a nonlinear oscillator. Finally, the different damping mechanisms are presented and related to the different gas properties.

In chapter 3, the preliminary numerical investigations are presented. These include both, a finite element simulation of the eigenfrequency and an estimation of the damping effects based on the Navier-Stokes equations. In addition, a newly designed magnetic field concentrator is introduced for the study of the paramagnetic effect of oxygen by means of simulations.

Chapters 4 and 5 contain the experimental details of this dissertation. First, the manufacturing chain for the fabrication of the micro-oscillator structures is described and then the methods for quality assurance of the individual processing steps are shown. Next, the measurement environment and electronic circuit used for recording the damping behavior are introduced and characterized.

The experimental results and new findings are collected in chapter 6, where six journal publications and two sections of unpublished data can be found. More precisely, these are measurements of the molecular flow regime, thermal effects in the transitional flow regime, the consideration of higher modes, measurements in liquids, an equivalent circuit model for the damping effects and two applications (pressure sensor and oxygen sensor).

In chapter 7, the thesis is briefly summarized and in chapter 8, an outlook is given for possible future projects based on this dissertation.

2 Theoretical Background

In this chapter, the fundamental physical principles of the topic are explained and the latest available results from the literature are presented. It is divided into three parts, introducing and discussing the most relevant properties of gases, the theory of the harmonic oscillator and the damping mechanisms acting on a micro-oscillator.

2.1 Properties of Gases

In the following section, the basic properties of the experimentally measured gases are presented. First, the ranges of validity of the different models for the description of the properties are introduced and then the physical, thermal and magnetic properties are discussed. All these properties influence the oscillator and can be inferred from its response by evaluating the damping. The influence and strength of the individual properties differ widely between the flow regimes, thus depending strongly on the pressure of the gas atmosphere.

2.1.1 Flow Regimes

The properties of gases in a pressure range from high vacuum ($p = 10^{-3}$ mbar) to atmospheric pressure and above cannot be uniformly described by a single physical approach. In a dense gas, the gas molecules interact with each other and continuum theory is applicable, whereas in a highly diluted gas, the gas molecules only interact with the surrounding system and rarely with each other. The important parameter for distinguishing between the individual flow regimes is the so-called Knudsen number Kn . It is defined by the ratio of the mean free path length l_{mfp} to a characteristic length of the observed system l^* [11]. The mean free path in turn is a function of the diameter of the gas molecules (effective cross section) σ_{gas} , the pressure p and the absolute temperature T , thus yielding

$$Kn = \frac{l_{\text{mfp}}}{l^*} = \frac{k_{\text{B}}T}{\sqrt{2}\pi \cdot \sigma_{\text{gas}}^2 \cdot p \cdot l^*}, \quad (2.1)$$

with k_{B} the Boltzmann constant.

The Knudsen number divides the entire pressure range into three flow regimes: the molecular flow regime occurring in the low pressure range ($Kn > 1$), the viscous flow regime for higher pressures ($Kn < 0.01$) and in between the transition regime ($1 < Kn < 0.01$), also called Knudsen flow (see Figure 1) [12, 13]. Various values can be found in the literature for the boundaries between the flow regimes. In particular, for the transition to the molecular flow, values up to $Kn > 10$ can be found [10]. As will be shown later, the activation process of molecular degrees of freedom is investigated. For this purpose, a low intermolecular interaction is assumed, for which Knudsen numbers of $Kn = 0.5$ and 0.01 are taken as boundaries.

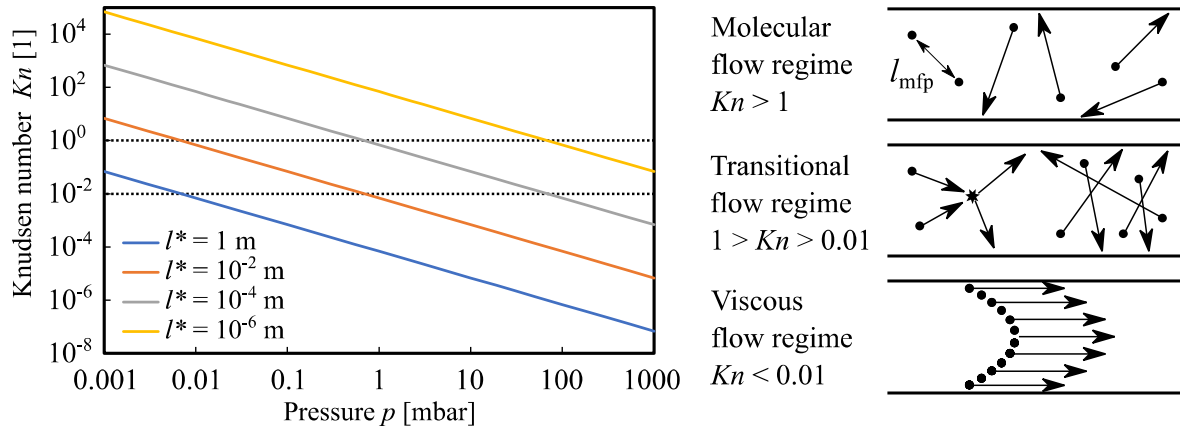


Figure 1. Knudsen number as a function of ambient pressure for various characteristic lengths. The Knudsen number divides the flow into the three schematically drawn regimes.

The characteristic length l^* is usually chosen by the smallest dimension of the system inclosing the gas. In this work, l^* is given by a variable gap width between the oscillator and a fixed counterplate. The behavior of the Knudsen number for different orders of magnitude of the characteristic length is shown in Figure 1. As can be seen at the transition into the micrometer range, the molecular flow already appears at medium pressures. Thus, for a microsystem, the rarefaction effects of Knudsen flow and molecular flow can be realized experimentally already by a relatively moderate vacuum.

In the viscous flow regime, the gas medium is considered as a continuum, whereby the behavior can be described via the Navier-Stokes equations. The microscopic structure is negligible, since the gas properties are defined by macroscopic quantities and distribution functions. In the molecular flow regime, on the other hand, the gas is described by means of the kinetic theory of gases. Here, there are no collisions or interactions between the individual gas molecules, but only with the geometric boundary. For the mathematical description, the Boltzmann equation is used, which can be solved by Monte Carlo simulations. For the transition regime, no closed theoretical description exists since both effects of the molecular and viscous flow regime are overlapping. With the help of these models, the physical and thermal properties of the gases can be predicted in the respective flow regime and will be explained in the following section.

2.1.2 Physical Properties

In Section 2.2.1 it is shown that the oscillatory behavior of our microstructures depends significantly on the damping. An essential part is given by the extrinsic damping of the surrounding gas medium. The strength of the damping thereby depends strongly on the physical properties of the individual gas atmosphere.

Table 1 lists the main physical properties of all gases used in this thesis. These are the monatomic noble gases He, Ne, Ar and Kr as well as the polyatomic gases H_2 , N_2 , CO_2 , N_2O and SF_6 . The gases differ strongly in their molar mass M_{mol} and their molecular structure. The large dynamic viscosity η of Ne is remarkable and leads to strong viscous friction losses.

Table 1. Listing of the main physical properties of the gas atmospheres investigated in this thesis for SATP conditions including the speed of sound c_{gas} and the number of atoms of the gas molecule N_{gas} [14].

Gas	M_{mol} [g/mol]	ρ [kg/m ³]	η [$\mu\text{Pa}\cdot\text{s}$]	c_{gas} [m/s]	N_{gas} -
H₂	2.016	0.082	8.915	1303	2
He	4.0026	0.164	19.85	1007	1
Ne	20.18	0.824	31.11	449	1
N₂	28.014	1.145	17.81	349	2
Ar	39.9	1.634	22.62	319	1
CO₂	44.009	1.808	14.93	268	3
N₂O	46.006	1.808	14.84	260	3
Kr	83.8	3.431	25.13	220	1
Xe	131.29	5.394	22.99	176	1
SF₆	146.06	6.038	15.12	135	7

The three essential state variables of a gas - volume V , pressure p and temperature T - are related to each other by the general gas equation [15]

$$pV = Nk_{\text{B}}T = n_{\text{mol}}R_{\text{gas}}T, \quad (2.2)$$

with N the number of molecules, n_{mol} the molar amount of the substance and R_{gas} the gas constant.

A constant quantity for all gases is the molar volume V_{mol} , the volume occupied by one mole of a gas

$$V_{\text{mol}} = \frac{M_{\text{mol}}}{\rho} = \frac{R_{\text{gas}}T}{p} = 24.47 \cdot 10^{-3} \frac{\text{m}^3}{\text{mol}}, \quad (2.3)$$

under standard ambient temperature and pressure (SATP) of $T = 298.15$ K and $p = 1.013$ bar.

This relationship shows that the size of the molar mass respectively the weight of the gas molecule m ($= M_{\text{mol}}/N_{\text{A}}$) and the density of a gas are equivalent. Following the microscopic view, the molecular mass is used as correlating quantity in the range of the molecular flow regime, whereas the density as macroscopic quantity is used for the viscous flow regime.

The dynamic viscosity μ of an ideal gas can be derived from the momentum flux of parallel neighboring gas layers [16]:

$$\mu = \frac{1}{3} n_{\text{mol}} m \tilde{v} l_{\text{mfp}} = \frac{2 \sqrt{mk_{\text{B}}T}}{3 \pi^2 \sigma_{\text{gas}}^2}, \quad (2.4)$$

where Equation (2.5) was used for the mean thermal velocity \tilde{v} and Equation (2.1) for the mean free path length l_{mfp} .

For the viscous flow range, a dynamic viscosity is obtained which is independent of the pressure. At the transition to the molecular flow range, the mean free path is given by the characteristic length, which results in a linear dependence of the viscosity to the pressure.

2.1.3 Thermal Properties

In this work, a novel concept is presented for the description of the transition regime, which is based on the energy dissipation by resonance effects of standing thermal waves. The efficiency of this loss mechanism is strongly depending on the frequency and on the thermal properties of the gases. For this reason, the thermal properties of the gases deserve special attention. They are listed in Table 2.

Table 2. Thermal properties of the gases measured in this work [14]. The adiabatic index κ , the number of degrees of freedom (DOF) f_{DOF} and the thermal diffusivity a are calculated from the material properties according to the given equations.

Gas	λ [mW/m·K]	C_p [kJ/kg·K]	κ -	f_{DOF} -	a [mm ² /s]	\tilde{v} [m/s]
H ₂	184.88	14.31	1.405	4.93	157.02	1555
He	155.31	5.19	1.667	3.00	182.92	1103
Ne	48.08	1.03	1.667	3.00	56.62	491
N ₂	25.84	1.04	1.401	4.98	21.67	417
Ar	17.75	0.52	1.670	2.99	20.83	349
CO ₂	16.64	0.85	1.294	6.80	10.82	333
N ₂ O	18.45	0.88	1.280	7.13	11.55	325
Kr	9.36	0.25	1.672	2.98	10.95	241
Xe	5.54	0.16	1.677	2.95	6.41	193
SF ₆	13.41	0.67	1.098	20.33	3.32	183

The thermal velocity of the gas molecules can be calculated using the kinetic theory of gases and results in the Maxwell-Boltzmann distribution. The expected value of the distribution corresponds to the mean velocity [16]

$$\tilde{v} = \sqrt{\frac{8k_B T}{\pi m}}. \quad (2.5)$$

An important factor for describing thermal losses is the ability of a gas to transport heat through a gas medium. This property is described by the thermal conductivity λ and can be derived analogously to the dynamic viscosity (see Equation (2.4)) as a function of the specific heat capacity at constant volume C_V and the number of degrees of freedom (DOF) f_{DOF} [16]:

$$\lambda = \frac{1}{3} C_V \rho \tilde{v} l_{\text{mfp}} = \frac{f_{\text{DOF}}}{3\sigma_{\text{gas}}^2} \sqrt{\frac{k_B^3 T}{\pi^3 m}}. \quad (2.6)$$

Similarly to the dynamic viscosity, the thermal conductivity is a pressure-independent quantity within the viscous flow regime. In the molecular flow regime, l_{mfp} can be replaced by the constant characteristic length, resulting in a thermal conductivity, which decreases with pressure.

The isentropic exponent κ defined by the ratio of the heat capacity at constant pressure C_p to the heat capacity at constant volume C_V

$$\kappa = \frac{C_p}{C_V} = \frac{f_{\text{DOF}} + 2}{f_{\text{DOF}}} \quad (2.7)$$

describes the thermal characteristic behavior in adiabatic processes. The ratio is strongly dependent on the number of active degrees of freedom and is thus a temperature-dependent quantity. A pressure dependence results from the fact that in the molecular flow regime the required number of molecular collisions for the activation of rotational or vibrational degrees of freedom is no longer given. However, this effect can only occur in the case of polyatomic gases since the monoatomic noble gases possess only three translational degrees of freedom and cannot exhibit any higher degrees of freedom.

Equally crucial is the thermal diffusivity

$$a = \frac{\lambda}{\rho C_p} \quad (2.8)$$

of a gas. This ratio of thermal conductivity to the product of density and heat capacity at constant pressure reflects the ability of a gas to conduct or store thermal energy. This thermal diffusivity is a measure of the efficiency of heat transport through a gas medium. Noble gases exhibit the highest values in this context. This is attributed to the fact that noble gases have only three translational degrees of freedom and therefore cannot store thermal energy effectively. Furthermore, they have a high particle velocity, which means that heat can be transported quickly. Polyatomic gases, on the other hand, have more degrees of freedom in which thermal energy can be stored and are significantly slower due to their larger mass, which together leads to a lower thermal diffusivity.

2.1.4 Magnetic Properties

Based on the micro-oscillators presented in this work, a new concept for the detection of oxygen concentration is presented. Within these measurements, the paramagnetic effect of oxygen will be explored [17, 18, 19]. Here oxygen is selectively accumulated in a spatially defined area in the vicinity of the oscillator and proofed with the aid of the resulting change in the oscillation behavior.

The magnetic properties of materials under the influence of a magnetic field \vec{H} are divided into three classes: diamagnetism, paramagnetism and ferromagnetism. The resulting magnetic flux density \vec{B} is given as a superposition of the externally applied magnetic field \vec{H} and the generated magnetization \vec{M} within the material:

$$\vec{B} = \mu_0(\vec{H} + \vec{M}), \quad (2.9)$$

with μ_0 the vacuum permeability $1.26 \cdot 10^{-6} \text{ N/A}^2$.

The magnetization is strongly dependent on the material class and is given by the magnetic susceptibility χ_r or, alternatively, by the magnetic permeability μ_r :

$$\vec{M} = \chi_r \vec{H} = (\mu_r - 1) \vec{H}. \quad (2.10)$$

In the case of diamagnetism ($\chi_r < 0$, $0 < \mu_r < 1$), the magnetization is opposite to the external magnetic field and therefore leads to an attenuation of the magnetic flux density. The reason for this phenomenon is that magnetic dipoles are generated according to Lenz's law, which are opposite to their source. Paramagnetic materials ($\chi_r > 0$, $\mu_r > 1$), on the other hand, orient their magnetic moments along the external magnetic field and thus amplify the resulting magnetic flux density. These materials possess magnetic moments of electron spins that align under the action of an external magnetic field. The oxygen molecule O_2 belongs to this class due to two unpaired electrons in the outer L-shell. The class of ferromagnetic materials is characterized by a complex dependence between the magnetic permeability to the external magnetic field as well as the temperature ($\mu_r = \mu_r(\vec{H}, T)$). Further characteristics are a strong nonlinearity as well as a residual magnetization, so-called remanence, after switching off the external magnetic field.

Table 3 lists the main components of air. It can clearly be seen that, except for oxygen, all the main components exhibit diamagnetic behavior. This makes it possible to use the paramagnetic effect to distinguish oxygen from the other components. Besides oxygen, there are three other diamagnetic gas molecules, ozone O_3 and the nitrogen oxides NO_2 and NO . However, these gases are present in such low concentrations that no significant influence on the measurement can be expected.

Table 3. Listing of the essential components of air and their volume fraction φ_V as well as the molar χ_{mol} and volume magnetic susceptibility χ_{vol} .

Gas	φ_V % [20]	χ_{mol} $10^{-12} \text{ m}^3/\text{mol}$ [21]	X_{vol} 10^{-9}
N₂	78.08	-150.80	-6.7
O₂	20.95	42914.15	1909
Ar	0.93	-242.78	-10.8
CO₂	0.0413 [22]	-263.89	-11.7
Ne	0.00182	-87.46	-3.9
He	0.00052	-25.38	-1.1
CH₄	0.00017	-218.65	-9.7
O₃	0.0001	84.19	3.8
NO₂	0.000035	1884.96	83.9
NO	0.000028	18359.47	817.1

The magnetic force F_{magn} on a gas volume V under the influence of an inhomogeneous magnetic field \vec{H} is given by [23]:

$$\vec{F}_{\text{magn}} = V\mu_0\chi_r(\vec{H} \cdot \nabla)\vec{H}. \quad (2.11)$$

The direction of the force effect depends on the material class. Paramagnetic gas molecules are accelerated in the direction of the magnetic field gradient towards the focal point of the magnetic field. Diamagnetic gas molecules, on the other hand, are pushed out of the magnetic field focus. This results in an enrichment of paramagnetic oxygen molecules with simultaneous expulsion of diamagnetic gas components such as nitrogen N_2 and argon Ar. Ueno *et al.* describes this effect by introducing a “magnetic curtain” created by the oxygen enrichment zone [24]. The strength of the enrichment depends on the initial concentration of the oxygen molecules and therefore allows the concentration to be determined [25]. The change of oxygen concentration in the magnetic field focus in the vicinity of the oscillator is indicated by a change of the damping. In this work, a correlation between the oxygen concentration and the change of the oscillatory behavior, given by quality factor Q and resonance frequency f_r , will be shown as a functional proof of the oxygen sensor concept and the paramagnetic effect will be investigated (see Section 6.8).

2.2 Harmonic Oscillator

The theory of the harmonic oscillator is widely used to describe both mechanical and electrical oscillating systems. With this approach, the oscillation behavior of vibrating systems and the amplitude increase in the resonance case can be described precisely. The oscillator and its damping are unambiguously determined based on two characteristic quantities, the resonance frequency f_r and the quality factor Q .

2.2.1 Linear Harmonic Oscillator

The micro-oscillators investigated in this thesis can be seen as an externally excited damped harmonic oscillator and thus be modeled by the theory known in the literature. The micro-oscillators are simplified to a suspended mass m , which can be deflected by a beam structure with spring constant k . The actuation is realized via the force of a piezoelectric thin film acting on the beam structure. Due to the oscillation in a medium, the oscillator suffers a damping given by the linear damping constant d , which leads to the following differential equation [26]:

$$m\ddot{x} + d\dot{x} + kx = F(t) = F_0 \sin \omega t. \quad (2.12)$$

The periodic force $F(t)$ with the angular frequency $\omega (= 2\pi f)$ of the piezoelectric thin film can be calculated via the mechanical stress σ acting on the actuator surface S as a function of the applied electric field E and the piezoelectric coefficients d_{ij} . The electric field is given by the ratio of the applied voltage U to the piezoelectric layer thickness H_{AlN} , which results in a force amplitude

$$F_0 = \sigma S = d_{31}E_3S = d_{31}S \frac{U}{H_{\text{AlN}}}. \quad (2.13)$$

In a simplified way, the matrix is reduced to one dimension. In our case, an electric field is generated in the z -direction (3rd axis) which leads to a lateral expansion (in the x -direction, 1st axis). This expansion of the piezoelectric thin film is converted into a deflection in the z -direction, due to the rigid connection to the underlying silicon solid bulk material.

A special phenomenon of harmonic oscillators is the amplitude magnification when the oscillating system is actuated in its eigenfrequency, the so-called resonance frequency ω_r . The deflection amplitude $A(\omega)$ when excited with the angular frequency ω is given by [26]:

$$A(\omega) = \frac{F_0}{m \sqrt{(\omega^2 - \omega_r^2)^2 + \left(\frac{\omega\omega_r}{Q}\right)^2}} \quad (2.14)$$

with the new abbreviations

$$\omega_r = \sqrt{\frac{k}{m}} \quad (2.15)$$

for the resonance frequency of the oscillators and its quality factor

$$Q = 2\pi \frac{E_0}{\Delta E} = \frac{1}{2D} = \frac{m\omega_r}{d} = \frac{f_r}{\Delta f} \quad (2.16)$$

The quality factor Q is a measure of the dissipation-free nature of an oscillator and the reciprocal of the damping ratio D . It is defined by the ratio of the energy E_0 stored in the oscillator to the energy losses within one oscillation period ΔE . Experimentally it can be measured by the ratio of the resonance frequency f_0 to the 3 dB bandwidth Δf (see Figure 2a). Figure 2a shows the normalized amplitude function for various Q factors. For decreasing Q (equivalent to the increase in damping), the maximum achievable amplitude drops significantly.

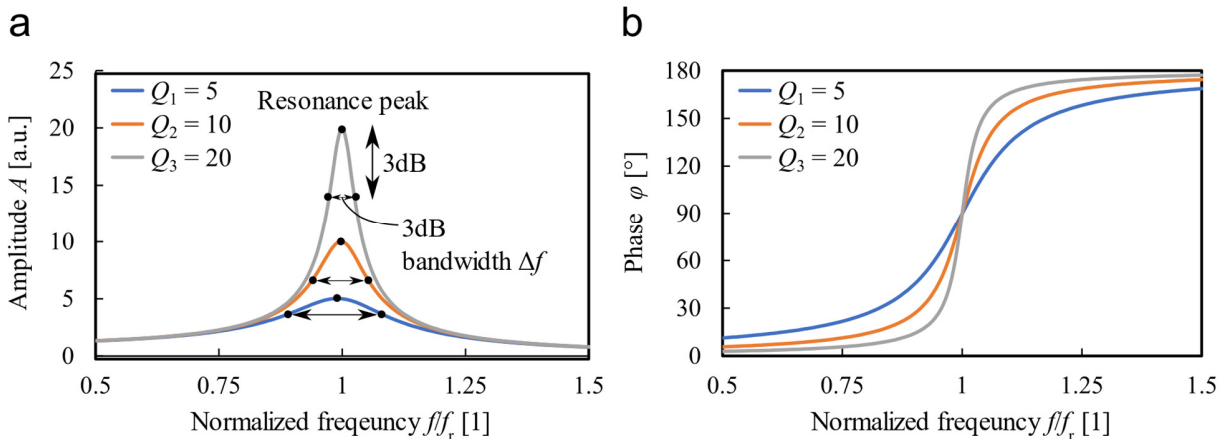


Figure 2. Normalized amplitude function (a) and phase shift (b) in the resonance case shown for different quality factor values Q .

Furthermore, the resonance frequency shifts slightly to the left, which is described by Equation (2.17):

$$\omega_D = \omega_r \sqrt{1 - \frac{1}{4Q^2}}. \quad (2.17)$$

The phase shift φ between the actuation and the deflection movement of the oscillators is given by following equation and is displayed in Figure 2b:

$$\varphi = \tan^{-1} \left(\frac{1}{Q} \frac{\omega_r \omega}{\omega_r^2 - \omega^2} \right). \quad (2.18)$$

As can be seen, for a low excitation frequency, the oscillator can follow the excitation with only a small phase shift. In the resonance case, the phase shift is exactly 90° , whereby the excitation energy is always supplied to the oscillator with exact timing and consequently there is a buildup of the amplitude, the so-called resonance peak. When the frequency increases above resonance, the system can no longer follow the excitation and will start oscillating in the opposite direction to the excitation. The amplitude drops significantly as a result.

When driving the oscillator in its resonance frequency, the system needs a certain period of time τ until the oscillation amplitude reaches its maximum value according to Equation (2.14). In the transient process, energy is supplied to the oscillator until the supplied energy and the energy dissipated per oscillation are equal [27]. The higher the quality factor of the oscillator, the longer the time period until the oscillator reaches the stationary range. The same applies for the decay process. After switching off, the oscillator vibrates for a decay time τ until the dissipation of its complete energy. The entire transient behavior can be seen in Figure 3 and is described as follows:

$$A(t) = \begin{cases} \frac{F_0}{k} Q \left(1 - e^{-\frac{\omega_D t}{2Q}} \right) \sin(\omega_D t) \\ \frac{F_0}{k} Q \sin(\omega_D t) \\ \frac{F_0}{k} Q e^{-\frac{\omega_D t}{2Q}} \sin(\omega_D t). \end{cases} \quad (2.19)$$

The transient behavior can therefore also be used to determine the quality factor experimentally by evaluating the time constant τ until the amplitude reaches the decay value [28]:

$$\tau = \frac{2Q}{\omega_D}. \quad (2.20)$$

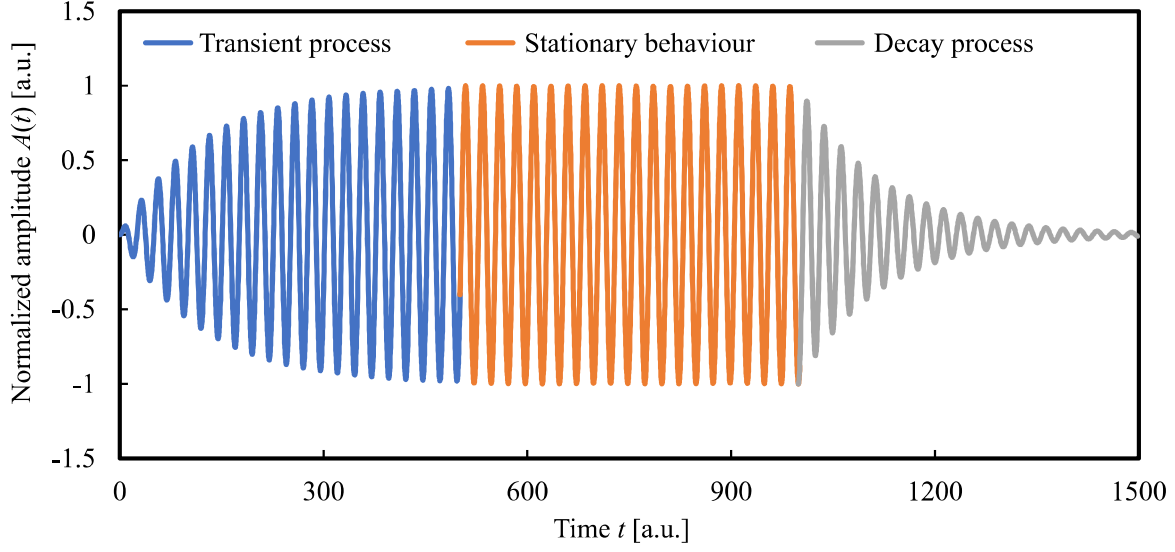


Figure 3. Normalized amplitude of an oscillator during transition (blue), stationary, (red) and decay (green) process.

The micro-oscillators investigated in this thesis are divided into three categories regarding their shape: Paddle-oscillators (PO), Beam-oscillators (BO) and Cantilever-oscillators (CO). The schematic geometries including the variable parameters are illustrated in Figure 4.

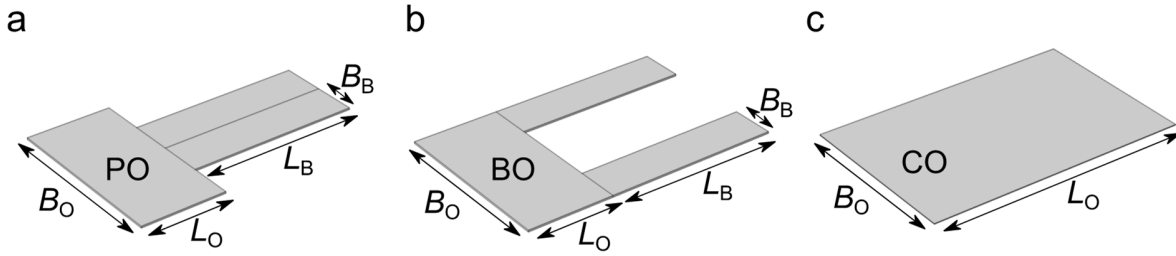


Figure 4. 3D illustration of the investigated micro-oscillators including the geometric sizes for the variation of the eigenfrequency for a paddle-oscillator (a), beam-oscillator (b) and cantilever-oscillator (c).

For the analytical derivation of the resonance frequency of such an oscillating structure with thickness H , the expression for the spring constant of a rectangular beam is required [29, 30]:

$$k_B = \frac{3EI}{L^3} = \frac{EB_B H^3}{4L^3}. \quad (2.21)$$

In the following, the structures PO and BO are assumed as two spring constants connected in parallel $k = k_B || k_B = 2k_B$, representing the two identical beams with a length of $L = L_B + L_O$. For the cantilever structures CO, the width of the beam B_B and the length of the Beam L_B are equal to the width B_O and the length L_O of the cantilever, respectively.

The mass can be calculated by the density-volume product, whereby an effective mass m_{eff} is introduced. The mass of the micro-oscillator is reduced by a factor α_{eff} ($0 < \alpha_{\text{eff}} < 1$) attributed to the effect that not the entire structure is oscillating. In [31] a value of $\alpha_{\text{eff}} = 0.24$ is given for a cantilever structure:

$$m_{\text{eff}} = \alpha_{\text{eff}} \cdot m = \alpha_{\text{eff}} \cdot \rho \cdot V = \alpha_{\text{eff}} \cdot \rho \cdot H \cdot \begin{cases} 2B_B L_B + B_O L_O & \text{for PO and BO} \\ B_O L_O & \text{for CO} \end{cases}. \quad (2.22)$$

Considering Equation (2.15), this leads to an eigenfrequency of the micro-oscillator as function of the material properties (E Young's modulus and ρ density) and the geometric dimensions:

$$\omega_r = \begin{cases} H \sqrt{\frac{E}{2\alpha_{\text{eff}}\rho} \frac{B_B}{(L_B + L_O)^3 (2B_B L_B + B_O L_O)}} & \text{for PO and BO} \\ \frac{H}{2L_O^2} \sqrt{\frac{E}{\alpha\rho}} & \text{for CO} \end{cases} \quad (2.23)$$

Besides the fundamental eigenfrequency, an oscillator possesses a variety of eigenfrequencies respectively eigenmodes which can be classified into four groups: Bending modes, torsional modes, lateral modes and more complex modes like the roof-tile-shape modes [32]. The eigenfrequencies ω_n of the higher bending modes with mode number n can be derived from the Timoshenko beam theory [33, 34] as a function of the fundamental frequency and the eigenvalue λ :

$$\omega_n = \lambda_n^2 \omega_r. \quad (2.24)$$

The eigenvalues are given as a transcendent equation ($\cos(\lambda_n) \cosh(\lambda_n) + 1 = 0$) leading to $\lambda_n = 1.88; 4.69; 7.86; 11.00; 14.14$ for the first five bending modes [31].

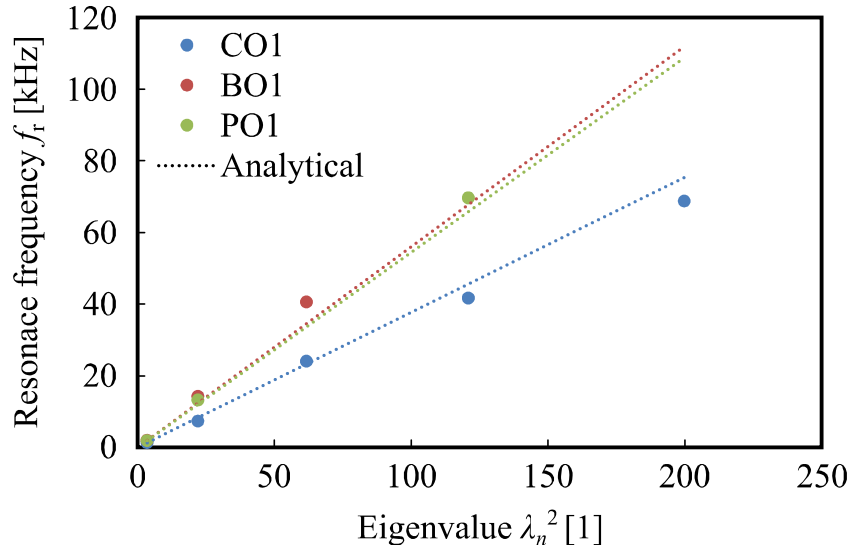


Figure 5. Resonance frequency of different geometric shapes of micro-oscillators versus the squared eigenvalue of the higher bending modes.

Figure 5 shows the plot of the eigenfrequencies for various micro-oscillator shapes presented in this thesis. The experimentally determined eigenfrequencies are in good agreement with the analytical expression derived in Equation (2.23). The effective mass factor α_{eff} is determined to be $\alpha_{\text{eff, CO}} = 0.88$ for cantilevers, $\alpha_{\text{eff, BO}} = 0.62$ for beam-oscillators and $\alpha_{\text{eff, PO}} = 0.63$ for paddle-oscillators.

Further discussion of this analytical approach is presented in the simulation section (see Section 3.1), where the model is compared with the results of three-dimensional finite element simulations as well as in the experimental section (see Section 6.5), where the experimental results are taken into account.

2.2.2 Nonlinear Harmonic Oscillator

An extension of the previously presented theory of the linear harmonic oscillator is offered by the concept of G. Duffing from 1918 [35], where nonlinearities are included by adding a cubic term for the restoring force. These effects can occur e.g. in the case of high oscillation amplitudes, when the restoring force is no longer linear with the deflection. The differential Equation (2.12) is expanded by the nonlinear cubic stiffness parameter β :

$$m\ddot{x} + d\dot{x} + kx + \beta x^3 = F(t) = F_0 \sin \omega t. \quad (2.25)$$

The frequency response of nonlinear Duffing oscillators can be solved by different approaches [36] (e.g. homotopy analysis method [37]) and the result for linear viscous damping can be found in [38]:

$$A(\omega)^2 = \frac{F_0^2}{m^2 \sqrt{\left(\omega^2 - \omega_r^2 - \frac{3\beta}{4m} A(\omega)^2\right)^2 + \left(\frac{\omega \omega_r}{Q}\right)^2}} \quad (2.26)$$

The phase shift between the amplitude and actuation can be specified by:

$$\varphi = \tan^{-1} \left(\frac{\omega_r}{Q} \frac{1}{\omega - \omega_r - \frac{3\beta}{8m\omega_r} A(\omega)^2} \right). \quad (2.27)$$

The frequency response of the amplitude (and phase) is given in an implicit form, leading to a not single-valued function. Depending on the sign of the nonlinear stiffness parameter β , the resonance curve tilts to the left ($\beta < 0$) or to the right ($\beta > 0$). A value of $\beta = 0$ leads to the solution of the linear harmonic oscillator (compare Figure 2a). Phenomenologically, a negative value of β means a softening of the spring, whereas a positive value of β means a hardening of the spring.

Solutions of Equations (2.26) and (2.27) are illustrated in Figure 6. Three regions can be identified: A stable range with one solution, a jump point with two solutions and an unstable range with three solutions for the amplitude at a given frequency. Depending on the frequency direction, the oscillator follows the amplitude function until the discontinuous transition at the jump point. Therefore, a hysteresis curve results when comparing the amplitude curves in both frequency directions. Due to the correlation of the phase with the amplitude function, this jump behavior can also be seen in the phase.

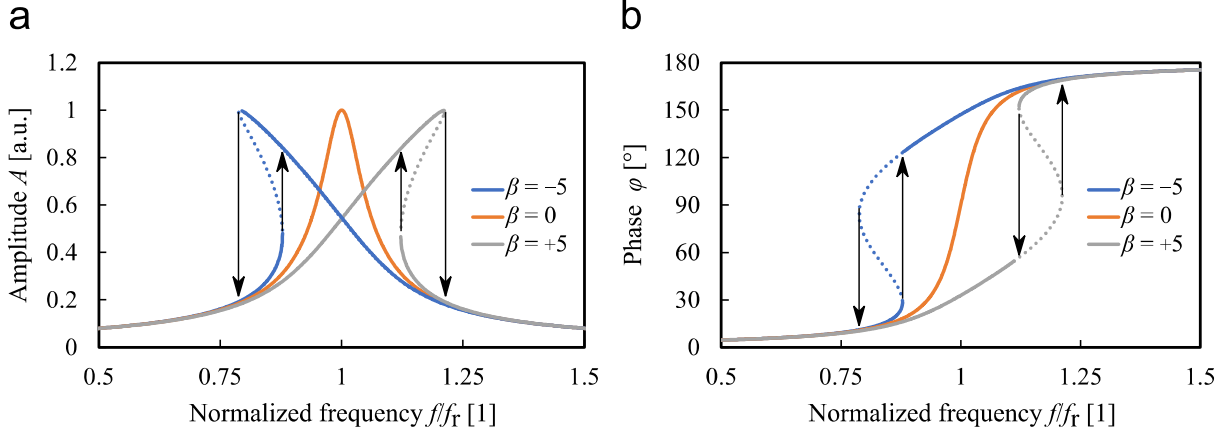


Figure 6. Frequency response of a nonlinear oscillator for various nonlinear stiffness parameters: Amplitude (a) and phase (b).

The composition and calculation of the nonlinear stiffness parameter to influence the nonlinearity regarding softening/hardening effect (sign of β) as well as the strength (absolute value of β) is recently being discussed in the literature. In general, two competing effects occur [39]: the geometrical part β_{geo} , which has a hardening effect and inertial effects β_{inertial} , which exhibit a softening behavior [40, 41]. Due to the stiffness of the solid (especially at the anchorage), the geometry of the oscillator counteracts the deflection movement towards the neutral position and therefore hardens the spring. Inertial effects are enhanced by higher kinetic energies, which occur at higher resonance frequencies respectively higher modes. Additionally, piezoelectrically actuated oscillators possess a piezoelectric nonlinearity β_{piezo} with a softening influence [42]. The total nonlinear stiffness parameter is given by the superposition of these three effects:

$$\beta = \beta_{\text{geo}} - \beta_{\text{inertial}} - \beta_{\text{piezo}}. \quad (2.28)$$

Based on this description, the nonlinearity can be adjusted by varying the geometry (size as well as anchoring), the eigenmode and the piezoelectric layer. For use in some pressure sensing applications, the aim is to maximize the nonlinear effect. Previous works by Kulygin *et al.* [43] and by Nabholz *et al.* [44] already showed the nonlinear behavior of electrostatically excited oscillators in dependence of the ambient pressure. Based on this phenomenon, a novel concept for the detection of ambient pressure based on nonlinear piezoelectric oscillators is presented in this thesis (see Section 6.7).

2.3 Damping Mechanism

In the previous section, the model of the damped harmonic oscillator was discussed. On closer inspection it turns out that the damping, respectively the quality factor, is composed of several loss mechanisms. The resulting total quality factor Q_{tot} measured in the experiment is given by the superposition of various damping mechanisms in the following way [31]:

$$Q_{\text{tot}} = \left(\frac{1}{Q_{\text{int}}} + \frac{1}{Q_{\text{gas}}} \right)^{-1} = \left(\frac{1}{Q_{\text{int}}} + \frac{1}{Q_{\text{mol}}} + \frac{1}{Q_{\text{trans}}} + \frac{1}{Q_{\text{vis}}} \right)^{-1}. \quad (2.29)$$

The individual damping mechanisms are listed and explained in the following sections. They are also classified with respect to their relevance for piezoelectrically driven oscillators. Furthermore, the models of extrinsic damping by the surrounding gas molecules are subdivided into three categories based on the flow regimes (see Section 2.1.1). One is the viscous damping following the continuum mechanics and the other is molecular damping, which relies on the energy transfer of the oscillator to the gas molecules via collision processes. For the transitional regime in between, a new approach to describe the prevailing damping effect based on thermal resonance effects is introduced.

2.3.1 Intrinsic Damping

The intrinsic damping refers to the loss mechanisms that occur within the solid-state material. These losses are divided into several classes (anchor [45], surface [46], Akhiezer [47], internal friction/thermoelastic [48], residual-stress [49]), which were investigated by the group of T. Kenny, among others. The strength of this attenuation results in a quality factor in the range of a few hundred up to about a million. Such high quality factor values cannot be achieved with piezoelectric micro-oscillators because of the damping due to the intrinsic stress caused by the piezoelectric thin film layer, which is in the range of several thousand. Therefore, the stress induced damping from the piezoelectric layer stress is the dominant loss effect. There are no analytical solutions for the damping caused by layer stress in the literature available. Qiu *et al.* gives an empirical model for cantilevers with the proportionality to the ratio of the cantilever thickness H to thickness of the coating H_{coat} as well as the ratio of the cantilever length L to the length of the coated thin film L_{coat} [49]:

$$Q_{\text{coat}} = k \frac{H}{H_{\text{coat}}} \frac{L}{L_{\text{coat}}}, \quad (2.30)$$

k is a proportionality factor to be determined experimentally, which depends on the geometry and the bulk viscoelasticity of the coated thin film.

Fundamental to this thesis is the thermoelastic damping model developed by Zener [50, 51]. This theory describes the intrinsic damping in a solid-state oscillator based on the resonance effect of thermal waves. Due to the bending movement of an oscillator, the surfaces of the solid-state material get heated and cooled, caused by the mechanical stress on the structures. This temperature gradient between the stretched and compressed area leads to an irreversible heat flow via thermal waves through the structure dissipating energy and thus reducing the quality factor. When the mechanical and the thermal resonance frequency match each other, this effect leads to a maximum of heat dissipation within the bulk material. The resulting quality factor Q_{TED} can be specified as a function of the bulk properties of the micro-oscillator (ρ density, C_p heat capacity at constant stress, α coefficient of thermal expansion, E Young's modulus, λ thermal conductivity and a thermal diffusivity), its thickness H and its resonance frequency f_r [52]:

$$Q_{\text{TED}} = \frac{\rho C_p}{\alpha^2 T E} \frac{f_r^2 + f_{\text{th}}^2}{f_r f_{\text{th}}} \text{ with } f_{\text{th}} = \frac{\pi \lambda}{2 \rho C_p H^2} = \frac{\pi a}{2 H^2}, \quad (2.31)$$

whereby T is indicating the absolute temperature and f_{th} the thermal resonance frequency of the micro-oscillator.

This model of energy dissipation via the resonance of thermal waves is applied in this thesis to the oscillation of a micro-oscillator in a gas medium limited by a gap. The derivation of this approach can be found in Section 2.3.4 and is experimentally investigated in Section 6.3.

2.3.2 Molecular Damping

The extrinsic damping by a surrounding gas medium is differentiated with respect to the density of the gas molecules, respectively the flow regime (see Section 2.1.1). In the case of a low density, the gas is present in a highly diluted form and is referred to the molecular flow regime. The interaction of the gas molecules with each other is reduced to a few collisions and therefore takes place mainly with the geometric boundaries in the vicinity as well as with the oscillator.

Christian [53] developed in 1968 the first theoretical approach for the damping of oscillating structures within the molecular flow regime. The concept is based on a pressure gradient between the top and bottom side of the oscillator caused by its displacement. The pressure gradient is assumed to be caused by the change of momentum of the surrounding gas molecules, striking the oscillator. Consequently, the quality factor Q_{Chr} in the molecular flow regime can be specified as [54]:

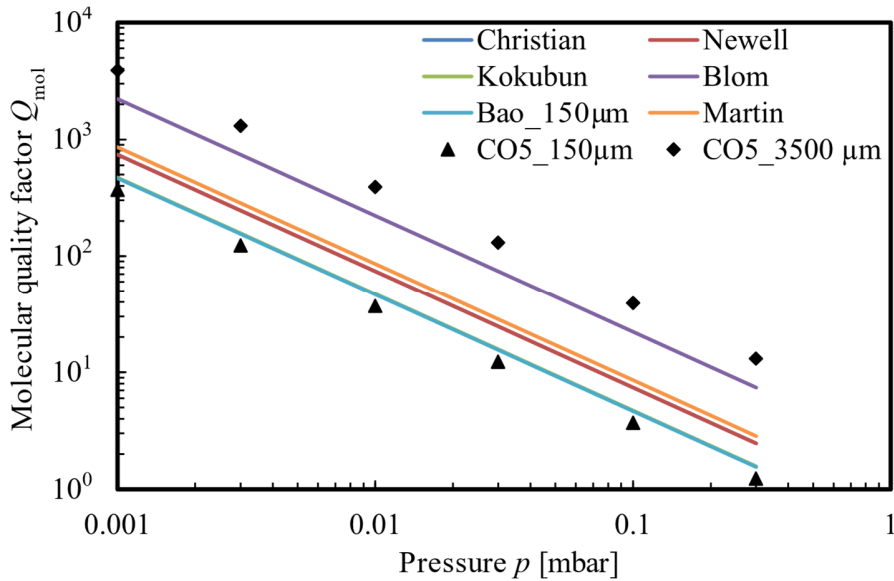
$$Q_{\text{Chr}} = \frac{\lambda_n^2}{4} \left(\frac{H}{L}\right)^2 \sqrt{\frac{\rho E}{12}} \sqrt{\frac{\pi k_B T}{2 M_{\text{mol}} p}}. \quad (2.32)$$

This model is the fundamental basis of further works with the aim of describing the damping behavior in the molecular flow regime. A limitation of the model is its restricted validity only in the case that there are no geometrical boundaries near the oscillator. Therefore, the model of Bao *et al.* considering an oscillator located nearby a wall is an important extension to the theory of damping in the molecular flow regime. In contrast to Christian's momentum transfer model, Bao describes the damping by means of an energy transfer through elastic collisions, leading to an additional dependence on the gap width h and on the oscillator perimeter U_O (see Table 4). However, Bao's theory is only valid for narrow gap widths in the squeeze film damping regime (see Section 2.3.5). The newest development was presented by Martin *et al.* by taking the thermal effects as well as accommodation efficiency into account. In Table 4, an approximation is given for the case of an isothermal system with full momentum accommodation [55]. Further investigations lead to comparable results, which all can be related to Christian's quality factor and are differing only in a proportionality constant. Moreover, the interaction between the gas molecules and the oscillatory movement in the molecular flow regime can be investigated numerically by the lattice Boltzmann method [56] and also by direct simulation with the Monte Carlo method [57].

Table 4. Comparison of theories for the quality factor of micro-oscillators in the molecular flow regime.

Theory	Quality factor
Newell [58]	$Q_{Newell} = Q_{Chr}$
Kokubun [59]	$Q_{Kokubun} = \left(\frac{2}{\pi}\right) Q_{Chr}$
Blom [60]	$Q_{Blom} = 3 Q_{Chr}$
Bao [61]	$Q_{Bao} = 16\pi \left(\frac{h}{U_O}\right) Q_{Chr}$
Martin [55]	$Q_{Martin} = \frac{8}{\sqrt{\pi}} \frac{1}{1 + \sqrt{\pi} + \frac{2}{\sqrt{\pi}}} Q_{Chr} \approx 0.65 Q_{Chr}$

A summary of the theories for the damping in the molecular flow regime can be found in Table 4 and the corresponding curves are plotted in Figure 7. For comparison, the experimental results of the minimum and maximum values for the gap width used in our investigations are included. They run parallel to the theoretical curves and enclose them, but differ significantly. Therefore, an open issue is a better description of the damping mechanism as well as the transition from a nearly freely vibrating micro-oscillator to narrow gap widths. Within the scope of this thesis, a new model for the description of the transition from squeeze film gap width ($h = 150 \mu\text{m}$) up to huge gap widths of several millimeters (up to $3500 \mu\text{m}$) is presented (see Section 6.2 and 6.4).

**Figure 7.** Plot of the molecular quality factor Q_{mol} as function of the ambient pressure. The experimental results (points) of the maximum and minimum gap width used in our investigations enclose the presented theories (solid lines) listed in Table 4.

2.3.3 Viscous Damping

In the viscous flow regime, continuum mechanics can be applied to describe the damping effects. For the mathematical formulation the Navier-Stokes equation is used, which is based on the macroscopic quantities of a gas like density and viscosity. For simple cases, closed-form solutions exist, using special approximations and semi-empirical formulations [62]. As an example, Kokubun *et al.* [59] and Blom *et al.* [60] approximate the geometry of the micro-oscillator by a chain of oscillating spheres or discs, respectively. The quality factor in the viscous flow regime is derived analytically by Hosaka *et al.* [63] by means of the Navier-Stokes equation for a beam oscillator as function of the ambient pressure p , which is equivalent to the expression by Kokubun:

$$Q_{\text{Hosaka}} = \frac{\rho B H}{3\pi \left(\frac{\mu}{\omega_r} + \frac{B}{4} \sqrt{\frac{2\mu M_{\text{mol}} p}{\omega_r k_B T}} \right)} = Q_{\text{Kokubun}}, \quad (2.33)$$

with density ρ , width B and thickness H of the micro-oscillator with resonance angular frequency $\omega_r (= 2\pi f_r)$ vibrating in a fluid with dynamic viscosity μ , molecular Mass M_{mol} and temperature T .

Recent developments by Zhang *et al.* [64] and by Vignola *et al.* [65] discuss different approximations depending on the aspect ratio of the width of the micro-oscillator to its thickness. This results in the fact that the pressure independent part in Equation (2.33) can be neglected and leads to a reciprocal dependence on the square root of the ambient pressure [66]. Advanced theories introducing hydrodynamic functions presented by Sader [67] and applied by Dufour [68] for MEMS devices as well as based on Bessel functions used by Aoust *et al.* [69] lead to comparable results but require a higher computational effort.

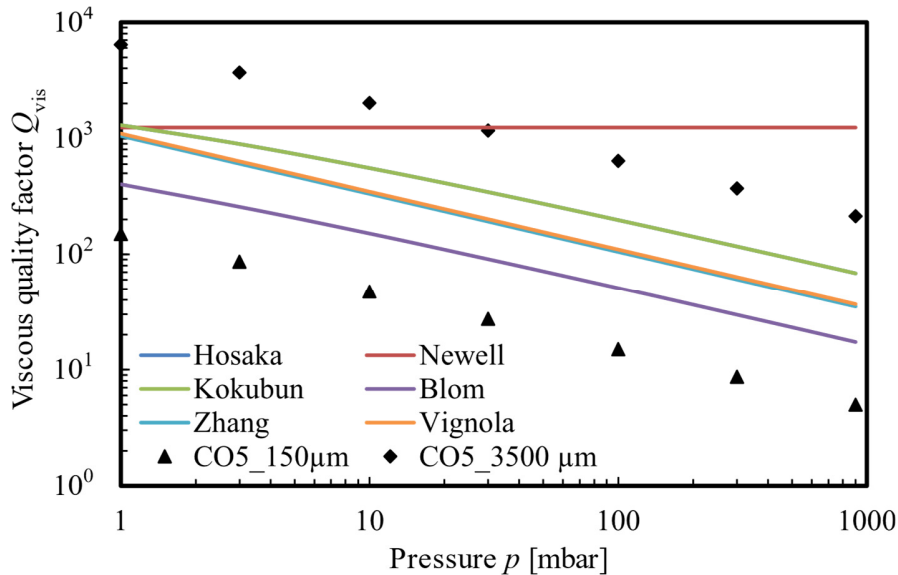


Figure 8. Plot of the viscous quality factor Q_{vis} as function of the ambient pressure. The experimental results (points) of the maximum and minimum gap width enclose the presented theories (solid lines). The blue line (Hosaka) is masked by the green line (Kokubun), due to the equality of the equations.

2.3.4 Damping in the Transitional Flow Regime

The description of the transition regime between molecular (single particle) and viscous flow (continuum) is extremely challenging since none of the previously presented theories can be applied directly. Partially, some of the theories mentioned before can be extended to cover some effects, but are not valid for the whole transitional flow regime [70]. Up to a Knudsen number of $Kn = 0.1$ the Navier-Stokes equations can be applied with the additional slip flow boundary condition at the solid-gas interface [71, 72]. Therefore, this regime is also called slip flow regime. At the crossover between molecular flow regime and transitional flow regime, the lattice Boltzmann method still can be used but requires higher numerical efforts because of the increasing number of particles and particle interactions [73, 74]. For the transition regime, a higher development of the Navier Stokes equations was successfully introduced [70]. It is the development in the second order of the Knudsen number from the thermal equilibrium and leads to the so-called Burnett equation. As for the Navier-Stokes equations, analytical solutions can only be derived for individual special problems (e.g spheres and discs) and require numerical methods for their solution [75, 76, 77, 78].

In a rarefied gas, the thermal transport distance is in the range of the mean free path of the energy carriers so that there is a significant difference to thermal conduction of the bulk material in the continuum regime. Therefore, special effects in the transitional flow regime like temperature discontinuities, respectively jumps appear [79, 80]. Below a Knudsen number $Kn < 1$, the thermal conduction starts to get depending on the ambient pressure because of the increased number of molecular collisions. This effect will also lead to an activation of additional rotational and vibrational DOF. Thus, the gas molecules can additionally store thermal energy which leads to an increase of the heat capacity. This activation process of the rotational and vibrational DOF is strongly depending on the available space of the gas molecules, which is limited within this thesis by an adjustable aluminum (Al) plate in the vicinity above the micro-oscillator. In Section 6.2, the influence of polyatomic DOF on the quality factor is investigated and the activation process of polyatomic DOF is determined from these results.

At lower Knudsen numbers, the thermal transport effects can be described by thermal waves propagating within the gap between the micro-oscillator and the limiting counter-plate. The description of thermal diffusion processes by wave equation is under discussion in recent literature [81, 82, 83]. Even though thermal energy can only be transported in the negative direction of the temperature gradient from hot to cold (second law of thermodynamics¹ [84]) and therefore reflection effects would contradict this gradient equation, experimental results indicating the wave like behavior of thermal diffusion processes. For example, the group of A. Mandelis *et al.* verify the resonance effect by the utilization of a thermal-wave resonator cavity (TWRC) for measuring the thermal diffusivity of gases with very high precision [85, 86]. This thermal wave resonator principle is adapted and the transitional flow regime is described by an analytical approach taken from the previously presented thermoelastic damping model by Zener. In our case, we assume a heat source

¹ Clausius formulation: “Heat can never pass from a colder to a warmer body without some other change, connected therewith, occurring at the same time” (original: “es kann nie Wärme aus einem kälteren in einen wärmeren Körper übergehen, wenn nicht gleichzeitig eine andere damit zusammenhängende Änderung eintritt”)

respectively sink due to the compression and expansion caused by the micro-oscillator movement, thus creating a temperature oscillation within the gap. The gap between the micro-oscillator and the Al plate as well as the thermal properties of the gas are determining the efficiency of the heat losses. Therefore, we assume a thermal resonance frequency of the gas locked within the gap $f_{T,\text{gas}}$ modelled in the following way (*cf.* Equation (2.31)):

$$f_{T,\text{gas}} = B_{\text{trans}}(h) \cdot p^{\varepsilon_{\text{trans}}}, \quad (2.34)$$

whereby B_{trans} includes all constants, i.e. the thermal diffusivity at ambient pressure and the gap width h dependency. The pressure dependency of the thermal diffusivity can be deduced from Equation (2.8) and is modelled by an exponential fit factor $\varepsilon_{\text{trans}}$. The resulting quality factor Q_{trans} is given in analogy to Zener as:

$$Q_{\text{trans}} = A_{\text{trans}}(h) \frac{f_r + f_{T,\text{gas}}}{f_r f_{T,\text{gas}}}. \quad (2.35)$$

Additionally, we assume a gap dependent prefactor A_{trans} , giving the minimal quality factor in the resonance case where the mechanical resonance frequency f_r and the thermal resonance frequency $f_{T,\text{gas}}$ match. This approach is justified because heat waves are strongly attenuated and therefore the amount of heat loss is strongly dependent on the gap width h [81]. This new approach for the transitional flow regime is applied on experimental results presented in this thesis and explored in Section 6.3.

2.3.5 Squeeze Film Damping

The last gas damping mechanism presented within this theory section is the so-called squeeze film damping [87]. This loss effect occurs for very small gap widths compared to the lateral dimensions of the oscillator. It is based on a strong compression or expansion of the fluid within this gap, which can only escape or enter via the edges on the side. T. Veijola *et al.* have successfully described this loss mechanism by a lumped element model, which allows to predict the frequency response of a micro-oscillator in appearance of squeeze film damping [88]. The interaction between the micro-oscillator and the fluid is thereby modeled by a series of parallel springs connected with resistive damping components. Analytically, this regime can also be described by means of two simplifications. First, an incompressible fluid is assumed and second, a constant density and viscosity within the gap. Both assumptions are valid for narrow gaps and therefore lead to a reduction of the Navier Stokes equations to the Reynold's equation [89, 90]. The resulting quality factor of a micro-oscillator is given by Qiu *et al* as [91]:

$$Q_{\text{sqf}} = \frac{2\pi\rho_{\text{Si}}Hf_r}{\mu B^2} h^3. \quad (2.36)$$

The resulting quality factor Q_{sqf} is independent of the pressure p and depends, besides the density ρ_{Si} , the thickness H and the width B of the micro-oscillator, only on the viscosity μ and on the gap width h . Therefore, the quality factor plots show a plateau-like behavior (see Figure 9). Since many micro-oscillator applications (e.g. timing [92], gyroscope [93], ...) are based on electrostatic excitation, which requires a narrow gap between the electrodes, this effect is widely discussed in the

literature [94, 95]. In addition, the effect can also be used as a sensing principle for the detection of the viscosity of an enclosed gas medium [96]. In the case of piezoelectric actuators such as the presented one, this damping mechanism can only be observed at the smallest gap widths and is mostly negative since the squeeze film effect is very dominant and superimposes the other damping phenomena such as viscous damping and the thermal resonance effect. The transition from viscous damping to squeeze film damping is found to occur around an aspect ratio of the gap width to the oscillator dimension in the range of 0.1 (*cf.* Figure 9).

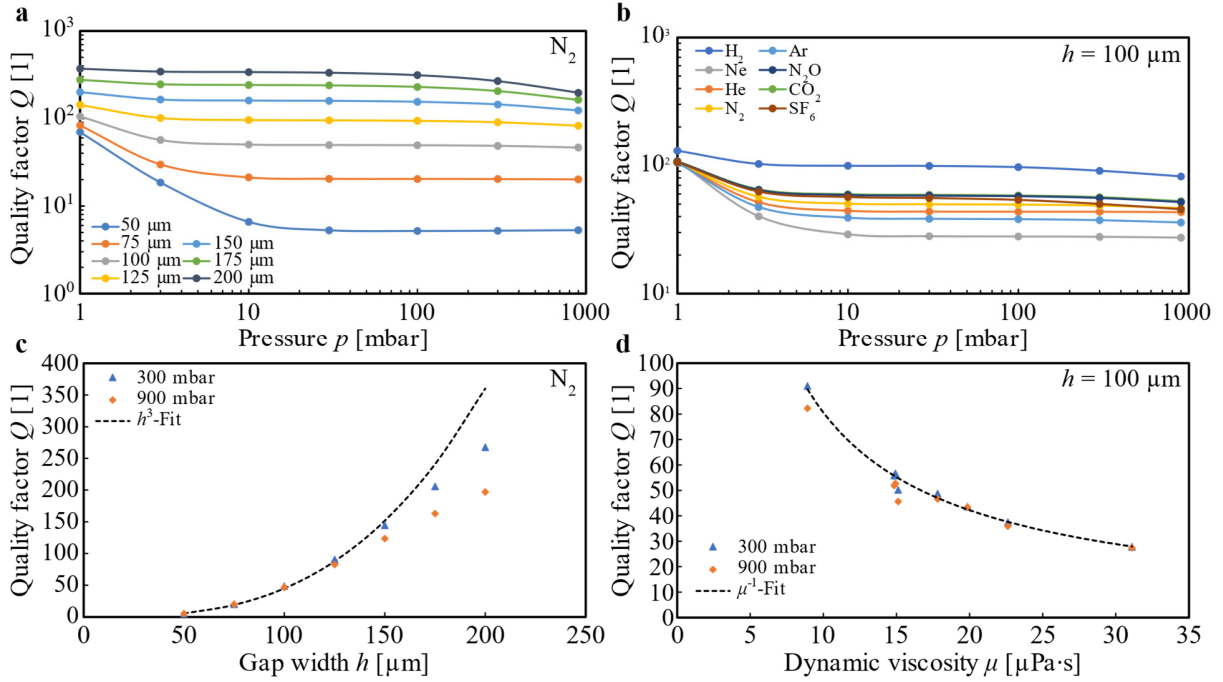


Figure 9. Quality factor plots of the squeeze film damping for a BO with $1600 \times 1600 \mu\text{m}^2$ plate. In (a) the quality factor plot for different gap widths within a nitrogen atmosphere is shown and in (b) for different gas atmospheres for a gap width of $100 \mu\text{m}$. In (c) and (d) the evaluated proportionalities according to Equation (2.36) are depicted. For gap widths larger than $150 \mu\text{m}$, a clear deviation from the squeeze film theory is observed.

2.3.6 Damping in Liquids

The last section of this theory chapter is about the damping effects of liquids on micro-oscillators. The fundamental description of this loss mechanism was developed by Sader in 1998 and is based on hydrodynamic loading forces [67]. The resulting resonance frequency f_{liquid} and quality factor Q_{liquid} are given as function of the hydrodynamic force functions g_1 and g_2 [9]:

$$f_{\text{liquid}} = \frac{\sqrt{1 - \frac{1}{2Q_{\text{liquid}}^2}}}{\sqrt{1 + g_2 \frac{L_0}{m}}} f_r \quad (2.37)$$

$$Q_{\text{liquid}} = \frac{2\pi\sqrt{1 + g_2 \frac{L_0}{m}}}{g_1 \frac{L_0}{m}} f_r, \quad (2.38)$$

with the length L_0 , the mass m and the undamped vacuum resonance frequency f_r of the micro-oscillator, respectively.

The hydrodynamic force functions can be attributed to losses to the liquid (g_1) and added mass effects (g_2) which depend on the resonance frequency f_0 as well as on the fluid properties, density ρ and dynamic viscosity η [97]:

$$g_1(f_r) = C_1\sqrt{f_r}\sqrt{\rho\mu} + C_1\mu \quad (2.39)$$

$$g_2(f_r) = C_3\rho + \frac{C_4}{\sqrt{f_r}}\sqrt{\rho\mu}. \quad (2.40)$$

The constants C_1, \dots, C_4 must be determined experimentally by best fit method. In [98] empirical formulations for the hydrodynamic force functions g_1 and g_2 of a cantilever are given for example.

From an academic point of view, an interesting aspect to be explored in this work is the difference in the damping characteristics of liquids compared to gases [99]. In addition, there are many fields of application for micro-oscillators in liquid media. This includes technical tasks like the monitoring of liquids by means of a precise real-time measurement of density and viscosity [100, 101] and biological investigations of e.g. serum and blood plasma [102, 103]. The main difficulty in these applications is the large damping in liquids, which makes compact electrical measurements challenging. For this reason, more complex modes and special geometries are chosen, which are less attenuated. These modes include the wine glass mode [104], the roof-tile shape mode [32] and the butterfly mode [105], as well as special geometries such as hammerhead resonators [106] (*cf.* Figure 10). These modes will be investigated in the scope of the thesis in gases and examined for possible applications as physical gas and pressure sensors (see Section 6.7).

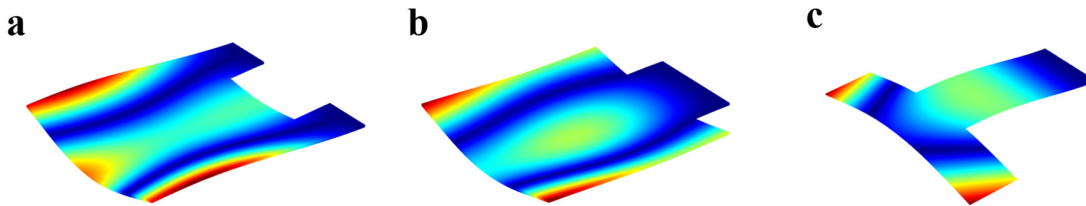


Figure 10. Simulated shape of the complex eigenmodes specially designed for measurement in liquids. In (a) the 1st roof-tile-shape mode, in (b) the butterfly mode and in (c) the corresponding eigenmode of a hammerhead resonator is illustrated.

3 Simulations

In this chapter, the preliminary numerical investigations for the design of the sensor are presented. First, the eigenmodes and their eigenfrequencies are investigated by performing an eigenfrequency study under variation of the sensor geometry. Subsequently, the geometries are analysed in terms of their damping to obtain oscillators with the lowest possible damping, respectively a high quality factor. Furthermore, steady-state magnetic field simulations are presented for the design of an inductive coil structure creating a high and focused magnetic field in a defined volume.

3.1 Eigenfrequency Study

An eigenfrequency study is performed to determine the eigenmodes of a harmonic oscillator as well as the corresponding eigenfrequencies. Three basic oscillator geometries were used for this study: A bending beam structure (cantilever CO), a bending structure with slit (bending oscillator BO) and a paddle shaped structure (paddle oscillator PO) (compare Figure 4). All structures are clamped on one side (fixed constraints) and are deflected at the free end with a Dirac pulse. The analysis of the frequency spectrum yields further eigenmodes besides the fundamental bending mode and the higher bending modes presented in Section 2.2.1. These eigenmodes can be associated with torsional modes or more complex modes, like roof-tile shape modes, by evaluating the three-dimensional deflection profile. The simulations do not take damping mechanisms into account and, in the best case, result in the resonance frequency determined experimentally in the high vacuum range (neglecting all extrinsic damping mechanisms).

3.1.1 Micro-oscillator Design

Several points have to be considered when designing a micro-oscillators for our experiments. The resonance frequency of the fundamental bending mode must be in the range of 1 to 5 kHz, so that the higher bending modes can still be measured. The limitation here is given by the cut-off frequencies of the electronic circuit, which is 120 kHz (see Section 5.2). In addition, the structure should exhibit as many other complex modes as possible that can be investigated for physical gas sensor applications.

In Figure 4, all geometric parameters that are available for variation are marked. The influence of thickness of the oscillator H as well as the length L_O and width B_O of the oscillating plate is investigated. For the structures BO and PO, additional degrees of freedom are given by the actuator beams which can be modified in length L_B and width B_B .

As can be seen in Figure 11a, the resonance frequency possesses a linear dependence on the thickness of the oscillator, independent of the oscillator structure. This behavior is also predicted in the theoretical derivation of the resonance frequency (*cf.* Equation 2.23). In Figure 11b, the cantilever structure CO is investigated in terms of the change in the resonance frequency under variation of the length L_O and width B_O . The theoretically predicted proportionality of the resonance frequency to the square of the reciprocal length L_O is obtained (*cf.* Equation 2.23). Furthermore, a weak linear dependence on the width of the oscillator is found. This phenomenon is a slight deviation from the theory, which predicts an independence of the resonance frequency from the width of the oscillator.

In the case of the structures BO and PO, the theoretical prediction of the resonance frequency is more complex. The individual influences result from the interaction of all four geometric quantities and are therefore strongly dependent on the aspect ratio between beam size and oscillator size. In all cases, except for the beam width, we find a reciprocal dependence of the resonance frequency on the geometric size. This is in accordance with the derived theory for predicting the resonance frequency. In the case of the beam width, we find a square root dependency. This is since the beam term in the denominator of Equation 2.23 is negligibly small compared to the oscillator term and therefore the influence of the beam width of the numerator term is decisive.

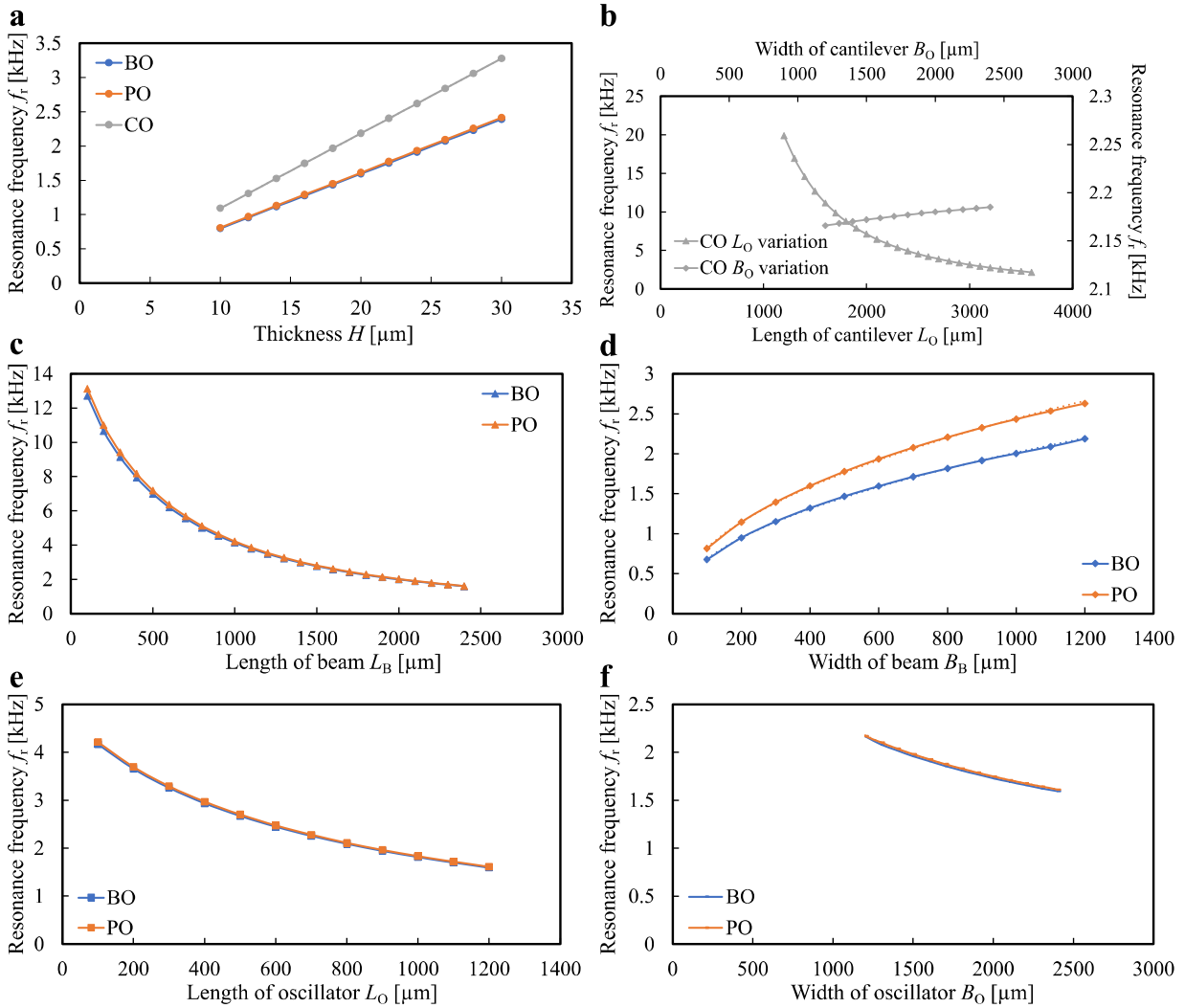


Figure 11. Simulated resonance frequency in dependency of the geometry. The base of the simulations is a cantilever CO with the length $L_O = 3600 \mu\text{m}$, width $B_O = 2400 \mu\text{m}$ and thickness $H = 20 \mu\text{m}$. The bending oscillator BO and paddle oscillator PO possess a length $L_O = 1200 \mu\text{m}$, width $B_O = 2400 \mu\text{m}$ and thickness $H = 20 \mu\text{m}$ attached to the substrate by two beams with length $L_B = 2400 \mu\text{m}$ and width $B_B = 600 \mu\text{m}$. In (a) and (b) all geometrical influences on the resonance frequency of the CO structure are shown. In (c) and (d) the geometric influence of the beam structures is illustrated. In (a), (e) and (f) the proportionalities of the resonance frequency of BO and PO to the size and the thickness of the oscillating plate is displayed.

3.2 Thermo-Viscous Damping

Besides the description and prediction of the resonance frequency, the estimation of the expected damping is an important factor. As described in Section 2.3, the overall damping is composed of different damping mechanism, which all play a decisive role depending on the ambient pressure. The numerical work is limited to the viscous flow regime and liquid damping, since here the highest damping values and thus the lowest quality factors are to be expected. The aim is that the oscillators in the ambient pressure range have a quality factor above 10. This is the limit range of weakly damped oscillations, which can still be detected well by electrical measurements via the piezoelectric effect. Below this quality factor, optical measurement methods such as laser Doppler vibrometry (LDV) are required.

For the description of the behavior of the fluid in the viscous flow regime, the linearized Navier Stokes equations and the continuity equation are used. In addition, the energy balance equation of fluid dynamics is introduced and the motion of the oscillator with the fluid at the interface is coupled with the boundary condition "moving wall". Here, the fluid at the interface adopts the velocity of the moving solid ($u_{\text{solid}} = u_{\text{fluid}}$). All equations are given in frequency representation so that they can be solved in the framework of an eigenfrequency simulation. The equations implemented in COMSOL Multiphysics 5.4 are listed below [107, 108]:

$$i\omega\rho_0\vec{u} = \nabla \cdot [-\rho\mathbf{I} + \mu(\nabla\vec{u} + (\nabla\vec{u})^T) - \left(\frac{2}{3}\mu - \mu_B\right)(\nabla \cdot \vec{u})\mathbf{I}] \quad (3.1)$$

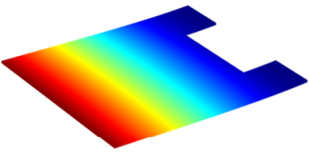
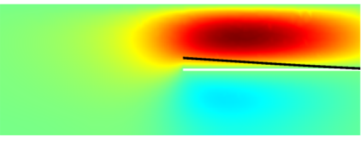
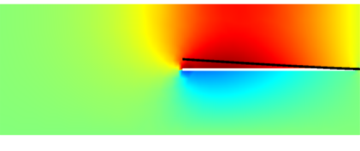
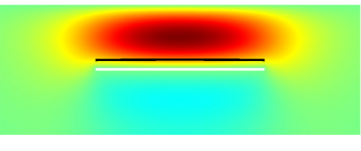
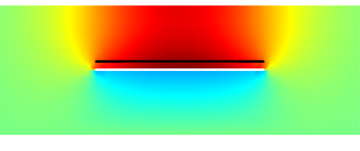
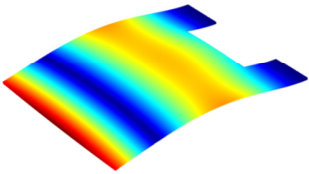
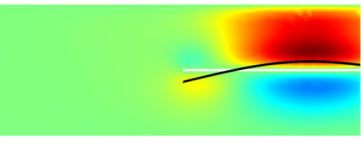
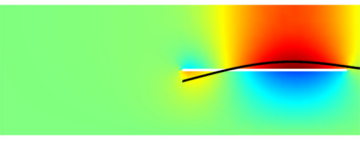
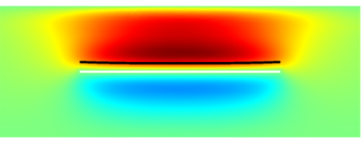
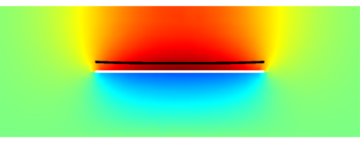
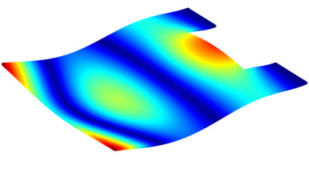
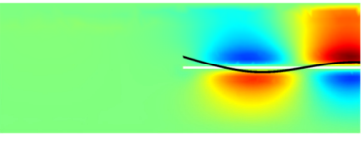
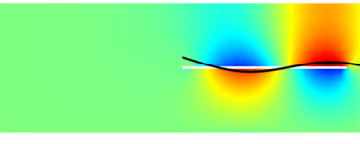
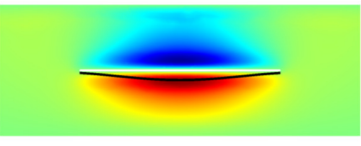
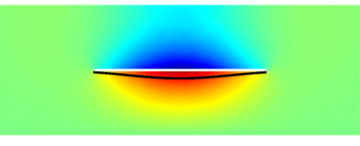
$$i\omega\rho + \rho_0\nabla \cdot \vec{u} = 0 \quad (3.2)$$

$$i\omega\rho_0C_pT = -\nabla \cdot (-\kappa\nabla T) + i\omega\alpha_0T_0p + Q, \quad (3.3)$$

with the density ρ , the velocity \vec{u} , the dynamic viscosity μ , the bulk viscosity μ_B , the heat capacity at constant pressure C_p , the temperature T , the thermal conductivity κ , the pressure p and the thermal expansion coefficient α of the fluid. The parameters indexed with zero indicate the reference ambient values. The Nabla operator ∇ is used as mathematical operator as well as the imaginary unit i and the identity matrix is denoted by \mathbf{I} .

By solving the equation system, the temperature and pressure distribution inside the gap can be computed numerically. Table 5 shows the results for the first three eigenmodes in front and side view. The deflection of the micro-oscillator due to the oscillation leads to a compression of the fluid inside the gap. An asymmetry can be seen since the top is confined by an Al-plate in a distance of 550 μm and the bottom is opened with the boundary condition "spherical wave radiation". Therefore, the compression effect is mainly seen in the upper segment. Due to the relatively small amount of heat or the high heat capacity of the oscillator and the plate, only negligible temperature rise is to be expected in the solids and they are therefore coupled with the boundary condition isothermal (temperature variation $\Delta T = 0$). An upward deflection leads to an increase in pressure at the interfaces between gas and solid due to the compression. The increase in temperature can be seen mainly in the area between the oscillator and the Al-plate.

Table 5. Overview of the FEM simulated displacement, temperature and pressure distribution for the first three bending modes (BM). The temperature and pressure distribution are shown from the side (top) and front (bottom) view. In the mode column, the color is indicating the displacement from low (blue) to high (red). In the case of the temperature and pressure distribution the color is indicating the variation from the ambient values (green). Red is indicating a region with higher temperature/pressure and blue representing lower temperature/pressure relative to the ambient value. The displacement is magnified for visualization and is not to scale.

	Mode	Temperature	Pressure
1.BM			
			
2.BM			
			
3.BM			
			

As can be seen in Table 5, the first bending mode leads to a spheroid shaped temperature rise. The magnitude of this temperature rise and the associated heat losses are strongly dependent on the ambient pressure and the gap distance. This effect is discussed in Section 6.3 for the purpose of describing the damping behavior of micro-oscillators in the transition region by means of thermal wave resonances.

The second bending mode, due to its shape, has a more spatially limited temperature increase and an additional cooled area due to an expansion of the gas. This effect is even more pronounced in the third bending mode, which has a clear separation between a compression and an expansion region. As the number of modes increases, the influence of the gap decreases. The maximum of the temperature increase is located nearer to the oscillator for higher bending modes and therefore the influence due to an interaction with a counter plate is reduced to narrow gaps. This effect will be investigated and discussed in Section 6.4.

In addition to the temperature and pressure distributions, a complex natural frequency f_c of the eigenmode is obtained. This frequency can be used to determine the quality factor Q_{sim} of the system by the ratio of real part to imaginary part [109]:

$$Q_{\text{sim}} = \frac{\text{Re}(f_c)}{2 \text{Im}(f_c)}. \quad (3.4)$$

The simulated quality factor and the real part of the frequency which is the resulting mechanical resonance frequency are shown in Figure 12. In (a) and (b) the results for the first bending mode for various gap widths can be seen. The results show clearly that the damping is strongly affected by the gap width and an increase of the gap leads to less viscous losses respectively higher quality factors. For lower pressures, the quality factor seems to reach a plateau which can be found experimentally. In this range the validity of the Navier-Stokes equations and the whole system of equations are not given anymore and therefore lead to a big deviation from the experimental data. In the range of the validity of the Navier-Stokes equations, the simulated values as well as the proportionality to the reciprocal square root of the pressure are in good agreement with the analytical prediction and with the experimental results. The shift of the mechanical resonance frequency is in the range of several ‰ regarding the vacuum resonance frequency. An increase of the pressure leads to additional mass effects on the micro-oscillator which results in a drop of the mechanical resonance frequency. This shift of the resonance frequency is also affected by the gap width, leading to a larger attenuation, i.e. a larger drop of the resonance frequency for smaller gaps.

In (c) and (d), the results for higher bending modes and more complex modes are presented. As can be seen, for higher mode numbers the quality factor is increasing by about one order of magnitude. This effect is due to the significantly lower viscous friction losses and the decreasing influence of the gap (*cf.* Table 5). The range of viscous losses in a gas medium with dynamic viscosity μ and density ρ can be approximated by the size of the viscous boundary layer δ_{vis}

$$\delta_{\text{vis}} = \sqrt{\frac{\mu}{\pi \rho f_n}}, \quad (3.5)$$

which decreases with increasing operating frequency f_n .

The shift of the resonance frequency behaves in the same way, so that the less damped higher modes show a smaller shift in relation to the vacuum resonance frequency. For comparison, the

more complex eigenmodes, the roof-tile shape mode and the butterfly mode (see Figure 10a and b), are also included. The strength of damping correlates with the mode number leading to the highest quality factor values for the 3rd bending mode. The complex eigenmodes are in the same order of magnitude like the 3rd bending mode at atmospheric pressure. Furthermore, the complex eigenmodes exhibit a lower slope indicating a weaker dependence on the ambient pressure.

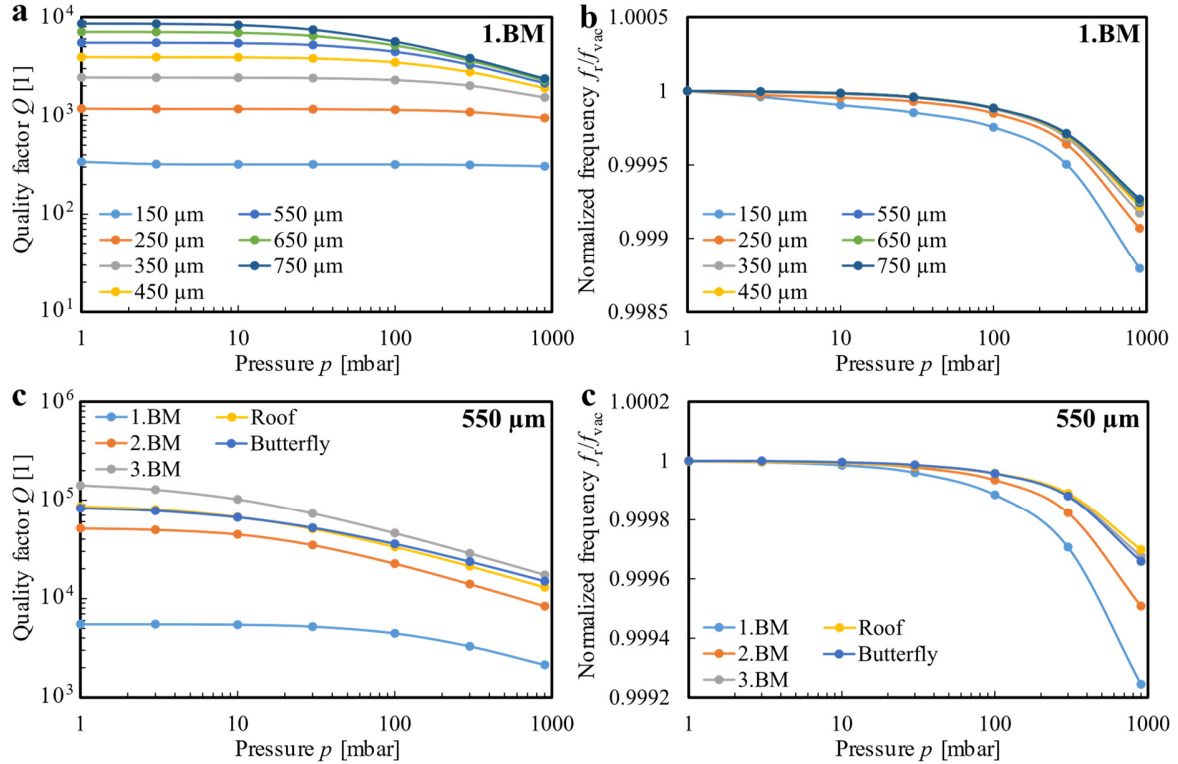


Figure 12. Simulated quality factor plots and shift of the resonance frequency as function of the ambient pressure for the first bending mode for various gap widths (a) and (b) as well for different eigenmodes for a gap width of 550 μm (c) and (d).

3.3 Fluid-Structure Interaction

The damping of micro-oscillators in fluid media is solved using the fluid-structure interaction module. In contrast to the previous model, the full nonlinear Navier-Stokes equations is used. In liquids, thermoacoustic effects are negligible and convection effects are more pronounced due to the higher kinematic viscosity or larger Reynolds numbers. A more accurate description of the damping is therefore provided by the full use of the Navier-Stokes equations including the nonlinear convection terms. Due to the nonlinearity, it is not possible to solve the system within an eigenfrequency study and is therefore solved iteratively in a time study. The micro-oscillator is operated near its natural frequency and released to oscillate at a time $t = 0$ s. Due to the damping effect caused by the surrounding liquid medium, the micro-oscillator loses energy in each oscillation until it finally stops in the neutral position. Such decay curves are shown in Figure 13 for four different liquids. The liquids are deionized (DI) water, isopropanol and the standard viscosities D5 and N10. The fluids are all non-electrically conductive and the densities ρ and viscosities η used for the numerical simulations are listed in Table 6.

Table 6. Listing of the fluid properties investigated numerically regarding their damping behavior. A measure of the strength of the damping is given by the reciprocal square root of the density viscosity product. The properties of water and isopropanol are taken from [110]. The properties of the standard viscosities are taken from the producer *Paragon Scientific Ltd.* [111].

Liquid	ρ [kg·m ⁻³]	η [mPa·s]	$\frac{1}{\sqrt{\rho\mu}}$ [m ² ·s ^{1/2} ·kg ⁻¹]
DI water	998	0.890	0.034
Isopropanol	781	2.038	0.025
D5	835	4.695	0.016
N10	841	14.34	0.009

From the time constant or from the exponential fit of the envelope of the decay process, the quality factor can be determined according to Equation (2.19). Another possibility is the decomposition of the time signal into the frequency spectrum by means of a Fourier analysis. An advantage of this method is that, besides the fundamental mode, additional higher modes can be examined. The quality factor can be calculated from the resulting resonance peaks of the Fourier spectrum using the half-power bandwidth method (see Equation (2.16)).

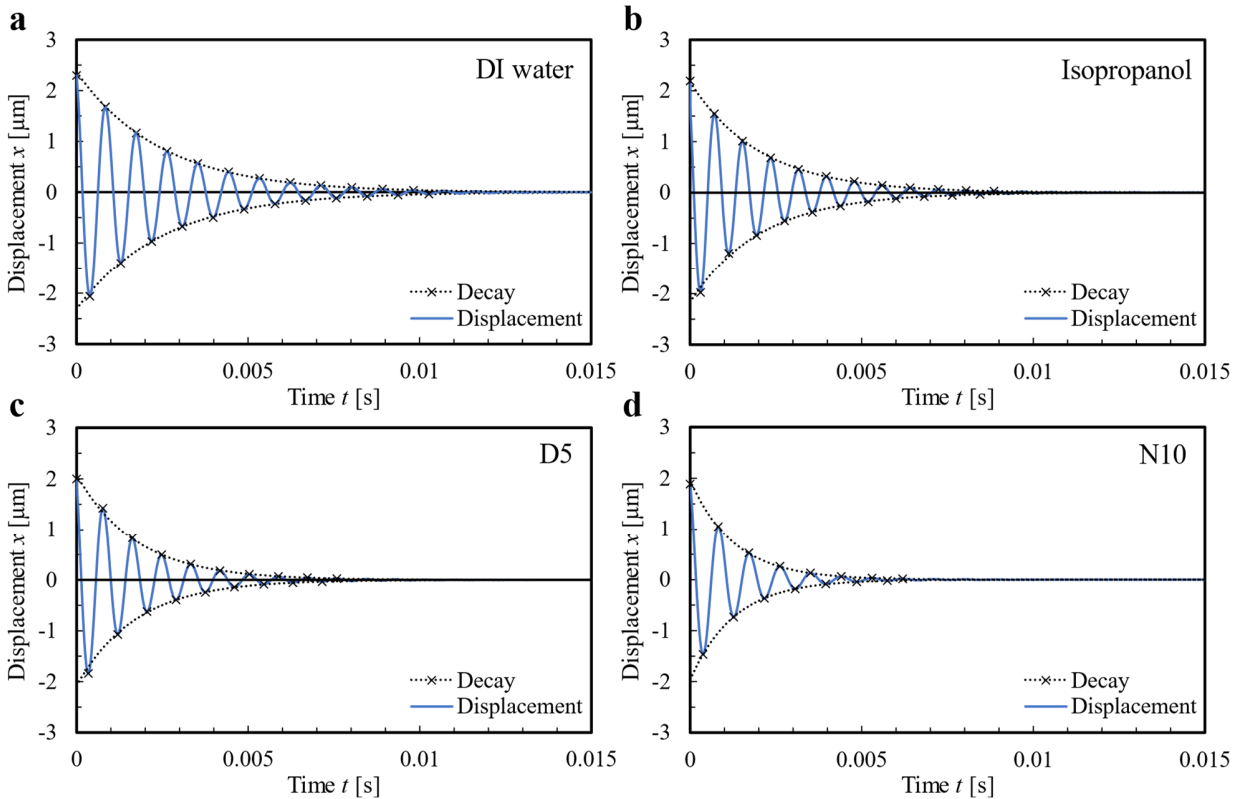


Figure 13. Decay curves of a micro-oscillator in water (a), isopropanol (b), D5 (c) and N10 (d) (blue solid line). The maxima and minima of the oscillation movement are marked with crosses and fitted using an exponential fit (dotted line).

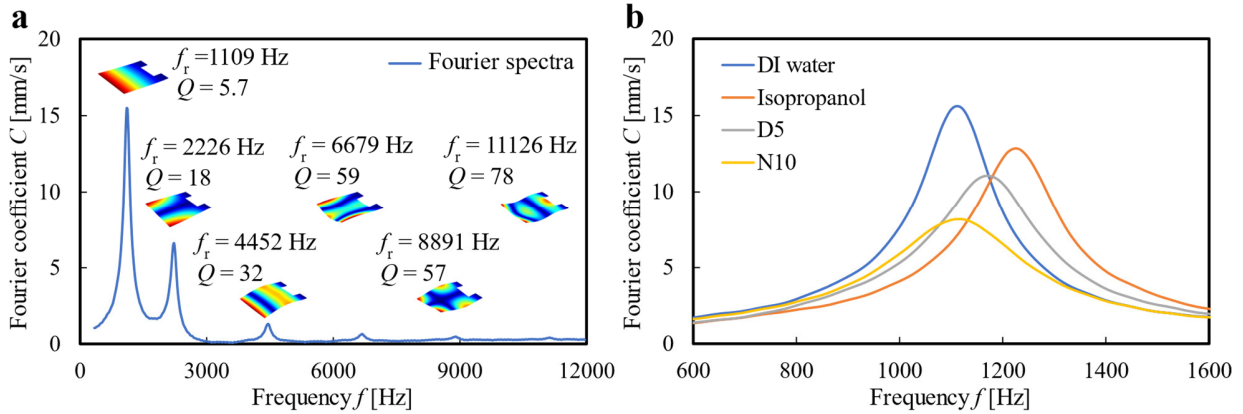


Figure 14. Fourier analysis of the decay plot of micro-oscillator in water (a). The corresponding eigenmodes as well as the associated quality factor and resonance frequency are included. In (b) the resonance peaks resulting from the Fourier analysis of the first bending mode for various liquids are shown.

In Figure 14a, the quality factors for the different eigenmodes have been calculated applying the half-power bandwidth method on each resonance curve. It is noticeable that the quality factor increases with increasing operating frequency, respectively with a higher mode number. This effect was also observed in gases and persists in liquids. Within the observed selection, the roof-tile shape mode exhibits the smallest bandwidth and is therefore the most moderately damped eigenmode with respect to the resonance frequency. This is consistent with previous work, which reported roof-tile shape modes to be very weakly damped and therefore well suited for applications in liquid media [32]. In Figure 14b, the resonance peaks of the fundamental mode in different liquids are depicted. The resonance frequency shows mainly a dependence on the density of the liquid which is additionally superimposed with effects of the dynamic viscosity (*cf.* Equation (2.37)). A higher density causes a reduction of the resonance frequency due to the additional mass acting on the oscillator. The influence of the viscosity part is depending on the geometry and can be adjusted by the aspect ratio of the micro-oscillator (Parameter C_4 of Equation (2.40)). The amplitude, respectively the quality factor, depends not only on the density but also on the dynamic viscosity of the liquid. A measure for the quality factor of micro-oscillators in liquids is the reciprocal square root of the density-viscosity product. Therefore, DI water exhibits the highest amplitude and quality factor among the four liquids. The other liquids have approximately the same density and differ essentially in their dynamic viscosity. Thus, a decrease of the amplitude respectively of the quality factor with increasing viscosity from low (Isopropanol) to high (N10) can be seen.

3.4 Stationary Magnetic Field Simulation

In Section 2.1.4, the paramagnetic magnetic force on oxygen was introduced. This effect is based on both a high magnetic field and on a high gradient of the magnetic field. For this purpose, simulations were performed with different geometries to create an enrichment zone of paramagnetic oxygen with the highest possible force and approximately the size of the micro-oscillator.

The magnetic circuit is designed as shown in Figure 15. The whole construction consists essentially of three components: The field generation part, the field transporting part and the focusing unit. The field generation is realized by FeNdB permanent magnets with a remanence field strength of

1.4 T and in a second case by electromagnetic coils. In order to achieve the highest possible magnetic field, two oppositely directed field generating elements are used, which are placed symmetrically around the focusing unit. The field transport for closing the magnetic circuit is formed by cuboidal elements made of ARMCO® Telar 57. This is a noble magnetic material with high magnetic permeability $\mu_r (> 1000)$ and high saturation magnetization ($B_{\text{Sat}} = 2.15 \text{ T}$) [112]. These very good magnetic properties reduce the losses of magnetic field strength on the way to the focusing unit. For the focusing unit, different geometries have been tested numerically, including semicircles and pyramids in various combinations. The best results in terms of size of the enrichment zone and maximum force effect were obtained with the setup shown in Figure 15, consisting of two flattened pyramids. The distance between the two flattened elements is also a decisive factor for the magnitude of the magnetic field and the magnetic field gradient. A distance of 1 mm was chosen, which results form a compromise between high magnetic force and low viscous friction losses due to a narrow gap.

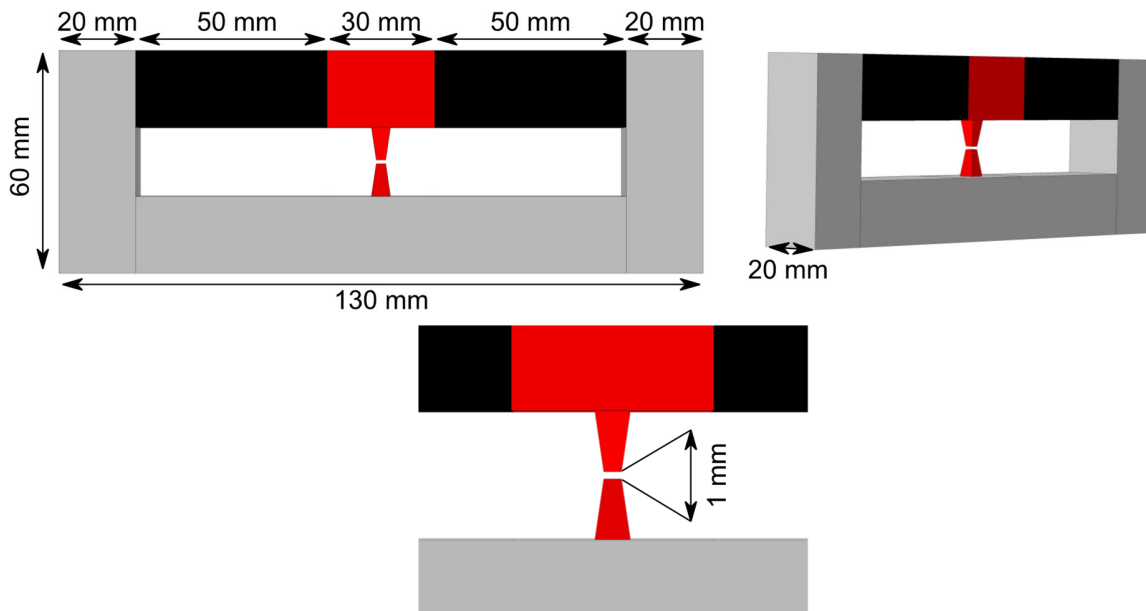


Figure 15. Schematic diagram of the magnetic circuit including all dimensions. In grey, the magnetic noble material for transporting the magnetic field is highlighted. The magnetic field generators are colored in black and the focusing unit is marked in red.

In Figure 16a and b, the magnitude of the resulting magnetic field in between the two flattened pyramids is shown. In the internal region between the flattened parts there is a homogeneous magnetic field with a strength of about 1 MA/m ($\approx 1.3 \text{ T}$), which drops sharply at the edge of the structure. The sharp drop of the magnetic field in a range of a few hundred μm leads to a high magnetic force in this area. Figure 16c shows an example of the calculated magnetic force in the x -direction. The maximum values can be found in the area of the edge and are symmetric to the coordinate origin. The direction of the paramagnetic force is always towards the center, where a local enrichment zone is created. In Figure 16d the magnitude of the magnetic force is displayed, revealing a symmetric attraction of oxygen into the zone of the homogeneous magnetic field. The direction is represented by the vector arrows thus indicating an attraction of the oxygen atoms into a spatially

confined region in-between the flattened area of the pyramids, the enrichment zone. The force direction for the diamagnetic gases is directed in the opposite direction because of the sign of their magnetic permeability (*cf.* Table 3) and therefore these gas components are pushed out of the enrichment zone. The size of the enrichment zone is mainly determined by the flat area of the pyramid tips and can be adjusted via this parameter. In this region, the oscillator is placed to measure the local increase of the oxygen via change of the quality factor Q as well as the resonance frequency f_r .

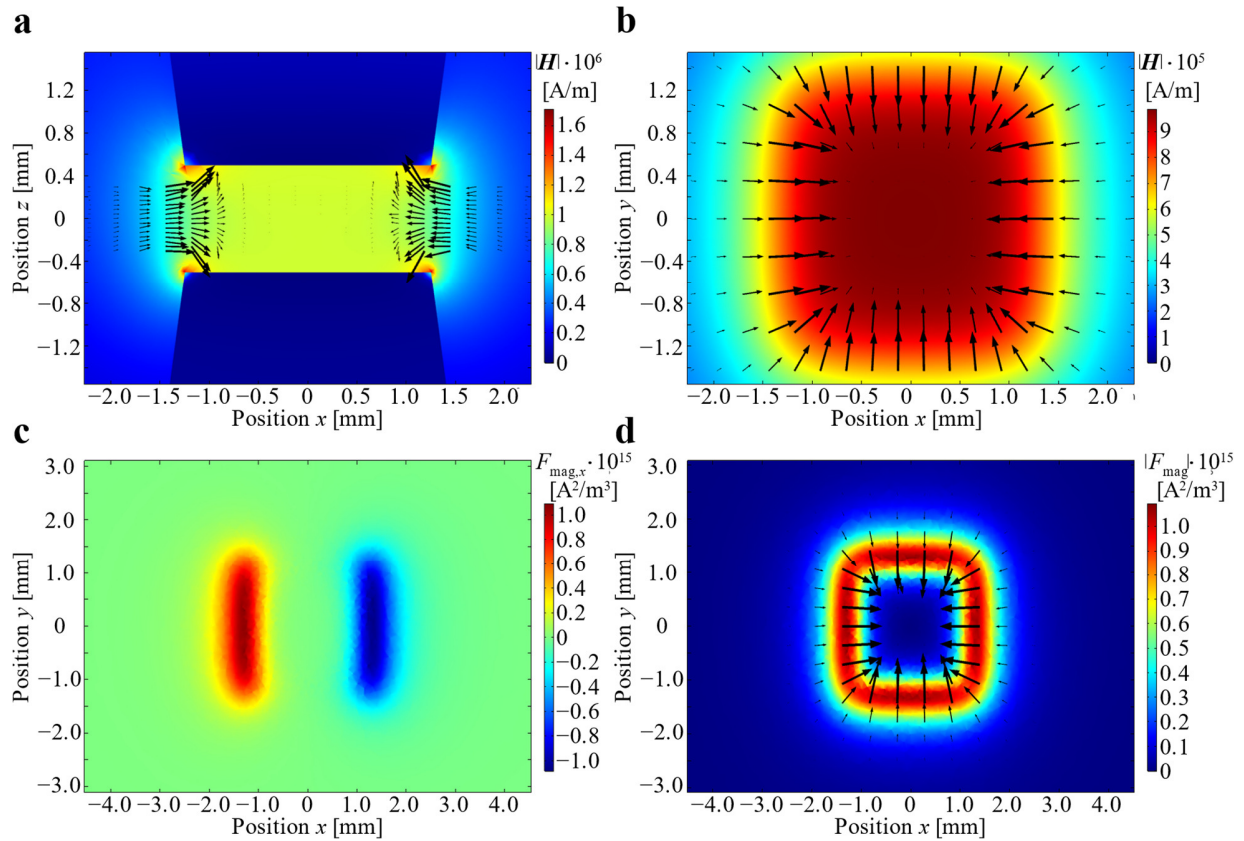


Figure 16. Magnitude of the magnetic field strength in the x - z -plane side view (a) and in the top view on the x - y -plane (b). In (c) the calculated magnetic force in the x -direction is depicted and in (d) the magnitude of the magnetic force as well as the vectorial representation of the force direction is shown.

4 Manufacturing

In the following chapter, the fundamental process steps of the micro-oscillator fabrication are presented. In the first section the process steps are introduced and in the second section the processing is analyzed with respect to the quality and inhomogeneities (tolerances). This allows to identify uncertainties in the manufacturing process which influence the experimentally measured quantities, such as resonance frequency f_r and quality factor Q .

4.1 Process Flow

An overview picture of all the manufacturing steps is shown in Figure 17. The initial substrate is a 4" Si wafer with a high concentration of p-boron ($0.005 \Omega\text{cm}$) and a thickness of $525 \pm 20 \mu\text{m}$ in a (1 0 0) orientation.

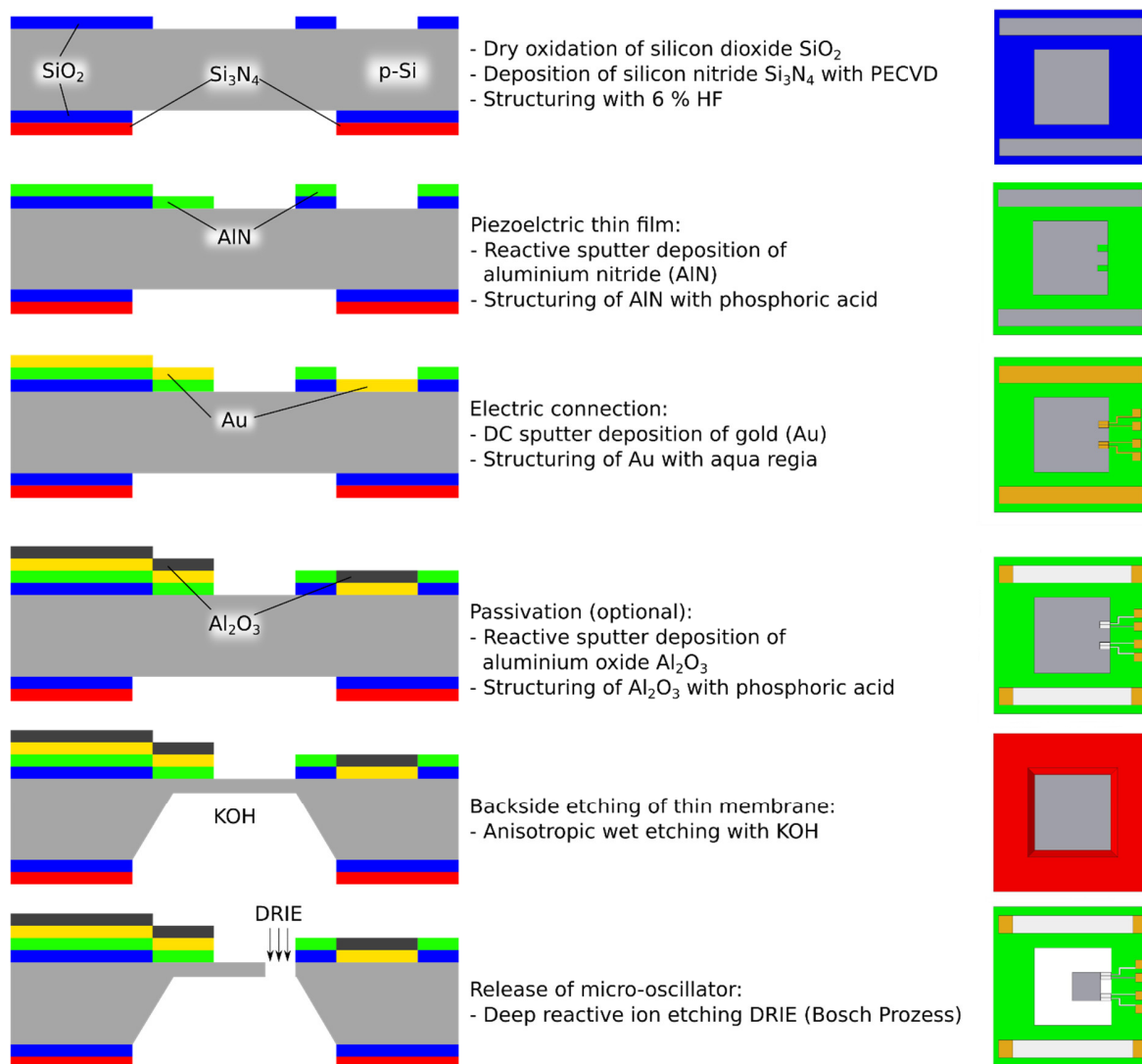


Figure 17. Schematic overview of the process flow, which includes the key manufacturing steps. On the left side in cross-section and on the right side in top view. The thickness ratios in the side view are not to scale.

The low resistivity of the silicon wafer allows the substrate to be used as a common ground. For electrical insulation, silicon dioxide SiO_2 is grown in a thickness of 120 nm on both sides in a dry oxidation process. Afterwards, Si_3N_4 is deposited in a thickness of 550 nm on the backside using a plasma enhanced chemical vapor deposition (PECVD) process. This layer is required as passivation for structuring the backside cavities with potassium hydroxide (KOH) for thinning the Si-membranes. Both sides are structured simultaneously in a 6 % hydrogen fluoride (HF) etching solution. The piezoelectric aluminum nitride (AlN) thin film is then deposited in a thickness of 1100 nm by a reactive sputtering process and subsequently patterned by 85 % phosphoric acid (H_3PO_4) at a temperature of 80 °C [8]. The AlN elements as well as the substrate (ground) are contacted by gold (Au) electrodes which are deposited in a DC sputtering process in a thickness of about 500 nm and etched with aqua regia ($\text{HNO}_3 + 3 \text{HCl}$) at a temperature of 25 °C. This process is followed by an optional passivation step, which is only necessary for the measurement of electrically conductive liquids. For this purpose, aluminum oxide (Al_2O_3) is reactively sputtered in a thickness of about 500 nm and etched with phosphoric acid (H_3PO_4) at a temperature of 60 °C [113]. This is followed by a backside etching step using 40 % KOH at a temperature of 85 °C [114]. Within about 14 h of KOH etching, a very thin membrane in the range of 10 – 30 μm is created from the backside. These KOH cavities are then refilled with photoresist AZ1518 from *Micro-Chemicals GmbH* to mechanically stabilize the structure and they are acting as etch stop for the releasing process (see Figure 18a). The micro-oscillator structure itself is structured from the top side by a deep reactive ion etching process (DRIE). The Bosch process is used, consisting of alternating passivation and etching steps (see Figure 18b). Subsequently, the micro-oscillator chips are diced by a wafer dicing saw and are singularized. Afterwards, the micro-oscillators are released by dissolving the photoresist with acetone and cleaned in an ultrasonic bath with isopropanol, water and ethanol. Examples of the fabricated micro-oscillators are depicted in Figure 19.

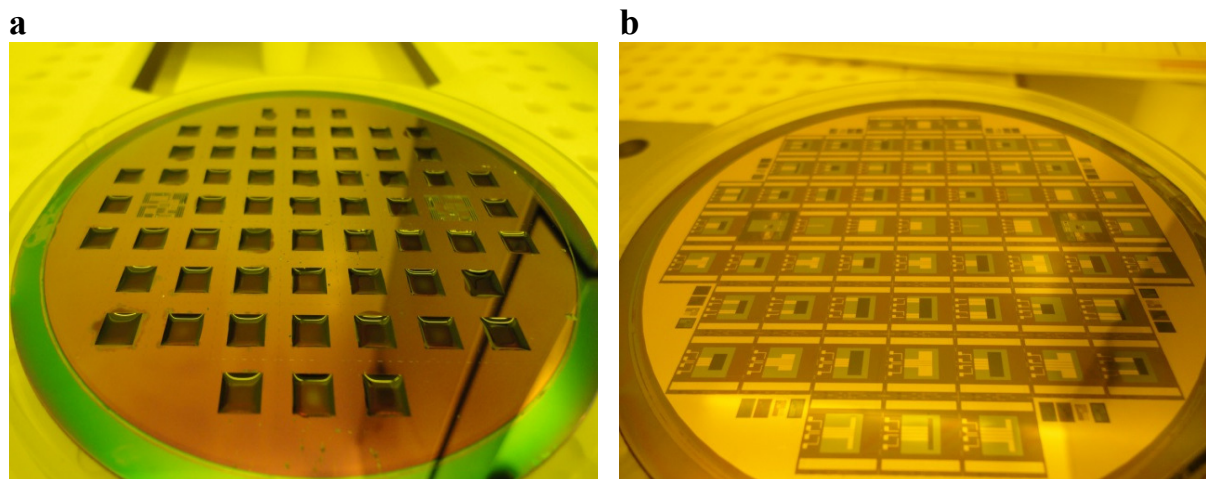


Figure 18. Back side view showing the refilled KOH cavities with photoresist AZ 1518 (a) and top view on a processed wafer covered with the DRIE photomask before the DRIE process (b).

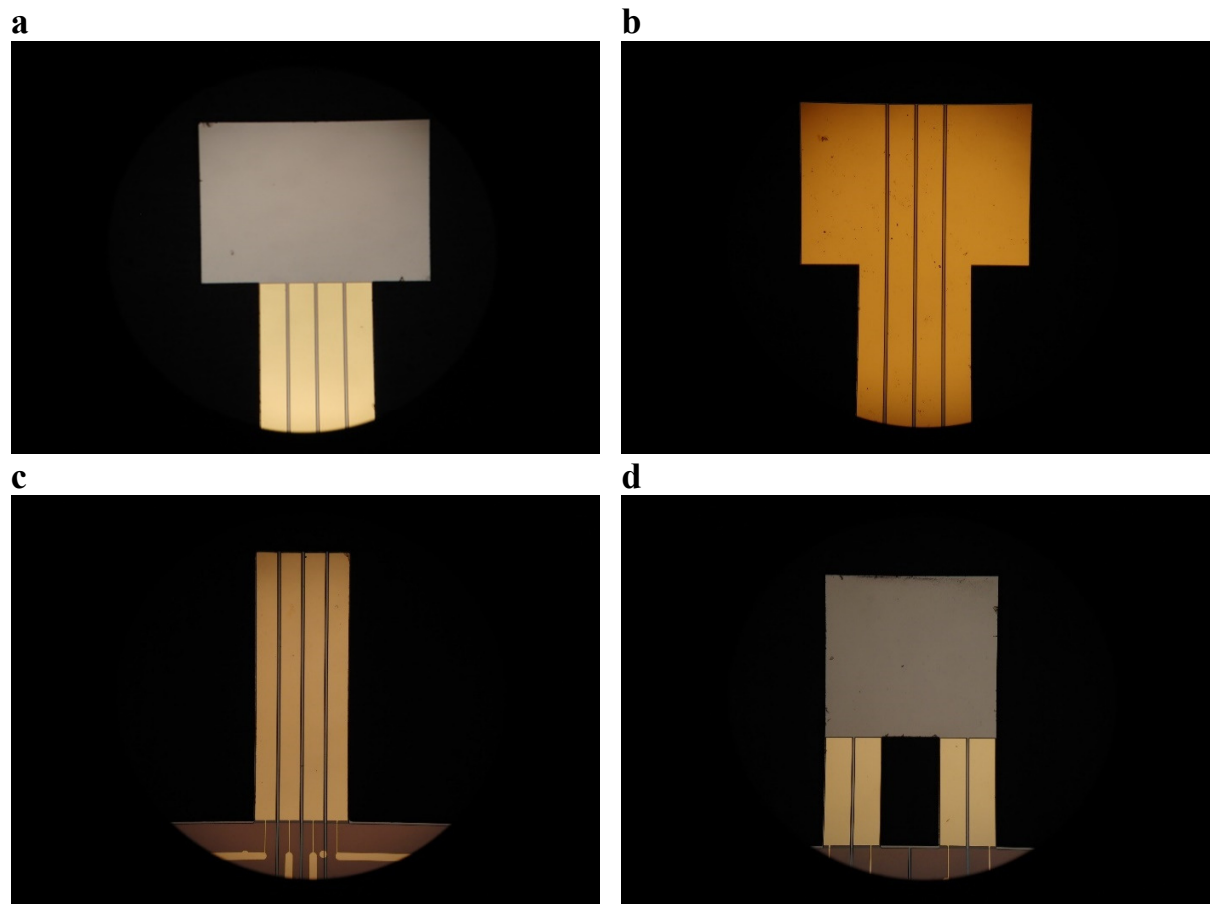


Figure 19. Microscopic image of the fabricated micro-oscillators: PO (a), PO fully covered (b), CO (c) and BO (d).

4.1.1 Mask Production

The individual fabrication steps must first be defined photo lithographically, before applying the etching chemical. This requires five or, in the case of the optional passivation step, six masks. A single mask blank consists of a glass substrate, a chrome thin film and a positive photoresist.

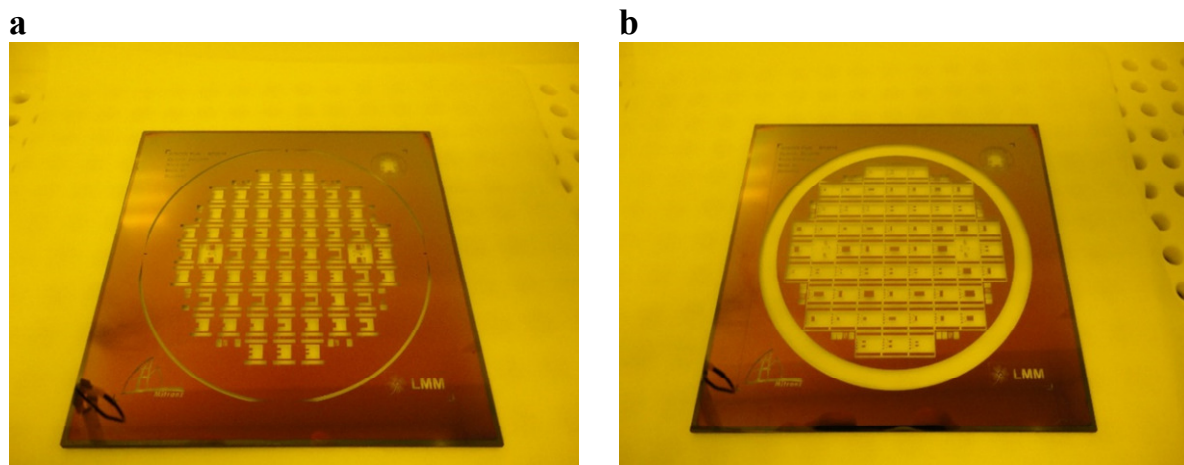


Figure 20. Lithographic masks for DRIE process (a) and Au electrode structuring after the chrome etching.

In a first step, the structural data implemented with the mask layout software CleWin 3.3 are transferred to a physical mask via the laser writing system DWL 66 from *Heidelberg Instruments Mikrotechnik GmbH*, using a 20 mm writing head, which allows a resolution of 5 μm . Afterwards, the photoresist is developed and the chrome film is etched by the chrome etching solution TechniEtch CR01 from *MicroChemicals GmbH*. The remaining photoresist is removed with Caro's acid, which simultaneously removes other impurities and therefore cleans the surface. This is an important factor, because the mask is in contact with the wafers in the exposure step. In Figure 20, two examples for lithographic masks are shown after the structure transfer by the chrome etching process.

4.1.2 Lithography

Lithography is a necessary step before any etching process in order to structure the defined areas where the deposited material has to be removed. For this purpose, the positive photoresist AZ1518 is spun on in a thickness of about 2 μm . This is achieved by applying a drop of a few milliliters on the wafer, which spreads over the surface in a defined thickness by the rotation of a spin coater. The rotation speed is 3000 rpm with an acceleration of 3500 rpm/s and a time of 60 s. Only the DRIE mask is an exception. Here, the speed is reduced to 2500 rpm in order to produce a thicker photoresist, which is necessary for the longer etch time (approximately 30 min.). After the photoresist is deposited on the wafer, the structure is transferred by an exposure system. The mask aligner MA/BA6 from *SÜSS MicroTec AG* is used to align the mask to the wafer and a mercury vapor lamp with a wavelength of 405 nm is used for exposure. The alignment is done via two markers placed on both sides, left and right, to eliminate an angular error (see Figure 21). The photochemically activated photoresist is then removed by the development solution (AZ351B) in the illuminated areas. The quality of the lithography, the alignment and the resolution are controlled after development to ensure a good pattern transfer (cf. Figure 21).

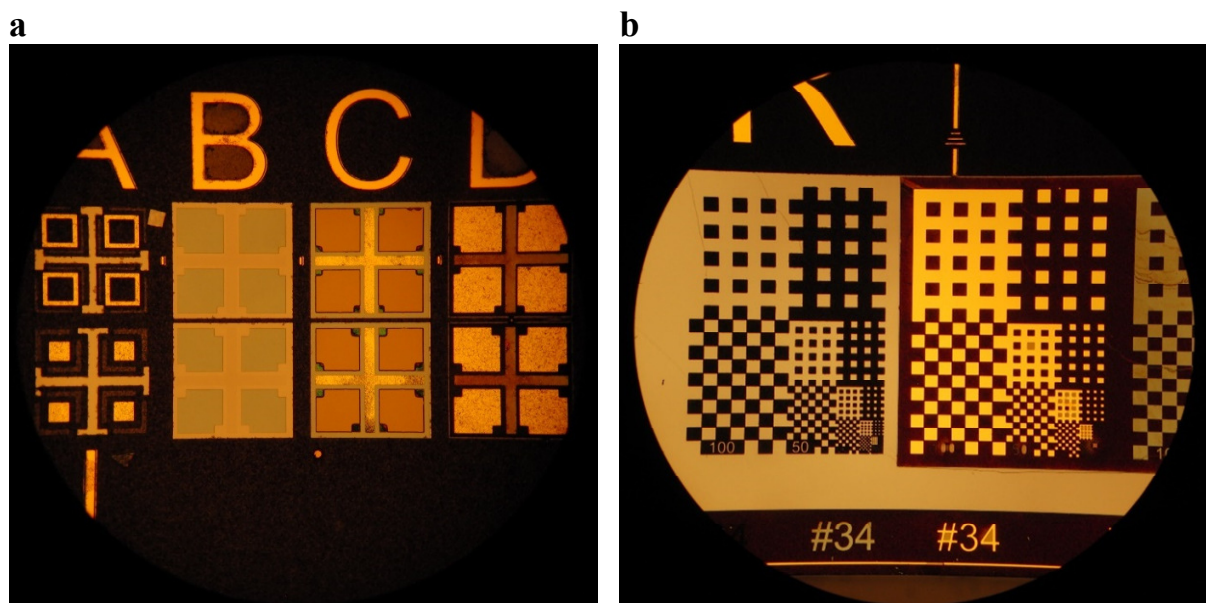


Figure 21. Alignment structures to adjust the masks to the wafer (a) and test structures to control the resolution of the lithography step as well as the etching process (b).

4.1.3 Thin Film Deposition

The thin films must first be deposited, before structuring them photo lithographically, as described in the previous section. In this work, three different techniques are used to create thin films of different materials in a defined thickness and orientation: thermal oxidation, chemical vapor deposition (CVD) and sputtering. The silicon dioxide thin film is grown on top of the silicon surface by a dry oxidation process. The process takes place in a furnace at a temperature of 1000 °C in an oxygen atmosphere for about 5 h. The silicon nitride thin film is deposited with a PECVD process in a Plasmalab System 133 from *Oxford Instruments*. A 550 nm thick layer is produced at a temperature of 350 °C and a process time of 2400 s. The aluminum compounds as well as the metallization with Au were deposited using a magnetron sputtering system LS 730S from *Von Ardenne GmbH*. Au is deposited in a standard DC sputter process, while the AlN and the Al₂O₃ thin films are created using a reactive sputtering process. In the case of the AlN deposition, the orientation in the c-axis direction is crucial for achieving good piezoelectric properties. This is controlled via the process parameters [8]. The piezoelectric AlN thin film with a thickness of 1100 nm is produced with a sputter power of 1000 W at a vacuum of 0.004 mbar with a nitrogen gas flow of 50 sccm in a process time of 3200 s. The 500 nm thick Al₂O₃ passivation layer is deposited with a sputter power of 500 W at a vacuum of 0.004 mbar with an oxygen gas flow of 60 sccm and an argon gas flow of 60 sccm in a process time of 1800 s. The Au metallization layer with a thickness of 500 nm was sputtered with a power of 100 W under a vacuum of 0.003 mbar with an argon gas flow of 60 sccm in a process time of 300 s.

4.1.4 Etching

The different layer materials described in the previous chapter are photo lithographically structured and then etched to transfer the pattern onto the substrate. For this purpose, various etching media are used, each adapted to the material to be removed. Each etching combination forms its own etching profile, which must be taken into consideration. The wet chemical attack during etching of Au, AlN and Al₂O₃ is mostly isotropic, resulting in a significant underetching of the photoresist mask. Especially for AlN, this effect is predominant due to the layer thickness and therefore requires a lateral tolerance of 10 µm to the overlaying Au layer. An overlap of the gold electrodes due to an underetching of the AlN patterns would lead to a short circuit with the substrate below (common ground) and thus would lead to a short circuit of the piezoelectric element. Figure 22a shows the underetching of the AlN mask (light brown area at the edge of the mask) and Figure 22b shows the lateral distance of about 5 µm to the gold electrode, which should be the lithographically intended 10 µm. The KOH etching of silicon, on the other hand, forms a partially anisotropic etching profile, which is determined by the crystal structure. The (1 0 0) orientation of the Si wafer exhibits an etch profile illustrated in Figure 22e and f. This results in square-shaped Si membranes with a thickness of several µm from which the micro-oscillator is fabricated by the front side using a DRIE process. The thickness of the micro-oscillator is thus given by the KOH etching and can be controlled by measuring the etching rate and adjusting the etching time. The DRIE process (Bosch process) forms a fully anisotropic etch profile with very high aspect ratio. The alternating etch step with SF₆ and passivation step with C₄F₈ for 6 seconds each, results in a sharp edge with

a scalloped sidewall. This structure can be seen on the edge of a micro-oscillator under an SEM image as, shown in Figure 22c and d.

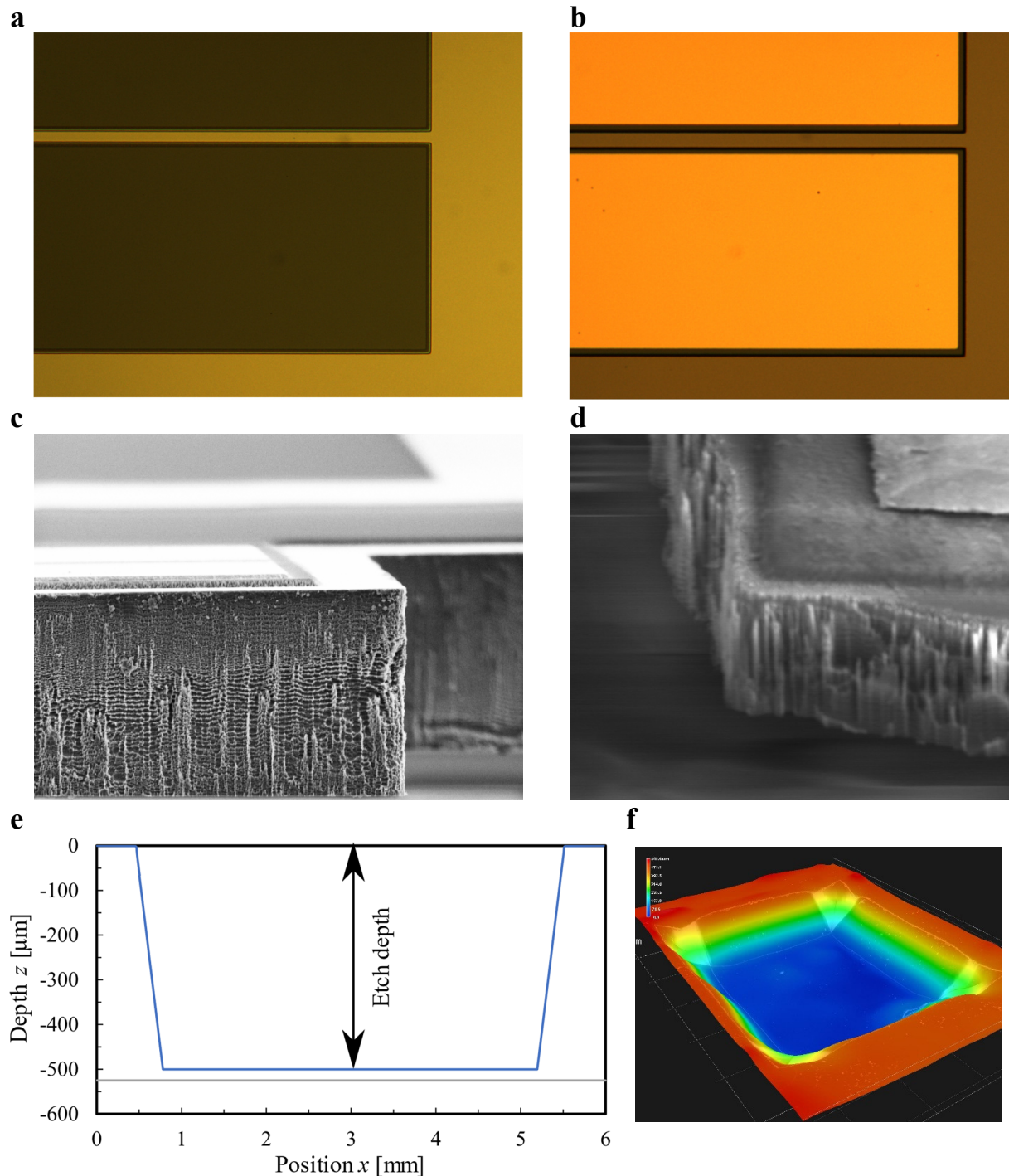


Figure 22. Microscopic image of the photomask of an AlN piezo element after the phosphoric acid etching (a) and after the Au structuring (b). SEM image of a micro-oscillator showing the edge in a side view. The scalloped sidewall of the DRIE process can be observed (c), as well as the piezo element composed of an AlN and Au stack (d). In (e) the stylus profilometer measurement of a KOH etched profile is shown as well as a 3D microscopic image (f).

4.2 Process Control

The control of the individual process steps is a fundamental intermediate step to ensure a properly working component. In this way, errors in the process chain can be identified and corrected at an early stage. Furthermore, the geometrical parameters that influence the oscillation behavior as described in the theoretical part (see Section 2.2) are inspected. In the following, the results for the layer thickness, the membrane thickness as well as the initial displacement due to residual mechanical stress are presented.

4.2.1 Thin Film Thickness

The thickness of each thin film layer was controlled after the etching process by measuring the depth of an edge with a contact profilometer Dektak 150 from *Veeco Instruments*. The test structure shown in Figure 21b was used for this purpose. In Figure 23, the result for a test structure in the middle area of the wafer is illustrated. The thicknesses of the SiO_2 layer and the AlN layer correspond to the expected target values and are almost homogeneous over the entire wafer. Since the dry oxidation is a growth mechanism and not a deposition process, no dependence on the location is to be expected. The AlN deposition, on the other hand, shows a slight radial dependence from the center of the wafer, which leads to a decrease of the thickness towards the edge of the wafer of a few nm. The good homogeneity of the thickness is ensured by a large 8" Al target used for the reactive sputter process. In contrast, the thickness of the gold layer is significantly larger than the nominal value and shows a strong decrease towards the edge of the wafer. The thickness at the edge is only about 500 nm, which can be attributed to the small 4" Au target. The thickness is still sufficient for good electrical contact as well as adhesion to the substrate.

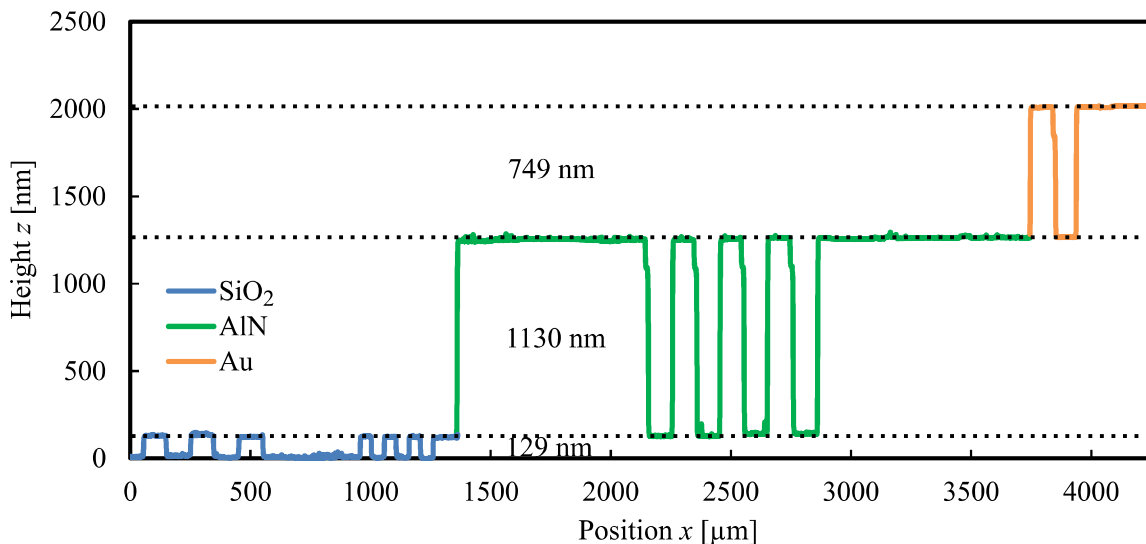


Figure 23. Height measurement of a stylus profilometer over the test structures to determine the layer thicknesses of SiO_2 (blue), AlN (green) and Au (gold).

4.2.2 Membrane Thickness

A critical step in the manufacturing process is the production of the thin Si membranes from which the oscillators are fabricated. The thickness of the membrane also determines the thickness of the oscillator and thus has a decisive effect on its resonance frequency as well as on the quality factor. The membrane thickness was determined by the difference between the measured wafer thickness and the etch depth. The wafer thickness was measured with a capacitive wafer bow instrument (MX203 form *EH-Metrology GmbH*) at seventeen positions to ensure a homogenous wafer thickness. The etch rate was determined by measuring the etch depth after an initial etching step of seven hours. In Figure 22, the stylus profilometer measurement is illustrated to obtain the etch depth of a single cavity. The mean value for the etching rate of the highly doped wafers was slightly above $35 \mu\text{m/h}$. Subsequently, in a second etching step, the desired etching depth respectively membrane thickness was achieved by adjusting the exact etching time. The resulting array of cavities (see Figure 18a) are systematically measured to determine the exact thickness of the membrane and to identify its thickness distribution over the entire wafer. Consequently, the chip number can be used to identify the position on the wafer and thus the thickness of the oscillator can be deduced.

Two special features can be observed in the thickness distributions shown in Figure 24. On the one hand, there is a radially symmetric distribution. This can be attributed to the doping, since higher doping leads to a reduction in the etch rate and thus to a thicker membrane [115]. For example, doping in the crystal pulling process has a radial dependence, as well as doping by spin-on processes. This leads to a variation of the membrane thickness by a few μm from the wafer center to the wafer edge. The second effect, which can be observed is a distribution of the membrane thickness from top to bottom. This effect on the thickness distribution is particularly pronounced for the thinner wafer illustrated in Figure 24b. During the etching process of KOH with Si, hydrogen H_2 is formed, which rises in the liquid etching solution in the form of bubbles. These bubbles block the overlying cavities and therefore slightly reduce the etch rate.

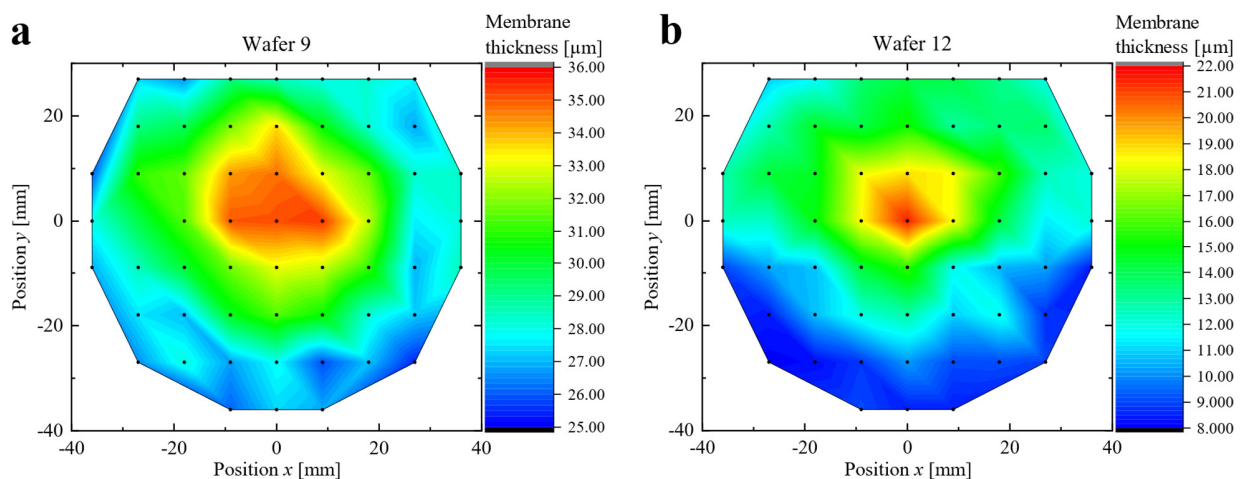


Figure 24. Thickness distribution for two wafers with the targeted thickness of $30 \mu\text{m}$ (a) and $15 \mu\text{m}$ (b).

4.2.3 Residual Stress

The last point of the manufacturing process, which will be considered in the following section, is the initial mechanical stress of the micro-oscillator due to the deposited thin film layers. The mechanical stress results from the differences in the thermal expansion coefficients of the materials, which are deposited at higher temperatures. A general distinction is made between nitrides such as AlN and Si₃N₄, which lead to tensile stresses and oxides such as SiO₂ and Al₂O₃ on the other side, which lead to compressive stresses. For the micro-oscillator, the aluminum components AlN and Al₂O₃ are decisive layers since they are located in the area of the suspension and lead to a deflection of the attached beam and plate. The mechanical stress under varying deposition parameters has been investigated by Ababneh *et al.* and can be determined with the Stoney formula measuring the initial bending of wafers [8]. For a fully covered cantilever structures Nazeer *et al.* gives the following formula to calculate the residual stress σ from the tip displacement δ [116]:

$$\delta = \frac{3\sigma H_{\text{AlN}} L_0^2}{EH^2}, \quad (4.1)$$

with the abbreviations H_{AlN} , L_0 , E , H for the thickness of the AlN layer, the length of the cantilever, its Young's modulus and its thickness, respectively.

In Figure 25, the Dektak profilometer measurement for different micro-oscillators is displayed. The measurement along the two beams for a sensor BO shows that the bending is symmetrical and that there is no additional rotation of the oscillating plate (*cf.* Figure 25a). The comparison between the different geometries is shown in Figure 25b and indicates no major difference between the anchoring structures. Rather, the size of the pre-stressed elements is more decisive. This becomes evident when comparing a cantilever structure with different coverage sizes. Figure 25c illustrates the initial displacement caused by the residual stress of a cantilever with a coverage of a third, a half and the entire oscillator surface. The fully covered cantilever exhibits the largest deflection and the height of the initial displacement respectively the curvature is decreasing with a decreasing coverage size. The bending can only be observed in the area of the AlN piezo elements, the plate itself rises in linear extension given by the angle of inclination created by the curvature. In addition, passivated micro-oscillators were fabricated which were coated with an additional Al₂O₃ layer. In comparison with these cantilevers, a strong decrease of the initial displacement is observed. This is due to the fact, that the additional oxide layer has a compressive impact, which counteracts the tensile stress of the Si₃N₄ layer. The resulting initial displacement can thus be significantly reduced. The effect of the initial displacement must be taken into account when evaluating the gap width to the Al counter plate, since the magnitude is in the range of the smallest gap widths.

Furthermore, the residual stresses have an influence on the oscillation behavior of the oscillator and must therefore be considered. On the one hand, stresses lead to a change in the spring constant, which shifts the resonance frequency [117]. This has a direct influence on the quality factor, since after Equation (2.16) there is a direct correlation between the resonance frequency and the quality factor. The resulting spring constant k can be given as superposition of the beam spring constant k_B (see Equation (2.21)) and a stress induced part k_σ [118]:

$$k = k_B + k_\sigma = \frac{EB_O H^3}{4L_O^3} + \frac{24HB_O}{5L_O} \sigma, \quad (4.2)$$

with the same abbreviations as used above as well as the width of the cantilever B_O . The frequency shift can be acting in both directions since the sign of the residual stress is changing from negative (compressive stress) to positive (tensile stress).

On the other hand, these additional AlN actuation and Al₂O₃ passivation layers lead to frictional losses within the material, which limit the maximum achievable quality factor in the high vacuum regime. According to Equation (2.30), a larger layer results in larger friction and consequently reduces the quality factor. Additional oxide layers do not have the same compensating effect as with the initial deflection, since the frictional losses are still present in the material. The resulting maximum quality factor, which is limited by the material attenuation of coated thin films, is therefore always in the range of a few thousand or below.

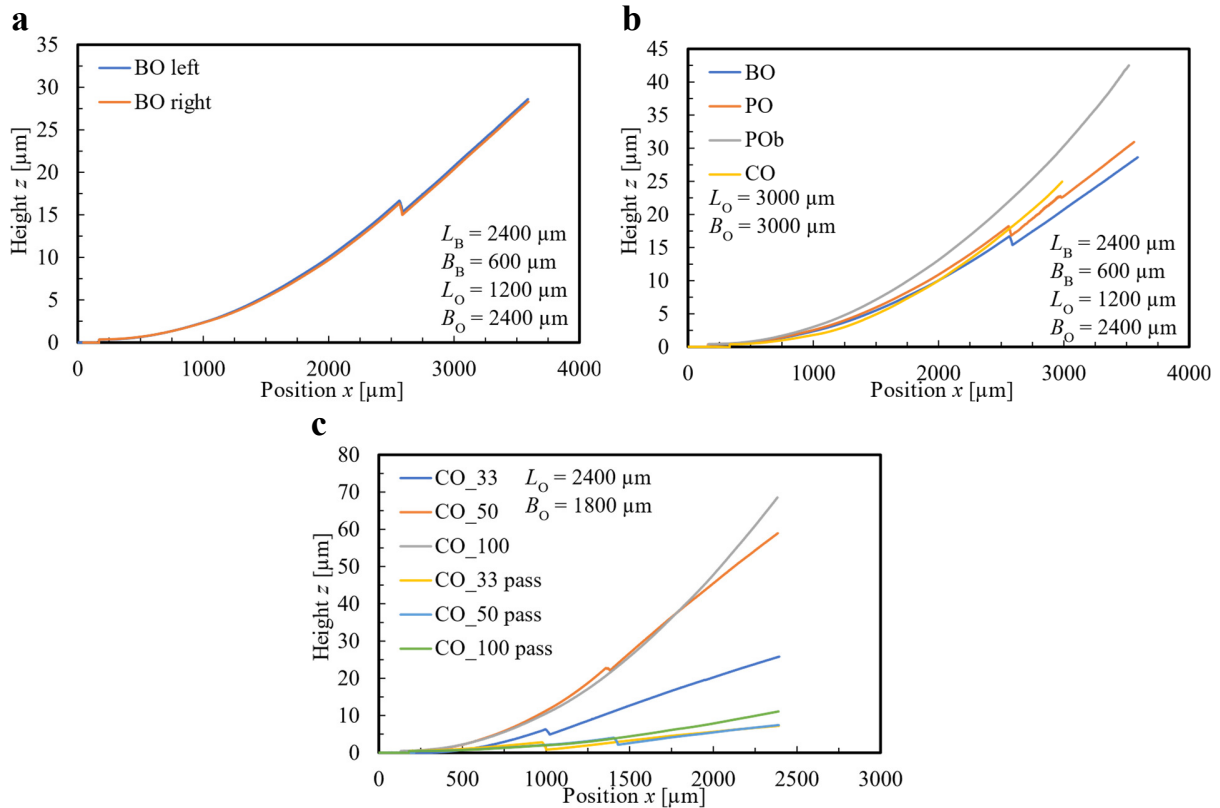


Figure 25. Measurement of the initial displacement with a Dektak profilometer on two beam side of a BO sensor (a), for different geometries (b) and varying coverage sizes of the AlN thin films as well as additional Al₂O₃ passivation layers (c).

5 Measurement

In the following chapter, the basic experimental setups for measurement are discussed. This includes the vacuum chamber, the contacting of the sensors, the electronic circuitry and the setup for distance variation of the gap. Finally, the setup for generating a high magnetic field gradient for the local enrichment of oxygen is presented.

5.1 Vacuum Chamber

The measurements to characterize the oscillation behavior of the micro-oscillators under different gas atmospheres as well as ambient pressures were performed in a custom-built vacuum chamber. Nine different gases with a purity greater than 99.999 % from *Air Liquide Deutschland GmbH* were used for these investigations. These include four noble gases He, Ne, Ar and Kr, as well as five polyatomic gases H₂, N₂, CO₂, N₂O and SF₆. In addition, technical air was used for the investigation of micro-oscillators as paramagnetic oxygen sensor. Technical air constitutes a mixture of nitrogen and 20.5 ± 0.5 % oxygen. The pressure of the gas was varied from 10^{-4} mbar up to 900 mbar. Three physical pressure sensors, which are independent of the gas type, are used to set a defined pressure within a feedback loop: CMR 264 from 10^{-2} to 10^0 mbar, CMR 362 from 10^0 to 10^2 mbar and CMR 261 from 10^2 to 900 mbar. All pressure sensors are capacitive membrane systems from *Pfeiffer Vacuum*. For the rough vacuum range, the rotary vane pump DUO 5 from *Pfeiffer Vacuum* is used, which is additionally supported by the turbomolecular pump TMH 071P also from *Pfeiffer Vacuum* for the pressure range below 0.1 mbar. Pressures below 10^{-2} mbar were measured by the Pirani cold cathode sensor PKR 251 from *Pfeiffer Vacuum*, which exhibits a dependency on the type of gas due to the indirect measurement principle. Therefore, this pressure range is not considered for the extrinsic damping analysis, since the effect of the gas type is not negligible. This pressure range is therefore only used to determine the intrinsic material damping since all the extrinsic gas damping mechanisms are erased at that vacuum level. The whole construction of the vacuum chamber possesses a volume of about 50 l to accommodate the entire measurement circuit and the experimental setup, which are presented in the following sections.

5.2 Measurement Circuit

For the characterization of the micro-oscillators, an electronic measurement circuit was designed and constructed to record the resonance curves. Based on these curves, the evaluation is then performed regarding the two characteristic quantities resonance frequency f_r and quality factor Q , as presented in Section 2.2.1. The excitation of the micro-oscillators is realized by supplying two of four piezo elements by a sinusoidal signal with an amplitude of 1 V and a varying frequency. The excitation via the function generator 33220A from *Agilent Technologies Inc.* is additionally decoupled by a high-impedance buffer amplifier (LMC6482 from *Texas Instruments*) to ensure a constant supply. Due to the resulting oscillation, the other two piezo elements emit electric signals in the form of induced charges, which are measured. Since the amount of charge is in the range of a few fC ($= 10^{-15}$ C), this requires a high measurement accuracy. Therefore, charge amplifiers are used to measure even very small amounts of charges. They consist of an active amplifier circuit and a

parallel RC circuit ($R_{CA} = 8.2 \text{ M}\Omega$, $C_{CA} = 47 \text{ pF}$). The integrating function of the circuit allows the detection of very small amounts of charge, which are directly converted into a voltage signal. The integration of the charge quantity leads to a time constant and thus to a limiting lower cutoff frequency f_{cut} down to which the circuit can be operated:

$$f_{\text{cut}} = \frac{1}{2\pi R_{CA} C_{CA}} \approx 350 \text{ Hz.} \quad (5.1)$$

In order to detect the signal as free of interference as possible, the cable length is minimized and therefore the electronics are housed inside the vacuum chamber. In addition, an inverting amplifier with a constant gain ($= -R_4/R_3$) of about two orders of magnitude is connected behind the charge amplifier to raise the output signal into a range of a few hundred mV ($R_3 = 2.7 \text{ k}\Omega$, $R_4 = 240 \text{ k}\Omega$). The entire measurement circuit is schematically illustrated in Figure 26 and was realized on a printed circuit board (PCB) in quadruplicate for simultaneous connection of four micro-oscillators within the vacuum chamber. The electric signal is then lead out of the chamber and recorded by a lock-in amplifier SR-5210 from *Signal Recovery*. The amplifier compares the amplitude of the measuring signal with the excitation signal, locked to the excitation frequency, thus filtering out all DC components as well as other frequencies from the measurement signal. Depending on the magnitude of the measurement signal, the lock-in amplifier gives a signal between 0 V and 4 V as well as the phase angle between the excitation and the measurement signal. The operating range of the lock-in amplifier is in the range from 0.5 Hz to 120 kHz and thus limits the measurable frequency range upwards.

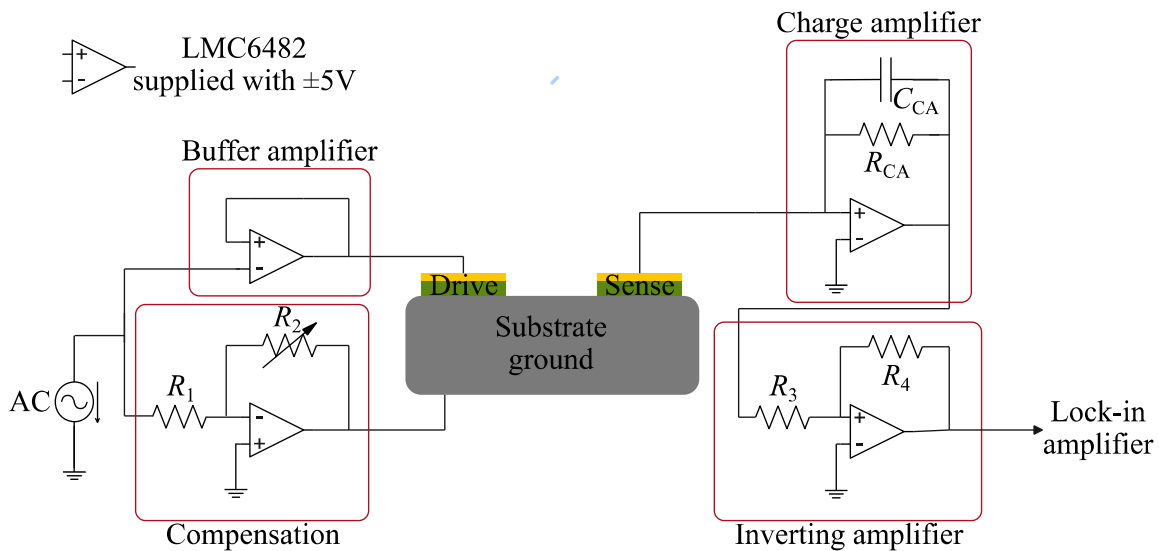


Figure 26. Schematic of the measurement circuit for the compensation of the electrical crosstalk as well as the signal amplification of the sensing element (reused in [119]).

A problem with micromechanical oscillators is the small distance between the excitation and the measurement elements as well as the common ground substrate, which causes a capacitive coupling of the excitation signal into the measurement signal. For this reason, resonance plots like the “double resonance peak” curves shown in Figure 27a and c are initially obtained. These curves can also

be evaluated by means of the resonance frequency and quality factor but can be compensated with an additional active electronic circuit. For this purpose, the mass is virtually shifted by an inverting amplifier and the real part of the curve is shifted to the zero point (*cf.* Figure 27e and f). The compensation strength can be adjusted via the gain factor ($= -R_2/R_1$) and should ideally correspond to the ratio of the measurement capacitance C_{sense} to the crosstalk feedthrough capacitance C_{ft} . This concept was introduced by Qiu *et al.* [120] for the compensation of the electrical crosstalk and was implemented on the electronic board ($R_1 = 470 \Omega$, $R_2 = 0 \dots 200 \Omega$). After successful compensation, the resulting resonance curves have the expected shape (see Figure 27b and d) and can be evaluated according to the equations of Section 2.2.1.

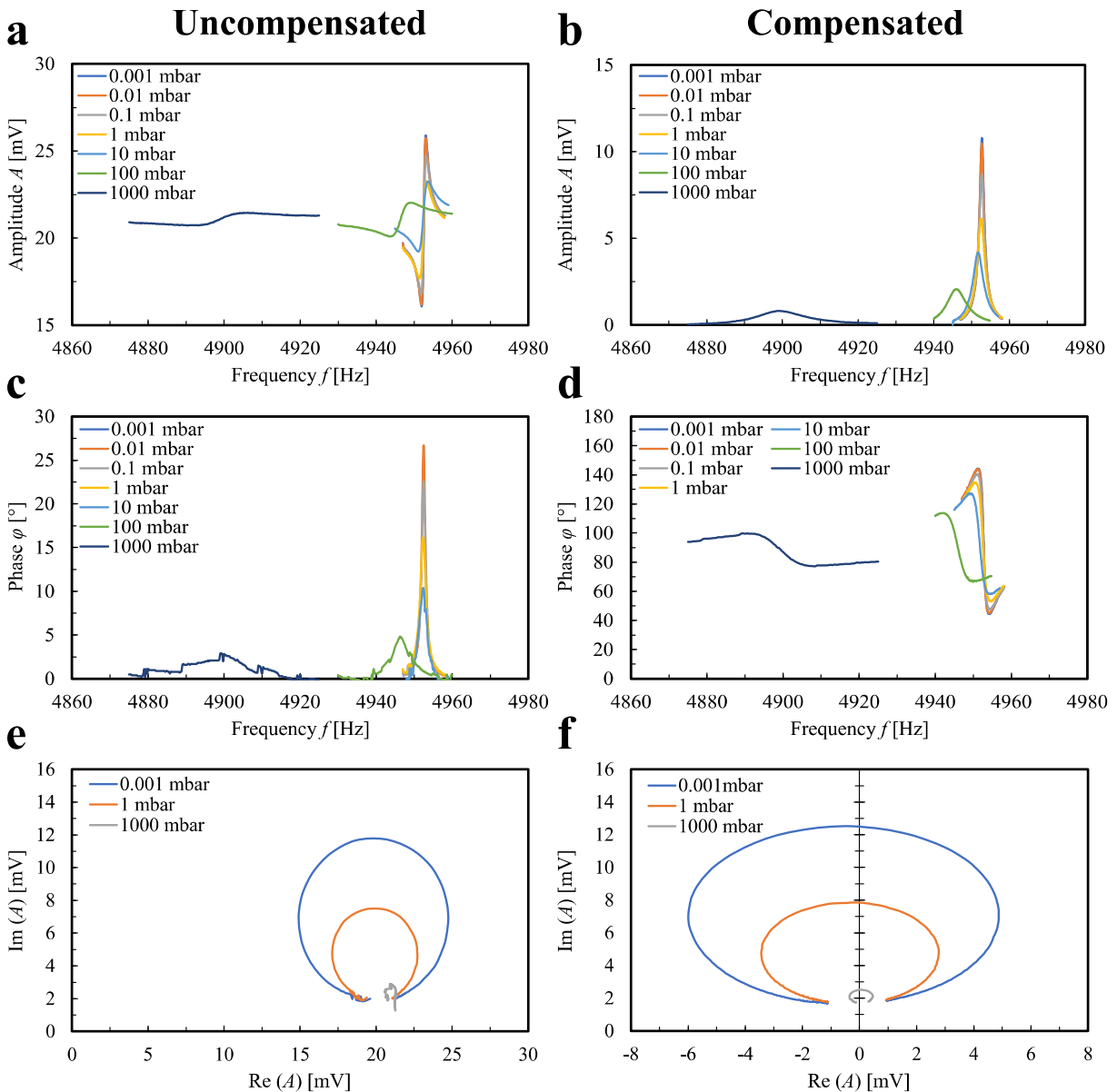


Figure 27. Measurement of resonance curves under varying ambient pressures with the proposed charge amplification circuit. In (a, c, e) the amplitude, phase and bode plot are depicted without capacitive feedthrough compensation and in (b, d, f) with this compensation.

In a further development step of the PCB board, the chip-scale lock-in amplifier AD630 from *Texas Instruments* was included on the board as part of a bachelor thesis, resulting in a significant reduction in the size of the experimental setup [121]. Furthermore, this more compact design is a first step towards a stand-alone solution. In addition, an instantaneous evaluation of the resonance shift by using a phased-lock loop (PLL) as well as the quality factor via measurement of the resonance amplitude is conceivable. The circuit was used experimentally for measurements in liquids as part of a master thesis and led to good results [122]. The circuit board with integrated amplifier circuit, compensation and lock-in amplifier is shown in Figure 28.

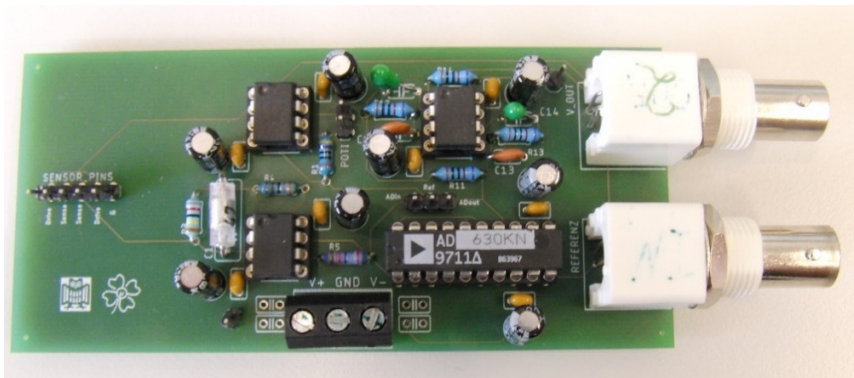
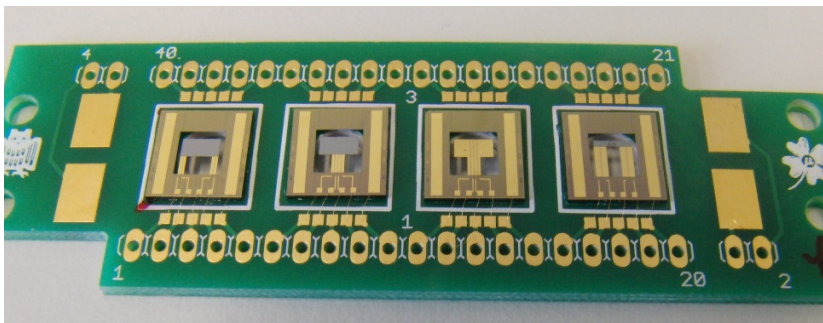


Figure 28. PCB with the measurement electronics consisting of an amplification circuit, a compensation part and a chip scale lock-in amplifier. The total dimensions are $104.5 \times 50 \text{ mm}^2$.

5.3 Experimental Setup

In the following section, the sensor placement will be presented. Two different PCBs were designed for this purpose, which are depicted in Figure 29. In Figure 29a, the board for placing the micro-oscillators in a defined gap width to a geometrical boundary is shown. The PCB is first prepared for this by drilling holes at the four locations of the sensors. This prevents the smallest distance from being limited downward by the board. Then the four micro-oscillators are glued to the board by a pick-and-place machine and they are electrically contacted by bonded gold wires. Finally, the board is connected via connectors to the measurement electronics presented in Section 5.2.

a



b

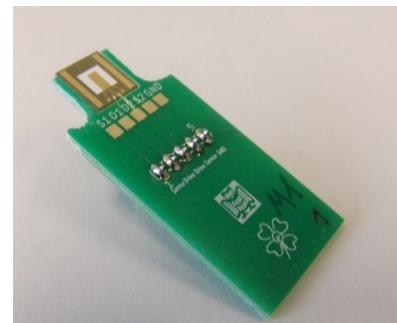


Figure 29. PCB for connecting the micro-oscillators and place them within the experimental setup. In (a), the board for the measurements in dependence of the adjusted gap width under varying ambient pressure is shown and in (b), the board for the investigation as oxygen sensor in the magnetic field construction can be seen.

The board itself is then mounted upside down in the construction shown in Figure 30. Four threaded rods guide the board through the holes on the outside and the board can be fixed at a defined height by tightening the countered nuts. First, the board is aligned parallelly to the Al counterplate using two gauge blocks with a thickness of $800 \pm 2 \mu\text{m}$ and then the board is fixed at the defined distance. The exact gap width between the micro oscillator and the Al counterplate can be derived from the height of the glued oscillators above the board, which was measured by means of a length measuring probe Millimar C 1208 from *Mahr*. The gap width is adjusted by varying the height of the Al counter plate which is controlled by the linear motor M-228 11S from *Physik Instrumente (PI)*. The whole construction is then placed in the vacuum chamber to investigate the influence of the gap width under varying ambient pressures as well as for different gas atmospheres on the damping behavior of micro-oscillators.

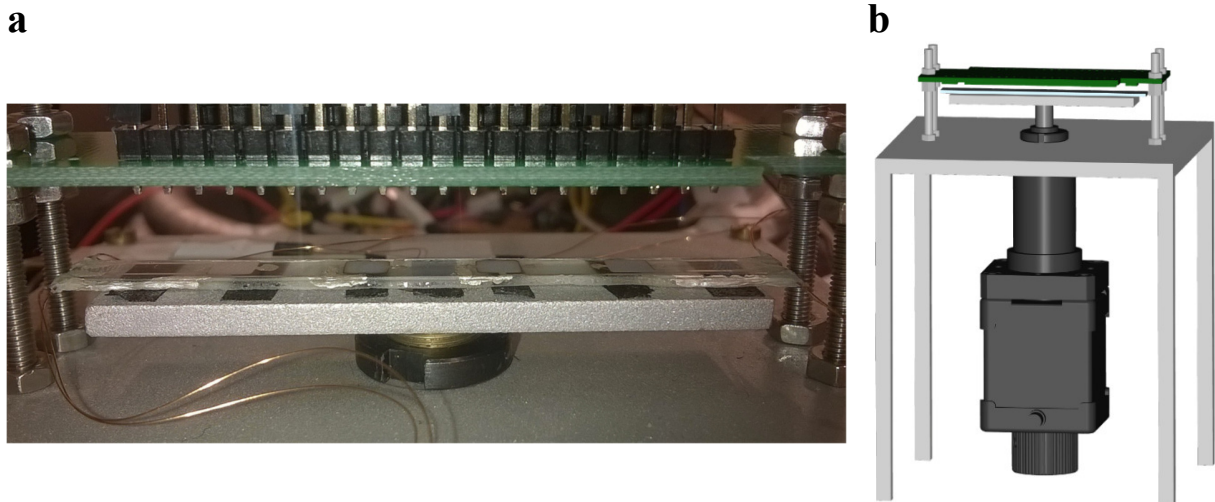


Figure 30. Construction to place the micro-oscillators in a defined gap width to a geometrical boundary. In (a), the cross-section for mounting the board is shown and in (b), the entire construction including the linear motor for controlling the gap width by regulating the height of the Al plate can be seen [123].

The second board shown in Figure 29b was developed for the positioning of micro-oscillators in a concentrated magnetic field. Due to the geometry of the field focusing part for generating the magnetic field gradient, the holder is designed in such a way that only the micro-oscillator is placed free-standing in the field and the electrical signals are led away to the back. The further details for placing the sensor by means of this board in the generated magnetic field can be found in the next section.

5.4 Magnetic Field Construction

The magnetic field structure for generating the highest possible product of magnetic field and magnetic field gradient has already been modelled numerically in Section 3.4. The simulation was used for optimizing the magnetic field focusing unit. As shown in Figure 15, both the magnetic circuit and the focusing unit are made of the noble magnetic material Telar 57 from *AKSteel International BV*. All components for this circuit, in particular the flattened pyramid elements for the focusing

unit, are precision-engineered in the workshop of the *Fraunhofer IZFP* institute. Due to the magnetic force, the structure sticks together without any further clamping and must be actively separated in the focusing area. Two column structures are used as stop to protect the structures against a collision of the two flattened pyramids. The holding structures are completely made of plastic in order not to cause a magnetic short circuit of the field. With an additional plastic screw, the gap width can be controlled by the adjusting wheel and the gap is fixed with two plastic counter nuts. Using a 1 mm gauge block, the gap is adjusted within the setup. For the placement of the sensor, a support structure with a sled was designed to hold the sensor board at the height of the gap. Then, the sensor can be moved into the magnetic field by means of this sled and read out via electrical connections on the bottom side. The entire setup with the built-in micro-oscillator is shown in Figure 31.

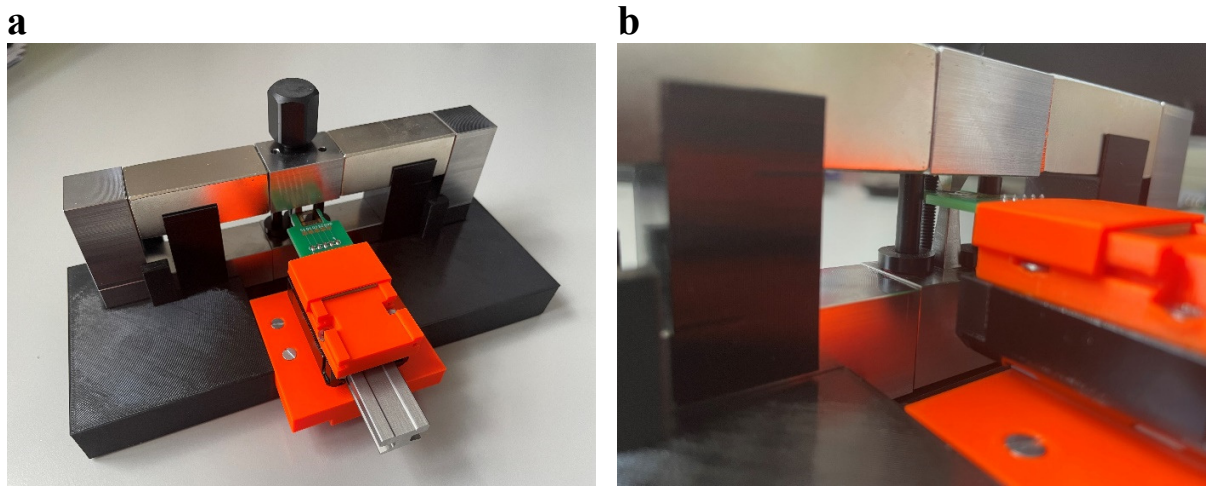


Figure 31. Picture of the mounted magnetic circuit. The distance can be adjusted precisely via the adjusting wheel by means of a plastic screw and two countered nuts (a). In (b) a detailed view on the gap where the sensor is placed can be seen.

Prior to the micro-oscillator measurements, the magnetic field within the gap was characterized using a Hall sensor, which is read out via a magnetometer (KOSHAVA 5 from *Wuntronic GmbH*). The measuring probe has a sensing head with a width of 2 mm. The spatial expansion of the sensor head is therefore not negligible compared to the spatial resolution of the magnetic field (see insert of Figure 32). The measured results are thus the superposition of the magnetic field with the measurement geometry of the sensing head, which mathematically represents a convolution of the two functions. As a result, the maximum value is significantly higher than the numerical value as well as the remanence value of the FeNdB magnet since the magnetic field is accumulated over the entire sensor surface and thus leads to an increase of the measuring signal of the Hall sensor. For approximation, the magnetic field is assumed to have a Gaussian profile and the measuring tip is described with the Heaviside function $\theta(x)$. The convolution of the two functions yields the following result:

$$(f * g)(x) = \int_{-\infty}^{\infty} A e^{-\frac{(x-\tilde{x})^2}{\sigma}} [\theta(\tilde{x} + 1) + \theta(\tilde{x} - 1)] d\tilde{x} \quad (5.2)$$

$$= \frac{A\sqrt{\pi\sigma}}{2} \left(\operatorname{erf}\left(\frac{x+1}{\sqrt{\sigma}}\right) + \operatorname{erf}\left(\frac{x-1}{\sqrt{\sigma}}\right) + 1 \right), \quad (5.3)$$

whereby $\operatorname{erf}(x)$ denotes the Gaussian error function. A_{Gauss} and σ_{Gauss} are fitting parameter obtained by the curve fitting method where the fit parameter A_{Gauss} represents the maximum value of the magnetic field and σ_{Gauss} represents the variance of the Gaussian function.

Figure 32 shows the measured values for a bidirectional transit of the Hall sensor through the gap. Due to the uncertainty of the motor joint, the position accuracy is $\pm 30 \mu\text{m}$. According to the manufacturer, the measurement error of the Hall sensor is $\pm 2\%$. A fit of the Gaussian function in combination with the convolution shows a good agreement with the measured data. The maximum value of the magnetic flux, slightly over 1 T, corresponds to the numerically determined value ($B_{\text{sim}} = 1.3 \text{ T}$). The exact shape of the magnetic field cannot be resolved due to the size of the measuring probe and therefore the magnetic field as well as the corresponding gradient can only be determined approximately. This leads to the deviation between the determined profile and gradient to the numerical results. Qualitatively, however, the resulting force (product of magnetic field and gradient) is correct and leads to an accumulation of paramagnetic materials in the focusing area.

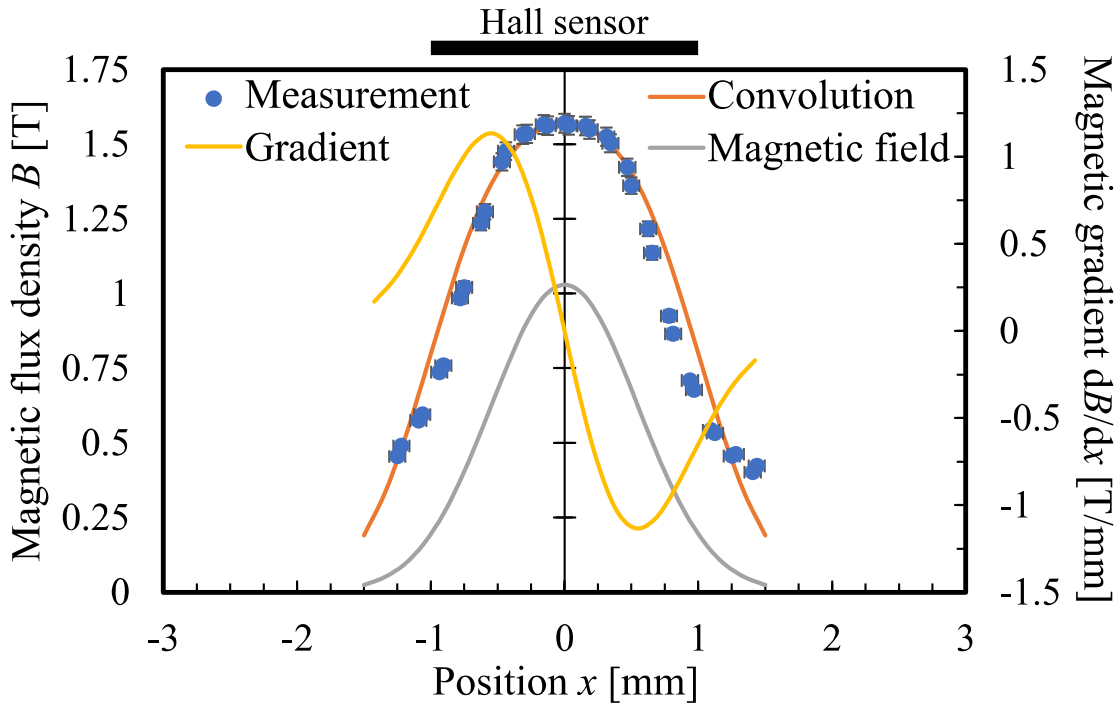


Figure 32. Measurement of the magnetic field within the gap (blue points) showing the convolution of the actual magnetic field and the sensor geometry. The points are fitted with the convolution using Equation (5.3) (orange line) to reconstruct the real magnetic field (grey line). From this result the gradient of the magnetic field (yellow line) is calculated.

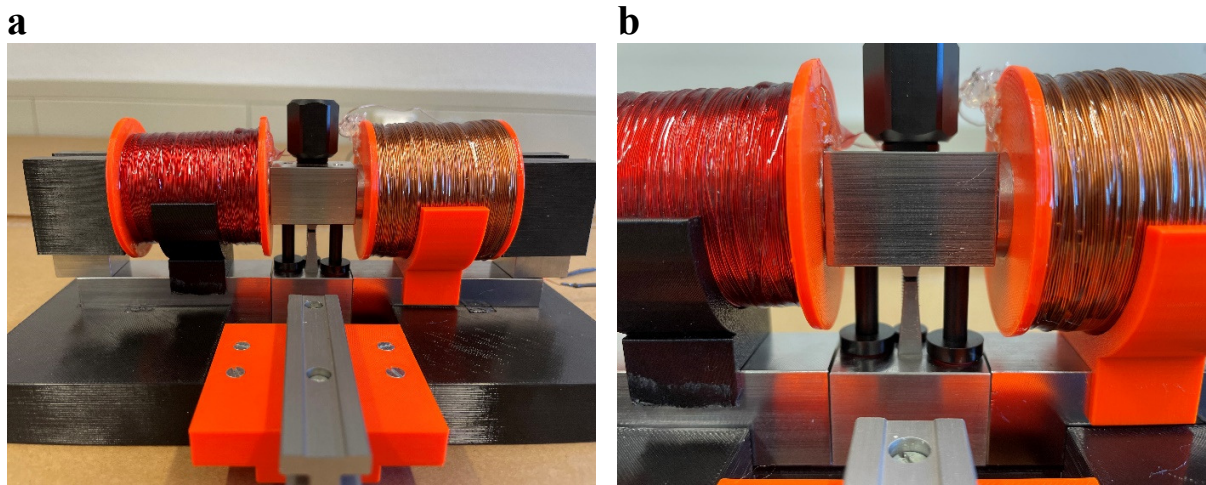


Figure 33. Magnetic field circuit with the coils as active field generating component (a) to create a high magnetic field gradient between the two flattened pyramid structures (b). Two different wire diameters are used, indicated by different colors (280 μm red and 315 μm copper).

For the measurement to detect the paramagnetic effect of oxygen, coils are used to generate the magnetic field, replacing the permanent magnets (see Figure 33). Two types of coils were used due to manufacturing problems with the thinner wire diameter. Coil 1 possesses a wire of 280 μm diameter with a resistance of 110 Ω and an inductance of 582 mH, whereas coil 2 is constructed using a wire of 315 μm resulting in a resistance of 43 Ω and an inductance of 342 mH. Analogous to previous measurements, the maximum of the magnetic field inside the gap is recorded with the magnetometer as a function of the applied voltage (see Figure 34). The result is a magnetic field of 1.02 T, which is comparable to the permanent magnet structure. When only one coil is switched on (blue and orange line), the magnetic field is reduced considerably, since a portion of the magnetic field is lost via the inactive coil. By activating both coils in opposite directions (grey line), a significantly higher magnetic field can be generated than by the individual coils (yellow line showing the linear superposition of coil 1 and coil 2).

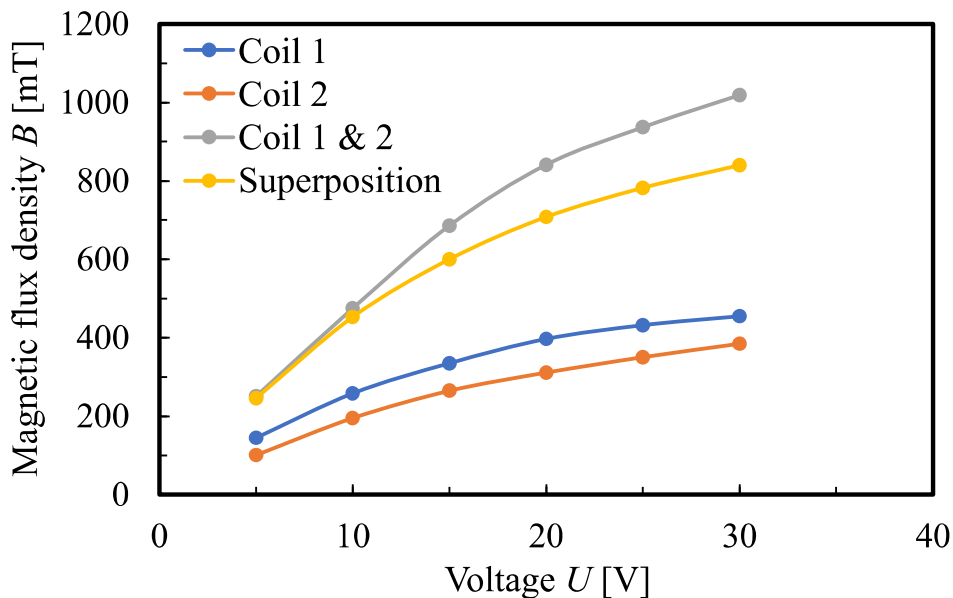


Figure 34. Magnetic flux density measured within the gap between the flattened pyramid structure as function of the operating voltage applied to the coils.

6 Results

The following publications are presented in this cumulative dissertation. All co-authors of the peer-reviewed journal articles and conference proceedings listed below have agreed that these publications may be used. The authors' contributions are indicated as follows:

1. „Polyatomic degrees of freedom and their temporal evolution extracted from the damping of micro-oscillators”, *Sensors and Actuators A: Physical*, vol. 297, 111460, 2019.

T. Zengerle: Investigation, Software, Formal analysis, Data curation, Writing - original draft, Writing - review & editing. **J. Joppich:** Methodology, Software. **P. Schwarz:** Conceptualization, Visualization. **A. Ababneh:** Supervision, Funding acquisition. **H. Seidel:** Writing - review & editing, Supervision, Project administration, Funding acquisition.

2. „Modeling the damping mechanism of MEMS oscillators in the transitional flow regime with thermal waves”, *Sensors and Actuators A: Physical*, vol. 311, 112068, 2020.

T. Zengerle: Investigation, Software, Formal analysis, Data curation, Writing - original draft, Writing - review & editing. **J. Joppich:** Methodology, Software. **P. Schwarz:** Conceptualization, Visualization. **A. Ababneh:** Supervision, Funding acquisition. **H. Seidel:** Writing - review & editing, Supervision, Project administration, Funding acquisition.

3. „Thermal resonance model for micro-oscillators in the vicinity of a geometric boundary”, *Sensors and Actuators A: Physical*, vol. 341, 113614, 2022.

T. Zengerle: Investigation, Software, Formal analysis, Data curation, Writing - original draft, Writing - review & editing. **A. Ababneh:** Supervision, Funding acquisition. **H. Seidel:** Writing - review & editing, Supervision, Project administration, Funding acquisition.

4. “Generalized damping model for MEMS oscillators from molecular to viscous flow regime”, *Eng*, vol. 3, no.1, 2022

T. Zengerle: Investigation, Software, Formal analysis, Data curation, Writing - original draft, Writing - review & editing. **A. Ababneh:** Supervision, Funding acquisition. **H. Seidel:** Writing - review & editing, Supervision, Project administration, Funding acquisition.

5. „Equivalent circuit model for the damping of micro-oscillators from molecular to viscous flow regime”, *Journal of Micromechanics and Microengineering*, vol. 31, 095010, 2021.

T. Zengerle: Investigation, Software, Formal analysis, Data curation, Writing - original draft, Writing - review & editing. **J. Joppich:** Methodology, Investigation, Writing - original draft **H. Lensch:** Formal analysis, Conceptualization. **A. Ababneh:** Supervision, Funding acquisition. **H. Seidel:** Writing - review & editing, Supervision, Project administration, Funding acquisition.

6. „Using the nonlinear Duffing effect of piezoelectric micro-oscillators for wide-range pressure sensing”, *Actuators*, vol. 10, no. 8, 2021.

T. Zengerle: Investigation, Formal analysis, Data curation, Writing - original draft, Writing - review & editing. **M. Stopp:** Methodology, Investigation **A. Ababneh:** Project administration, Supervision, Funding acquisition. **H. Seidel:** Writing - review & editing, Supervision, Project administration, Funding acquisition.

6.1 Summary of the Appended Publications

In the following, the publications are briefly summarized and placed in the context of the overall thesis. They will be presented in the following sections and accompanied by a short introduction to the topic, in which the current literature and the state of the art are reviewed. In addition, further investigations are presented that did not find a place in the attached papers. The chapter is completed by two sections with unpublished data, comparing the damping in liquids and gases and the utilization of micro-oscillators as oxygen detectors as well as the measurements on the paramagnetic effect. All publications are reprinted with permission of the journals.

Addendum I Polyatomic degrees of freedom and their temporal evolution extracted from the damping of micro-oscillators

The results of the investigations on the damping behavior of different gas atmospheres in the molecular flow regime were published in 2019 in the journal **Sensors and Actuators A: Physical** (Impact Factor: 3.407). The study demonstrates the influence of polyatomic degrees of freedom on the quality factor of micro-oscillators and reveals a possibility to observe the development of polyatomic degrees of freedom with an increasing gap width. In conclusion, a theory was presented covering the effect of the additionally activated polyatomic degrees of freedom and connecting the theory of Bao *et al.* [61] for small gap widths and Christian [53] for a freely oscillating structure.

Addendum II Modeling the damping mechanism of MEMS oscillators in the transitional flow regime with thermal waves

The new description of the damping behavior of micro-oscillators in the transitional flow regime based on resonance effects of thermal waves was introduced in **Sensors and Actuators A: Physical** (Impact Factor: 3.407) published in 2020. The concept was presented and derived based on a constructive interference model as well as verified for a nitrogen atmosphere.

Addendum III Thermal resonance model for micro-oscillators in the vicinity of a geometric boundary

Subsequently, the theory was studied experimentally on further micro-oscillator structures and on other gas atmospheres. These results confirmed the presented approach and provided further insights into the dependence of the theory on the thermodynamic properties of the gases, such as thermal diffusivity and isentropic coefficient. This study was also presented in **Sensors and Actuators A: Physical** (Impact Factor: 3.407) in 2022.

Addendum IV Generalized damping model for MEMS oscillators from molecular to viscous flow regime

In this work published in 2022 in the journal **Eng**, the damping model was applied to three different micro-oscillator structures with different sizes and

coverages of the actuator area. The experimental data showed a very good agreement with the model for all sensors for the fundamental mode as well as for higher bending modes. From the results generalized statements about the strength of the damping were obtained, which refer only to the size of the frequency dependent viscous and thermal boundary layer

Addendum V Equivalent circuit model for the damping of micro-oscillators from molecular to viscous flow regime

In the following publication released in **Journal of Micromechanics and Microengineering** (Impact Factor: 1.881) in 2020, the damping phenomena from the molecular up to the viscous flow regime were reconstructed by an equivalent circuit model. This model was compared and verified with the experimental data of two micro-oscillators, including higher bending modes.

© IOP Publishing. Reproduced with permission. All rights reserved.

Addendum VI Using the nonlinear Duffing effect of piezoelectric micro-oscillators for wide-range pressure sensing

The concept of a new pressure sensing system based on a nonlinear micromechanical duffing oscillator was presented in the journal **Actuators** (Impact Factor: 1.994) in 2021. The measurement principle reveals a very wide measurement range, which can be adjusted by the actuation voltage in a trade-off with the sensitivity. In contrast to other mechanical measurement methods, this principle can also be used in the high vacuum range, where it even has its highest sensitivity.

6.2 Influence of Polyatomic Degrees of Freedom

6.2.1 Introduction

In the first result section, new findings on the damping behavior of polyatomic gas molecules in the molecular flow regime are presented. The fundamental theoretical base of molecular flow regime damping was introduced by R. Christian for a completely freely oscillating structure [53], disregarding effects of any geometrical restrictions in the near vicinity (*c.f.* Section 2.3.2). Recent developments have been achieved by expanding the theory with a gap width dependency to a geometric boundary [61] and taking thermal effects such as device temperature and thermal velocity into account [55]. However, a missing part in the molecular flow damping theory is the investigation of different gas atmospheres and the impact of the different molecular structures and their thermodynamic properties. Therefore, the damping of a micro-oscillator is experimentally examined in various gas atmospheres consisting of noble gases and polyatomic gases. In addition to the standard three translational degrees of freedom, polyatomic gas molecules can exhibit additional rotational and vibrational degrees of freedom. Within these additional degrees of freedom, the gas molecules can store energy they receive from the collision with the micro-oscillator and heat losses caused by the oscillation movement. With a higher number of degrees of freedom, the heat capacity

increases and, subsequently, the temperature gradient as well as the associated losses are decreasing. This effect is measured by the quality factor and thus the evolution of polyatomic degrees of freedom with the adjusted gap is observed.

6.2.2 Degrees of freedom

The mathematical description of the influence of molecular degrees of freedom can be derived by using statistical physics. In the theory chapter, the influence of the degrees of freedom on the macroscopic quantities, thermal conductivity (2.6) and isentropic coefficient (2.7), were presented. This view is now extended to the molecular level, demonstrating the connection of the heat capacity with the molecular degrees of freedom. The decisive factor for the heat capacity is in fact the number of degrees of freedom, which are available to absorb thermal energy and store it in a molecular motion (translation, rotation, or vibration). The average amount of energy $\langle E \rangle$ per degree of freedom is equal and given by the equipartition theorem [124]:

$$\langle E \rangle = \frac{1}{2} k_B T. \quad (6.1)$$

The energy of a molecule is subdivided into the three different degrees of freedom, the translational degrees of freedom, the rotational degrees of freedom and the vibratory degrees of freedom. The total energy E_{tot} is decomposed into the translational part E_{trans} , the rotational part E_{rot} and the vibrational part E_{vib} [125]:

$$\langle E_{tot} \rangle = \langle E_{trans} \rangle + \langle E_{rot} \rangle + \langle E_{vib} \rangle = \frac{\langle p_{mol}^2 \rangle}{2m} + \frac{h}{4\pi I} j(j+1) + \frac{h}{2\pi} \omega_{vib} \left(\langle o \rangle + \frac{1}{2} \right), \quad (6.2)$$

with the momentum p_{mol} , the mass m , the moment of inertia I , the rotational quantum number j , the vibration oscillation ω_{vib} and the occupancy o of the gas molecule. In addition, Planck's constant h is used and expected values are indicated by $\langle \rangle$ brackets.

The translational heat capacity results from the integration of the canonical partition function over all impulses and as a derivative of the resulting energy with respect to the temperature:

$$C_{V,trans} = \frac{f}{2} N k_B. \quad (6.3)$$

For the translatory part, the number of degrees of freedom is typically given by $f_{DOF,trans} = 3$ at ambient temperature. Only in special cases this number is reduced, for example in presence of geometrical limitations as in two-dimensional electron gas trough heterostructures.

The total rotational energy results in the same manner by taking the sum over all rotational quantum numbers and subsequently from the derivative with respect to temperature. A closed form of the sum can only be achieved in an approximation for either small or for high temperatures, relative to the defined rotational temperature θ_{rot} :

$$C_{V,rot} = N k_B \begin{cases} 3 \left(\frac{\theta_{rot}}{T} \right)^2 e^{-\frac{\theta_{rot}}{T}}, & \text{for } \frac{\theta_{rot}}{T} \gg 1 \\ 1, & \text{for } \frac{\theta_{rot}}{T} \ll 1 \end{cases} \quad \theta_{rot} = \frac{h}{4\pi k_B I} \quad (6.4)$$

The rotational temperature θ_{rot} can be associated with the required thermal energy to activate the rotational degrees of freedom. In Table 7, all data for the investigated gas molecules are summarized and the structure of the gas molecules can be seen in Figure 35. The linear gas molecules (H_2 , N_2 , CO_2 , N_2O), where all atoms are arranged on a single bonding axis, exhibit two moments of inertia. The third axis corresponding to the bonding axis does not lead to a moment of inertia. Therefore, only the more complex molecule SF_6 possesses a third moment of inertia where thermal energy can be accumulated.

Table 7. Listing of the investigated gas molecules and their corresponding bond length and bond angle [126]. With these informations and with the masses from Table 1, the moment of inertia is calculated according to Steiner's theorem [127]. The rotational temperature and the corresponding rotational energy were calculated using Equation (6.4). The number of moments of inertia is given by #.

Molecule	Bond length a [Å]	Bond angle θ [°]	Moment of inertia I [kg·m ²]	Rotational Temperature θ_{rot} [K]	Rotational energy E_{rot} [μeV]	#
H_2	H-H: 0.74	< (H,H): 180	$4,6 \times 10^{-48}$	88,16	7597,68	2
N_2	N-N: 1.10	< (N,N): 180	$1,4 \times 10^{-46}$	2,88	248,2	2
CO_2	C-O: 1.16	< (C,O,C): 180	$7,2 \times 10^{-46}$	0,56	48,3	2
N_2O	N-N: 1.13 N-O: 1.19	< (N,N,O): 180	$6,67 \times 10^{-46}$	0,60	51,7	2
SF_6	S-F: 1.56	< (F,S,F): 90	$3,07 \times 10^{-45}$	0,13	11,2	3

The values for the activation of the rotational degrees of freedom are in the same range, except for hydrogen, which requires a significantly higher amount of energy to get activated. Nevertheless, at room temperature ($T = 300$ K), the rotational degrees of freedom are fully developed for all gases.

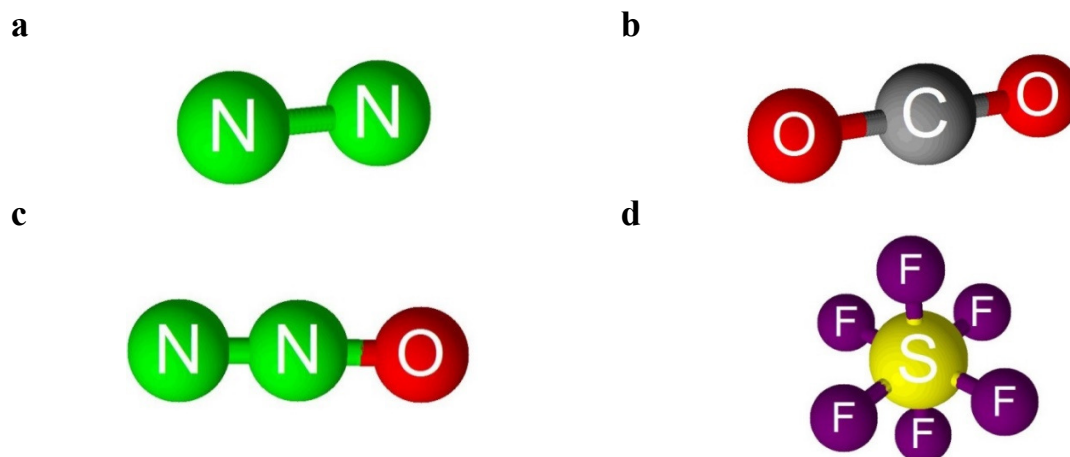


Figure 35. Schematic drawing of the molecular structure of the polyatomic gas molecules. In (a) the diatomic N_2 is shown, in (b) and (c) the triatomic gases CO_2 and N_2O are depicted and in (d) the gas molecule SF_6 is illustrated.

For the calculation of the vibrational portion, the canonical partition function of the vibratory energy part is evaluated. Therefore, all occupation densities are summed up and can be resolved by means of a geometric series. The resulting heat capacity for the vibrational part can be specified for the two limiting ranges of high and low temperatures (referred to the vibrational temperature θ_{vib}):

$$C_{V,\text{vib}} = Nk_B \begin{cases} \left(\frac{\theta_{\text{vib}}}{T}\right)^2 e^{-\frac{\theta_{\text{vib}}}{T}}, & \text{for } \frac{\theta_{\text{vib}}}{T} \gg 1 \\ 1 - \frac{1}{12} \left(\frac{\theta_{\text{vib}}}{T}\right)^2, & \text{for } \frac{\theta_{\text{vib}}}{T} \ll 1 \end{cases} \quad \theta_{\text{vib}} = \frac{h\omega_{\text{vib}}}{2\pi k_B} \quad (6.5)$$

The values of the vibrational temperature of the gases are summarized in Table 8. The natural frequencies are collected experimentally from different works, which use different measurement methods to determine the frequency of the molecular vibration. In general, the required vibrational energy is about four orders of magnitude higher than the rotational energy. This leads to the fact that the vibrational temperature is elevated by the same factor and the vibrational degrees of freedom cannot be activated thermally at room temperature. Only SF₆ shows a partial excitation of the vibrational degrees of freedom due to the thermal energy of the ambient temperature.

Table 8. Listing of all investigated gas molecules and their vibrational frequencies and eigenmodes. From the vibrational frequencies, the associated vibrational temperature and corresponding vibrational energy is calculated according to Equation (6.5). In the last column, the number of the individual eigenmodes and the total number of the vibrational modes is given.

Molecule	Vibrational frequency f_{vib} [THz]	Vibrational temperature θ_{vib} [K]	Vibrational energy E_{vib} [meV]	Mode	#	
H ₂ [128]	130.26	6250.11	538.34	Stretch	1	1
N ₂ [128]	82.26	4165.53	340.21	Stretch	1	1
CO ₂ [129]	40.57	2054.83	167.83	Sym. Stretch	1	4
	20.16	1021.04	83.39	Bend	2	
	71.02	3596.71	293.76	Assym. stretch	1	
N ₂ O [130]	38.92	1970.88	160.97	Sym. stretch	1	4
	17.87	905.21	73.93	Bend	2	
	68.41	3464.49	282.96	Asym. stretch	1	
SF ₆ [131]	23.22	1175.80	96.03	Sym. stretch	1	15
	28.41	1439.08	117.53	Asym. stretch	3	
	15.69	794.79	64.91	Bend	3	
	19.28	976.64	79.77	Stretch	2	
	18.43	933.63	76.25	Bend	3	
	10.43	528.40	43.16	Bend	3	

The experimentally available degrees of freedom are calculated from the isentropic exponent at room temperature according to Equation (2.7) using the data from National Institute of Standards and Technology [14]. The values obtained are listed in Table 1 of the appended journal article (see Section 6.2.3 Addendum I) and show a range from three degrees of freedom for the noble gases to about thirteen for the SF_6 gas molecule, which has additional vibrational and rotational degrees of freedom.

The complete development of the heat capacity of a gas molecule can thus be reconstructed as a function of temperature. Taking the individual effects of the degrees of freedom into account, an evolution of the heat capacity with the ambient temperature is obtained. This evolution plot is schematically shown in Figure 36 for a diatomic gas as an example. In addition to the description of the degrees of freedom evolution with temperature, there is also a description in the literature of intermolecular collisions for the activation of individual degrees of freedom. This is also taken up in the following work and the required number of intermolecular collisions for the excitation of individual degrees of freedom is determined experimentally. For this purpose, the presented theory is adapted and transferred to the problem. We assume a gas molecule, which can perform a limited number of intermolecular collisions within the gap (besides the collision with the micro-oscillator). This affects the thermal property of the gas molecules and, thus, the heat capacity of the surrounding gas atmosphere. This change in the heat capacity influences the energy losses of the micro-oscillator to the environment, which is read out by the quality factor measurement. The higher number of degrees of freedom of the polyatomic gases has the consequence that, due to the higher heat capacity, the temperature gradient within the gap is reduced and thus also the dissipative heat flux is decreased. Such effects were already shown in the 1930s by Kneser in sound absorption measurements and attributed to relaxation times of the gas molecules in the range of a few μs [132].

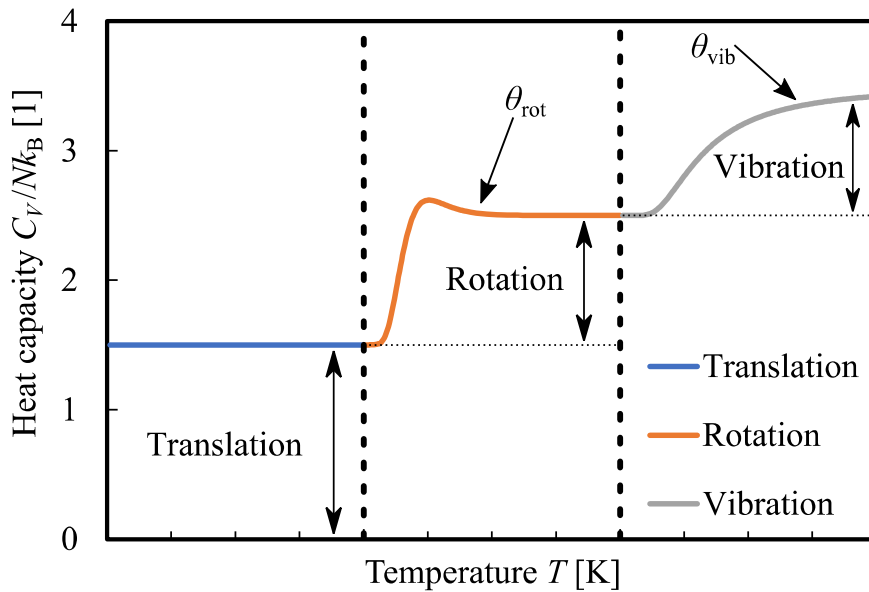


Figure 36. Schematic plot of the heat capacity of a diatomic gas molecule as function of the ambient temperature. The total heat capacity is divided into three storage mechanism (translation, rotation, vibration) for accumulating thermal energy in the gas molecule.

6.2.3 Addendum I

Sensors and Actuators A 297 (2019) 111460



Contents lists available at ScienceDirect

Sensors and Actuators A: Physical

journal homepage: www.elsevier.com/locate/sna

Polyatomic degrees of freedom and their temporal evolution extracted from the damping of micro-oscillators

T. Zengerle^{a,*}, J. Joppich^b, P. Schwarz^a, A. Ababneh^{a,c}, H. Seidel^a^a Chair of Micromechanics, Microfluidics and Microactuators, Saarland University, Campus A5.1, 66123, Saarbrücken, Germany^b Laboratory of Measurement Technology, Saarland University, Campus A5.1, 66123, Saarbrücken, Germany^c Electronic Engineering Dept., Hijawi Faculty for Engineering Tech., Yarmouk University, Jordan

ARTICLE INFO

Article history:

Received 18 April 2019
 Received in revised form 6 June 2019
 Accepted 19 June 2019
 Available online 23 July 2019

Keywords:

Molecular flow
 Rotational and vibrational degrees of freedom
 Collision number
 Relaxation time
 MEMS oscillator
 Q factor

ABSTRACT

This paper investigates for the first time the influence of molecular degrees of freedom (DOF) on the damping behavior of micro-oscillators in the molecular flow regime. None of the existing theories of damping does take this aspect into account. The damping of piezoelectrically driven bending oscillators is determined by measuring the pressure dependent quality factor Q in an atmosphere consisting of noble gases or polyatomic gases. A neighboring plate with an adjustable gap width ranging from 150 to 3500 μm was mounted above the oscillator, limiting the time of flight of the gas molecules in between the delimitation to several microseconds. Taking the behavior of the noble gases with three translational DOF as a reference, the development of additional rotational and vibrational DOF of polyatomic gas molecules is determined as a function of the gap width, which can be correlated to the time of flight. The determined relaxation times and collision numbers of the DOF are compared to existing theories and to experimental results explored by other methods. Based on the experimental evidence, additions to the existing molecular damping theory are derived by including the higher DOF and adapting an existing thermodynamic excitation model.

© 2019 Elsevier B.V. All rights reserved.

1. Introduction

Micromechanical oscillators are widely used in different types of sensors and can reach a high resolution. Examples are the detection of small masses [1] or small mass changes [2], mostly for bioanalytical purposes based on an antibody-antigen reaction [3]. They are also used for the detection of small forces in atomic force microscopy [4,5]. Gyroscopes for inertial angular rate sensing are another prominent example having found widespread dissemination in cars and in smart phones [6].

The damping effects on a mechanical oscillator can be separated into a purely mechanical and a pressure dependent fluidic part. The mechanical, so called intrinsic damping is dominated by internal losses in the solid state material, including a thermoelastic effect described by Zener [7]. The fluidic part strongly depends on the nature and pressure of the surrounding ambient atmosphere and this in turn has a strong influence on the sensor performance. For this reason, oscillator based sensors are usually packaged or

operated under a well defined reduced pressure (e.g. gyroscopes [8]).

It was found that the fluidic damping regime can be separated into three parts: the molecular flow part for low pressures, the viscous part for high pressures and a transition regime in between the two [9–13]. The decisive parameter distinguishing between the different flow regimes is the Knudsen number Kn , being defined as the quotient of the mean free path l_{mfp} of the gas molecules and a characteristic length parameter l' of the system under observation:

$$Kn = \frac{l_{\text{mfp}}}{l'} \quad (1)$$

In our case, the characteristic length is the width of the gap between the oscillating cantilever and a neighboring wall. For $Kn \ll 1$, the gas molecules will frequently collide with each other, defining the viscous flow regime where the continuum theory of gases is applicable. When $Kn \gg 1$ it is obvious that the individual gas molecules will hardly interact (collide) with each other anymore but only with the walls of the surrounding system. This is defined as the molecular flow regime, which cannot be described by continuum theory. In between is a transition regime, which is difficult to describe physically. Different authors use different numbers for the boundaries between the three zones. We follow Wutz et al. [14]

* Corresponding author.

E-mail address: t.zengerle@imm.uni-saarland.de (T. Zengerle)

and Pfeiffer [15] using a boundary of 0.5 for the molecular regime and 10^{-2} for the viscous regime.

In this work, we focus on damping effects within the molecular flow regime

2. Theory

2.1. Quality factor

Damping effects are usually quantified by the quality factor Q , which is defined as the ratio of the total energy E stored within the oscillator to the energy dissipated per cycle ΔE :

$$Q = \frac{E}{\Delta E}. \quad (2)$$

In the presence of more than one damping mechanism the total energy dissipation can be calculated by summing up the inverse contributions of every factor within the relevant region in the following manner:

$$\frac{1}{Q_{\text{tot}}} = \sum_i \frac{1}{Q_i} = \frac{1}{Q_{\text{int}}} + \frac{1}{Q_{\text{mol}}} + \frac{1}{Q_{\text{trans}}} + \frac{1}{Q_{\text{vis}}}, \quad (3)$$

where Q_i are the contributions in the intrinsic, molecular, transitional and viscous regimes. This equation can be used to extract the individual contributions from the measured data, as demonstrated by Schwarz et al. [9].

2.2. Degrees of freedom (DOF)

The number of degrees of freedom f of a gas molecule plays a crucial role in its thermodynamic properties and is directly linked to its heat capacity C_V by the following relation:

$$C_V = \frac{f}{2} N k_B, \quad (4)$$

where N is the number of atoms in the molecule and k_B is the Boltzmann constant. Every molecule has three translational degrees of freedom relating to the linear motion in three-dimensional space. Noble gas atoms exhibit only these degrees of freedom. Polyatomic molecules can have additional rotational and vibrational degrees of freedom.

From Eq. (4) the number of thermally excited DOF can be calculated based on heat capacity data (e.g. from NIST) at ambient temperature [16] (Table 1).

2.3. Damping phenomena

This paper focuses on the molecular flow regime, therefore the quality factor Q_{gas} will be very high compared to the large friction between the fluid and the oscillator in the viscous regime. For this reason, the unavoidable parallel intrinsic mechanical damping has to be very low, which is equivalent to a high quality factor Q_{int} , in order to achieve a good resolution for measuring the molecular flow fluidic influence on the quality factor. The quality factor Q_{gas} is modeled by the following expressions depending on the explicit flow regime and the pressure p , respectively [9]:

$$Q_{\text{mol}} = \frac{\xi_{\text{mol}}}{p}, \quad \text{molecular flow} \quad (5)$$

$$Q_{\text{trans}} = \xi_{\text{trans}} \frac{f_{\text{res}}^2 + f_{T,\text{gas}}^2}{f_{\text{res}} f_{T,\text{gas}}} \quad \text{with} \quad (6)$$

$$f_{T,\text{gas}} = \frac{\pi a(p)}{2h^2}, \quad \text{transition regime}$$

$$Q_{\text{vis}} = \frac{\xi_{\text{vis}}}{\sqrt{p}}, \quad \text{viscous flow} \quad (7)$$

The fitting parameters ξ_{mol} , ξ_{trans} and ξ_{vis} are tuned by a nonlinear curve fitting algorithm implemented in LabVIEW. The formalism to describe the intermediate transition regime is adapted from the thermoelastic damping model for solids introduced by Zener [7]. In this model, the energy dissipation is due to the propagation of a heat wave across the solid and is maximal when the thermal propagation frequency f_T matches the mechanical frequency f_i of the oscillator. Schwarz et al. [9] transferred this model to an oscillator operating in the presence of a neighboring wall by taking the gap width h and the pressure dependent heat diffusivity $a(p)$ of the enclosed gas instead of the thickness and the heat diffusivity of the solid material.

Up to now, there are two existing models for the damping of oscillators in the molecular flow regime. In 1966, Christian developed a model for completely free oscillators [17], undisturbed by the surrounding setup. He derived an inverse proportionality of the quality factor Q_{mol} to the pressure p and to the square root of the molecular mass M_{mol} :

$$Q_{\text{mol,Chr.}} = \frac{k_n^2}{4} \left(\frac{d}{l}\right)^2 \sqrt{\frac{\rho E}{12}} \sqrt{\frac{\pi k_B T}{2M_{\text{mol}}}} \frac{1}{p}, \quad (8)$$

where d , l , ρ , E are the thickness and length of the oscillator, and the density and Young's modulus of its material. k_n , k_B and T are a mode depend constant, the Boltzmann constant, and the temperature, respectively.

In 2002, Bao et al. investigated the oscillation under a defined gap h to a fixed plate [18]. They added an energy transfer model, which includes the dependence of the molecular quality factor on the width of the gap h and on the circumference of the oscillator given by twice the length l plus the width w of the oscillator:

$$Q_{\text{mol,Bao}} = 16\pi \frac{h}{2(l+w)} Q_{\text{mol,Chr.}} \quad (9)$$

These two models provide the basis for our investigations in the molecular flow regime. So far, the DOF of gas molecules are not explicitly included in the theory for modelling the quality factor in the molecular flow regime. This implies that, apart from the known influence of the molecular masses, no difference in the damping behavior would be expected between polyatomic gas molecules and monoatomic noble gases with only three translational DOF. This aspect is investigated in the following.

3. Experimental

3.1. Manufacturing

The silicon-based micro-oscillators consist of two beams and a vibrating plate. The plate is clamped to the two beams on one side (see Fig. 1(b)). On top of these beams, piezoelectric aluminum nitride (AlN) actuators are placed and covered by Au electrodes. The small deflection of the beams results in an oscillating amplitude of the plate up to a few micrometer. The resonant behavior was simulated with the FEM package COMSOL Multiphysics ("Eigenfrequency Analysis") and the geometries were chosen such that the first bending mode was in the range from about 1 to 10 kHz. This results to an oscillator of $1600 \times 1600 \mu\text{m}^2$ plate size, a length of $350 \mu\text{m}$, a width of $400 \mu\text{m}$ and a thickness of $20 \mu\text{m}$, having an eigenfrequency of about 5 kHz.

The micro-oscillators were fabricated by standard microtechnology processes like lithography, sputter deposition and wet/dry etching. The process flow can be seen in Fig. 1(c). The substrate is a highly doped p-Si wafer ($\rho = 0.01 \Omega\text{cm}$). In the first step, SiO_2 is thermally grown with a thickness of 120 nm for electric insulation and a Si_3N_4 film is deposited using PECVD with a thickness of 550 nm as KOH passivation layer. Both films were structured in a lithography

Table 1

Listing of the used polyatomic gases and their physical properties regarding DOF. Translational, rotational and vibrational DOF are calculated with heat capacity data from NIST [16]. The collision numbers Z_{rot} and Z_{vib} are taken from the references given in the table.

Gas	Translation	Rotation	$Z_{rot,lit}$	$Z_{rot,exp}$	Vibration	$Z_{vib,lit}$	$Z_{vib,exp}$	Total
H ₂	3	1.93	200 [22]	n.a.	0	>10 ³ [27]	n.a.	4.93
N ₂	3	1.98	4.5 [22]	5.2	0	>10 ⁶ [21]	n.a.	4.98
CO ₂	3	2	2.5 [22]	4.5	0.91	1000 [24]	11	5.91
N ₂ O	3	2	1 [22]	2.5	1.07	1000 [28]	15	6.07
SF ₆	3	3	3 [25]	3	6.67	3500 [26]	21.5	12.67

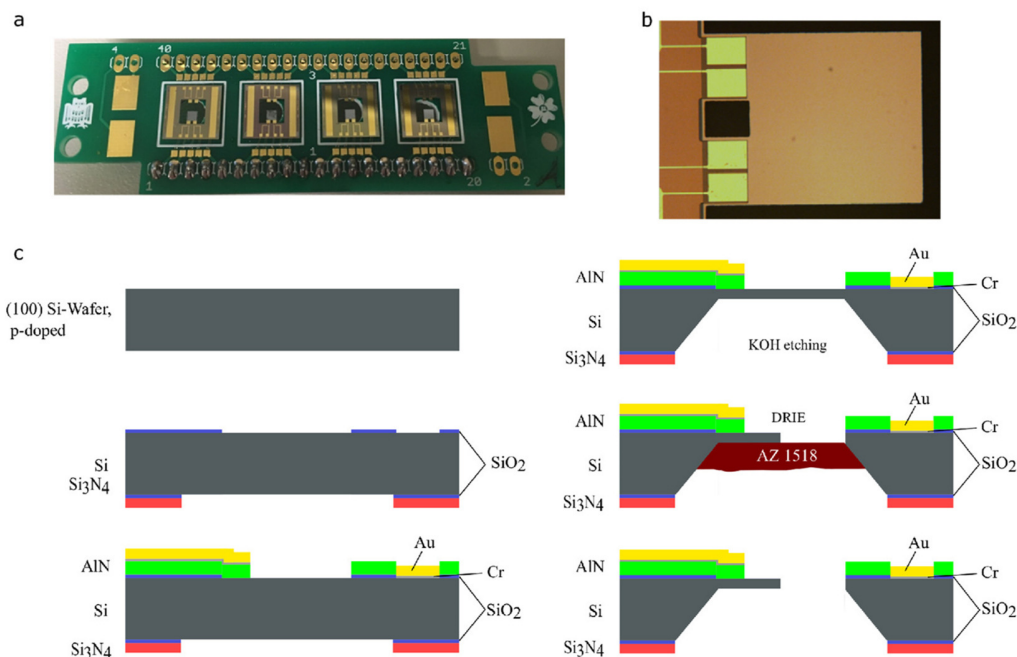


Fig. 1. Printed circuit board (PCB) with the mounted micro-oscillators (a) and light microscope picture of a single micro-oscillator (b). Schematic fabrication process flow diagram of the micro-oscillators (c). (Thickness ratios are not to scale).

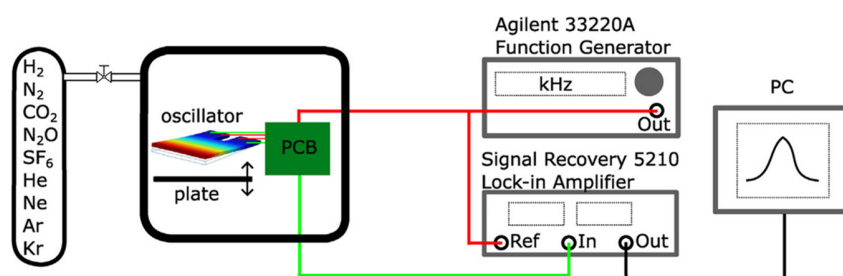


Fig. 2. Schematic diagram of the experimental setup.

step using AZ 1518 resist and they were etched in 6% HF solution. Then the piezoelectric AlN film with a thickness of 1100 nm is deposited by a reactive sputter process [19]. The AlN layer is structured lithographically and etched with 85% phosphoric acid at 80 °C. The electrodes consisting of Au are deposited via DC sputtering. The Au layer was etched using aqua regia at 25 °C. The thickness of the oscillators was set by a time-controlled KOH etching step from the back up to a thin membrane and they were released from the front utilizing the Bosch dry etching process. Before completely releasing the oscillators, the KOH cavity is filled with AZ 1518 photo resist to stop the dry etching process and prevent the free hanging struc-

tures from mechanical damage. Afterwards the chips were diced and finally cleaned with acetone, isopropanol, water and ethanol in an ultrasonic bath.

3.2. Experimental setup

The measurements were performed in a custom-built vacuum chamber (see Fig. 2). The pressure ranges from high vacuum (10^{-3} mbar) to atmospheric pressure ($\bar{1}0^3$ mbar) and is controlled by one cold cathode system covering the range of 10^{-3} to 10^{-2} mbar (PKR 251) and three capacitive sensors for the remaining pressure

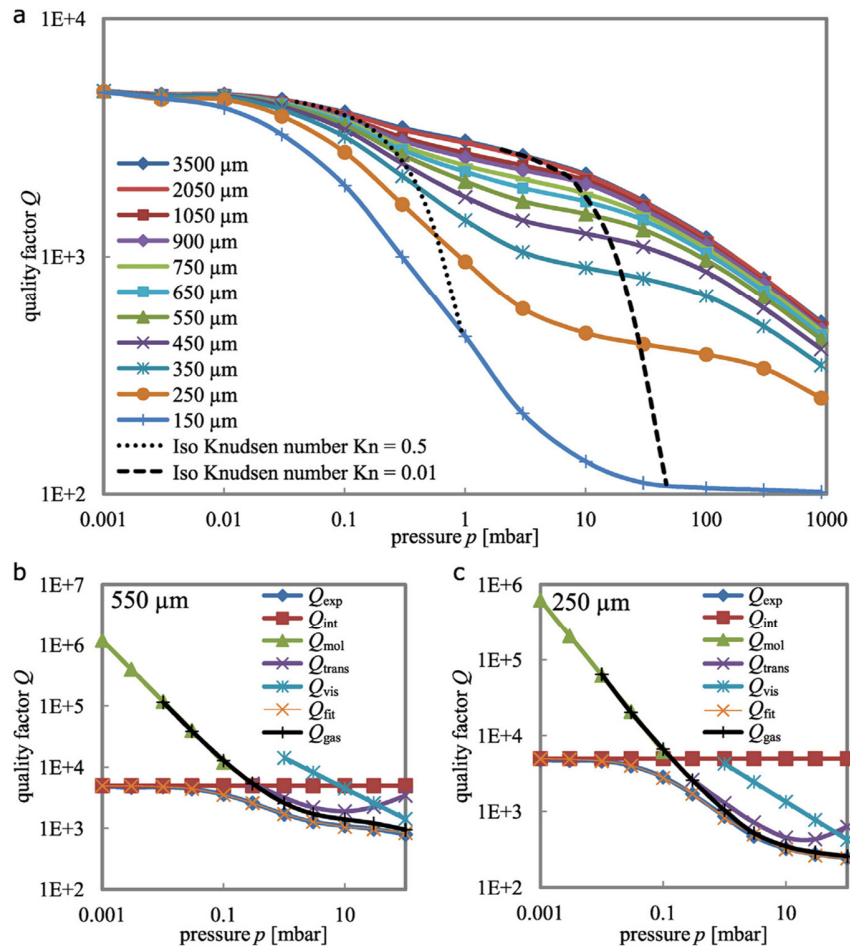


Fig. 3. Measurement of the quality factor for various gap widths (a). The used gas atmosphere is N_2 . Evaluation model for the measured quality factor. Results for N_2 with a gap width of 550 μm (b) and 250 μm (c).

region (CMR 264/362/261, all from Pfeiffer Vacuum). The cold cathode system is strongly dependent on the type of gas and therefore this region is only used to measure the intrinsic damping of the oscillator in high vacuum. The gases were let in by mass flow controllers, operating in a feedback loop, so that a dynamic equilibrium of a defined gas pressure can be adjusted. The vacuum chamber was cleaned by evacuating to a pressure of less than 10^{-4} mbar, then it was filled with the desired gas up to 10 mbar and subsequently evacuated once more. This procedure was repeated twice to ensure a purified gas atmosphere.

Before the sensors were die bonded onto the PCB, holes were drilled at the positions of the sensor cavities so that the maximal gap width is not confined on either side of the oscillator. The exact height of each sensor including the silicate glue was determined with a surface profilometer (C 1208 from Mahr GmbH). In the following, the gap between the oscillator surface and the neighboring plate was set by a linear actuator (M-228.11S from PI). The distance between the plate and the sensor PCB (Fig. 1a) is initially calibrated with two copper plates with a known thickness of 800 (± 5) μm . The gap can be set to a defined value in the range from 150 μm to 3500 μm with an accuracy of ± 20 μm . The total maximum variation is given by the thickness tolerance of the glue (± 12 μm) and

of the copper plates (± 5 μm), as well as by the repeatability of the linear actuator (± 3 μm).

The oscillator was driven by a function generator (Agilent33220A) with a sinusoidal signal in the range of the resonant frequency and an amplitude of 1 V. The actuation was decoupled electrically with a buffer amplifier and, additionally, the capacitive crosstalk between actuation and sensing was compensated by a specially designed circuit [20]. The measurement PCB was used to obtain "normal resonant curves" rather than so called "double resonant curves", occurring in an uncompensated setup. These curves were recorded by correlating the actuation and sensing signal with a lock-in amplifier (Signal Recovery 5210) (see Fig. 2).

4. Results

To investigate the activation of molecular DOF and their influence on damping, we first measure the quality factor for different gap widths over the whole pressure range from 10^{-3} to 10^3 mbar. The results of the N_2 measurement done at room temperature are shown in Fig. 3(a). Such quality factor curves were also measured for the noble gases He, Ne, Ar, Kr and for the polyatomic gases H_2 , CO_2 , N_2O and SF_6 , applying the same gap widths. Larger gap

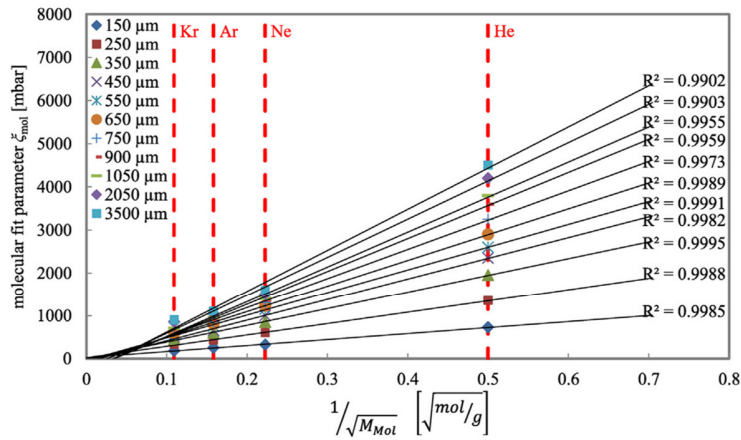


Fig. 4. Comparison of the determined molecular fit parameters with the theoretical model for noble gases.

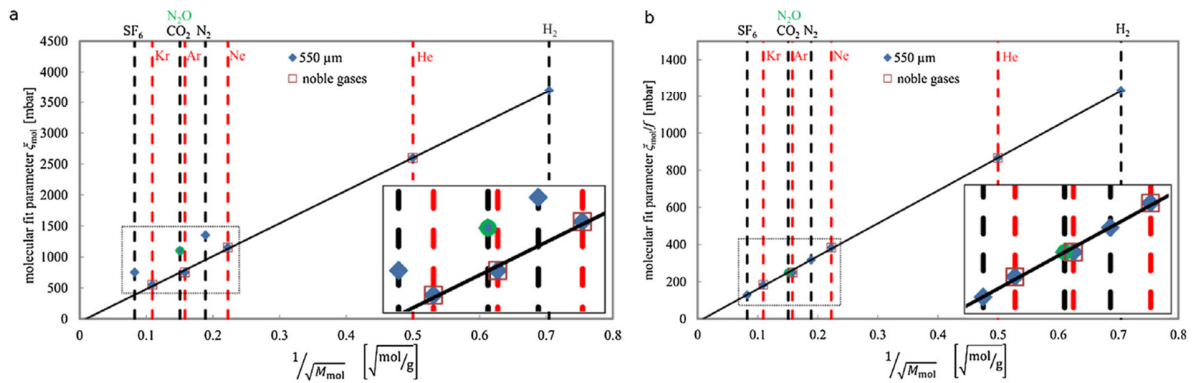


Fig. 5. The molecular fit parameter of all measured gases (a). The fit parameters normalized to one DOF for a gap width of 550 μm (b). N_2O and CO_2 are differently colored and marked for differentiation. Insert zooms into indicated area.

widths above 3500 μm were not measured, because an asymptotical behavior is already reached there. Thus, it can be assumed that the oscillator is not significantly influenced by the neighboring plate in a distance of more than 3500 μm (the next neighboring surface under the oscillator is much larger compared to the gap width because of the drilled hole (see Fig. 1(a)), so the influence of this surface is assumed to be negligible).

The molecular damping is separated from the other damping phenomena by fitting the quality factor plot for each gap width with the model presented above (see Section 2.3 *Damping Phenomena* and Eqs. (3), (5)–(7)). Examples for the validity of this model are shown in Fig. 3(b) and (c) for a gap width of 550 μm in a nitrogen atmosphere. From this we extract the intrinsic fit parameter ξ_{int} ($= Q_{\text{int}}$), the viscous fit parameter ξ_{vis} , the transitional fit parameter ξ_{trans} and the molecular fit parameter ξ_{mol} for every gap width and gas.

In the following, only the molecular fit parameter is discussed and is used to derive molecular properties. The noble gases provide a reference for the three translational DOF. The curves defined by the four noble gases He, Ne, Ar and Kr are used to calibrate the molecular fit parameter for a known number of three activated DOF. For every gap width, a linear fit is obtained by only considering the noble gases in a plot of the molecular fit parameter versus the inverse square root of the molecular mass (see Fig. 4). The quality

of the linear trend according to Eq. (8) is indicated by R^2 , with the value 1 indicating a perfect match between experimental data and theory.

By adding the values of the polyatomic gases as shown in Fig. 5(a) a deviation to the linear fit and, thus, to the existing theory, appears. The size of the deviation increases with the gap width and can be connected to an increasing molecular quality factor due to the activation of higher DOF of polyatomic gases. The additionally activated rotational and vibrational DOF lead to a higher heat capacity (Eq. (4)) and, thus, to reduced thermal losses due to the smaller temperature increase induced by the heat loss from the oscillator (the transport of heat loss is driven by the temperature gradient). The number of activated DOF is determined by dividing the molecular quality factor by a factor f , which directly represents the number of activated DOF. This is done by dividing the noble gas value by their three translational DOF and determining the factor f for which the values of the polyatomic gases match with the linear curve as can be seen in Fig. 5(b).

5. Discussion

The number of activated DOF was determined with the presented method as a function of the gap size. Taking the thermal velocity (calculated from $v = \sqrt{2RT/m}$) into account to estimate

6

T. Zengerle et al. / Sensors and Actuators A 297 (2019) 111460

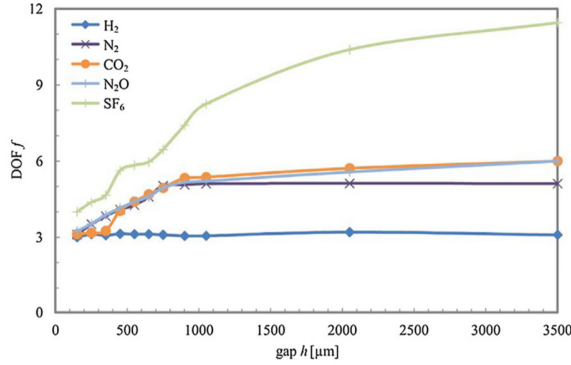


Fig. 6. Determined DOF for all polyatomic gases in dependence of the adjusted gap width.

the time of flight (TOF) between the micro-oscillator and the neighboring plate, the activation dynamics of the rotational and vibrational DOF can be investigated experimentally in a time resolved manner with μs resolution.

In Fig. 6, the determined number of activated DOF f as a function of the gap width is presented. Interestingly, all gases with the exception of the complex molecule SF_6 start at three translational DOF at the smallest gap value ($h = 150 \mu\text{m}$). This exception of SF_6 can be explained by the very small energy required to excite the first rotational mode in this complex molecule ($E_{\text{rot}} = 11.2 \mu\text{eV}$). The energy provided by a collision with the oscillator can be estimated by a formula given by Bao's energy transfer model¹⁸ to be $E_{\text{collision}} = 14.0 \mu\text{eV}$, which exceeds the energy required to excite the first rotational mode. In contrast, the first rotational energy level of all other investigated gases exceeds the energy transferred by the collision with the oscillator ($E_{\text{rot}} = 51.7 \mu\text{eV}$ and $E_{\text{collision}} = 7.7 \mu\text{eV}$ for N_2O).

As can be seen, all gases except hydrogen increase their number of activated DOF within the expected range (compare Table 1). Nitrogen gains two rotational DOF by increasing the gap width h up to $750 \mu\text{m}$. The vibrational DOF of nitrogen is not available at room temperature and therefore is not expected to be activated in this experiment. The triatomic gases CO_2 and N_2O exhibit nearly the same physical properties and therefore would be expected to perform similarly. Surprisingly, there is a significant difference in the range of small gap widths (up to $450 \mu\text{m}$). At first, this was not understood. However, theoretical approaches suggest that these two gases differ in the number of collisions needed to activate their rotational DOF [21]. This was confirmed experimentally by several groups and the resulting collision numbers for various gases are summarized by Mahallawy [22].

Based on the results explained above, a model has been developed in analogy to the thermal excitation model given by Fließbach [23]:

$$C_{\text{rot}} \propto \begin{cases} \left(\frac{\theta_{\text{rot}}}{T}\right)^2 \exp\left(-\frac{\theta_{\text{rot}}}{T}\right), & \text{for } \frac{\theta_{\text{rot}}}{T} \gg 1 \\ \left(1 + \frac{1}{180} \left(\frac{\theta_{\text{rot}}}{T}\right)^2\right), & \text{for } \frac{\theta_{\text{rot}}}{T} \ll 1 \end{cases} \quad (10)$$

$$C_{\text{vib}} \propto \left(\frac{\theta_{\text{vib}}}{T}\right)^2 \frac{\exp\left(\frac{\theta_{\text{vib}}}{T}\right)}{\left[\exp\left(\frac{\theta_{\text{vib}}}{T}\right) - 1\right]^2} \quad (11)$$

This model describes the activation dynamic of polyatomic DOF as a function of the ratio of the characteristic temperature θ

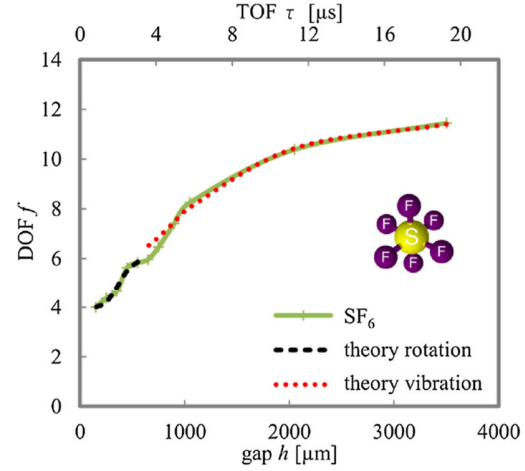


Fig. 7. Comparison of the number of DOF for SF_6 molecules as extracted from the measurement (solid line) and as predicted from the developed theory (dotted lines) in dependence of the gap width. The corresponding relaxation times are also indicated.

required to excite a higher DOF, and the ambient temperature T , being equivalent to an energy ratio. The energy required for exciting higher DOFs is transferred by a certain number of collisions, defined as collision number Z . These values were previously investigated in various different types of experiments, like acoustic absorption [24], thermal transpiration [25], and optoacoustic measurements [26]. The number of available collisions Z_{avail} in our experiment is given by the ratio of the gap width h to the mean free path of the molecules l_{mfp} . Thus, the temperature ratio can be correlated directly to the collision number ratio Z/Z_{avail} as indicated in Eq. (12). Furthermore, when taking the molecular velocity into account, we can relate this collision number ratio to the time ratio between the relaxation time τ_{rel} , which is necessary for the development of a higher DOF, and the time of flight τ_{flight} :

$$\frac{\theta}{T} \leftrightarrow \frac{Z}{Z_{\text{avail}}} = \frac{Z l_{\text{mfp}}}{h} = \frac{\tau_{\text{rel}}}{\tau_{\text{flight}}} \quad (12)$$

In consequence, we propose to adapt Eqs. (10) and (11) by substituting this temperature ratio by the derived time ratio. Additionally, by using Eq. (4) we can derive the number of rotational and vibrational DOF:

$$N_{\text{rot}} = \begin{cases} \left(\frac{\tau_{\text{rot}}}{\tau_{\text{flight}}}\right)^2 \exp\left(-\frac{\tau_{\text{rot}}}{\tau_{\text{flight}}}\right), & \text{for } \frac{\tau_{\text{rot}}}{\tau_{\text{flight}}} \gg 1 \\ \left(1 + \frac{1}{180} \left(\frac{\tau_{\text{rot}}}{\tau_{\text{flight}}}\right)^2\right), & \text{for } \frac{\tau_{\text{rot}}}{\tau_{\text{flight}}} \ll 1 \end{cases} \quad (13)$$

$$N_{\text{vib}} = \left(\frac{\tau_{\text{vib}}}{\tau_{\text{flight}}}\right)^2 \frac{\exp\left(\frac{\tau_{\text{vib}}}{\tau_{\text{flight}}}\right)}{\left[\exp\left(\frac{\tau_{\text{vib}}}{\tau_{\text{flight}}}\right) - 1\right]^2} \quad (14)$$

Therefore, the molecular quality factor can be written as Christians' quality factor Q_{Chr} , normalized on three translational DOF multiplied by the number of activated DOF N_{DOF} which can be separated into a rotational N_{rot} and vibrational N_{vib} part.

$$Q_{\text{mol}} = \frac{Q_{\text{Chr}}}{3} \cdot N_{\text{DOF}} = \frac{Q_{\text{Chr}}}{3} \cdot (3 + N_{\text{rot}} + N_{\text{vib}}) \quad (15)$$

This theoretical approach is compared to the measured values of the developed DOF in Fig. 7 and shows very good agreement.

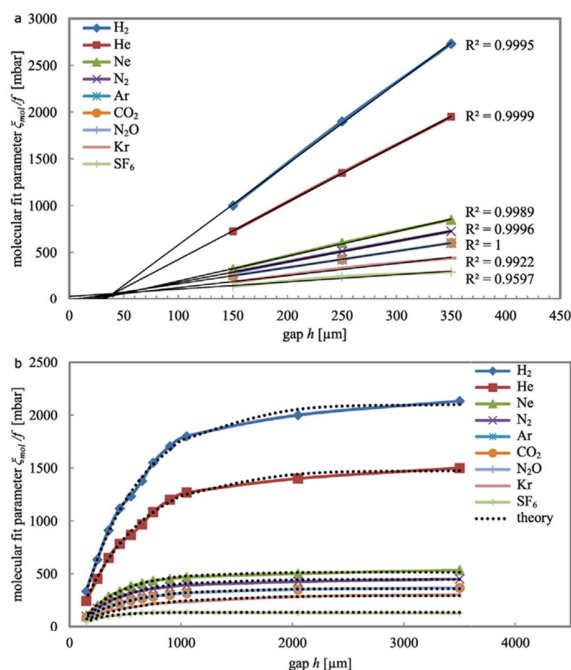


Fig. 8. The molecular fit parameter normalized to one DOF for small gap values showing a linear behavior according to the theory of Bao (a). Measured molecular quality factor as a function of the gap width. The developed transition model between the models of Bao and Christian is included (b).

By fitting the proposed model, we can determine the rotational and vibrational relaxation times from our experimental results (see Fig. 7). They are found to be on the order of several microseconds, which is in accordance with previous results obtained by acoustic measurements [24]. In addition, we average the mean free path l_{mfp} for the fitted range (l_{mfp} at 0.065 mbar) to achieve the pressure independent collision number Z for the activation of molecular DOF (Eq. (12)). In case of N₂ and SF₆, we achieve good agreement with the values given by Mahallawy [22] and Raw [25].

The triatomic gases CO₂ and N₂O show qualitatively the expected behavior. The values are higher by about a factor of two (compared to Mahallawy [22]). The values for the vibrational collision numbers do not match with the values given in the literature. A part of this discrepancy can be explained by the following: The vibrational DOF were measured by setting large gap widths (up to 3500 μm) exceeding the width of the oscillator (1600 μm). Therefore, the model of gas molecules being locked in a volume built by the oscillator and the neighboring plate is not quite sufficient for these gap widths ($h > 1000 \mu\text{m}$) any more. The effect of completely free moving gas molecules, which can leave the mentioned volume, increases and leads to an increase of molecules with activated vibrational DOF. On the other hand, not all the numbers $Z_{vib,lit}$ given in the literature are verified experimentally. For hydrogen, it is not possible to measure rotational or vibrational effects because of the high number of collisions needed to activate these DOF and also because of the large mean free path and the high thermal velocity of the hydrogen molecules. It can be calculated that the distance to activate the rotational DOF is approximately 70 cm, which is even larger than the geometry of the vacuum chamber.

The results show a new effect of the polyatomic gases when the gap is adjusted to more than 150 μm . Bao *et al.* [18] developed an energy transfer model for squeeze film gaps and verified his model for gap widths of several micrometers (squeeze film range). Fig. 8

shows that this model can be expanded to gap widths ranging up to 500 μm by taking the influence of the additionally activated rotational and vibrational DOF into account. As can be seen in Fig. 5, the molecular quality factor of heavier polyatomic gases can be larger than the molecular quality factor of lighter noble gases (depending on the gap width). This cannot be explained within the frame of the previous theories. After calibrating the molecular quality factor on the number of activated DOF, the results fit better to the prediction of Bao and Christian (see Fig. 8(a) and (b)). Additionally, a new model has been developed to achieve the transition between the theory of Bao for squeeze film gaps and the model of Christian for a completely free oscillator.

$$Q_{mol} \propto Q_{Chr.} (1 - a \cdot b^h [\mu\text{m}]) \quad (16)$$

with the molecular quality factor Q_{mol} and the quality factor according to Christian $Q_{Chr.}$. The fit parameters are found to be nearly constant in the range $a = 1.11 (\pm 0.01)$ and $b = 0.9976 (\pm 0.0009)$ for all measured gases. The quality factor $Q_{Chr.}$ behaves in good agreement with the theory of Christian¹⁷.

6. Conclusions

In this paper, comprehensive damping measurements in the molecular flow regime are presented. The results are compared with existing theories and deviations are shown. A new approach by taking the DOF of polyatomic gases into account was developed and shows good agreement with the experimental results. A method was introduced to determine the number of activated DOF as a function of the gap width. In addition, the temporal evolution of the DOF activation dynamics can be investigated. From this, one can derive relaxation times and collision numbers for the gas molecules. Finally, two models are derived to improve the modeling of the damping phenomena on micro-oscillators in the molecular flow regime and thus to contribute to the understanding of these effects. The first approach explains the influence of the DOF of polyatomic gases on the molecular damping as function of the gap width. The second model describes the transition of the two already existing theories of Bao and Christian. In conclusion, the measurements show the possibility to experimentally determine thermodynamic properties of gas molecules with high temporal resolution by using micromechanical oscillators.

Acknowledgements

The authors wish to thank the German Science Foundation (DFG) for financial support within the grant SE 1425/14-1. The authors also thank Dipl.-Ing. Günter Marchand and the Mitranz Laboratory for providing the cleanroom environment for the fabrication process.

References

- [1] J. Schmöle, M. Dragosits, H. Hepach, M. Aspelmeyer, A micromechanical proof-of-principle experiment for measuring the gravitational force of milligram masses, *Class. Quantum Grav.* 33 (2016), 125031, <http://dx.doi.org/10.1088/0264-9381/33/12/125031>.
- [2] M. Bertke, G. Hamdana, W. Wu, H.S. Wasisto, E. Uhde, E. Peiner, Analysis of asymmetric resonance response of thermally excited silicon micro-cantilevers for mass-sensitive nanoparticle detection, *J. Micromech. Microeng.* 27 (2017), 064001, <http://dx.doi.org/10.1088/1361-6439/aa6b0d>.
- [3] D.G. Hwang, Y.M. Chae, N. Choi, I. Cho, J.Y. Kang, S.H. Lee, Label-free detection of prostate specific antigen (PSA) using a bridge-shaped PZT resonator, *Microsyst. Technol.* 23 (2017) 1207–1214, <http://dx.doi.org/10.1007/s00542-015-2804-0>.
- [4] N. Satoh, K. Kobayashi, S. Watanabe, T. Fujii, K. Matsushige, H. Yamada, Optical and mechanical detection of near-field light by atomic force microscopy using a piezoelectric cantilever, *Jpn. J. Appl. Phys.* 55 (2016), <http://dx.doi.org/10.7567/JJAP.55.08NB04>, 08NB04-1.

- [5] C.F. Reiche, S. Vock, V. Neu, L. Schultz, B. Büchner, T. Mühl, Bidirectional quantitative force gradient microscopy, *New J. Phys.* 17 (2015), 013014, <http://dx.doi.org/10.1088/1367-2630/17/1/013014>.
- [6] E. Mounier, Future of MEMS: A Market and Technologies Perspective, Yole Developments, MEMT Tech Seminar, 2014, Oct 2014. <http://www1.semi.org/eu/sites/semi.org/files/images/Eric%20Mounier%20-%20Future%20of%20MEMS.%20A%20Market%20and%20Technologies%20Perspective.pdf> (Accessed 15 April 2019).
- [7] C. Zener, Internal friction in solids. I. Theory of internal friction in reeds, *Phys. Rev.* 52 (1937) 230–235, <http://dx.doi.org/10.1103/PhysRev.52.230>.
- [8] T. Aono, K. Suzuki, M. Kanamaru, R. Okada, D. Maeda, M. Hayashi, Y. Isono, Development of wafer-level-packaging technology for simultaneous sealing of accelerometer and gyroscope under different pressures, *J. Micromech. Microeng.* 26 (2016), 059601, <http://dx.doi.org/10.1088/0960-1317/26/10/059601>.
- [9] P. Schwarz, Investigations on Gas- and Airgap-Specific Damping Behaviour of Micromechanical Resonators from Molecular to Viscous Flow, Doctoral dissertation, 2014 <https://publikationen.sulb.uni-saarland.de/handle/20.500.11880/23051>.
- [10] T. Veijola, H. Kuisma, J. Lahdenpera, Model for gas film damping in a silicon accelerometer, *Proc. Transducers 2* (1997) 1097–1100, <http://dx.doi.org/10.1109/SENSOR.1997.635391>.
- [11] A.K. Pandey, R. Pratap, F.S. Chau, Effect of pressure on fluid damping in MEMS torsional resonators with flow ranging from continuum to molecular regime, *Exp. Mech.* 48 (2008) 91–106, <http://dx.doi.org/10.1007/s11340-007-9076-2>.
- [12] W. Zhang, K.L. Turner, Pressure-dependent damping characteristics of micro silicon beam resonators for different resonant modes, *Proc. IEEE Sens.* (2005) 357–360, <http://dx.doi.org/10.1109/ICSENS.2005.1597710>.
- [13] A. Minikes, I. Bucher, G. Avivi, Damping of a micro-resonator torsion mirror in rarefied gas ambient, *J. Micromech. Microeng.* 15 (2005) 1762–1769, <http://dx.doi.org/10.1088/0960-1317/15/9/019>.
- [14] M. Wutz, H. Adam, W. Walcher, K. Jousten, *Handbuch Vakuumtechnik, Vieweg+Teubner Verlag*, 2000, pp. 45.
- [15] *The Vacuum Technology Book*, Pfeiffer Vacuum GmbH, 2013, Ch. 1.2.6.
- [16] E. Lemmon, M. McLinden, D. Friend, Thermophysical Properties of Fluid Systems NIST, 1998 (Accessed 15 April 2019) <https://webbook.nist.gov/chemistry/fluid/>.
- [17] R. Christian, The theory of oscillating-vane vacuum gauges, *Vacuum* 16 (1966) 175–178, [http://dx.doi.org/10.1016/0042-207X\(66\)91162-6](http://dx.doi.org/10.1016/0042-207X(66)91162-6).
- [18] M. Bao, H. Yang, H. Yin, Y. Sun, Energy transfer model for squeeze-film air damping in low vacuum, *J. Micromech. Microeng.* 12 (2002) 341–346, <http://dx.doi.org/10.1088/0960-1317/12/3/322>.
- [19] A. Ababneh, U. Schmid, J. Hernandez, J. Sánchez-Rojas, H. Seidel, The influence of sputter deposition parameters on piezoelectric and mechanical properties of AlN thin films, *Mater. Sci. Eng. B* 172 (2010) 253–258, <http://dx.doi.org/10.1016/j.mseb.2010.05.026>.
- [20] H. Qiu, P. Schwarz, H. Völlm, D. Feili, X. Wu, H. Seidel, Electrical crosstalk in two-port piezoelectric resonators and compensation solutions, *J. Micromech. Microeng.* 23 (2013), 045007, <http://dx.doi.org/10.1088/0960-1317/23/4/045007>.
- [21] J. Parker, Rotational and vibrational relaxation in diatomic gases, *Phys. Fluids* 2 (1595) 449–462, <http://dx.doi.org/10.1063/1.1724417>.
- [22] F. El-Mahallawy, S. E-Din Habik, *Fundamentals and Technology of Combustion*, Elsevier, 2002, pp. 93–94.
- [23] T. Fließbach, *Statistische Physik: Lehrbuch zur Theoretischen Physik IV*, Spektrum Akademischer Verlag, 2018, pp. 225.
- [24] H. Kneser, Schallabsorption in mehratomigen gasen, *Ann. Phys.* 408 (1933) 337–349, <http://dx.doi.org/10.1002/andp.19334080305>.
- [25] C. Raw, Thermal transpiration and rotational relaxation in some polyatomic gases, *Chem. Phys. Lett.* 28 (1974) 229–230, [http://dx.doi.org/10.1016/0009-2614\(74\)80059-X](http://dx.doi.org/10.1016/0009-2614(74)80059-X).
- [26] K. Beck, A. Ringwelski, R. Gordon, Time-resolved optoacoustic measurements of vibrational relaxation rates, *Chem. Phys. Lett.* 121 (1985) 529–534, [http://dx.doi.org/10.1016/0009-2614\(85\)87134-7](http://dx.doi.org/10.1016/0009-2614(85)87134-7).
- [27] J. Parker, Vibrational relaxation times of deuterium and hydrogen. A comparison of theory and experiment, *J. Chem. Phys.* 45 (1966) 3641–3645, <http://dx.doi.org/10.1063/1.1727382>.
- [28] Z. Baalbaki, H. Teitelbaum, Are vibrational relaxation times really constant? I. The vibrational relaxation of N₂O, *Chem. Phys.* 104 (1986) 83–106, [http://dx.doi.org/10.1016/0301-0104\(86\)80156-2](http://dx.doi.org/10.1016/0301-0104(86)80156-2).

Biographies

Tobias Zengerle gained the B.Sc., M.Sc in microtechnology and nanostructures from the Saarland University in Saarbücken in 2015, and 2017, respectively. He is currently working toward the Ph.D degree from Saarland University, Germany. His research interests include MEMS oscillators and their application as gas sensing systems.

Julian Joppich studied microtechnology and nanostructures at Saarland University and gained his M.Sc. in 2018. He worked on various fields of sensors, sensor systems and measurement technology, including nanomagnetism and micro-oscillators. Currently, he is a doctoral researcher at Saarland University and is studying possibilities of sensing odors

Patrick Schwarz received the Dipl.-Ing. degree in electrical engineering and the Ph.D. degree in mechatronics from Saarland University, Saarbrücken, Germany in 2004 and 2014, respectively. The subject of his Ph.D. at the Chair of Micromechanics, Microfluidics/Microactuators was the investigation on gas- and airgap-specific damping behavior of micromechanical resonators.

Abdallah Ababneh received his Dipl.-Ing. (B.Sc. + M.Sc.) and Ph.D. degrees in electrical engineering from Saarland University/ Germany in 2002 and 2009, respectively. He is currently an Associate Professor at Yarmouk University/ Jordan. His research interests include piezoelectric thin films and microresonators..

Prof. Helmut Seidel received the diploma degree in physics from Ludwig-Maximilians-University, Munich, Germany, in 1980, with work in theoretical elementary particle physics and the Ph.D. degree in physical chemistry from the Free University, Berlin, Germany, in 1986. In 1980, he joined Fraunhofer-Society, Munich, as a Research Scientist focusing on MEMS. From 1986 until 2002, he held various positions in industry, starting at MBB, then Daimler-Benz, and Temic. Since 2002, he has been a Professor at Saarland University, Saarbrücken, Germany, holding the Chair for Micromechanics, Microfluidics/Microactuators. He has obtained more than 40 patents and has coauthored a large number of publications. His current interests focus on inertial sensors, microfluidics, and flexible substrates, among others. Prof. Seidel served on International Steering Committees and Program Committees of various important conferences and is currently an Editor of the IEEE Journal of Microelectromechanical Systems.

6.3 Damping Model for the Transitional Flow Regime

6.3.1 Thermal Wave Concept

For the transitional regime in-between the molecular and the viscous flow regime there is no analytical description available. Neither a molecular view nor a view by means of continuum mechanics and the Navier-Stokes equations can be used for the description. For this reason, an analytical approach is adapted from the solid-state model of Zener, which is transferred on a gas atmosphere enclosed in a small gap. Based on our experimental results, we come to the conclusion that the gap can be considered as a resonance cavity of a standing thermal wave. The thermal fluctuation is generated by the nearly adiabatic compression and expansion of the gas due to the oscillatory motion. The resonance frequency of the thermal wave here depends on the thermal properties of the gas, especially on the thermal diffusivity, which is also affected by the ambient pressure (see Section 2.1.3).

This approach is first of all contrary to the original idea of thermal phenomena which is not described by a wave equation but based on a temperature gradient driven flow. The heat flow J due to a temperature gradient through a medium with thermal conductivity λ is given by the first Fourier law [81]:

$$J = \lambda \cdot \nabla T \quad (6.6)$$

By extension with the conservation of energy and assumption of an oscillating heat source $Q_{\text{heat}}(t)$ with the spatial distribution $f(\vec{x})$, the differential equation can be extended to a wave equation with the wave vector q [133]:

$$\nabla^2 T + q^2 T = -\frac{f(\vec{x}) \cdot Q_{\text{heat}}(t)}{\lambda} \text{ with } q = \frac{(1+i)}{\delta_{\text{therm}}}. \quad (6.7)$$

The reciprocal of the wave vector is the thermal diffusion length δ_{therm} , which is a measure for the range of the thermal effects. This will be considered in more detail in the following chapter when higher modes or higher frequencies are investigated (see Chapter 6.4).

Besides the mathematical description of thermal effects with the wave equation, wave phenomena like resonances can also be observed experimentally. For example, Shen *et al.* presented a comparable setup with a variable gap and a laser-induced heat flux [85]. The heat flow through a medium was read out by a PVDF sensor and resonance phenomena were clearly observed. Due to the dependence of the thermal resonance frequency of the medium on the thermal diffusivity, this quantity can be determined very precisely.

A model based on thermal resonance to describe a dissipation process in solids is already known from the literature [51] and has been described in Section 2.3.1. This dissipation mechanism describes intrinsic heat losses due to thermal waves within the solid, originating from the temperature gradient caused by the deformation of the solid. These thermal losses are strongly dependent on the actuation frequency and have a maximum when the mechanical resonance frequency matches the thermal resonance frequency of the system. The thermal resonance frequency of the solid-state system depends on the geometrical boundary, i.e. on the thickness of the solid, which forms the

resonance body and on the thermal properties of the solid summarized in the thermal diffusivity. In our case we adapt this solid-state model for describing the loss mechanism in the transitional gas flow regime. This can be achieved by assuming the occurrence of thermal waves in the gas entrapped between the oscillator and a spatial boundary. The mathematical formalism is adapted and only the thermal frequency is newly derived with a standing wave approach.

In the upper pressure range of the transitional flow regime, the numerical description via continuum mechanics and thus by means of the Navier-Stokes equations is still possible. This enables the computation of the temperature and pressure distribution within the gap. The validity as well as the accuracy of this description decreases with the pressure but it remains applicable up to a Knudsen number of $Kn = 0.1$. The magnitude of the deviation of the simulated quality factor to the experimental data is investigated for this purpose and evaluated in both papers. Qualitatively, however, the temperature and pressure distribution can be evaluated and used for the physical justification of the proposed model (see Figure 37).

From the numerical results, an ellipsoidal temperature cloud can be observed with a maximum in the center of the gap. The magnitude of the maximum and thus the losses via heat flow to the environment depend on both the ambient pressure, which influences the thermal diffusivity and on the size of the resonance body, i.e. the gap width. These effects will be discussed in more detail in the second publication on this topic. The pressure evolves in the opposite direction. Here the maximum values are found at the edges due to the congestion of the gas molecules at the solids.

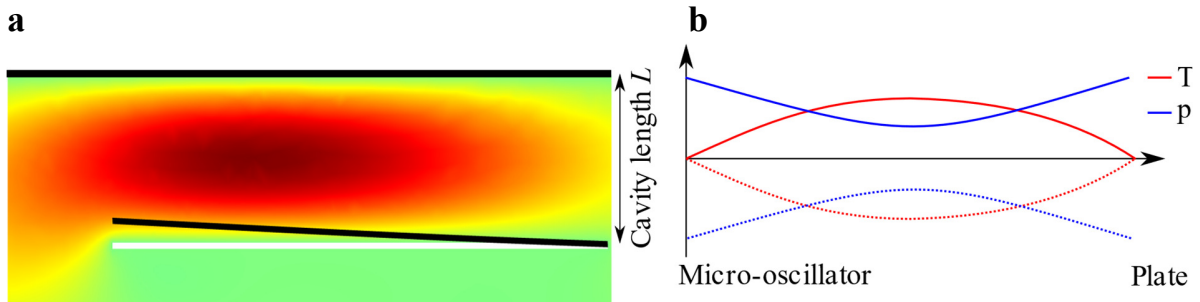


Figure 37. Simulated temperature distribution within the gap (a). Due to the upwards movement of the micro-oscillator (not to scale), a compression of the gas atmosphere arises and a corresponding temperature increase. The temperature and pressure plots are shown for the cut line through the maximum temperature value from the micro-oscillator surface to the top plate for the compression (solid) and expansion (dotted) case (b).

6.3.2 Addendum II

Sensors and Actuators A 311 (2020) 112068



Contents lists available at ScienceDirect

Sensors and Actuators A: Physical

journal homepage: www.elsevier.com/locate/sna

Modeling the damping mechanism of MEMS oscillators in the transitional flow regime with thermal waves

T. Zengerle^{a,*}, J. Joppich^{a,1}, P. Schwarz^a, A. Ababneh^{a,b}, H. Seidel^a^a Chair of Micromechanics, Microfluidics and Microactuators, Saarland University, Campus A5.1, 66123, Saarbrücken, Germany^b Electronic Engineering Dept., Hijjawi Faculty for Engineering Tech., Yarmouk University, Jordan

ARTICLE INFO

Article history:

Received 6 March 2020
 Received in revised form 28 April 2020
 Accepted 12 May 2020
 Available online 23 May 2020

Keywords:

Transitional flow regime
 Thermal waves
 Thermal diffusivity
 Thermoelastic damping
 MEMS oscillator
 Q factor
 Damping

ABSTRACT

This paper investigates the damping behavior of a vibrating micro-oscillator caused by a surrounding gas in the transitional flow regime ($0.01 < Kn < 0.1$). In this regime, neither the continuum theory given by the Navier-Stokes equations nor the Boltzmann equation for the molecular flow regime can be applied to describe the damping effects correctly. We propose that the well-known Zener formalism developed for describing thermoelastic damping in solid oscillators can be adapted to include thermoacoustic effects in gases. In this newly proposed model, the damping is caused by thermal waves traveling from the micro-oscillator to a neighboring plate which is placed with a gap width ranging from 150 to 750 μm . This theoretical approach can be brought to a nearly perfect fit with the experimental data, including the observed concave zone of the quality factor plot within the transitional flow regime. The resonance frequency of thermal waves of gas within the gap is derived from standard wave theory, verifying the proportionalities extracted from the experimental results. Consequently, the theory in the transitional flow regime can be expanded by the thermal wave concept and the usage of MEMS oscillators for the thermal wave resonator cavity method (TWRC) is feasible.

© 2020 Elsevier B.V. All rights reserved.

1. Introduction

MEMS oscillators are used in a large variety of applications due to their high sensitivity when operating at or near resonance. Examples are scanning probe microscopy [1] and the usage as micro-/nanobalance especially for bioanalytic purposes [2]. Looking at consumer applications, micro-oscillators are present as clock signal generators in microelectronics [3] and as gyroscopes in mobile devices and cars [4]. Possible upcoming applications are in energy harvesting for autonomous systems [5], in high resolution pressure sensing [6] and as cryptographic keys in the form of physical unclonable functions [7].

The resonant behavior of micro-oscillators strongly depends on the surrounding fluid and on geometric boundary conditions. Important factors are ambient pressure, type of fluid being characterized by viscosity and molecular mass, as well as geometric boundaries given by the anchorage and the surrounding package

[8]. It is important to know the influence of these parameters to predict the attenuation on the quality factor of micro-oscillators.

An important factor to characterize the type of interaction of the surrounding fluid is the Knudsen number. This dimensionless number represents the ratio of the mean free path l_{mfp} to a characteristic length l^* , being determined by the particular experimental situation:

$$Kn = \frac{l_{\text{mfp}}}{l^*} \quad (1)$$

For Knudsen numbers $Kn > 1$, gas molecules are moving without significant interaction (collisions) amongst each other. Therefore, this is called the molecular flow regime when molecules only collide with the boundaries given by the periphery. For $Kn < 0.01$ the density of gas molecules per volume is very high so that they collide frequently with each other. In this so-called viscous regime the continuum theory can be applied and macroscopic properties of the fluid, such as density and viscosity, are decisive parameters for the damping behavior of the oscillator. In between the two the transition regime is placed which, up to now, is difficult to be described with a straightforward mathematical formalism. It can be subdivided further into a free flow dominated regime ($Kn > 0.1$) and a continuum dominated regime, the so called slip flow regime ($Kn < 0.1$) [9].

* Corresponding author.

E-mail address: t.zengerle@imm.uni-saarland.de (T. Zengerle).¹ Present address: Laboratory of Measurement Technology, Saarland University, Campus A5.1, 66123 Saarbrücken, Germany.

2

T. Zengerle, J. Joppich, P. Schwarz et al. / Sensors and Actuators A 311 (2020) 112068

This paper mainly focuses on the prediction of the damping behavior on micro-oscillators in the slip flow regime including the viscous regime ($Kn < 0.1$).

2. Theory

2.1. Quality factor

The most important parameter to describe and quantify damping on any oscillator is the quality factor Q , which is defined as the ratio of the total energy E stored in the oscillator to the dissipated energy per cycle ΔE :

$$Q = 2\pi \frac{E}{\Delta E} = \frac{f_r}{\Delta f_{3dB}}, \quad (2)$$

being equivalent to the more convenient definition as ratio of the mechanical resonance frequency of the oscillator f_r to the 3 dB bandwidth Δf_{3dB} .

The measured Q factor appears in most cases as a superposition of different damping loss mechanisms. Each one contributes to the total quality factor Q_{tot} in the following manner [10]:

$$\frac{1}{Q_{tot}} = \sum_i \frac{1}{Q_i} = \frac{1}{Q_{int}} + \frac{1}{Q_{mol}} + \frac{1}{Q_{trans}} + \frac{1}{Q_{vis}}, \quad (3)$$

where Q_i are the contributions to the quality factor in the intrinsic, molecular, transitional and viscous regime. This formula is used to extract the individual damping phenomena for further investigations. In case when a single damping mechanism becomes dominant in a certain regime, Eq. 3 can be simplified, e.g. to $Q_{tot} \approx Q_{vis}$ in the viscous regime.

2.2. Thermoacoustics

The damping behavior of the investigated micro-oscillator was numerically calculated with *COMSOL Multiphysics*. Within the thermoacoustic module, the Navier-Stokes equation, continuity equation and the energy conservation equation, all given in the frequency domain for an eigenfrequency analysis, are implemented:

$$i\omega\rho_0\vec{u} = \nabla \cdot [-\rho\mathbf{I} + \mu(\nabla\vec{u} + (\nabla\vec{u})^T)] - \left(\frac{2}{3}\mu - \mu_B\right)(\nabla \cdot \vec{u})\mathbf{I} \quad (4)$$

$$i\omega\rho + \rho_0\nabla \cdot \vec{u} = 0 \quad (5)$$

$$i\omega\rho_0C_pT = -\nabla \cdot (-k\nabla T) + i\omega\alpha_0T_0p + Q \quad (6)$$

where ω , ρ , \vec{u} , μ , μ_B , C_p , T , k , p , α_0 , Q are the angular frequency, density, velocity field, dynamic viscosity, bulk viscosity, heat capacity at constant pressure, temperature, thermal conductivity, ambient pressure, thermal expansion coefficient of the fluid and heat, respectively. Additionally, \mathbf{I} is the identity matrix and the ambient background values ρ_0 , p_0 , T_0 are characterized by an index zero. These formulas represent the viscous and thermal losses in the continuum regime for which the Navier-Stokes equation is valid ($Kn < 0.01$).

2.3. Thermoelastic damping (TED)

The thermoelastic damping model introduced by Zener in 1937 is a well-known loss mechanism, which is mainly responsible for intrinsic losses of a solid-state (micro-) oscillator [11]. These losses are due to a temperature gradient generated by compressive and tensile stress zones within the material of the oscillating structure,

resulting in an irreversible heat dissipation flow (see Fig. 1 (a)). The resulting quality factor is given by:

$$Q_{TED} = \frac{C_p\rho}{\alpha^2TE} \frac{f_r^2 + f_T^2}{f_r f_T} = A(\rho, T) \frac{f_r^2 + f_T^2}{f_r f_T}, \text{ with } f_T(h) = \frac{\pi}{2} \frac{a}{h^2} \quad (7)$$

with the following parameters: C_p heat capacity at constant mechanical stress, ρ density, α isotropic coefficient of thermal expansion, T temperature, E Young's modulus, and a the thermal diffusivity of the vibrating solid material of the micro-oscillator with thickness h . f_r and f_T stand for the resonance frequency of the mechanical oscillator and the resonance frequency of the thermal wave propagating through the solid, respectively. In analogy to the thermal losses given by the Zener model for solid-state oscillators, we adapt this formalism to describe the transition regime by assuming the occurrence of thermal losses within the fluid surrounding the oscillator:

$$Q_{trans} = A_{trans}(h) \frac{f_r^2 + f_{T, Gas}^2}{f_r f_{T, Gas}} \quad (8)$$

In this case the vibrating plate is generating a temperature gradient within the gas leading to irreversible diffusion processes across the gap width h (see Fig. 1 (a)). The efficiency of the heat dissipation depends on the pressure dependent heat diffusivity of the gas medium and on the matching of the mechanical resonance frequency of the micro-oscillator and thermal resonance frequency of the gas. Besides the similarities described above, there is one significant difference between the Zener model and our system. In the classical Zener model, there is a heat source and a heat sink on the top and bottom of the beam depending on the bending movement (compare Fig. 1 (b)). In our setup, the heat source/sink is given by the nearly adiabatic compression or expansion of the fluid caused by the oscillation. The fixed plate located at a gap width h as well as the micro-oscillator itself can be regarded as nearly isothermal. These assumptions are reasonable because of the large heat capacity respective thermal time constant of the fixed plate and the micro-oscillator. Therefore, the temperature fluctuations caused by the oscillation of approximately 5 kHz lead to temperature variations only within the gas. The work done to expand/compress respectively cool/heat the gas is the main loss, which leads to a reduction of the quality factor of the micro-oscillator in the transition regime.

In the following, the new model for describing the transition regime of damped micro-oscillators in fluids is investigated with the help of FEM simulations and is verified by experimental results.

3. Results

The simulations were performed using *COMSOL Multiphysics 5.0* in an eigenfrequency analysis. The micro-oscillator and the surrounding fluid were meshed manually to provide a mesh size smaller than the thickness of the viscous δ_{vis} and of the thermal boundary layer δ_{therm} given by [12]:

$$\delta_{vis} = \sqrt{\frac{\mu}{\pi f_r \rho}}, \quad \delta_{therm} = \sqrt{\frac{k}{\pi f_r C_p \rho}} \quad (9)$$

The losses via viscous drag and via thermal conduction are only taken into account if the mesh size is smaller than the width of the respective boundary layer. For gases, the widths of these two boundary layers have the same order of magnitude, and they are related to each other by the dimensionless Prandtl number Pr [13]:

$$Pr = \frac{C_p \mu}{k} = \left(\frac{\delta_{vis}}{\delta_{therm}}\right)^2 \left(= \frac{2}{3} \text{ for ideal gas}\right) \quad (10)$$

In Fig. 1 (a), the model of the simulated micro-oscillator can be seen. The model consists of a silicon bending oscillator suspended

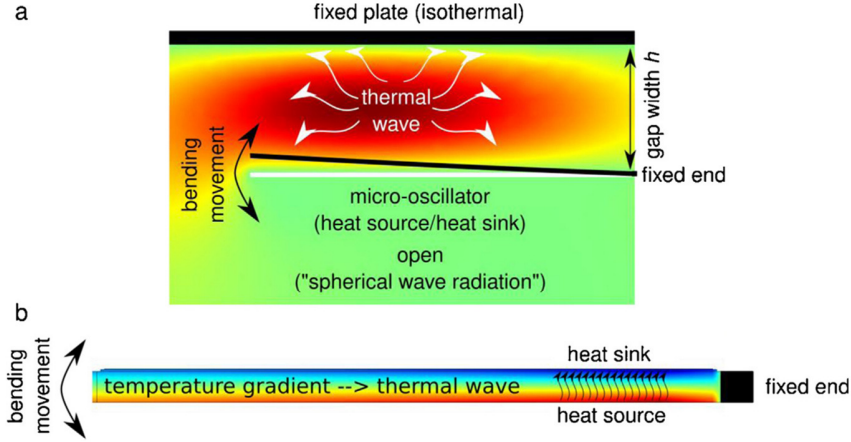


Fig. 1. Comparison between (a) the thermoacoustic effect for an oscillator suspended in a gas atmosphere enclosed by a fixed plate with gap width h , and (b) the thermoelastic Zener effect within the solid-state oscillator itself. The colors indicate the deviation from ambient temperature (red above ambient, blue below). The simulation was done for a gap width of $h = 550 \mu\text{m}$ and for a pressure $p = 100 \text{ mbar}$ (For the interpretation of the colored notes and legends, the reader is referred to the web version of this article).

on two beams on which the piezoelectric actuation elements are placed. The beams are fixed on one side with the boundary condition “fixed constraints” and completely freely suspended for the whole silicon domain. The surrounding medium is defined by the thermoacoustic model applied on the oscillators section and above. Underneath the oscillator, the thermoacoustic model is coupled to a pressure acoustic model with the boundary condition “spherical wave radiation”. This models the open side of the oscillator and is less time consuming for the simulation process.

The quality factor of a micro-oscillator with a plate of $1600 \times 1600 \mu\text{m}^2$ and two beams with the length $l = 400 \mu\text{m}$ and width $w = 350 \mu\text{m}$ (resulting eigenfrequency $f_r \sim 5 \text{ kHz}$) was simulated for gap sizes ranging from $150 \mu\text{m}$ to $750 \mu\text{m}$ in $100 \mu\text{m}$ steps. The simulations were performed for a nitrogen atmosphere for which experimental data are available from 10^{-3} mbar up to 900 mbar . Further details on the experimental setup can be found in the supplementary material and in previous work [14]. The quality factor Q_{sim} was calculated, utilizing the complex eigenfrequency f_c of the oscillating system in the following manner:

$$f_c = \text{Re}(f_c) + i\text{Im}(f_c) = f_r + \frac{\beta}{2\pi} \quad (11)$$

$$Q_{\text{sim}} = \frac{\pi f_r}{\beta} \quad (12)$$

The resulting quality factor plot for various gap sizes as function of the ambient pressure of the surrounding gas can be seen in Fig. 2 (a). Qualitative comparison with the experimental data (see Fig. 2 (b)) shows good agreement, especially for the regime $Kn < 0.01$. In the viscous regime ($Kn < 0.01$) the numerical results utilizing the Navier-Stokes equation coincide with the data from the experiment. In the range above this Knudsen number, the simulations strongly overestimate the damping from the surrounding gas. Moreover, the concave section of the quality factor plots being visible in the experimental data for $0.01 < Kn < 0.1$ cannot be observed in the simulation results. A deviation between the simulation and the experimental results appears, which is approximately in the range of $\pm 20\%$ for $Kn < 0.1$ (see Fig. 3). These results are comparable to previous numerical works and analytical models for predicting the quality factor of micro-oscillators in different flow regimes [15–18]. In the case of $h = 150 \mu\text{m}$, the effect of squeeze film damping is superposed, additionally. This effect is not taken into account in our simulation model, resulting in a larger deviation for this gap width.

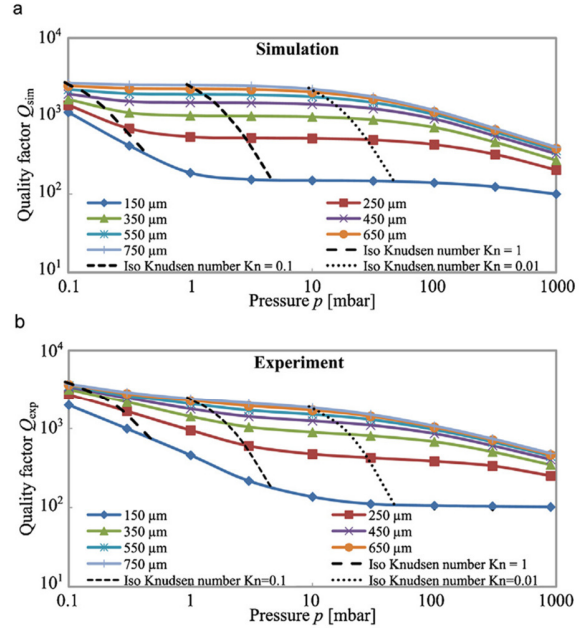


Fig. 2. Pressure dependent quality factor plots for various gap widths. The results for the simulation (a) and the experiment (b) are shown for a nitrogen atmosphere.

4. Discussion

The comparison between the experimental data and the numerical investigation indicates that the transition regime is not adequately described with the given Eqs. (4)–(6). Therefore, we propose an analytical formalism to achieve a better description of the transition regime. The Zener model is adapted as described in Eq. (7) and will be fitted to the experimental data in the following manner:

$$Q_{\text{trans}} = A_{\text{trans}}(h) \frac{f_r^2 + f_{r,\text{Gas}}^2}{f_r f_{r,\text{Gas}}}, \text{ with } f_{r,\text{Gas}}(p, h) = B_{\text{trans}}(h) p^{-\epsilon_{\text{trans}}}, \quad (13)$$

4

T. Zengerle, J. Joppich, P. Schwarz et al. / Sensors and Actuators A 311 (2020) 112068

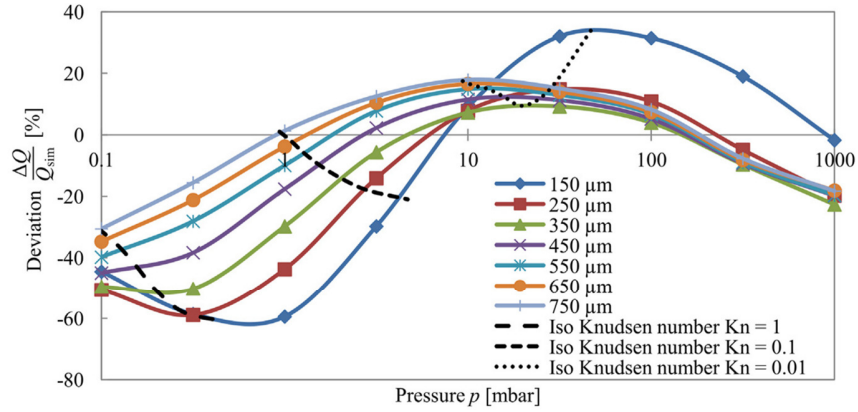


Fig. 3. Relative deviation between the experimental and numerical results for various gap widths.

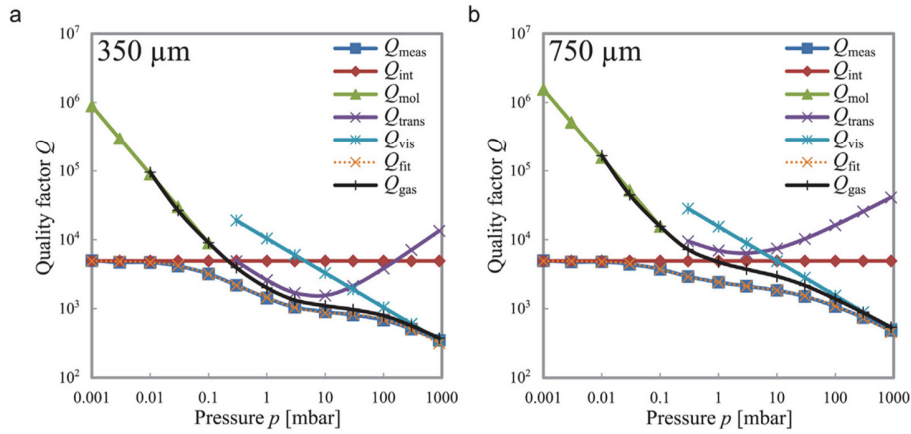
Fig. 4. Fitting model for reconstructing the damping contribution of the different flow regimes. Shown for a nitrogen atmosphere with a gap width of 350 μm (a) and 750 μm (b).

Table 1

Listing of the transitional fit parameters according to Eq. (13) for gap widths ranging from 150 to 750 μm . The determination coefficient R^2 close to one indicates a nearly perfect fit.

h [μm]	A_{trans}	B_{trans} [$\text{kHz}\cdot\text{bar}^{\varepsilon_{\text{trans}}}$]	$\varepsilon_{\text{trans}}$	R^2
150	71.742	37.250	0.7745	0.991
250	306.302	22.853	0.6346	0.9988
350	757.315	15.340	0.5889	0.9991
450	1314.274	11.797	0.5347	0.9993
550	1918.876	10.122	0.4987	0.9993
650	2578.152	8.689	0.4567	0.9995
750	3179.610	7.856	0.4384	0.9994

where A_{trans} is the fitted gap dependent prefactor, f_r is the given mechanical resonance frequency of the micro-oscillator, and $f_{T,\text{Gas}}$ the thermal resonance frequency of the system, consisting of B_{trans} the fitted gap dependent prefactor of the thermal frequency and $\varepsilon_{\text{trans}}$ the fitted exponential factor. As a first result, parabolic shaped damping curves are generated, which can be shifted in x-direction (pressure axis) via the fit parameter B_{trans} , in y-direction (quality factor axis) via A_{trans} , and stretched or compressed via $\varepsilon_{\text{trans}}$ (see Fig. 5). By adjusting these three fit parameters, the empiric model matches very well with the measured data. In Table 1, the fit parameters for the experimental results are given. The fitting was done

by a LabVIEW nonlinear curve fitting program. The molecular and viscous regimes are fitted by the equations given in [14].

The resulting fits (orange line Q_{fit}) are in very good agreement with the experimental data (dark blue line Q_{meas}) and can hardly be distinguished in Fig. 4. This fact is also indicated by a value of the determination coefficient $R^2 > 0.99$ with $R^2 = 1$ representing a perfect match. By the addition of the parabola shape damping effect adapted from the Zener model the concave zone can be modeled in a better way, resulting in a nearly perfect approximation for the transition regime. This empirical approach is a much easier way to describe the transition regime, which can hardly be defined by a mathematical formalism based on first principles only [19]. The latter requires big numerical efforts, either based on statistical Monte Carlo simulations [20] or else on a Lattice Boltzmann model [21].

In the following we discuss the thermoacoustic damping in the transition regime and derive the thermal resonance frequency of the gas. As can be seen in Fig. 5, the influence of this damping phenomenon is strongly decreasing with increasing gap width h . A linear dependency between the strength of the damping (mainly given by the y-shifting parameter A_{trans}) is found for gap widths $h > 350 \mu\text{m}$ (see Fig. 6 (a)). The shifting of the vertex is caused by varying the fitting parameter B_{trans} . This can be explained by the increasing gap width between the oscillator and the variable plate leading to a bigger thermal resonance wavelength (respective lower frequency) in between them. The gap width dependence of

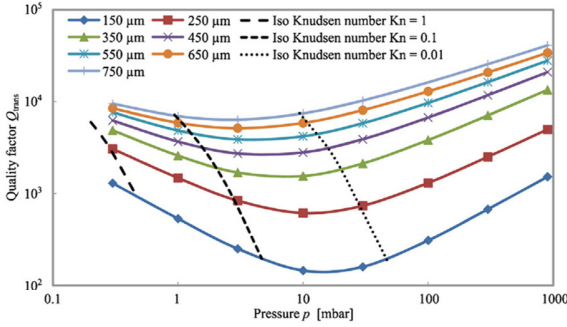


Fig. 5. Reconstructed transitional damping influence for various gap widths in a nitrogen atmosphere.

the thermal resonance frequency is qualitatively predicted by the Zener model. In the case of nitrogen we discover an inverse proportionality to the gap width h (compare Fig. 6 (b)) which is in contrast to Zener's thermal resonance frequency in solids ($1/h^2$, see Eq. (7)). The stretching factor $\varepsilon_{\text{trans}}$ only shows a small variation around the value of 0.5 over the investigated gap width range, when the narrowest gap width $h = 150 \mu\text{m}$ is neglected, where a squeeze film damping effect [22] is superposed.

Squeeze film damping occurs, when an oscillator is situated near a fixed plate with a gap width h being substantially smaller than the lateral dimensions l of the oscillator. Typically, a ratio of h/l less than 0.1 is assumed as the limit for the onset of squeeze film effects [23]. As a consequence, the gas volume within the cavity between oscillator and fixed plate gets trapped and can hardly escape to the sides (compare Fig. 1 for an assumed much smaller gap width).

Thus, the enclosed gas volume is acting as a spring and viscous losses only occur due to outflowing gas at the edges, whose cross-section decreases with the gap width [24]. The main damping is caused by the viscosity of the gas which is independent of pressure for the viscous regime and is strongly affected by the geometry ($Q \sim h^3$) [25]. This can be seen from a constant plateau-like behavior of the quality factor over the whole viscous flow regime for a gap width of $150 \mu\text{m}$ in Fig. 2 (b). For this reason the quality factor plot for a gap width of $150 \mu\text{m}$ does not show a distinct transition regime. The concave zone for this gap width is mainly built by the transition from the molecular damping zone into the squeeze film damping zone [19,25]. From this it can be concluded that squeeze film effect superposes thermoacoustic damping and therefore this can be neglected (compare approximation of Eq. 3).

The thermal resonance frequency of the locked gas within the gap width h can be derived theoretically by applying standard wave theory. The accuracy of the description of thermal diffusion processes as propagating thermal waves is discussed in the literature. Salazar et al. [26] show that thermal waves satisfy not all properties of a classical wave, as no energy transport occurs. Moreover, Mandelis et al. [Mandelis] argue that the description of thermal waves and reflection phenomena contradict the gradient equation of heat transport processes. Nonetheless, thermal waves are used to describe resonance effects, as can be seen in the thermal wave resonant cavity (TWRC) method for precise measurements of thermo-physical properties of materials locked within a cavity [27,28]. The requirement for the formation of a resonance is that the length of the resonance cavity L (in our case the gap width h) matches with a multiple of the half wavelength:

$$L = h = n \frac{\lambda}{2}, \quad n \in \mathbb{N} \quad (14)$$

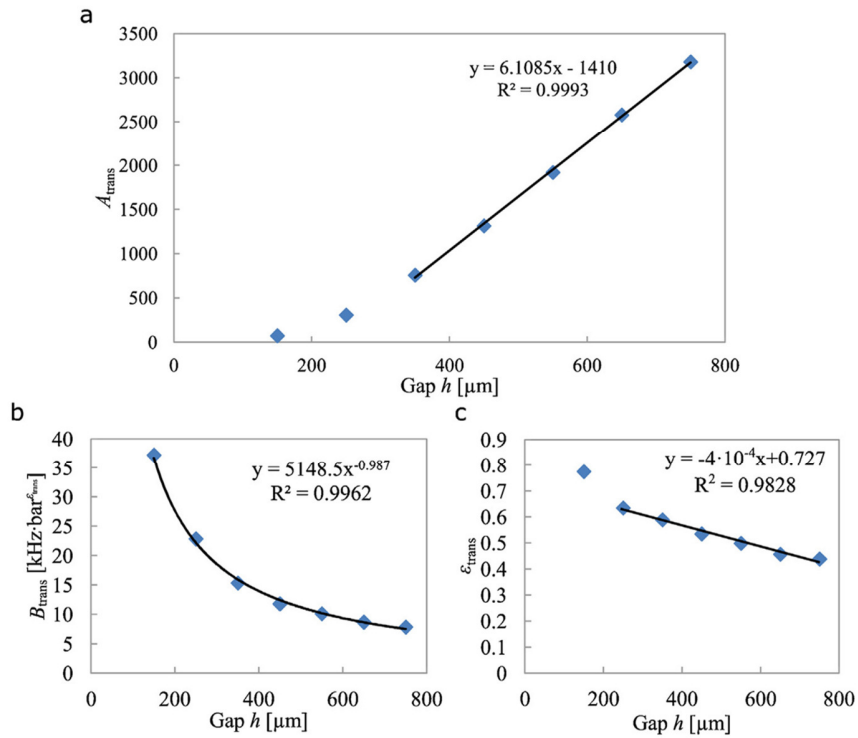


Fig. 6. Determined fit parameters in dependence of the adjusted gap width h : A_{trans} for shifting the vertex in y-direction (a), B_{trans} for shifting the vertex in x-direction (b), and the exponential fit parameter $\varepsilon_{\text{trans}}$ for stretching or compressing the parabola (c).

The wavelength of thermal waves can be expressed with the frequency by taking the phase velocity v_{ph} of the thermal wave into account. This leads to the following expression for the thermal resonance frequency of the locked gas volume within the gap width h :

$$f_{th, res} = \frac{v_{ph}}{\lambda_{res}} = \frac{nv_{ph}}{2h} = \frac{n\sqrt{2a(p)\omega}}{2h} \propto \frac{1}{h\sqrt{p}}, \quad (15)$$

with $f_{th, res}$, v_{ph} , λ_{res} , n , h , a , ω , p representing the thermal resonance frequency, the phase velocity, the resonance wavelength (Eq. (14)), the mode number, the gap width, the thermal diffusivity, the angular frequency of the micro-oscillator excitation, and the ambient pressure, respectively. The pressure dependence is derived by replacing the phase velocity with the expression given by Marin et al. [29] and using the thermal diffusivity given by [30]:

$$a = \frac{k}{\rho C_p} \propto \frac{1}{p}, \quad (16)$$

where k is the thermal conductivity, ρ is the density, and C_p the heat capacity at constant pressure.

The proportionalities derived from this thermal wave resonance model are in accordance with the results of the experimental data (compare Fig. 6 (b) and (c)). The inverse proportionality to the gap width h as well as the inverse proportionality to the square root of the pressure p for the thermal resonance frequency are derived and experimentally confirmed.

The results of the thermal wave model match the experimental data very well, as can be seen in Fig. 4. When the mechanical resonance frequency of the oscillator matches the thermal resonance frequency of the gas volume locked within the gap width, then the energy dissipation via the thermoacoustic effect reaches a maximum. The location of the resonance point strongly depends on the gap width, shifting to lower pressures when the gap size is increased. For large gap sizes, these resonance points can all be found within the transition regime ($0.01 < Kn < 0.1$) (see Fig. 5). Thus, thermoacoustic damping contributes significantly to the overall damping within this regime. For smaller gap widths, the resonance points shift to higher pressures. Therefore, they are masked either by dominant viscous damping or by squeeze film damping depending on the gap width. This masking effect can be counteracted by increasing the mechanical resonance frequency, which shifts the resonance point to lower pressures, or by using higher modes which are less damped by viscous losses.

Further investigations have to be done to verify this model for other gases and to expand the analytical approach for describing the damping effect on micro-oscillators in the transition regime. Taking more gases into account will open up the possibility to further analyze the fit parameters and evaluate their physical background. Furthermore, higher bending modes shall be investigated with respect to their behaviour in the transition zone.

5. Conclusions

In a first attempt, an analytical approach based on the Navier-Stokes equation is used to model the damping behavior within the transitional flow regime. However, when comparing these results with experimental data, a non-negligible deviation of about 30 % was found. As an alternative, we propose to use an adapted Zener formalism for modeling the observed concave zone in the quality factor plot. The thermal wave concept in solids is transferred into gas. By this semi-empirical method, an excellent match with the experimental data was achieved. The thermal resonance frequency of gas locked within the gap width between the micro-oscillator and a variable plate is derived theoretically, confirming the experimental results with an inverse proportionality to the gap width h and a pressure dependence $\sim p^{-0.5}$. This approach leads to an

expansion of the theory on the damping of micro-oscillators in the transitional flow regime. Further measurements with other gases and gap widths to verify the thermal wave theory have to be done. Moreover, this method opens the possibility for using micro-oscillators as an alternative to TWRC measurements for a precise determination of thermodynamic properties of gases, such as the thermal diffusivity.

CRedit authorship contribution statement

T. Zengerle: Investigation, Software, Formal analysis, Data curation, Writing - original draft, Writing - review & editing. **J. Joppich:** Methodology, Software. **P. Schwarz:** Conceptualization, Visualization. **A. Ababneh:** Supervision, Funding acquisition. **H. Seidel:** Writing - original draft, Writing - review & editing, Supervision, Project administration, Funding acquisition.

Declaration of Competing Interest

The authors declare that they have no known competing financial interests or personal relationships that could have appeared to influence the work reported in this paper.

Acknowledgment

The authors wish to thank the German Research Foundation (DFG) for financial support within the grant SE 1425/14-1.

Appendix A. Supplementary data

Supplementary material related to this article can be found, in the online version, at doi:<https://doi.org/10.1016/j.sna.2020.112068>.

References

- [1] G. Binnig, C.F. Quate, C. Gerber, Atomic force microscope, *Phys. Rev. Lett.* 56 (9) (1986) 930–934.
- [2] D. Hwang, Y. Chae, N. Cho, I. Cho, J. Kang, S. Lee, Label-free detection of prostate specific antigen (PSA) using a bridge-shaped PZT resonator, *Microsyst. Technol.* 23 (5) (2017) 1207–1214.
- [3] M. Lutz, A. Partridge, P. Gupta, N. Buchan, E. Klaassen, J. McDonald, K. Petersen, MEMS oscillators for high volume commercial applications, *Transducers 2007 – 2007 International Solid-State Sensors, Actuators and Microsystems Conference (2007)* 49–52.
- [4] G. Zhanshe, C. Fucheng, L. Boyu, C. Le, L. Chao, S. Ke, Research development of silicon MEMS gyroscopes: a review, *Microsyst. Technol.* 21 (10) (2015) 2053–20532066.
- [5] R. Elfrink, M. Renaud, T. Kamel, C. de Nooijer, M. Jambunathan, M. Goedbloed, D. Hohlfeld, S. Matova, V. Pop, L. Caballero, R. van Schaijk, Vacuum-packaged piezoelectric vibration energy harvesters: damping contributions and autonomy for a wireless sensor system, *J. Micromech. Microeng.* 20 (10) (2010), 104001.
- [6] X. Shi, Y. Lu, B. Xie, Y. Li, J. Wang, D. Chen, J. Chen, A resonant pressure microsensor based on double-ended tuning fork and electrostatic excitation/piezoresistive detection, *Sensors* 18 (8) (2018) 2494.
- [7] O. Willers, C. Huth, J. Guajardo, H. Seidel, P. Deutsch, On the feasibility of deriving cryptographic keys from MEMS sensors, *J. Cryptogr. Eng.* (2019) 1–17.
- [8] A. Partridge, M. Lutz, B. Kim, M. Hopcroft, R. Candler, T. Kenny, K. Petersen, M. Esashi, MEMS resonators: getting the packaging right, *Proceedings of the 9th SEMI Microsystem/MEMS Seminar (SEMICON) (2005)* 55–58.
- [9] G. Karniadakis, A. Beskok, N. Aluru, *Microflows and Nanoflows: Fundamentals and Simulation*, Springer Science & Business Media, 2006, pp. 16–17.
- [10] O. Brand, I. Dufour, S. Heinrich, F. Josse, *Resonant MEMS: Fundamentals, Implementation, and Application*, John Wiley & Sons, 2015, pp. 55–71.
- [11] C. Zener, Internal friction in solids, I. Theory of internal friction in reeds, *Phys. Rev.* 52 (3) (1937) 230–235.
- [12] H. Qiu, H. Seidel, Hydrodynamic loading on vibrating piezoelectric microresonators, in: *Piezoelectricity – Organic and Inorganic Materials and Applications*, Chapter 3, 2018.
- [13] G.L. Shires, Prandtl Number, Thermopedia Guide to Thermodynamics, Heat & Mass Transfer, and Fluid Engineering, 2011 (online available <http://www.thermopedia.com/content/1053/>), Accessed 23 April 2020.

- [14] T. Zengerle, J. Joppich, P. Schwarz, A. Ababneh, H. Seidel, Polyatomic degrees of freedom and their temporal evolution extracted from the damping of micro-oscillators, *Sens. Actuators A Phys.* 297 (2019) 111460.
- [15] G. De Pasquale, T. Veijola, A. Soma, Modelling and validation of air damping in perforated gold and silicon MEMS plates, *J. Micromech. Microeng.* 20 (2010), 015010.
- [16] A. Pandey, R. Pratap, Effect of flexural modes on squeeze film damping in MEMS cantilever resonators, *J. Micromech. Microeng.* 17 (2007) 2475–2484.
- [17] P. Li, R. Hu, On the air damping of flexible microbeam in free space at the free-molecule regime, *Microfluid. Nanofluidics* 3 (6) (2007) 715–721.
- [18] Y. Cho, A. Pisano, R. Howe, Viscous damping model for laterally oscillating microstructures, *J. Microelectromech. Syst.* 3 (2) (1994) 81–87.
- [19] A. Pandey, R. Pratap, F. Chau, Effect of pressure on fluid damping in MEMS torsional resonators with flow ranging from continuum to molecular regime, *Exp. Mech.* 48 (1) (2008) 91–106.
- [20] J. Park, P. Bahukudumbi, A. Beskok, Rarefaction effects on shear driven oscillatory gas flows: a direct simulation Monte Carlo study in the entire Knudsen regime, *Phys. Fluids* 16 (2) (2004) 317–330.
- [21] Q. Li, Y. He, G. Tang, W.Q. Tao, Lattice Boltzmann modeling of microchannel flows in the transition flow regime, *Microfluid. Nanofluidics* 10 (3) (2011) 607–618.
- [22] M. Bao, H. Yang, Squeeze film air damping in MEMS, *Sens. Actuators A Phys.* (1) (2007) 3–27.
- [23] A. Pandey, R. Pratap, A semi-analytical model for squeeze-film damping including rarefaction in a MEMS torsion mirror with complex geometry, *J. Micromech. Microeng.* 18 (2008), 105003.
- [24] T. Veijola, H. Kuisma, J. Lahdenperä, T. Ryhänen, Equivalent-circuit model of the squeezed gas film in a silicon accelerometer, *Sens. Actuators A Phys.* 48 (3) (1995) 239–248.
- [25] H. Qiu, P. Schwarz, D. Feili, X. Wu, H. Seidel, Air damping of micro bridge resonator vibrating close to a surface with a moderate distance, *J. Micromech. Microeng.* 25 (2015), 055016.
- [26] A. Salazar, Energy propagation of thermal waves, *Eur. J. Phys.* 27 (6) (2006) 1349–1355.
- [27] J. Shen, A. Mandelis, Thermal-wave resonant cavity, *Rev. Sci. Instrum.* 66 (10) (1995) 4999–5005.
- [28] J. Shen, A. Mandelis, T. Ashe, Pyroelectric thermal-wave resonant cavity: a precision thermal diffusivity sensor for gases and vapors, *Int. J. Thermophys.* 19 (2) (1998) 579–593.
- [29] E. Marin, L. Vaca-Oyola, O. Delgado-Vasallo, On thermal waves' velocity: some open questions in thermal waves' physics, *Rev. Mex. Fisica E* 62 (1) (2016) 1–4.
- [30] G. Pan, A. Mandelis, Measurements of the thermodynamic equation of state via the pressure dependence of thermophysical properties of air by a thermal-wave resonant cavity, *Rev. Sci. Instrum.* 69 (8) (1998) 2918–2923.

Biographies

Tobias Zengerle gained the B.Sc., M.Sc in microtechnology and nanostructures from the Saarland University in Saarbücken in 2015, and 2017, respectively. He is currently working toward the Ph.D degree from Saarland University, Germany. His research interests include MEMS oscillators and their application as gas sensing systems.

Julian Joppich studied microtechnology and nanostructures at Saarland University and gained his M.Sc. in 2018. He worked on various fields of sensors, sensor systems and measurement technology, including nanomagnetism and micro-oscillators. Currently, he is a doctoral researcher at Saarland University and is studying possibilities of sensing odors

Patrick Schwarz received the Dipl.-Ing. degree in electrical engineering and the Ph.D. degree in mechatronics from Saarland University, Saarbrücken, Germany in 2004 and 2014, respectively. The subject of his Ph.D. at the Chair of Micromechanics, Microfluidics/Microactuators was the investigation on gas- and airgap-specific damping behavior of micromechanical resonators.

Abdallah Ababneh received his Dipl.-Ing. (B. Sc. + M.Sc.) and Ph.D. degrees in electrical engineering from Saarland University/ Germany in 2002 and 2009, respectively. He is currently an Associate Professor at Yarmouk University/ Jordan. His research interests include piezoelectric thin films and microresonators.

Prof. Helmut Seidel received the diploma degree in physics from Ludwig-Maximilians-University, Munich, Germany, in 1980, with work in theoretical elementary particle physics and the Ph.D. degree in physical chemistry from the Free University, Berlin, Germany, in 1986. In 1980, he joined Fraunhofer-Society, Munich, as a Research Scientist focusing on MEMS. From 1986 until 2002, he held various positions in industry, starting at MBB, then Daimler-Benz, and Temic. Since 2002, he has been a Professor at Saarland University, Saarbrücken, Germany, holding the Chair for Micromechanics, Microfluidics/Microactuators. He has obtained more than 40 patents and has coauthored a large number of publications. His current interests focus on inertial sensors, microfluidics, and flexible substrates, among others. Prof. Seidel served on International Steering Committees and Program Committees of various important conferences and is currently an Editor of the IEEE Journal of Microelectromechanical Systems.

6.3.3 Addendum III

Sensors & Actuators: A. Physical 341 (2022) 113614



Contents lists available at ScienceDirect

Sensors and Actuators: A. Physical

journal homepage: www.journals.elsevier.com/sensors-and-actuators-a-physical

Thermal resonance model for micro-oscillators in the vicinity of a geometric boundary

T. Zengerle^{a,*}, A. Ababneh^{a,b}, H. Seidel^a^a Micromechanics, Microfluidics and Microactuators, Saarland University, Campus A5.1, 66123 Saarbrücken, Germany^b Electronic Engineering Dept., Hijjawi Faculty for Engineering Tech., Yarmouk University, Jordan

ARTICLE INFO

Keywords:

Transitional flow regime
Thermal waves
Thermal diffusivity
Thermoelastic damping
MEMS oscillator
Q factor

ABSTRACT

This study explores the damping behavior of micro-oscillators within the transitional flow regime between molecular flow and viscous flow, including the presence of a neighboring geometric boundary. The damping is described by a model based on standing thermal waves (STW), which form a thermal resonance depending on the pressure and on the gap width to the boundary. This concept was first introduced in a previous paper for a nitrogen atmosphere and is now examined for seven further gases (He, Ne, Ar, Kr, CO₂, N₂O, SF₆). The distance between the micro-oscillator and the confining geometry, given by an Al plate, is in the range of 150 μm to 3500 μm. Fitting the thermal wave model to the experimental data shows very good agreement and explains the convex region for the measured quality factor *Q* in the transition from the molecular to the viscous flow regime. The evaluation of the thermal resonance model shows a strong correlation between the ambient pressure at which thermal resonance occurs and the thermal properties of the gas (i.e. thermal diffusivity *a* and adiabatic index *κ*) including the gap width *h* which is in agreement with the proposed theory. This opens up the possibility of using micro-oscillators to measure the thermal properties of gases in a very precise way, comparable to the thermal wave resonator cavity principle, but with a much simpler and smaller setup.

1. Introduction

The applications of micro-oscillators fabricated in MEMS-technology (microelectromechanical systems) are diverse and widespread. Among others, they are used in inertial sensor technology [1] and scanning probe microscopy [2]. Their performance as sensors or actuators is mainly defined by the two most characteristic parameters: resonance frequency *f_r* and quality factor *Q*. In most cases, the resonance frequency can be predicted and adjusted very well by analytical models or by finite element (FEM) simulations. The quality factor is much harder to predict, since several loss mechanisms are superimposed. Besides the geometry of the oscillator itself, the boundary of the surrounding environment and the ambient atmosphere deliver major contributions to damping losses. Depending on the flow regime or pressure and on the distance to a spatial boundary, the individual damping effects (intrinsic, molecular, transitional, viscous) have a different impact on the overall quality factor. Therefore, for a more detailed investigation of the damping effects, they must be separated from each other in a full damping model. Only for certain cases there is an overall dominating damping effect (e.g. only intrinsic damping in the case of high vacuum, or only viscous

damping at atmospheric pressure), so that the influence of the other effects on the total quality factor can be neglected. For special geometries and flow regimes, analytical models for the quality factor are available from the literature [3–10]. However, the transition regime between molecular free flow and viscous flow is particularly difficult to model, since neither molecular theory nor continuum mechanics can be applied directly. This work follows up on a previous paper describing the transition regime with standing thermal waves (STW), leading to thermal resonance effects and extends this concept to other types of gases [11]. The results show good agreement between the experimentally measured quality factor and the thermal resonance model in the transitional and viscous flow regime (*Kn* < 1) for all types of gases. In further investigations, the model was examined in detail and clear correlations between the resonance parameters and the thermal gas properties of the gases are found. This offers the possibility to extend the application range of micro-oscillators to the TWRC (thermal-wave resonator cavity) method [12–15] for determining the thermal properties of gases.

* Corresponding author.

E-mail address: t.zengerle@lmm.uni-saarland.de (T. Zengerle).<https://doi.org/10.1016/j.sna.2022.113614>

Received 21 July 2021; Received in revised form 4 April 2022; Accepted 8 May 2022

Available online 11 May 2022

0924-4247/© 2022 Elsevier B.V. All rights reserved.

2. Theory

2.1. Quality factor

The quality factor Q of a freely vibrating oscillator is defined by its attenuation, i.e. by the ratio of the stored energy E to the energy loss per cycle ΔE :

$$Q = 2\pi \frac{E}{\Delta E} = \frac{f_r}{\Delta f} \quad (1)$$

This expression can be transformed into the ratio of the resonant frequency f_r to the 3 dB bandwidth Δf which can easily be measured and calculated from the recorded resonance curves. In general, the total quality factor (respectively damping) is a superposition of various loss mechanisms affecting the micro-oscillator (see Fig. 1). There are intrinsic damping mechanisms given by the losses within the solid-state material. In the case of piezoelectrically driven micro-oscillators, these losses are dominated by the residual stress of the piezoelectric thin film, limiting the maximum achievable quality factor to several thousand [16]. Intrinsic damping contributions are independent of the ambient pressure and limit the quality factor in the UHV regime ($p < 10^{-3}$ mbar). Losses depending on gas type and pressure are so-called extrinsic damping mechanisms, which are subdivided into three different flow regimes, according to the Knudsen number Kn [17], which is defined by the ratio of the mean free path l_{mfp} to a characteristic length l^* of the system. In our experiments, l^* is given by the gap width h of the oscillator to a neighboring plate:

$$Kn = \frac{l_{mfp}}{l^*} = \frac{l_{mfp}}{h} \quad (2)$$

For a Knudsen number $Kn > 1$ the density of the gas molecules starts getting so low that they hardly interact (collide) with each other, but rather with the outer geometric boundaries. In this low-pressure region, the so-called molecular flow regime, the quality factor exhibits a

reciprocal dependency on the ambient pressure, according to the theory of Bao et al. [3]. The theory of Bloom et al. is used for the viscous regime ($Kn < 0.01$) [9] with a reciprocal correlation to the square root of the ambient pressure. In the transition regime ($0.01 < Kn < 1$) the STW model is applied which was introduced in a previous publication [11]. Similarly, the exact fitting equations for the molecular and viscous regime can be found in [18]. The equation for the transitional part will be explained in more detail in the next section.

2.2. Thermal resonance model

For the transitional flow regime, no analytical theory is available since neither the assumption of molecular flow nor the principles or continuum mechanics can be applied. Therefore, we developed an approach describing the damping effects in this regime based on the resonance effect of STW. We adapted the analytical formalism from Zener's thermoelastic (TED) model, which is based on thermal wave resonance effects within an oscillating solid state material [19,20]. Our approach is thereby justified by the experimental findings and numerical simulations. In a first study [11], the STW model was introduced and applied on experimental results for an N_2 atmosphere. In the following, the physical problem is described and the analytical approach in analogy to Zener's model is presented.

In our case the vibrating movement of the micro-oscillator leads to a temperature gradient near the oscillating plate which diffuses across the gap (see Fig. 2). The efficiency of this heat transfer is depending on the match between the mechanical resonance frequency of the micro-oscillator f_r and the thermal frequency of the gas in-between the gap $f_{r,gas}$. A maximum transfer of heat is achieved when these two frequencies match, leading to a minimum of the quality factor. The quality factor for the transitional flow regime Q_{trans} is therefore suggested in analogy to Zener's analytical expression:

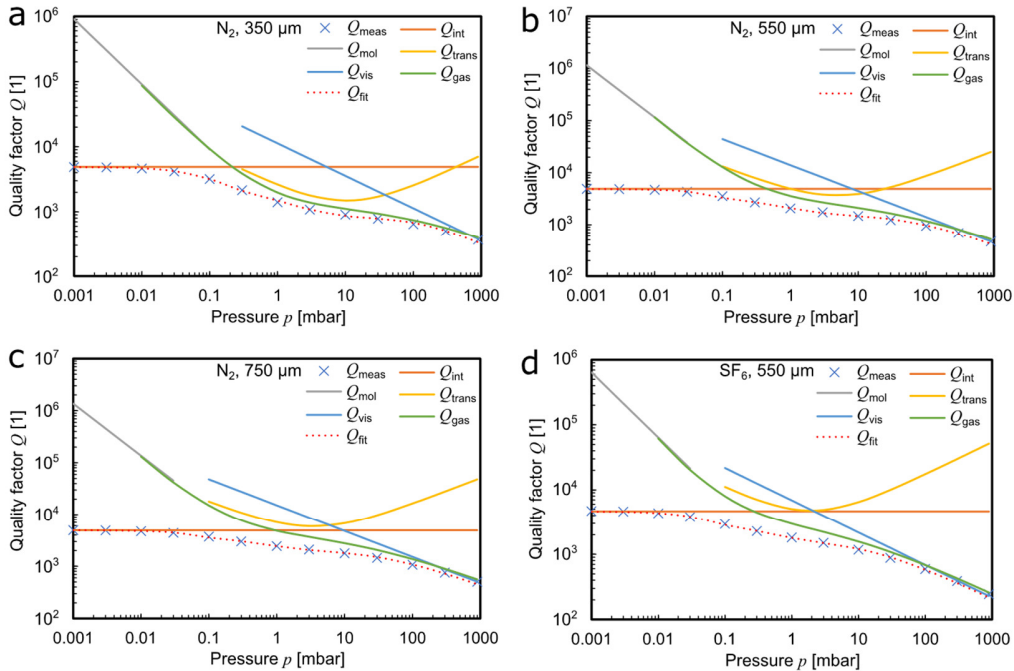


Fig. 1. Fitting of the complete damping model to the measured total quality factor of micro-oscillator BO for various gap widths and gas atmospheres. The reconstruction of the individual damping mechanisms is shown for a nitrogen atmosphere with a gap width of 350 μm (a), 550 μm (b), and 750 μm . In (d) the result for an SF_6 atmosphere and a gap width of 550 μm is shown.

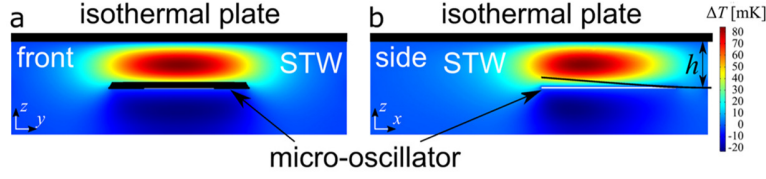


Fig. 2. Front view (a) and side view (b) on the FEM model. The color plot is indicating the temperature variation caused by the micro-oscillator. The bending of the micro-oscillator is scaled up for illustration.

$$Q_{trans} = \frac{A_{trans}(h) f_r^2 + f_{r,gas}^2}{2 f_r f_{r,gas}}, \quad (3)$$

with A_{trans} the minimal quality factor in the thermal resonance case. The thermal frequency of the gas $f_{r,gas}$ can be derived by a standing wave approach ($h = n \cdot \lambda/2$) [11]:

$$f_{r,gas} = \frac{nv_{ph}}{2h} = \frac{n\sqrt{\pi a(p)} f_r}{h} \propto \frac{1}{h\sqrt{p}}, \quad (4)$$

with v_{ph} , n , h , a , p representing the phase velocity [21], the mode number, the gap width, the thermal diffusivity, and the ambient pressure, respectively. The thermal diffusivity of a gas a is defined by the ratio of the thermal conductivity k to the product of density ρ and heat capacity at constant pressure C_p . Only the density of the gas is depending on the ambient pressure p and therefore the pressure dependence of the thermal diffusivity can be written with the thermal diffusivity at atmospheric pressure a_0 [22]:

$$a(p) = \frac{k}{\rho C_p} = \frac{a_0}{p} \frac{[1/\text{bar}] \propto p}{[1/\text{bar}] \propto p}. \quad (5)$$

With Eq. (4), the thermal resonance frequency f_r can be calculated as follows:

$$f_{r,gas} = f_r = \frac{n^2 \pi a_0}{p_{res} h^2}, \quad (6)$$

with p_{res} the resonance pressure leading to a match between the two frequencies at a given gap width h .

2.3. Thermoacoustics

The thermal resonance effects are calculated using the thermoacoustic module and the solid mechanics module of the FEM simulation software *COMSOL Multiphysics 5.4*. The model is shown in Fig. 2, and includes both the displacement of the micro-oscillator movement and the thermal effects within the gas. Therefore, the equations of solid mechanics and thermoacoustics are coupled with each other at the solid gas interface by boundary conditions (isothermal, and no slip). The linearized Navier-Stokes equation, continuity equation and the energy conservation equation, are all implemented in the frequency domain [23,24]. For a similar fluid structure interaction problem of a vibrating cantilever in liquid media, Ricci et al. showed the deviation of the equations into the frequency domain by a Laplace transformation [25]:

$$i\omega\rho_0 \vec{u} = \nabla \bullet [-\rho \mathbf{I} + \mu(\nabla \vec{u} + (\nabla \vec{u})^T) - \left(\frac{2}{3}\mu - \mu_B\right)(\nabla \bullet \vec{u})\mathbf{I}] \quad (7)$$

$$i\omega\rho + \rho_0 \nabla \bullet \vec{u} = 0 \quad (8)$$

$$i\omega\rho_0 C_p T = -\nabla \bullet (-k \nabla T) + i\omega a_0 T_0 p + Q, \quad (9)$$

where ω , ρ , \vec{u} , μ , μ_B , C_p , T , k , p , a_0 , Q are the angular frequency, density, velocity field, dynamic viscosity, bulk viscosity, heat capacity at constant pressure, temperature, thermal conductivity, ambient pressure, thermal expansion coefficient of the fluid and heat, respectively.

Furthermore, \mathbf{I} is the identity matrix and the ambient background values ρ_0 , p_0 , T_0 are indicated by an index zero. The validity of the equations is limited to the continuum regime ($Kn < 0.01$) [26]. Therefore, results obtained in the low-pressure region as well as results obtained for small gap widths with a Knudsen number of up to 0.1 may have significant error. Consequently, thermal resonance effects within the transitional flow regime ($0.001 < Kn < 0.1$) are not fully covered.

In Fig. 3, the temperature variation within the gap for a Ne atmosphere is depicted. The plots show the numerical data obtained by a cut line in z -direction through the maximum value of the temperature variation. In both cases, a maximum in the temperature increase with varying gap width and ambient pressure can be observed and thus the thermal resonance effect can be clearly seen. In comparison to the experimental results, which will be discussed in the next section, we observe some differences which will be stated briefly.

The resonance pressure determined by the FEM simulation turns out to be always somewhat larger than the experimental value. As an example, the numerical result for a Ne atmosphere is shown. The resonance pressure obtained numerically at a gap width of 450 μm is found to be 30 mbar, whereas experimentally a resonance pressure of about 20 mbar was obtained (cf. Fig. 4). The deviation between the numerical results and the experimental values is depending on the type of gas and can be in the range of up to a decade.

In addition, in the experimental results we do not see the effect that the damping by the STW model can decrease with a decreasing gap width. In Fig. 3(a), it can be seen that the temperature rise decreases for gap widths smaller than 450 μm , which is expected to result in an increase of the quality factor. This leads to the assumption that the efficiency of the heat diffusion process is not only depending on frequency match but also on the gap width. For this reason, we assume a minimal quality factor A_{trans} depending on the gap width (see Eq. 3).

3. Experiment

The transitional quality factor Q_{trans} is determined by fitting the proposed model to the experimental data of three types of micro-oscillators used in our experiments (yellow lines in Fig. 1). These types were a bending oscillator (BO) with an eigenfrequency of 4.95 kHz, and two cantilever shaped oscillators (CO_33 & CO_50) with an eigenfrequency of 1.33 kHz (details on the geometry can be found in the supplementary material). The numbers are indicating the coverage percentage with the AlN actuation patterns; otherwise, the cantilevers have the same geometry. The measurements with sensor BO were performed in six different gas atmospheres including the noble gases He, Ne and the polyatomic gases N_2 , CO_2 , N_2O and SF_6 for a gap width ranging from 150 to 3500 μm . The results obtained within a nitrogen atmosphere have been presented previously in the fundamental study of this topic, where the thermal resonance model was introduced [11]. In a second measurement series the cantilever sensors (CO_33 & CO50) were investigated, focusing on the noble gases He, Ne, Ar and Kr. An N_2 nitrogen atmosphere was included for comparison. Additional information about the manufacturing process, the measurement setup as well as the fitting process can be found in [18]. The transitional quality factor Q_{trans} is extracted by applying the fitting procedure illustrated in Fig. 1 and, subsequently, is further analyzed depending on the thermophysical

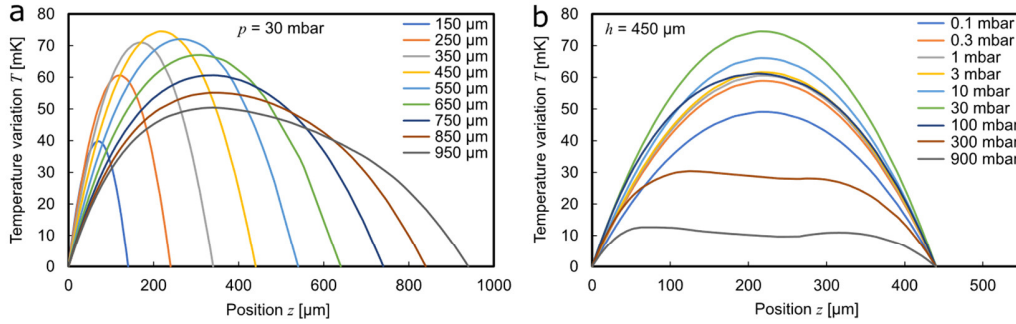


Fig. 3. Simulated temperature variation for a varying gap width at a constant pressure of 30 mbar in a Ne atmosphere (a) and for varying ambient pressure at a constant gap width of 450 μm (b).

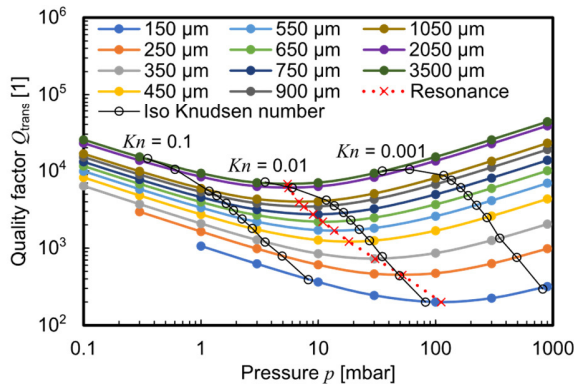


Fig. 4. Experimentally determined quality factor for the transitional flow regime. The data were measured in a Ne atmosphere with sensor BO; gap widths were varied from 150–3500 μm . Lines for Iso-Knudsen numbers are included to visualize the different flow regimes. The red dotted line indicates the position of minimal Q , where thermal resonance occurs.

properties of the gases and the adjusted gap width to a geometrical boundary.

In Fig. 4, the data of sensor BO for a Ne gas atmosphere measured within a wide range of gap widths are shown. Additionally, the Knudsen numbers are included to separate the flow regimes as well as the points of the thermal resonance leading to a minimum of the transitional quality factor. As can be seen, the effect of the thermal resonance model is decreasing with increasing gap width. Moreover, the thermal resonance point is shifting to lower pressures for an increasing gap width. The minimum of the quality factor, the resonance case of the STW, is always located in the middle of the transitional flow regime. In Fig. 1, the strength in relation to the viscous damping can be observed. The STW effect is dominant in the transitional flow regime, especially at small gap widths and for noble gases. The effect is relatively weaker for polyatomic gases and is in the same order of magnitude as the viscous damping. The difference in the strength of the STW damping of noble gases and polyatomic gases will be discussed in the following.

In Fig. 5 the transitional quality factor Q_{trans} for the different types of gases is shown. It can be observed that both the strength and the pressure at which thermal resonance occurs strongly depend on the type of gas. The noble gases exhibit the strongest damping effects on the micro-oscillators and the thermal resonance occurs at higher pressures. Therefore, a second series of measurements with the cantilever structures focusing on the noble gases was performed. In the following discussion, the two characteristic values of the thermal resonance model, i. e. the thermal resonance frequency respectively the pressure of the

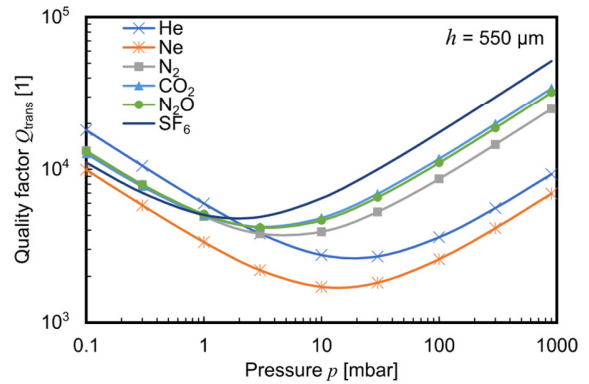


Fig. 5. Experimentally determined quality factor within the transitional flow regime for different gases at a constant gap width of 550 μm for sensor BO.

thermal resonance and the minimal quality factor are correlated to the thermal properties of the types of gases, according to the theory.

4. Discussion

In the previous section, the experimental data were evaluated to

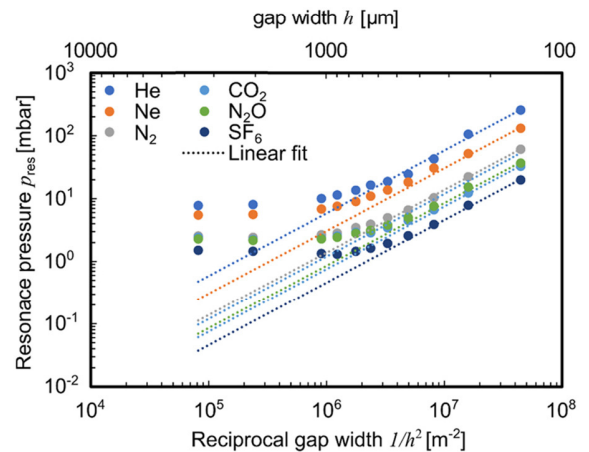


Fig. 6. Plot of the pressure p_{res} at which thermal resonance occurs vs. the squared reciprocal gap width measured with sensor BO. The linear fit shows the theoretical prediction according to Eq. 6.

extract the transitional quality factor. In Fig. 6, the pressure p_{res} at which thermal resonance occurs is shown for different gases as function of the reciprocal squared gap width measured with the sensor BO. According to Eq. (6), the plot should exhibit a linear behavior. From the linear fit we see that for small gap widths the data are in good accordance with the theoretical prediction. For larger gap widths (above 1000 μm) a saturation effect of the resonance pressure point can be observed. With the help of FEM simulations we can determine, that for large gap widths and also for high pressures there is no clear formation of a STW within the gap. The amount of heat produced by the oscillating movement leads to an increase of temperature in the range of up to 100 mK, leading to a STW up to a gap width of about 750 μm . For gap widths exceeding 750 μm , a deviation of the clear node-antinode formation appears. One can conclude that the range of the thermal resonance model is therefore depending on the heat necessary to build a standing wave within the gap width. In our experiment, the temperature variation created by the heat is 100 mK according to the FEM simulation leading to a limiting gap width of about 750 μm . This limitation is justified by the experimental results.

In Fig. 7, the dependency of the resonance pressure on the thermal diffusivity is additionally included [27]. In analogy to the TED model, we define a thermal resonance frequency given by the ratio of the thermal diffusivity to the squared gap width. By fitting a potential function to the measurement data, we get an exponential factor of about 0.75. From the theory, we would expect a linear dependency according to Eq. (6). One point is that for larger gap widths a deviation to the squared reciprocal behavior occurs which is also visible in Fig. 5. Furthermore, the thermal diffusivity is changing its dependency on the ambient pressure, when leaving the continuum regime. The thermal diffusivity given in Eq. (5) is valid for the viscous flow regime and changing its dependency on the ambient pressure to a constant behavior in the molecular flow regime. Therefore, it is to be expected that there is a weaker dependency in the transitional flow regime on the ambient pressure.

The second characteristic value besides the thermal resonance frequency (respectively the resonance pressure) is the minimal quality factor in the case of thermal resonance. In Fig. 8, the minimal value of each parabola is shown as function of the ambient pressure (compare Fig. 4). The data show a reciprocal behavior to the resonance pressure leading to the proportionality of the minimal quality factor in the case of thermal resonance. In analogy to the minimal quality factor of the Zener formalism ($Q_{Zener,min} = \frac{\rho C_p}{E \alpha^2 T_0}$ [28], with ρ density, C_p heat capacity at constant mechanical pressure/strain, E Young modulus, α thermal coefficient of expansion (CTE) of the solid state material, and T_0 ambient temperature) a dependence to the pressure p can be derived by replacing

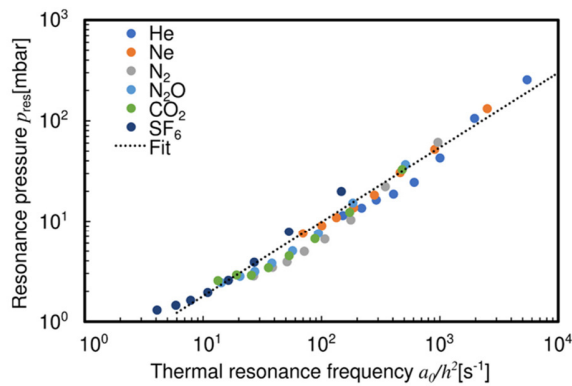


Fig. 7. Plot of the resonance pressure p_{res} vs. thermal resonance frequency a_0/h^2 measured with sensor BO. The potential fit shows qualitatively the prediction according to Eq. (6).

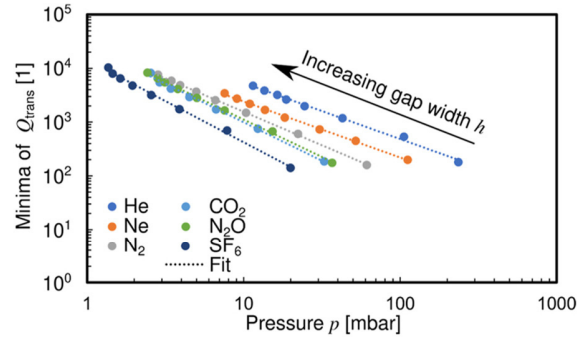


Fig. 8. Minimal point of the transitional quality factor of sensor BO as function of the ambient pressure for different gases as well as for different gap widths, ranging from 150 to 900 μm . Each curve is fitted by a potential function showing a reciprocal behavior to the ambient pressure.

the corresponding variables for solids with the gas equations for adiabatic compression/expansion ($E \rightarrow$ isentropic bulk modulus $K = \kappa p$ and $\alpha \rightarrow$ volume CTE $\alpha_{gas} = \frac{1}{(\kappa-1)T}$). Additionally, the relation between temperature and pressure in a adiabatic process is used $pT^{\frac{1-\kappa}{\kappa}} = const.$ leading to:

$$A_{trans}(h) \propto \frac{C_p(\kappa-1)^2 T_0}{\kappa p_{res}^{\frac{1}{\kappa}}} \propto \frac{1}{p^{\epsilon}} \quad (10)$$

The exponents ϵ of the potential fit function shown in Fig. 8 are listed in Table 1. They show a strong correlation to the adiabatic index κ of each gas. The dependence of the exponent on the adiabatic index leads to the conclusion that the temperature increase within the gap, caused by the oscillation of the micro oscillator, is an adiabatic process. The resonance pressure p_{res} is increased compared to the pressure p due to the adiabatic compression. For an adiabatic process, this pressure increase is only depending on the temperature variation and on the adiabatic index. A lower adiabatic index leads to lower thermal losses (Limit of $\kappa \rightarrow 1$ leading to an isothermal process). This confirms the results that thermal resonance loss effects of polyatomic gases are significantly lower than those of noble gases. As a function of the adiabatic index, which can be associated with the degrees of freedom f of the gas, the exponent can be expressed as (see Fig. 9):

$$\epsilon = \frac{A}{\kappa} = A \frac{f}{f+2} \quad \text{with } A = 1.758 \text{ leading to } R^2 = 0.9995 \quad (11)$$

Table 1

Listing of the determined exponent ϵ_{exp} for all measured gases and the deviation to the calculated exponent ϵ_{calc} according to Eq. (11). The results show a reciprocal dependence to the adiabatic index κ . The adiabatic index is calculated with the degrees of freedom given in [18].

Gas	κ [1]	ϵ_{calc} [1]	ϵ_{exp} [1]	Deviation [%]	Sensor
He	1.66	-1.077	-1.035	-3.9	BO
			-1.043	-3.2	CO_33
			-1.04	-3.4	CO_50
Ne	1.66	-1.077	-1.028	-4.5	BO
			-1.004	-6.8	CO_33
			-1.048	-2.7	CO_50
Ar	1.66	-1.077	-0.992	-7.9	CO_33
			-1.001	-7.1	CO_50
Kr	1.66	-1.077	-1.021	-5.2	CO_33
			-1.035	-3.9	CO_50
N ₂	1.4	-1.277	-1.240	-1.6	BO
			-1.228	-3.8	CO_33
			-1.235	-3.3	CO_50
CO ₂	1.3	-1.375	-1.404	5.1	BO
N ₂ O	1.29	-1.386	-1.384	2.1	BO
SF ₆	1.158	-1.54	-1.506	-1.2	BO

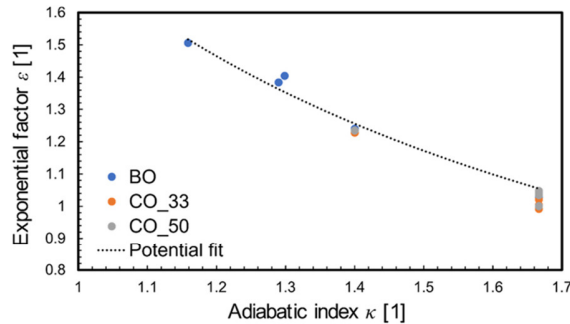


Fig. 9. Experimentally determined exponential factor as function of the adiabatic index. The potential fit is based on the data of sensor BO and is in accordance with Eq. (11).

Based on these results a second measurement series focusing on the noble gases was undertaken. On the one hand, this is to confirm that noble gases possess very strong thermal resonance effects and, on the other hand, to verify the dependence of the exponential factor on the adiabatic index. As can be seen in Fig. 10, the curves of the minimal quality factor of the noble gases are parallel to each other which indicates that the exponents ε are equal. Only the nitrogen curve has a different slope and rises steeper with decreasing resonance pressure, respectively increasing gap width. As a result, the noble gases have higher damping at medium distances (350–750 μm) due to thermal resonance effect (see also Fig. 8). The experimental results for the exponential factor ε are added in Table 1 as well as in Fig. 9 and are in good agreement with the data of the first measurement series with sensor BO. Further figures regarding the evaluation of the resonance pressure and minimal quality factor as presented in the paper for sensor BO can be found for the sensors CO_33 and CO_50 in the supplementary material.

Additionally, we find empirically the reciprocal proportionality of the minimal value to the density of the gas leading to:

$$A_{\text{trans}}(h) \propto \frac{1}{p_{\text{res}} \cdot \rho} \propto \frac{h^2}{a_0 \cdot \rho} \propto \frac{C_p \cdot h^2}{k} \quad (12)$$

which is a value independent of the ambient pressure and only a function of the gap width h as well as of the thermal properties of the gas. A higher thermal conductivity k leads to higher thermal losses and, therefore, decreases the minimal transitional quality factor. A higher heat capacity C_p leads to a lower temperature variation and consequently the thermal diffusive process, which is driven by the temperature gradient, is reduced. These effects of the thermal properties can be

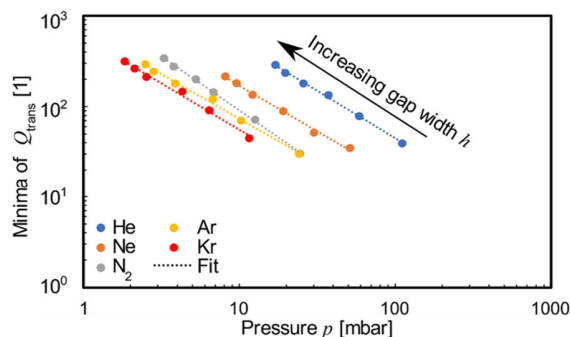


Fig. 10. Minimal point of the transitional quality factor vs. the ambient pressure for CO_33. The noble gases possess the same exponential slope indicated by the parallel potential fit functions (cf. Table 1) in a range from 250 to 750 μm .

observed in Fig. 5 and lead to a clear separation between the noble gases, exhibiting high thermal conductivity and low heat capacity and the polyatomic gases. In contrast, the polyatomic gases possess additional degrees of freedom in which they can store energy and therefore have a lower thermal conductivity and higher heat capacity. Consequently, the damping effect is more pronounced for the noble gases due to their thermal properties and leads to higher losses via the thermal resonance. In Fig. 11, the minimum of the transitional quality factor is shown according to Eq. (12), for all measured gases and gap widths. The data are in good agreement with the theory, except for the smallest and for the largest gap widths. As mentioned before, at large distances the amount of heat dissipated is not sufficient to generate a STW and thus to form a thermal resonance. At the smallest gap width of 150 μm , the so-called squeeze film damping effect occurs and becomes dominant [29], thus superimposing the thermal resonance damping. For this reason, the quality factor is smaller than expected.

5. Conclusions

In this work, the concept of the formation of STWs, which lead to a thermal resonance depending on the ambient pressure and the adjusted gap width was extended to a variety of gas types. The discussed effect of thermal resonance caused by STW was used to describe the damping behavior of micro-oscillators in the transition region. For validation, the model was applied to the measured data of eight different types of gases and a gap width ranging from 150 μm to 3500 μm for three micro-oscillators. A very good agreement with the measured data was obtained for all configurations. The determined quantities of the thermal resonance model, the thermal resonance frequency and the minimal quality factor were extracted from the results. For distances up to 750 μm , good agreement was found with the thermal resonance model. For larger distances, deviations occurred which can be attributed to the fact that STW cannot develop any more. This proves that micro-oscillators can be used as a tool for the measurement of thermal properties of gases.

CRedit authorship contribution statement

Tobias Zengerle: Investigation, Software, Formal analysis, Data curation, Writing – original draft, Writing – review & editing. **Abdallah Ababneh:** Supervision, Funding acquisition. **Helmut Seidel:** Writing – original draft, Writing – review & editing, Supervision, Project administration, Funding acquisition.

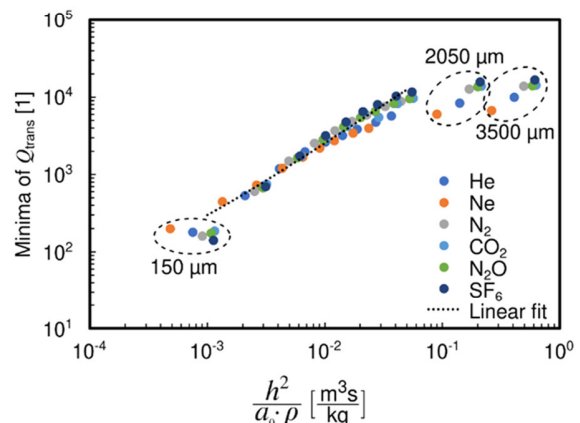


Fig. 11. Minimal transitional quality factor versus the proportionality according to Eq. (12) for all measured gases and gap widths for sensor BO. Deviations occurring at the smallest gap widths (squeeze film effect) and at the largest gap widths (no standing wave generated) are marked.

Declaration of Competing Interest

The authors declare that they have no known competing financial interests or personal relationships that could have appeared to influence the work reported in this paper.

Acknowledgment

The authors wish to thank the German Research Foundation (DFG) for financial support within the grant SE 1425/14-1.

Appendix A. Supporting information

Supplementary data associated with this article can be found in the online version at [doi:10.1016/j.sna.2022.113614](https://doi.org/10.1016/j.sna.2022.113614).

References

- [1] G. Pillai, S.-S. Li, Piezoelectric MEMS resonators: a review, *IEEE Sens. J.* 21 (11) (2020) 12589–12605.
- [2] N. Satoh, M. Nakahara, K. Kobayashi, S. Watanabe, T. Fujii, K. Matsushige, H. Yamada, Using dynamic force microscopy with piezoelectric cantilever for indentation and high-speed observation, *Nonlinear Theory Appl. IETCF* 8 (2) (2017) 98–106.
- [3] C. Lu, P. Li, M. Bao, Y. Fang, A generalized energy transfer model for squeeze-film air damping in the free molecular regime, *J. Micromech. Microeng.* 28 (8) (2018), 085003.
- [4] P. Fedeli, A. Frangi, G. Laghi, G. Langfelder, G. Gattere, Near vacuum gas damping in MEMS: simplified modeling, *J. Microelectromech. Syst.* 26 (3) (2017), 632–342.
- [5] M. Martin, B. Houston, J. Baldwin, M. Zalalutdinov, Damping models for microcantilevers, bridges, and torsional resonators in the free-molecular-flow regime, *J. Microelectromech. Syst.* 17 (2) (2008) 503–511.
- [6] A. Pandey, R. Pratap, Effect of flexural modes on squeeze film damping in MEMS cantilever resonators, *J. Micromech. Microeng.* 17 (12) (2007) 2475–2484.
- [7] J. Kaczynski, C. Ranacher, C. Fleury, Computationally efficient model for viscous damping in perforated MEMS structures, *Sens. Actuators A: Phys.* 314 (2020), 112201.
- [8] G. Aoust, R. Levy, B. Bourgeteau, O. Le Traon, Viscous damping on flexural mechanical resonators, *Sens. Actuators A: Phys.* 230 (2015) 126–135.
- [9] F. Blom, S. Bouwstra, M. Elwenspoek, J. Fluitman, Dependence of the quality factor of micromachined silicon beam resonators on pressure and geometry, *J. Vac. Sci. Technol. B: Microelectron. Nanometer Struct. Process. Meas. Phenom.* 10 (1) (1992) 19–26.
- [10] G. Pfusterschmied, C. Weinmann, M. Schneider, D. Platz, N. Shen, J. Sader, U. Schmid, Sound dissipation from plate-type resonators excited in non-conventional transversal modes in liquids, *J. Micromech. Microeng.* 30 (7) (2020), 075004.
- [11] T. Zengerle, J. Joppich, P. Schwarz, A. Ababneh, H. Seidel, Modeling the damping mechanism of MEMS oscillators in the transitional flow regime with thermal waves, *Sens. Actuators A: Phys.* 311 (2020), 112068.
- [12] J. Shen, A. Mandelis, Thermal-wave resonator cavity, *Rev. Sci. Instrum.* 66 (10) (1995) 4999–5005.
- [13] J. Shen, A. Mandelis, T. Ashe, Pyroelectric thermal-wave resonant cavity: a precision thermal diffusivity sensor for gases and vapors, *Int. J. Thermophys.* 19 (2) (1998) 579–593.
- [14] C. Gu, J. Shen, J. Zhou, K. Michaelian, R. Gieleciak, N. Astrath, M. Baesso, Thermal-wave resonant cavity signal processing, *Rev. Sci. Instrum.* 90 (2019), 014901.
- [15] A. Bedoya, M. Colom, A. Mendioroz, A. Salazar, E. Marin, Measurement of the thermal conductivity of fluids using laser spot lock-in thermography, *Measurement* 158 (2020), 107740.
- [16] J. Lu, T. Ikehara, Y. Zhang, T. Mihara, T. Itoh, R. Maeda, High quality factor silicon cantilever driven by piezoelectric thin film actuator for resonant based mass detection, *Microsyst. Technol.* 15 (2009) 1163–1169.
- [17] G. Karniadakis, A. Beskok, N. Aluru, *Microflows and Nanoflows: Fundamentals and Simulation*, Springer Science & Business Media, 2006, pp. 16–17.
- [18] T. Zengerle, J. Joppich, P. Schwarz, A. Ababneh, H. Seidel, Polyatomic degrees of freedom and their temporal evolution extracted from the damping of micro-oscillators, *Sens. Actuators A: Phys.* 297 (2019), 111460.
- [19] C. Zener, Internal friction in solids II. General theory of thermoelastic internal friction, *Phys. Rev.* 53 (1) (1938) 90–99.
- [20] H. Hao, C. Scalo, F. Semperlotti, Traveling and standing thermoacoustic waves in solid media, *J. Sound Vib.* 449 (2019) 30–42.
- [21] E. Marin, L. Vaca-Oyola, O. Delgado-Vasallo, On thermal waves' velocity: some open questions in thermal waves' physics, *Rev. Mex. De. Fis. E* 62 (1) (2016) 1–4.
- [22] G. Pan, A. Mandelis, Measurements of the thermodynamic equation of state via the pressure dependence of thermophysical properties of air by a thermal-wave resonant cavity, *Rev. Sci. Instrum.* 69 (8) (1998) 2918–2923.
- [23] J. Anderson, *Governing Equations of Fluid Dynamics in Computational Fluid Dynamics - An Introduction*, Springer-Verlag, Berlin, 2009, pp. 15–51.
- [24] COMSOL Multiphysics, *Vibrating micromirror with viscous and thermal damping*, COMSOL Inc.: Burlington, USA.
- [25] A. Ricci, G. Canavese, I. Ferrante, S. Marasso, C. Ricciardi, A finite element model for the frequency spectrum estimation of a resonating microplate in a microfluidic chamber, *Microfluid. Nanofluid.* 15 (2) (2013) 275–284.
- [26] M. Sagar, S. Ali, A. Manjari, L. Sushma, Effect of Knudsen number on blunt body during hypersonic speeds for reducing drag, *Int. J. Mech. Prod. Eng. Res. Dev.* 9 (6) (2019) 451–462.
- [27] E. Lemmon, M. McLinden, D. Friend, *Thermophysical Properties of Fluid Systems*, NIST Chemistry WebBook, 1998 retrieved January 28, 2021, (<https://webbook.nist.gov/chemistry/fluid/>).
- [28] Y. Yu, X. Tian, J. Liu, Size-dependent damping of a nanobeam using nonlocal thermoelasticity: extension of Zener, Lifshitz, and Roukes' damping model, *Acta Mech.* 228 (2017) 1287–1302.
- [29] M. Bao, H. Yang, Squeeze film air damping in MEMS, *Sens. Actuators A: Phys.* 136 (1) (2007) 3–27.

Tobias Zengerle gained the B.Sc., M.Sc. in microtechnology and nanostructures from the Saarland University in Saarbücken in 2015, and 2017, respectively. He is currently working toward the Ph.D degree from Saarland University, Germany. His research interests include MEMS oscillators and their application as gas sensing systems.

Abdallah Ababneh received his Dipl.-Ing. (B. Sc. + M.Sc.) and Ph.D. degrees in electrical engineering from Saarland University/ Germany in 2002 and 2009, respectively. He is currently an Associate Professor at Yarmouk University/ Jordan. His research interests include piezoelectric thin films and microresonators.

Prof. Helmut Seidel received the diploma degree in physics from Ludwig-Maximilians-University, Munich, Germany, in 1980, with work in theoretical elementary particle physics and the Ph.D. degree in physical chemistry from the Free University, Berlin, Germany, in 1986. In 1980, he joined Fraunhofer-Society, Munich, as a Research Scientist focusing on MEMS. From 1986 until 2002, he held various positions in industry, starting at MBB, then Daimler-Benz, and Temic. Since 2002, he has been a Professor at Saarland University, Saarbrücken, Germany, holding the Chair for Micromechanics, Microfluidics/ Microactuators. He has obtained more than 40 patents and has coauthored a large number of publications. His current interests focus on inertial sensors, microfluidics, and flexible substrates, among others. Prof. Seidel served on International Steering Committees and Program Committees of various important conferences and is currently an Editor of the IEEE Journal of Microelectromechanical Systems.

6.4 Higher Modes

6.4.1 Introduction

In this section, further eigenmodes besides the fundamental bending mode will be discussed. The first bending mode is characterized by a large interaction with the environment, due to its large displacement. Therefore, the strength of the damping is relatively high which is advantageous for sensors based on damping effects to detect the environmental properties such as viscosity [96]. For sensors that require high resolution, respectively a high quality factor, as in many scanning probe microscopy applications, this is disadvantageous. Furthermore, in highly viscous media such as liquids, the fundamental mode is often no longer detectable. For this reason, higher modes are often used to overcome the problem of a low quality factor of the fundamental bending mode. This increase of the quality factor is based on two effects. On the one hand, the resonance frequency is higher, which, according to Equation (2.16), is directly associated with a higher quality factor. Furthermore, higher oscillation modes have a significantly lower interaction with the medium, which leads to a weaker damping. In addition to lateral modes, for example, roof-tile shape modes result in higher quality factors in the liquid than comparable bending modes due to the special mode form [32].

This phenomenon is illustrated in Figure 38, in which the quality factor of the fundamental mode and the next higher bending modes is depicted as function of the resonance frequency. At a low pressure level, the quality factor is limited by the intrinsic damping due to the residual stress of the piezoelectric thin film. This quality factor is increasing nearly linearly with the frequency up to the third bending mode. The next higher modes are stronger attenuated due to the thermoelastic damping effect, which is increasing by approaching the thermal resonance frequency of the system.

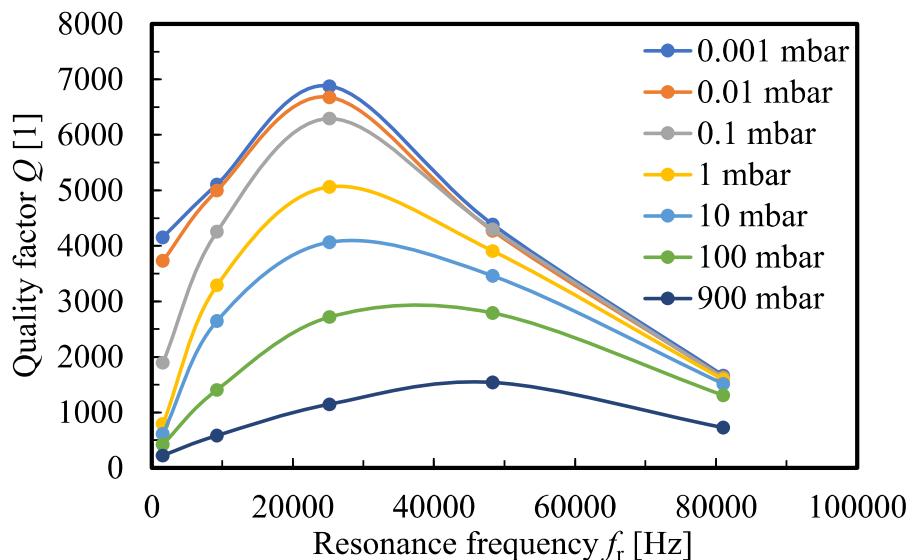


Figure 38. Quality factor of the fundamental bending mode and higher bending modes as function of the resonance frequency for different ambient pressure levels. The experimental data of micro-oscillator BO3 mentioned in the attached study is shown.

By increasing the ambient pressure, the extrinsic gas damping is increased and therefore the quality factor of the bending modes drops. Due to the different strength of the damping of the individual bending modes, the strength of the decrease is observed more strongly for the lower bending modes. In the atmospheric pressure regime at 900 mbar, the highest quality factor is found at the fourth bending mode. In theory, the next higher bending mode should have even lower viscous damping. Here, however, the strong intrinsic damping, which was already observed in the vacuum range, must be taken into account, which strongly reduces the overall measured quality factor.

In Figure 39, the ratio of resonance frequency and quality factor is illustrated. According to Equation (2.16), this ratio gives a measure for the strength of the damping. The initial value at a low pressure level is determined by the intrinsic damping and the curve shape for increasing pressure is determined by the increasing extrinsic damping effect of the gas atmosphere. Here, a strong difference between the bending modes becomes apparent. The damping of the first bending modes increases by more than one order of magnitude, whereas the higher bending modes increase by a much smaller factor. From this it can be concluded that the damping of higher bending modes is significantly lower than the damping of the fundamental mode.

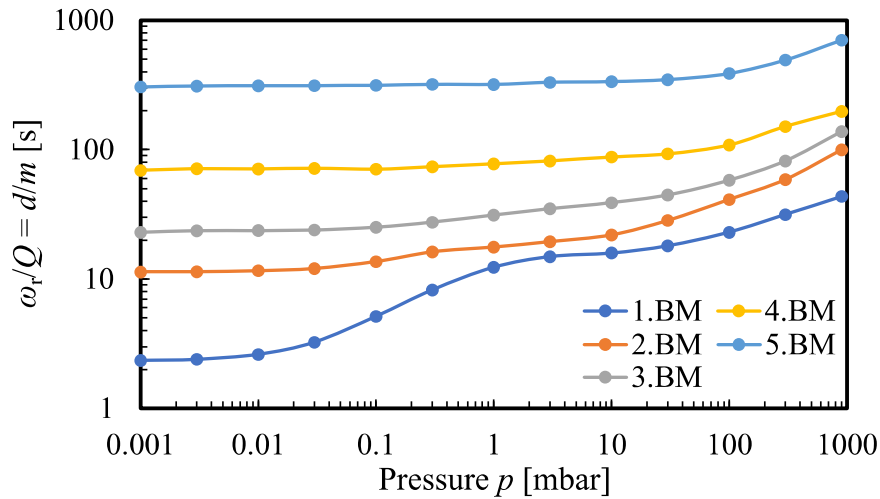


Figure 39. Measure of the damping obtained from the ratio of the quality factor to the resonance frequency is shown as a function of ambient pressure for the first five bending modes. The fundamental bending mode shows the biggest increase of damping for higher pressures. The experimental data of micro-oscillator CO1_33 mentioned in the attached study is shown.

The question posed in the following paper is if the previously presented model for describing the damping of the fundamental mode can be expanded on the higher bending modes. Therefore, the generalization of the model is investigated and will be related to standard quantities, such as viscous boundary layer and thermal boundary layer. The aim is to achieve a unified model for all modes covering the individual damping mechanisms from molecular up to the viscous flow regime.

In a later section, further eigenmodes will be discussed, especially the roof tile-shape modes, which will be examined regarding their nonlinearity behavior due to their high quality factor. These modes are explored for a new wide-range pressure sensing concept (see Section 6.7).

6.4.2 Addendum IV



Article

Generalized Damping Model for MEMS Oscillators from Molecular to Viscous Flow Regime

Tobias Zengerle ^{1,*} , Abdallah Ababneh ² and Helmut Seidel ¹ ¹ Department of Physics, Saarland University, 66123 Saarbrücken, Germany; seidel@imm.uni-saarland.de² Electronic Engineering Departement, Hijjawi Faculty for Engineering Technology, Yarmouk University, Irbid 21163, Jordan; a.ababneh@yu.edu.jo

* Correspondence: t.zengerle@imm.uni-saarland.de

Abstract: In this study, we investigate the damping phenomena acting on piezoelectrically driven MEMS oscillators. Three different geometrical shapes of MEMS oscillators are presented, including cantilevers, bending oscillators, and paddle oscillators. An analytical model for their resonance frequencies is derived. The bending modes of these micro-oscillator structures are characterized regarding their resonance frequency and their quality factor as a function of the ambient pressure in a nitrogen atmosphere as well as the dependence on the distance to a neighboring plate representing a geometrical boundary (e.g., to the package or to the mounting). The investigations cover a pressure range from 10^{-3} mbar up to 900 mbar and a gap width from 150 μm to 3500 μm . Consequently, a Knudsen number range over six orders of magnitude from 100 to 10^{-4} is covered. The measurement data are evaluated with a generalized damping model consisting of four parts representing the individual damping mechanisms (intrinsic, molecular, transitional, and viscous). The evaluated parameters are analyzed as a function of the resonance frequency and the gap width. The data reveal an exponential growing saturation behavior, which is determined by two characteristic lengths, being correlated with the viscous and the thermal boundary layer thickness, respectively. This leads to an estimation of the strength and of the range of the damping effect just by calculating the boundary layer thicknesses given by the resonance frequency and the gas properties. From these results, we gain fundamental insights on the viscous and transitional damping mechanisms as well as on the intrinsic losses. In conclusion, a basic concept is provided to reduce the damping of micro-oscillator bending modes and thus increase the quality factor. Additionally, the results are supported by finite element simulations revealing the temperature and pressure distribution within the gap.

Keywords: Q factor; damping model; transitional flow regime; viscous flow regime; MEMS oscillator; bending modes



Citation: Zengerle, T.; Ababneh, A.; Seidel, H. Generalized Damping Model for MEMS Oscillators from Molecular to Viscous Flow Regime. *Eng* **2022**, *3*, 124–141. <https://doi.org/10.3390/eng3010011>

Academic Editor: Van Dau

Received: 18 January 2022

Accepted: 23 February 2022

Published: 25 February 2022

Publisher's Note: MDPI stays neutral with regard to jurisdictional claims in published maps and institutional affiliations.



Copyright: © 2022 by the authors. Licensee MDPI, Basel, Switzerland. This article is an open access article distributed under the terms and conditions of the Creative Commons Attribution (CC BY) license (<https://creativecommons.org/licenses/by/4.0/>).

1. Introduction

MEMS oscillators are widely used in our technological world and are found in a variety of applications [1–5]. Based on their operating principle, the oscillators can be divided into two classes: electrostatic excitation and piezoelectric excitation. The advantages of electrostatic excitation include a high-quality factor Q and good frequency stability, especially for frequency timing applications [6]. However, disadvantages are a high operating voltage, occurring nonlinearities, and difficult processing due to the narrow gaps that are required between the two capacitor plates. Piezoelectric oscillators, on the other hand, are characterized by low operating voltage, high electromechanical coupling, and simple CMOS-compatible batch processing since there is no requirement for a gap. However, a disadvantage compared to electrostatic excitation is the lower Q factor and the associated impact on oscillator performance, such as resolution and frequency stability. For this reason, an important area of research is to increase the quality factor of piezoelectric oscillators [7]. This includes an enhancement of the material-related intrinsic quality factor, as well as the

reduction of extrinsic damping effects, being related to environmental ambient pressure and geometrical boundaries [8,9]. In many applications, MEMS oscillators are operated under various ambient conditions, e.g., in a liquid, in a gas atmosphere, or encapsulated under vacuum conditions. Furthermore, the distance of the micro-oscillator to a mounting or to a package is an important factor [10–12]. Therefore, we investigate the influence of an encapsulation package under various ambient pressure conditions and experimentally correlate them with the damping effects.

The overall quality factor of a micro-oscillator is determined by four different damping mechanisms. Therefore, in the first step, the main loss factor must be determined, which subsequently has to be minimized to increase the overall quality factor of the MEMS oscillator. At low pressure ($p = 0.01$ mbar), the intrinsic damping losses are dominant and the extrinsic losses due to the gas atmosphere can be neglected. The extrinsic damping mechanisms are subdivided further, corresponding to the Knudsen number, which is defined by the ambient pressure and the gap width. In the low-pressure range, with a respectively high Knudsen number ($Kn > 1$), molecular flow damping dominates, whereas in the high-pressure range up to atmospheric pressure and beyond viscous flow damping is defined ($Kn < 0.01$) [13]. In between, the transitional flow regime is encountered, where the damping is described by thermal wave resonance effects [14]. Within this paper, we examine a generalized damping model for various oscillator structure shapes with different coverage sizes of the piezoelectric thin film layer. The oscillators are characterized over a large pressure range and over a varying gap width. The generalized damping model shows good agreement with the experimental data, covering six orders of magnitude for the Knudsen number. Additionally, numerical simulations are performed to model the pressure and temperature distribution supporting the found damping fundamentals. With the help of the results, design rules for an optimization of the quality factor on the dependence of the gap width to the package are derived, based only on the resonance frequency.

2. Generalized Damping Model

2.1. MEMS-Oscillator

The investigated MEMS oscillator structures are shown in Figure 1 and are subdivided into three classes regarding their shape: paddle oscillator (PO), bending oscillator (BO), and cantilever oscillator (CO). The resonance frequency of such MEMS oscillators can be derived by the theory of an externally driven damped harmonic oscillator [15]. This results in the fundamental resonance frequency f_r :

$$f_r = \frac{1}{2\pi} \sqrt{\frac{k}{m}}, \quad (1)$$

where k and m denote the spring constant, and the mass of the MEMS oscillator, respectively.

The mass of the MEMS oscillator can be calculated easily by the density–volume product, and the spring constant is given by solid mechanics [16]:

$$k_B = \frac{3E_{Si}I}{L^3} = \frac{E_{Si}BT^3}{4L^3}, \quad (2)$$

with Young's modulus E_{Si} of the MEMS oscillator, as well as the moment of inertia I , the length L_B , the width B_B and the thickness T of the beam.

For the PO and BO structures, we assume two parallel-connected beam spring constants ($k = k_B \parallel k_B = 2k_B$) with the length $L = L_B + L_O$, and width $B = B_B$. For the CO structures, the length L and the width B are directly given by the oscillator dimension L_O and B_O .

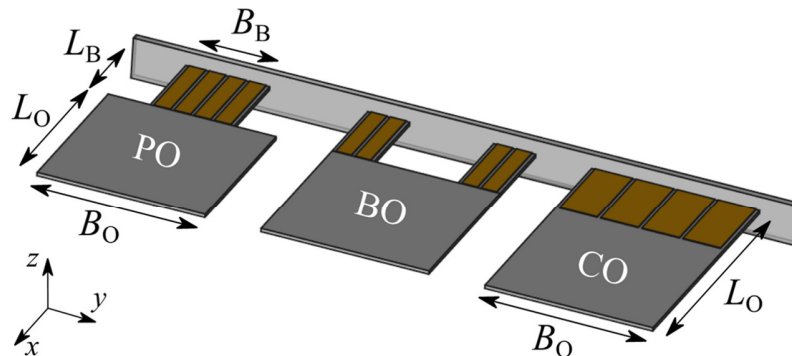


Figure 1. Schematic 3D view on the investigated MEMS oscillator structures. From left to right: paddle oscillator PO, bending oscillator BO, and cantilever oscillator CO. The oscillators with thickness T are actuated with piezoelectric AlN elements, which are covered with gold electrodes. Microscope images of the fabricated micro-oscillators can be found in Appendix A.

Moreover, we scale the mass m of the MEMS oscillator by a factor α attributing the effect that not the entire structure is vibrating [17]. Therefore, the effective mass $m_{\text{eff}} = \alpha \cdot m$ is used in the following calculations.

Taking everything into account, this leads to the resonance frequency of the MEMS oscillator as a function of its geometry and material properties:

$$f_r = \frac{1}{2\pi} \begin{cases} T \sqrt{\frac{E_{\text{Si}}}{2\alpha\rho_{\text{Si}}} \frac{B_B}{(L_B+L_O)^3 (2B_B L_B + B_O L_O)}} & \text{for PO/BO} \\ \frac{T}{2L_O^2} \sqrt{\frac{E_{\text{Si}}}{\alpha\rho_{\text{Si}}}} & \text{for CO} \end{cases} \quad (3)$$

This calculation is valid for the resonance frequency of the first fundamental bending mode (BM) of the MEMS oscillator. The resonance frequency of the higher bending modes f_n with mode number n can be calculated as a multiple of the squared eigenvalue λ_n [18]:

$$f_n = \lambda_n^2 f_r. \quad (4)$$

The eigenvalue λ_n is given by 1.88; 4.69; 7.86; 11.00 for the first four bending modes [17]. This analytical approach will be discussed in the experimental section, regarding the accuracy of the description as well as the influence of the different geometric shapes on the scale factor α , which is experimentally investigated.

2.2. Quality Factor Q

The second characteristic value besides the resonance frequency of a MEMS oscillator is the quality factor Q . This is a measure for the damping and is defined by the ratio of the total energy of an oscillator E to the energy dissipation per cycle ΔE . Its value can be measured from a resonance curve plot using the 3dB bandwidth $\Delta f_{3\text{dB}}$ [19]:

$$Q = \frac{E}{\Delta E} = \frac{f_n}{\Delta f_{3\text{dB}}}. \quad (5)$$

The experimentally measured quality factor always represents a combination of several individual damping mechanisms, which can be combined via the superposition principle.

The damping phenomena can be divided into two classes, the material related intrinsic ones, and the extrinsic ones from the surrounding gas atmosphere:

$$Q_{\text{exp}} = \left(\frac{1}{Q_{\text{int}}} + \frac{1}{Q_{\text{ext}}} \right)^{-1} = \left(\frac{1}{Q_{\text{int}}} + \underbrace{\frac{1}{Q_{\text{mol}}} + \frac{1}{Q_{\text{trans}}} + \frac{1}{Q_{\text{vis}}}}_{\frac{1}{Q_{\text{gas}}}} \right)^{-1}. \quad (6)$$

The intrinsic damping losses are independent of the external pressure and are determined by anchor losses [20], by the residual stress of the piezoelectric layer [21], and by thermoelastic damping effects [22]. Which of the three types of damping is dominant depends on the resonance frequency and on the bending mode.

The extrinsic damping influences can be further subdivided according to several flow regimes with respect to the Knudsen number Kn . The Knudsen number is given by the ratio of the mean free path l_{mfp} to a representative length scale l^* . In the context of the investigations, the Knudsen number is changed on the one hand by the pressure which influences the mean free path, and on the other hand by the representative length scale which can be adjusted by a variable gap width h .

For the different individual flow regimes, descriptions of the damping behavior in the literature are available which are summarized in a more generalized damping model. In the molecular flow regime ($Kn > 1$), the quality factor can be described by a reciprocal dependency on the external pressure which was expanded by Bao et al. with a linear gap width h dependency [23,24] (valid for small gap widths [25]):

$$Q_{\text{mol}} = \frac{\zeta_{\text{mol}}(h)}{p}. \quad (7)$$

The other dependencies on the geometric shape, the size of the oscillator, the gas atmosphere, and the ambient temperature are summarized in the fit parameter ζ_{mol} [bar].

For low Knudsen numbers ($Kn < 0.01$), the quality factor can be calculated for the viscous flow regime based on the Navier–Stokes equations under some simplifications (assumption of the MEMS oscillator as a chain of spheres/discs [26,27]). The result of these theories is a viscous quality factor exhibiting a dependency to the reciprocal square root of the external pressure:

$$Q_{\text{vis}} = \frac{\zeta_{\text{vis}}(h)}{\sqrt{p}}. \quad (8)$$

The fit parameter ζ_{vis} [bar^{0.5}] combines the influence of the geometry, the gas atmosphere, and temperature on the viscous quality factor. Dependence of the quality factor on the gap width is not covered by any of these works, except for the squeeze film regime, and is therefore specifically investigated in our work.

The transitional flow regime in-between the two previously presented flow regimes can be described by the resonance effect of thermal waves. The quality factor is described by a parabola-shaped function with a vertex located at the thermal wave resonance point where the mechanical resonance frequency f_n , matches with the thermal frequency of the gas locked within the gap width f_{th} . Here, the thermal frequency of the gas depends on its thermal diffusivity, which is changed by the external pressure, as well as on the adjusted gap width. The mathematical description of the quality factor plot of the transitional flow regime is as follows:

$$Q_{\text{trans}} = \zeta_{\text{trans}}(h) \frac{f_n \cdot f_{\text{th}}}{f_n^2 + f_{\text{th}}^2}, \quad \text{with } f_{\text{th}} = \frac{B_{\text{trans}}}{\sqrt{p}}. \quad (9)$$

Further elaboration on this theory including the fit parameters ζ_{trans} [1] and B_{trans} [Hz·mbar^{0.5}] can be found in [14]. In previous works [14,25] and in Appendix B, the process

steps of the sensor fabrication and the experimental procedure of recording resonance curves for the extraction of the quality factor and resonance frequency are described.

3. FEM Simulations

In addition to the analytical description and the experimental investigation of the MEMS oscillators, finite element (FEM) simulations were performed for modeling the temperature and pressure distribution within the gap caused by the oscillator movement and also for determining the thickness of the oscillator.

In the oscillator manufacturing process, the thickness of the oscillators is determined by a time-controlled wet chemical etching process in a KOH solution. This process is affected by variations on the order of $\pm 3 \mu\text{m}$ in the targeted oscillator thickness. For this reason, the thickness is determined numerically in COMSOL Multiphysics 5.4 with the solid mechanics' module using an eigenfrequency study of the MEMS oscillator [28]. The exact thickness of one micro-oscillator structure was measured by scanning electron microscopy (SEM). For this method of investigation, however, a thin Au layer is necessary for the conduction of the electrons, after which the oscillator is no longer suitable for further measurements. As an example, an SEM image is attached in Appendix A (see Figure A1d) and confirms the range of thickness of the micro-oscillators.

The pressure and temperature distribution within the gap are modeled by coupling the oscillator movement with the surrounding fluid using an adiabatic and no-slip boundary condition. The geometrical boundary at the top is a fixed plate placed in a defined spacing from the micro-oscillator. It possesses a nearly infinite heat capacity (relative to the amount of heat produced by the micro-oscillator movement) and is therefore modeled by an isothermal wall. Towards the bottom, the micro-oscillator is not confined, which is represented by the spherical wave radiation boundary condition. The behavior of the fluid is described by a linearized Navier–Stokes equation, which is valid for the continuum regime ($Kn < 0.1$). Furthermore, we use the continuity equation and the energy equation for fluids. The complete set of equations can be found in [14].

As a result, we obtain the pressure distribution and temperature distribution within the gap for the individual bending modes and geometric shapes. No significant difference between the distributions of the individual geometric shapes PO, BO, and CO is observed. Therefore, we only illustrate the distributions of a CO structure for the first three bending modes.

Figure 2a indicates a pressure increase Δp as well as the resulting temperature rise ΔT within the gap due to the compression by the MEMS oscillator. Correspondingly, the same behavior in the opposite direction (expansion leading to pressure and temperature drop) can be observed on the bottom side. Furthermore, an asymmetry between the upper and the lower side is significant due to the spatial limitation of the gap towards the top. This asymmetry in the distributions decreases with increasing mode number and disappears almost completely up to the 3rd BM. From this, it can be concluded that the range of an interaction of the oscillator with a spatial boundary decreases with the mode number, respectively, with the resonance frequency.

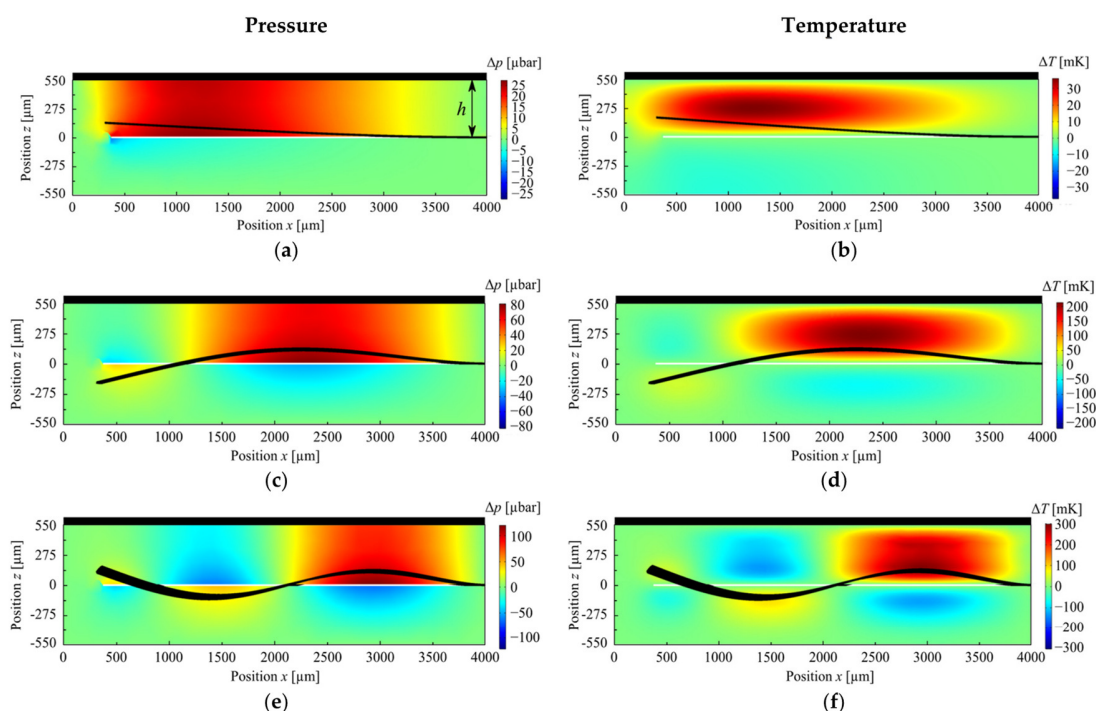


Figure 2. FEM-simulated pressure and temperature distribution for CO1 (cf. Table 1) at a gap width of 550 μm . In (a,c,e), the pressure distribution of the 1st, 2nd, and 3rd BM is displayed, respectively. In (b,d,f), the corresponding temperature distribution of the 1st, 2nd, and 3rd BM is shown. The ambient values are indicated by a green color. Deviations to the top are shown by red, or to the bottom by blue. The oscillator deflection (black) of the bending mode is shown enlarged and not to scale.

4. Experimental Results

Figure 3 shows a composition of the experimentally-measured quality factor Q_{exp} consisting of the individual damping components, according to the theory section. The data show the quality factor plots for the 1st BM of the three different geometries and the 3rd BM of sensor BO for a gap width of 550 μm in a nitrogen atmosphere.

The fitting of the composition of the four different damping mechanisms was performed by a LabView nonlinear fitting tool. The quality of the fitting procedure was ensured by the coefficient of determination R^2 which was exceeding the value of 0.99 for all cases ($R^2 = 1$ is representing a perfect match between the experimental data and the theoretical fit.) The relative deviation of the fit model to the experimental data is in the range of 5%. Consequently, a very good agreement between the fitted quality factor Q_{fit} and the experimental data over the entire pressure range can be achieved. The extrinsic gas part of the quality factor Q_{gas} is calculated by subtracting the intrinsic damping and then is inserted additionally. Subsequently, for each gap width and mode, a set of parameters is obtained.

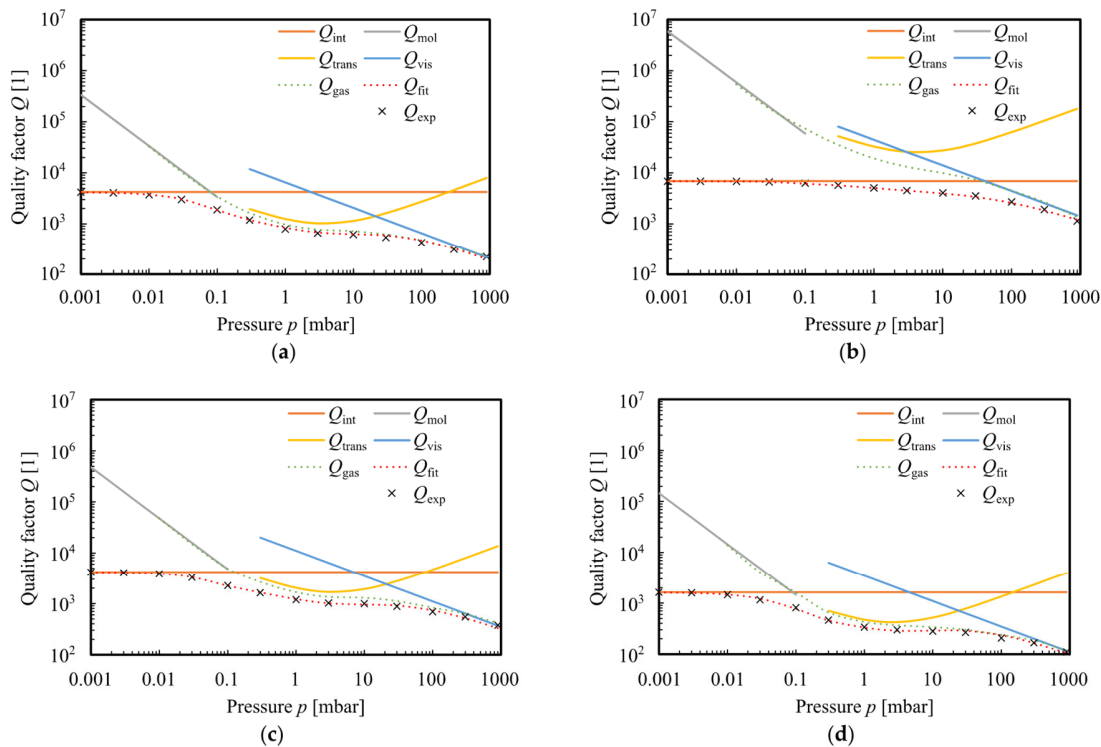


Figure 3. Reconstruction of the experimentally-measured quality factor plot Q_{exp} as function of the ambient pressure. The total quality factor Q_{fit} is composed of the individual damping mechanisms and shows very good agreement over the entire range from molecular to viscous flow regime for the 1st BM (a) and for the 3rd BM (b) of MEMS oscillator BO3 as well as for the 1st BM of the micro-oscillators PO1 (c) and CO1_33 (d). The data are measured at a gap width $h = 550 \mu\text{m}$ in an N_2 atmosphere.

In Figure 4a, the quality factor plot of micro-oscillator BO3 is depicted for the fundamental BM and the next higher bending modes up to a mode number of $n = 5$. The strong decrease in the quality factor of the first BM in the medium pressure range is particularly noticeable. This is due to the stronger damping in the molecular flow regime (up to $p = 0.1$ mbar) and due to the high thermal losses in the transitional flow regime caused by standing thermal waves [14]. The first bending mode also has the largest oscillation amplitude, which results in a stronger interaction with the surrounding gas atmosphere and, accordingly, to larger damping losses. The strength of the damping decreases with the mode number and is mainly visible in the viscous flow regime. For mode 5, the intrinsic damping is very pronounced, which leads to a masking of the extrinsic damping losses.

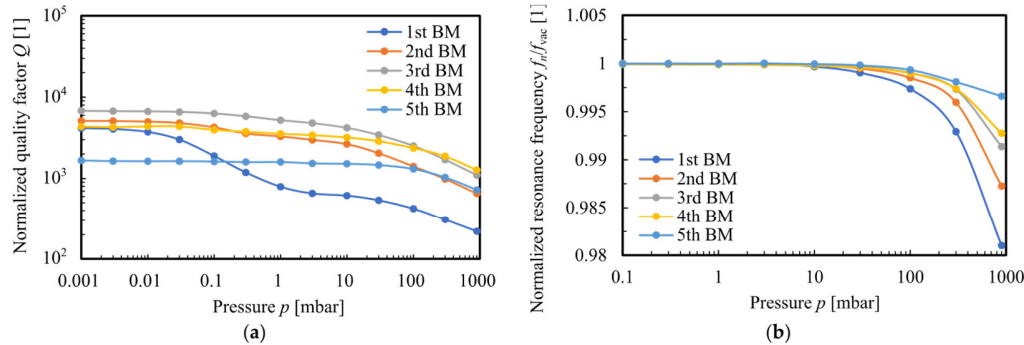


Figure 4. Quality factor plot (a) and normalized resonance frequency plot (b) as function of the ambient pressure of MEMS oscillator BO3 for the first five bending modes. The resonance frequency is normalized on the high vacuum value (at $p = 0.001$ mbar). All data are recorded for a gap width of $h = 550$ μm in an N_2 atmosphere.

For all bending modes, the strong damping in the viscous flow regime is common, which leads to a decrease in the quality factor as well as to a reduction of the resonance frequency (see Figure 4b). The highest shift of the resonance frequency due to the strongest damping can also be seen in the 1st BM. The other modes are sorted according to the mode number.

In addition to the quality factor, the resonance frequency of the fundamental mode, as well as the higher bending modes of the MEMS oscillators, are investigated. The frequencies are measured in the vacuum range at 0.001 mbar and then associated with the bending modes using a laser Doppler vibrometer. Besides the bending modes there are other modes, such as torsional oscillations or more complex roof-tile-shaped modes, which are not considered in this work. All electrically-measured bending modes are summarized in Appendix C. Based on the fundamental mode, the thickness of the MEMS oscillator is derived by means of FEM simulation. The results are shown in Table 1. The MEMS oscillators BO1, BO2, BO3, PO1, and PO2 were fabricated on a wafer with a target thickness of 20 μm and the CO structures on a second wafer with a target thickness of 10 μm . These thickness values could be found numerically and are in the range of the variations of the etching process.

Table 1. Listing of all investigated MEMS oscillator geometries and their dimensions. The thickness T is obtained from numerical simulations and the scale factor α is determined by applying best fit method of Equation (3) to resonance frequency plot shown in Figure 5. The Young's modulus $E_{\text{Si}} = 130$ GPa and density $\rho_{\text{Si}} = 2.330$ g/cm³ are taken from [29].

Name	L_{O} [μm]	B_{O} [μm]	L_{B} [μm]	B_{B} [μm]	T [μm]	α [1]
BO1	1200	2400	2400	600	24.5	0.36
BO2	1800	2400	1800	600	24	0.27
BO3	2400	1800	1200	600	17	0.47
PO1	1200	2400	2400	600	24	0.45
PO1_100 ¹	1200	2400	2400	600	21	0.30
PO2	1800	2400	1800	600	27	0.34
PO2_100 ¹	1800	2400	1800	600	27	0.30
CO1_33 ¹	3600	2400	-	-	12	0.84
CO1_50 ¹	3600	2400	-	-	12	0.58
CO1_100 ¹	3600	2400	-	-	8.5	0.61
CO2_33 ¹	3600	1800	-	-	12	0.95
CO2_100 ¹	3600	1800	-	-	9	0.67

¹ The value is indicating the percentage of coverage of the oscillator surface [30].

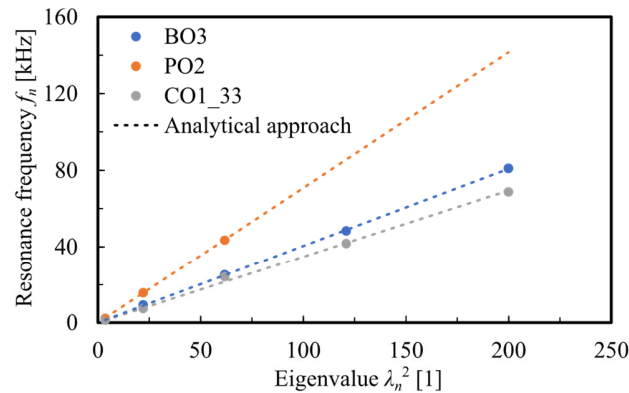


Figure 5. Exemplary resonance frequency plot of three oscillator geometries dependent on the eigenvalue. Additionally, the analytical calculation according to Equation (3) is included, which shows a very good agreement. Mode 4 and 5 of micro-oscillator PO2 were electrically not measurable with the piezoelectric elements because the deflection is not in the area of the sensing patches.

In the following, the resonance frequencies of the fundamental mode and the higher bending modes are plotted against the squared eigenvalue λ_n . By means of the scaling factor α , Equation (3) is fitted to the measurement points using the best fit method. Figure 5 shows this exemplarily for a MEMS oscillator of each geometric shape and indicates a very good agreement with the analytical approach. The determined scaling values are listed in Table 1. It is noticeable that the CO structures have the largest values. This is since the oscillator and the bending beam are congruent to each other. The dependence can also be observed on the coverage size. A larger actuator area counteracts the oscillation because the stress of the piezoelectric layer has an additional restoring effect. The smallest possible actuator area thus represents the ideal case of a fully oscillating structure.

For the BO and PO structures, on the other hand, the oscillating mass is mainly given by the oscillator plate dimension itself which is actuated via the beam structure. The larger the beam structure, the smaller the fraction of oscillating mass, after which the scale factor α decreases. Regarding the size of the coverage of the oscillator with the actuator surface, the same observation can be seen for the CO structures. The completely covered structures PO1_100 and PO2_100 show a lower scaling factor α than the regular structures PO1 and PO2.

In the following section, the determined parameters obtained by the fitting procedure shown in Figure 3 will be discussed. In Figure 6, the fitting parameters are depicted as a function of the gap width. The parameters of the individual damping mechanisms show an increase with the gap width which leads to saturation for larger values of the gap width. The molecular fit parameter ζ_{mol} has already been discussed in a previous paper [25] and is excluded in the following. The parameters of the transitional flow regime ($\zeta_{\text{trans}}, B_{\text{trans}}$) and the viscous flow regime (ζ_{vis}) are fitted with the following function which describes an upward limited growth function:

$$\zeta(h) = \zeta_{\text{sat}} \cdot \left(1 - e^{-\frac{h}{l^*}}\right). \quad (10)$$

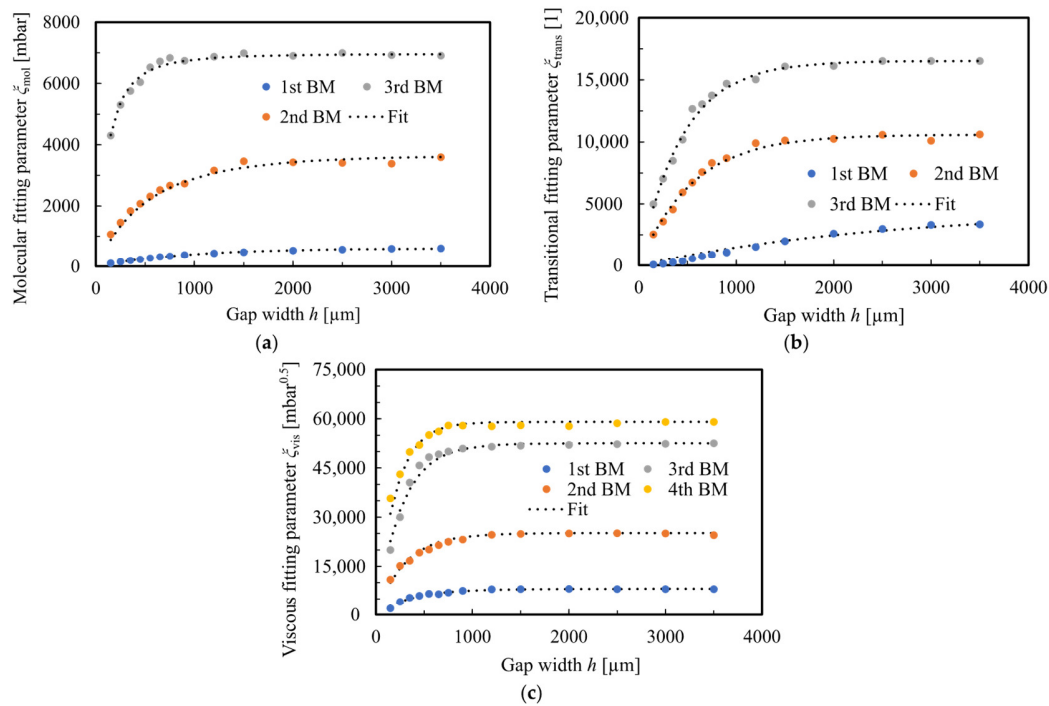


Figure 6. The determined fit parameters for MEMS oscillator BO3 of the higher bending modes as a function of the gap width. In (a) the curve is shown for the molecular fitting parameter, in (b) for the transitional fitting parameter, and in (c) for the viscous fitting parameter. Each plot was fitted by an upward limited exponential growth function to determine the characteristic length (cf. Equation (10)).

The course is determined by the saturation value ζ_{sat} , which represents the horizontal asymptote of the function and by the characteristic length l^* , which describes the speed of the increase of the gap width.

5. Discussion

By applying the generalized fit model, the quality factor plots of three different geometric shapes with different dimensions were fitted from the molecular to the viscous flow range and simultaneously for gap widths to a geometric boundary varying from 150 μm up to 3500 μm . As shown in the previous section, fit parameters were obtained that exhibit a gap width dependence, which can be described according to Equation (10). The determined quantities, the saturation value, and the characteristic length are analyzed in more detail in the following.

In Figure 7, the characteristic lengths for the viscous and thermal damping are depicted. These characteristic lengths represent the range of the interaction with the geometrical boundary. A gap width in the range of the characteristic length thereby means an increase in the quality factor by 63% ($=1 - e^{-1}$) of the saturation value of a freely oscillating structure.

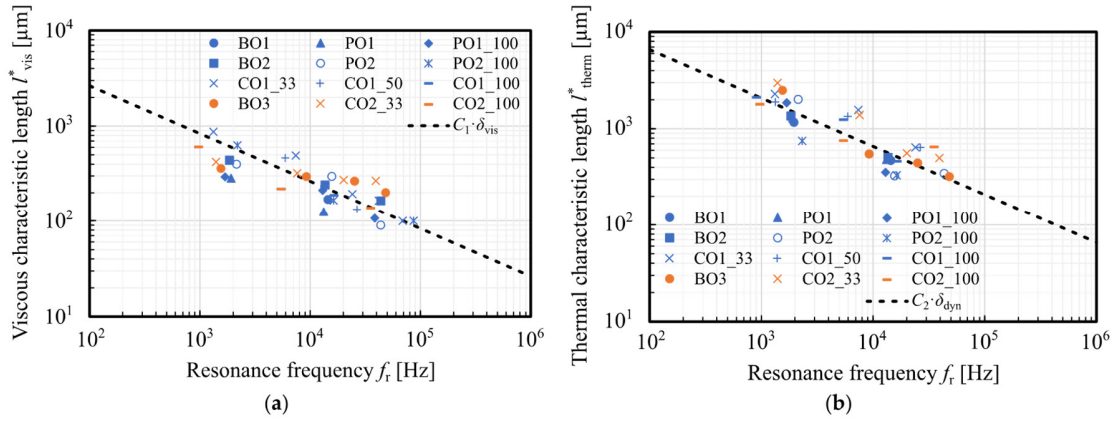


Figure 7. Determined characteristic length of the viscous damping (a) as well as of the thermodynamic damping of the transitional flow regime (b). In both cases, a multiple of the viscous or thermal boundary layer thickness is included ($C_1 = 12$, $C_2 = 25$).

At a distance larger than three times the characteristic length, the damping has dropped to 5% of the original value. Thus, knowledge of the ratio of the distance characteristic can be taken as a measure of the strength of the damping.

In Figure 7, a multiple of the viscous δ_{vis} and the thermal δ_{dyn} boundary layer thickness is inserted, which are given as a function of the frequency f by the following equations [31]:

$$\delta_{\text{vis}}(f) = \sqrt{\frac{\mu}{\pi \rho f}} \quad (11)$$

$$\delta_{\text{dyn}}(f) = \sqrt{\frac{k}{\pi \rho C_p f}} \quad (12)$$

with μ , ρ , k , C_p the dynamic viscosity, the density, the thermal conductivity, and the heat capacity at constant pressure, respectively. The gas properties for the fitting of the boundary layer thicknesses were taken from NIST [32].

For the viscous damping, we find a characteristic length l_{vis}^* in the order of $C_1 = 8$ –15 times the viscous boundary layer thickness depending on the MEMS oscillator and a mean value of 12. A similar consideration of the damping of the thermal resonance effects in the transitional flow regime yields to a thermal characteristic length l_{therm}^* in the range of $C_2 = 20$ –30 times the thermal boundary layer thickness also depending on the exact oscillator geometry with a mean value of about 25. Thus, the thermal effects are generally more long-range than the viscous losses. Furthermore, the decrease in the characteristic length with frequency is observed which agrees with the FEM simulations (*cf.* Figure 2). A higher mode or frequency interacts more short-range with a geometric boundary than the fundamental mode at a lower frequency.

At large distances, a saturation value is obtained, which represents the ideal case of free oscillatory movement without the influence of spatial constraints. In Figure 8, the saturation value for the thermal damping is illustrated. The measurement values clearly distinguish a difference between the MEMS oscillators regarding their width (Blue $B_O = 2400 \mu\text{m}$; Orange $B_O = 1800 \mu\text{m}$). The overall trend can be described by a logarithmic function which correlates with a strong decrease in the thermal damping with the frequency. Thermal resonance effects are therefore particularly pronounced at low frequencies or in the fundamental mode.

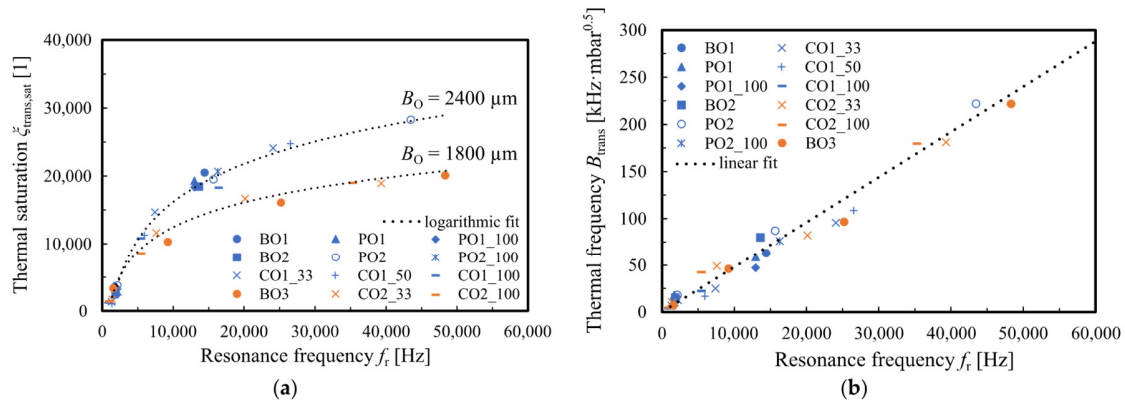


Figure 8. Saturation values of the thermodynamic damping for large gap widths determined according to Equation (10) (a). The data of the MEMS oscillators show a good agreement with a logarithmic function. The graph reveals two groups that differ in the width of the oscillators B_0 . The thermodynamic resonance frequency is determined by the fit parameter B_{dyn} which shows an almost linear trend to the resonance frequency of the oscillator (b).

The pressure-dependent factor of the thermal resonance frequency shows a linear dependence on the mechanical resonance frequency (see Figure 8b). This derives from the fact that the thermal and mechanical resonance frequencies match at a specific pressure, which we define as the thermal resonance pressure.

The viscous saturation value is predicted by various theories of a freely vibrating structure in a viscous medium. The resulting dependence of the viscous quality on the reciprocal root of the resonant frequency is plotted in Figure 9 and reflects the general trend of the measurements. The individual MEMS oscillators differed in strength from each other due to the different geometries. It is noticeable that the cantilever structures have the highest damping. The further sorting is carried out according to the size of the surface of the MEMS oscillators after which only the absolute area of interaction with the viscous medium is decisive. This is different from damping in liquids where the perimeter of the edges and thus additional slits and edges are counterproductive. According to Basak et al., additional edges lead to turbulence effects which decrease the quality factor [33].

The last point to be investigated is the intrinsic quality factor. All data are summarized in Appendix C and plotted in Figure 9b as a function of the resonance frequency. Several points are noticeable as a result. First, a larger beam structure leads to higher losses via the anchor. For this reason, the cantilever structures have the lowest intrinsic values. The BO and PO structures are sorted by their beam width. On the other hand, larger piezoelectric actuator films also have a negative effect on intrinsic quality. Up to a frequency of about 30 kHz, the quality factor increases approximately linearly with resonance frequency for all structures. At higher frequencies, the thermoelastic damping mechanism is dominant, which leads to a decrease in the intrinsic Q-factor [34]. In general, it can be concluded that the intrinsic quality factor can be improved with the smallest possible actuator area and minimal anchor structures.

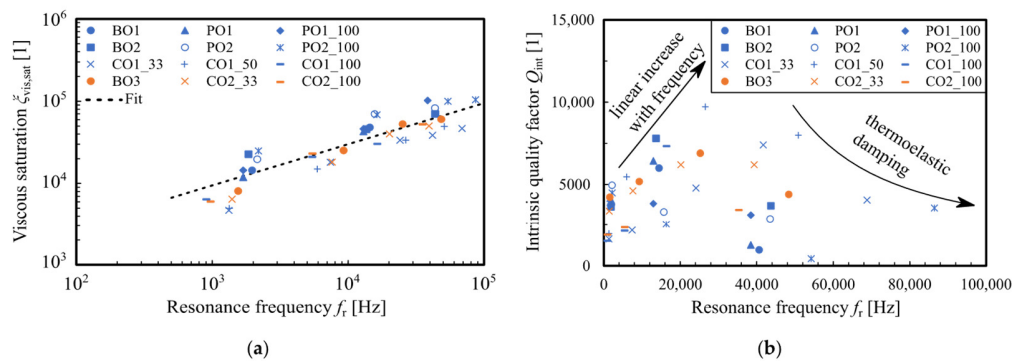


Figure 9. Viscous saturation values for large gaps of all investigated MEMS oscillators as a function of resonance frequency (a). The plotted fit line shows the dependence of the quality factor on the frequency in the viscous flow regime according to Equation (8). In (b), the intrinsic quality factors of all MEMS oscillators as well as all determined bending modes measured in the high vacuum range at a pressure level of 0.001 mbar are shown.

6. Conclusions

A generalized damping model based on the literature results for individual damping mechanisms was presented. First, an analytical description of the resonance frequency was presented, which is in good agreement with the experimental results for all considered geometries and allows numerical determination of the thickness T . The quality factor could be reproduced by superposition of four components for the three different oscillator geometries (BO, PO, CO) over six orders of magnitude of the Knudsen number Kn . The results of the fitting procedure were further analyzed and interpreted using FEM simulations. From these results, the pressure and temperature distributions within the gap caused by the micro-oscillator movement were obtained. The thermal and viscous interaction with the boundary was visualized and a decrease in the range of the effects with the resonance frequency and the mode number was observed. The decrease in the influence of the damping phenomena was also found experimentally and described with a saturation behavior, from which a characteristic length was obtained, which was used for the estimation of the range of the effects. From these results, indications for reducing the damping were found, thus giving opportunities for increasing the quality factor. Furthermore, the influence of a geometrical boundary due to the package or the mounting can be predicted. The results are briefly summarized below:

- The range of viscous damping is about 8–15 times the viscous boundary layer thickness.
- The measure of the strength is the surface which interacts with the viscous fluid and decreases with the resonance frequency.
- The range of thermal effects in the transitional flow regime is about 20–30 times the thermal boundary layer thickness.
- Exponential decreasing of thermal damping effects occurs with an increase in resonance frequency.
- The thermal resonance frequency of the gas depends linearly on the mechanical resonance frequency of the micro-oscillator.
- The intrinsic quality factor of the fundamental mode is limited by anchor losses and residual stress of the piezoelectric thin film. Therefore, the minimization of an anchor structure and the actuator area are recommended to maximize the intrinsic quality factor.
- At higher modes, thermoelastic damping is crucial, which leads to a lowering of the intrinsic quality of higher modes.

With this model, we give an approach to describing the resonance frequency and quality factor of various MEMS oscillators as well as optimization possibilities to improve the performance of piezoelectric-actuated oscillators.

Author Contributions: Investigation, T.Z.; Data curation, T.Z.; Project administration A.A. and H.S.; Funding acquisition A.A. and H.S., Writing—original draft T.Z. and H.S.; Writing—review and editing, T.Z. and H.S. All authors have read and agreed to the published version of the manuscript.

Funding: This research was funded by the German Science Foundation (DFG) within the grant SE 1425/14-1.

Institutional Review Board Statement: Not applicable.

Informed Consent Statement: Not applicable.

Data Availability Statement: Data available on request.

Conflicts of Interest: The authors declare that there are no conflict of interest.

Appendix A

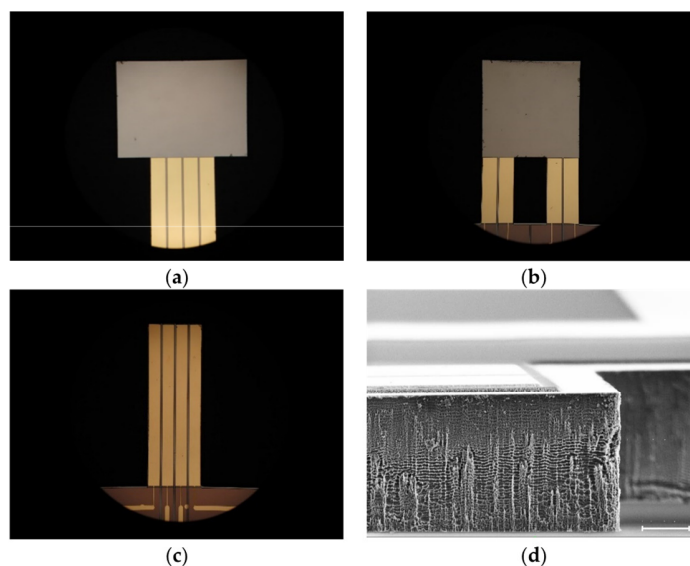


Figure A1. Microscopic image of the three different micro-oscillator structures: PO (a), BO (b), and CO (c) and a scanning electron microscope image illustrating the side view on a micro-oscillator revealing a thickness of 27 μm (d).

Appendix B

The micro-oscillators were fabricated as shown in the cross-sectional view depicted in Figure A2a. A highly p-doped 4" Si-wafer with a thickness of 525 μm was used as substrate. In the first step, SiO_2 was grown with a thickness of 120 nm on both sides for electrical insulation and as a bonding agent of the Si_3N_4 layer. The Si_3N_4 layer was deposited in a PECVD process in a thickness of 550 nm and was used as a passivation layer for the anisotropic KOH etching step to release the micro-oscillators. Both layers were structured simultaneously in a 6% HF solution. Next, the piezoelectric thin film was deposited in a reactive sputter deposition process in a thickness of 1100 nm and etched with phosphoric acid solution after a photolithographic structuring step. Subsequently, the piezoelectric elements are connected with a 500 nm thick Au layer using a DC sputtering process. The Au film is structured by an etching step with aqua regia. Afterward, the micro-oscillators

are released in a two-step process. Firstly, a thin membrane is etched anisotropically from the backside in a KOH etching solution, and released by a DRIE step (Bosch-process) from the top side. Before the DRIE process, the KOH cavities are filled with photoresists to mechanically stabilize the oscillator and to stop the DRIE etching process. The photoresist is removed after the dicing of the wafer within the cleaning process of the individual chips. Finally, the micro-oscillators are glued on PCB-boards to contact them electrically via Au bond wires. The PCB boards are drilled in advance at the locations of the micro-oscillator so that they are not confined to the bottom.

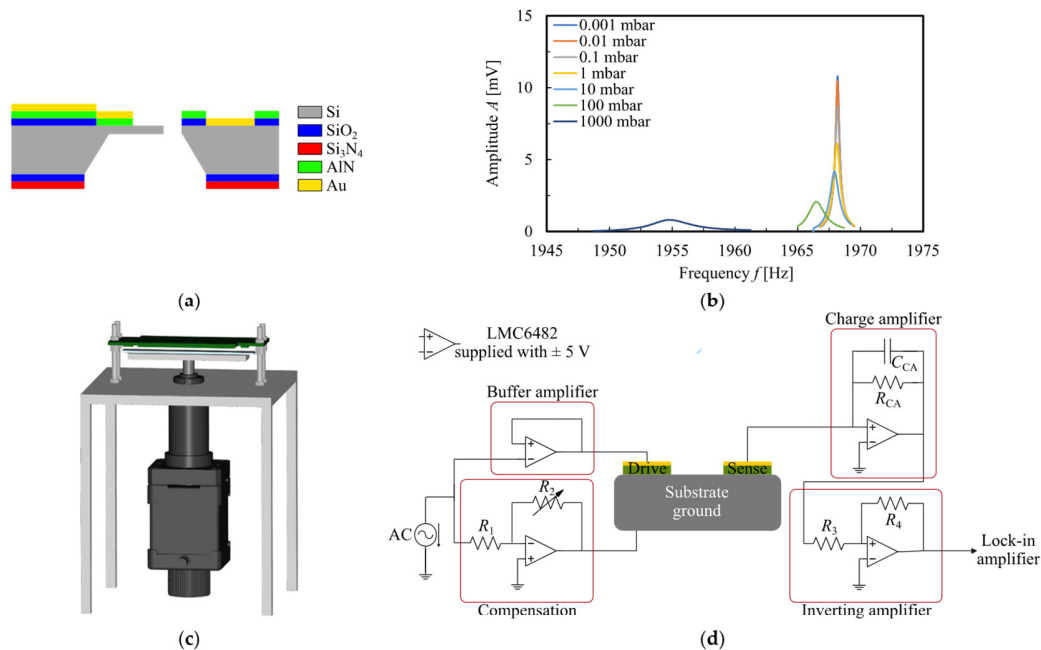


Figure A2. Cross-sectional view on a micro-oscillator (layer thickness are not to scale) (a), and recorded resonance curves of BO1 (b) for various ambient pressure levels. In (c), the construction for adjusting the gap width to the neighboring plate is depicted, and in (d) the electric circuit for the actuation and detection of the micro-oscillators.

The quality factor and resonance frequency of the micro-oscillators as shown in Figures 3–5 are measured by recording the resonance curves shown in Figure A2b for various ambient pressure conditions. Therefore, the micro-oscillators are placed in a vacuum chamber ranging from 10^{-3} mbar up to 900 mbar. Additionally, the PCB board containing four micro-oscillators is built in a construction shown schematically in Figure A2c to adjust the gap width to the neighboring plate. The distance between the plate and the micro-oscillator is initially calibrated with two cooper gauge blocks with a defined thickness of 800 μm . The actuation of the micro-oscillator and the sensing of the oscillation are achieved with the electric circuit illustrated in Figure A2d. The micro-oscillators are actuated with a sinusoidal signal with an amplitude of 1 V which is decoupled by a buffer amplifier. The electrical crosstalk between actuation and sensing is compensated by a shift of the substrate ground [35]. The amplitude of the oscillation movement is measured by collecting the charge of the sensing elements with a charge amplifier which amplifies the signal and converts it in the range of a few μV . Finally, this signal is lifted to several mV by an inverting amplifier. Then, the actuation and sensing signal is compared by a lock-in amplifier and evaluated regarding their amplitude and phase.

Appendix C

Name	L_O [μm]	B_O [μm]	L_B [μm]	B_B [μm]	T [μm]	α [1]	Mode	f_n [kHz]	Q_{int} [1]
BO1	1200	2400	2400	600	24.5	0.36	1st BM	1.97	3805
							2nd BM	14.3	6002
							3rd BM	40.6	965
BO2	1800	2400	1800	600	24	0.27	1st BM	1.85	3640
							2nd BM	13.6	7800
							3rd BM	43.7	3704
BO3	2400	1800	1200	600	17	0.47	1st BM	1.55	4230
							2nd BM	9.24	5175
							3rd BM	25.2	6905
							4th BM	48.3	4402
PO1	1200	2400	2400	600	24	0.45	1st BM	1.92	4170
							2nd BM	13.2	6436
							4th BM	69.7	1272
PO1_100	1200	2400	2400	600	21	0.30	1st BM	1.69	3722
							2nd BM	13.0	3832
							3rd BM	38.4	3133
PO2	1800	2400	1800	600	27	0.34	1st BM	2.15	4951
							2nd BM	15.7	3326
							3rd BM	43.4	2898
PO2_100	1800	2400	1800	600	27	0.30	1st BM	2.11	4488
							2nd BM	16.3	2555
							3rd BM	54.2	431
							4th BM	86.4	3571
CO1_33	3600	2400	-	-	12	0.84	1st BM	1.33	1635
							2nd BM	7.40	2174
							3rd BM	24.1	4781
							4th BM	41.7	7404
							5th BM	68.8	4050
CO1_50	3600	2400	-	-	12	0.58	1st BM	1.34	1956
							2nd BM	5.94	5459
							3rd BM	26.5	9718
							4th BM	50.9	7995
CO1_100	3600	2400	-	-	8.5	0.61	1st BM	0.90	1519
							2nd BM	5.45	2140
							3rd BM	16.4	7337
							4th BM	34.8	4002
CO2_33	3600	1800	-	-	12	0.95	1st BM	1.40	3371
							2nd BM	7.59	4614
							3rd BM	20.2	6199
							4th BM	39.3	6198
CO2_100	3600	1800	-	-	9	0.67	1st BM	0.97	1896
							2nd BM	5.47	2350
							4th BM	35.3	3448

References

1. Pillai, G.; Li, S. Piezoelectric MEMS resonators: A review. *IEEE Sens. J.* **2021**, *21*, 12589–12605. [[CrossRef](#)]
2. Weng, C.; Pillai, G.; Li, S. A thin-film piezoelectric-on-Silicon MEMS oscillator for mass sensing applications. *IEEE Sens. J.* **2020**, *12*, 7001–7009. [[CrossRef](#)]
3. Zengerle, T.; Stopp, M.; Ababneh, A.; Seidel, H. Using the nonlinear Duffing effect of piezoelectric micro-oscillators for wide-range pressure sensing. *Actuators* **2021**, *10*, 172. [[CrossRef](#)]
4. Ruiz-Diez, V.; Toledo, J.; Hernando-Garcia, J.; Ababneh, A.; Seidel, H.; Sanchez-Rojas, J. A geometrical study on the roof tile-shaped modes in AlN-based piezoelectric microcantilevers as viscosity–density sensors. *Sensors* **2019**, *19*, 658. [[CrossRef](#)]
5. van Beek, J.; Puers, R. A review of MEMS oscillators for frequency reference and timing applications. *J. Micromech. Microeng.* **2012**, *22*, 1–35. [[CrossRef](#)]
6. Kim, B.; Melamud, R.; Candler, R.; Hopcroft, A.; Jha, C.; Chandorkar, S.; Kenny, T. Encapsulated MEMS resonators—A technology path for MEMS into frequency control applications. In Proceedings of the IEEE International Frequency Control Symposium, Newport Beach, CA, USA, 1–4 June 2010; pp. 1–4.
7. Tu, C.; Lee, J.; Zhang, X. Dissipation analysis methods and Q-enhancement strategies in piezoelectric MEMS laterally vibrating resonators: A review. *Sensors* **2020**, *20*, 4978. [[CrossRef](#)] [[PubMed](#)]
8. Xu, C.; Piazza, G. Active boost in the quality factor of an AlN MEMS resonator up to 165,000. In Proceedings of the IEEE 32nd International Conference on Micro Electro Mechanical Systems (MEMS), Seoul, South Korea, 27–31 January 2019; pp. 907–910.
9. Haider, S.; Saleem, M.; Ahmed, M. Effect of environmental conditions and geometric parameters on the squeeze film damping in RF-MEMS switches. *AICPEF* **2019**, *100*, 357–368. [[CrossRef](#)]
10. Patocka, F.; Schneidhofer, C.; Dörr, N.; Schneider, M.; Schmid, U. Novel resonant MEMS sensor for the detection of particles with dielectric properties in aged lubricating oils. *Sens. Actuators A* **2020**, *315*, 112290. [[CrossRef](#)]
11. Kim, B.; Melamud, R.; Candler, R.; Hopcroft, M.; Kenny, T. MEMS packaging for reliable resonators and oscillators. In Proceedings of the IEEE/MTT-S International Microwave Symposium, Montreal, QC, Canada, 17–22 June 2012; pp. 1–3.
12. Brown, J.; Lutz, M.; Partridge, A.; Gupta, P.; Radza, E. MEMS as low-cost high-volume semiconductor solutions: It's all in the packaging and assembly. *SPIE MOEMS-MEMS* **2008**, *6884*, 183–188.
13. Karniadakis, G.; Beskok, A.; Aluru, A. *Microflows and Nanoflows: Fundamentals and Simulation*, 1st ed.; Springer: New York, NY, USA, 2005.
14. Zengerle, T.; Joppich, J.; Schwarz, P.; Ababneh, A.; Seidel, H. Modeling the damping mechanism of MEMS oscillators in the transitional flow regime with thermal waves. *Sens. Actuators A* **2020**, *311*, 112068. [[CrossRef](#)]
15. Alrasheed, S. Oscillatory motion. In *Principles of Mechanics*, 1st ed.; Springer International Publishing: Cham, Switzerland, 2019; pp. 155–171.
16. Young, W.; Budynas, R. *Roark's Formulas for Stress and Strain*, 7th ed.; McGraw-Hill Professional: New York, NY, USA, 2001; pp. 799–812.
17. Boisen, A.; Dohn, S.; Keller, S.; Schmid, S.; Tenje, M. Cantilever-like micromechanical sensors. *Rep. Prog. Phys.* **2011**, *74*, 3. [[CrossRef](#)]
18. Timoshenko, S.; Young, D.; Weaver, W. *Vibration Problems in Engineering*, 4th ed.; Wiley: New York, NY, USA, 1974.
19. Petersan, P.; Anlage, S. Measurement of resonant frequency and quality factor of microwave resonators: Comparison of methods. *J. Appl. Phys.* **1998**, *84*, 3392–4002. [[CrossRef](#)]
20. Rodriguez, J.; Chandorkar, S.; Glaze, G.; Gerrard, D.; Chen, Y.; Heinz, D.; Flader, I.; Kenny, T. Direct detection of anchor damping in MEMS tuning fork resonators. *J. Microelectromech. Syst.* **2018**, *27*, 800–809. [[CrossRef](#)]
21. Qiu, H.; Ababneh, A.; Feili, D.; Wu, X.; Seidel, H. Analysis of intrinsic damping in vibrating piezoelectric microcantilevers. *Microsyst. Technol.* **2016**, *22*, 2017–2025. [[CrossRef](#)]
22. Zener, C. Internal friction in solids: II. General theory of thermoelastic internal friction. *Phys. Rev.* **1937**, *53*, 90–99. [[CrossRef](#)]
23. Christian, R. The theory of oscillating-vane vacuum gauges. *Vacuum* **1966**, *16*, 175–178. [[CrossRef](#)]
24. Bao, M.; Yang, H.; Yin, H.; Sun, Y. Energy transfer model for squeeze-film air damping in low vacuum. *J. Micromech. Microeng.* **2002**, *12*, 341–346. [[CrossRef](#)]
25. Zengerle, T.; Joppich, J.; Schwarz, P.; Ababneh, A.; Seidel, H. Polyatomic degrees of freedom and their temporal evolution extracted from the damping of micro-oscillators. *Sens. Actuators A* **2019**, *297*, 111460. [[CrossRef](#)]
26. Kokubun, K.; Hirata, M.; Ono, M.; Murakami, H.; Toda, Y. Unified formula describing the impedance dependence of a quartz oscillator on gas pressure. *J. Vac. Sci. Technol. A* **1987**, *5*, 2450–2453. [[CrossRef](#)]
27. Blom, F.; Bouwstra, S.; Elwenspoek, M.; Fluitman, J. Dependence of the quality factor of micromachined silicon beam. *J. Vac. Sci. Technol. B* **1992**, *10*, 341–346. [[CrossRef](#)]
28. Kurmendra, S.; Kumar, R. Design analysis, modeling and simulation of novel rectangular cantilever beam for MEMS sensors and energy harvesting applications. *Int. J. Inf. Technol.* **2017**, *9*, 295–302. [[CrossRef](#)]
29. Hopcroft, M.; Nix, W.; Kenny, T. What is the Young's modulus of silicon? *J. Microelectromech. Syst.* **2010**, *3*, 229–238. [[CrossRef](#)]
30. Zengerle, T.; Stopp, M.; Ababneh, A.; Seidel, H. Investigations on nonlinearities of roof tile-shape modes for pressure measurement applications. In Proceedings of the 21st International Conference on Solid-State Sensors, Actuators and Microsystems (Transducers), Orlando, FL, USA, 20–24 June 2021; pp. 1343–1346.

31. Qiu, H.; Seidel, H. Hydrodynamic loading on vibrating piezoelectric microresonators. In *Piezoelectricity—Organic and Inorganic Materials and Applications*, 1st ed.; IntechOpen Limited: London, UK, 2018; pp. 43–64.
32. Lemmon, E.; McLinden, M.; Friend, D. Thermophysical Properties of Fluid Systems NIST. 1998. Available online: <https://webbook.nist.gov/chemistry/fluid/> (accessed on 10 February 2022).
33. Basak, S.; Raman, A.; Garimella, S. Hydrodynamic loading of microcantilevers vibrating in viscous fluids. *J. Appl. Phys.* **2006**, *99*, 114906. [[CrossRef](#)]
34. Duwel, A.; Candler, R.; Kenny, T.; Varghese, M. Engineering MEMS resonators with low thermoelastic damping. *J. Microelectromech. Syst.* **2006**, *15*, 1437–1445. [[CrossRef](#)]
35. Qiu, H.; Schwarz, P.; Völlm, H.; Feili, D.; Wu, X.; Seidel, H. Electrical crosstalk in two-port piezoelectric resonators and compensation solutions. *J. Micromech. Microeng.* **2013**, *23*, 4. [[CrossRef](#)]

6.5 Lumped Element Model

6.5.1 Equivalent Circuit

The use of equivalent circuit models to represent complex physical problems is found frequently in the literature [134]. The idea of using a lumped element model is based on a simplification of the problem by replacing physical mechanisms with electronic components within an electrical network. Thus, our three-dimensional problem, which must be solved with the Navier-Stokes equations (see Section 3.2) can be solved in a much simpler methodology. By reducing the problem into an analogous electrical network, a comparatively easier calculation by means of analytical expressions or Spice methods is possible [135]. Exemplary is the description of an optimization study of an energy harvesting module [136]. In particular interesting is the description of the squeeze-film effect of MEMS oscillators by Veijola *et al.* [88]. The lumped element model of Veijola is based on a parallel circuit of resistive-inductive R-L elements, which take into account both the viscous friction losses and the spring effect of the squeezed gas.

In the study presented below, a much larger range than just the squeeze film range is to be covered by the lumped element model for both the gap width and the pressure. The equivalent circuit represents the quality factor plot from the vacuum range up to atmospheric pressure for gap widths from 150 μm to 3500 μm . This corresponds to a Knudsen range of seven orders of magnitude from $Kn = 100$ to 10^{-4} . The analogies listed in Table 9 are used to describe the individual physical dissipation mechanisms. In addition to the usual resistance and inductive elements, an inductive constant phase element (CPE) is introduced. Constant phase elements themselves have been introduced in the literature to describe imperfect capacitances in impedance spectroscopy analysis [137]. In the present case, however, we are dealing with collision processes between gas molecules and the oscillator, which requires inductive elements for the transfer of kinetic energy. Therefore, an inductive constant phase element is introduced which is currently discussed in the literature [138]. Overall, the previously presented physical based damping model is transformed into an equivalent circuit, covering the individual loss effects. The dissipation mechanisms are translated into electrical components, resistors and inductors as well as combinations of them.

Table 9. List of the electro-mechanical analogies applied for the representation of the individual dissipation mechanisms with electrical components and networks.

Electric component	Representation
Resistor R	Mechanical dissipation/Viscous Friction
Inductor L	Kinetic energy (single collision process)
Inductive constant phase element CPE_L	Kinetic energy (collision processes)
Impedance Z	Measure for losses/ Damping D
Admittance Y	Measure for lossless/ Quality factor Q
Frequency ω	Measure of the number of collisions

6.5.2 *Addendum V*

IOP Publishing

Journal of Micromechanics and Microengineering

J. Micromech. Microeng. 31 (2021) 095010 (10pp)

<https://doi.org/10.1088/1361-6439/ac1a51>

Equivalent circuit model for the damping of micro-oscillators from molecular to viscous flow regime

T Zengerle^{1,*} , J Joppich², H Lensch², A Ababneh^{1,3}  and H Seidel¹ ¹ Chair of Micromechanics, Microfluidics and Microactuators, Saarland University, Campus A5.1, 66123 Saarbrücken, Germany² Lab for Measurement Technology, Department of Mechatronics Engineering, Saarland University, Campus A5.1, 66123 Saarbrücken, Germany³ Electronic Engineering Department, Hijjawi Faculty for Engineering Tech., Yarmouk University, Irbid 21163, JordanE-mail: t.zengerle@lmm.uni-saarland.de

Received 14 June 2021, revised 15 July 2021

Accepted for publication 3 August 2021

Published 18 August 2021



CrossMark

Abstract

This paper presents an equivalent circuit (EQC) model for describing the damping mechanism of micro-oscillators from the molecular flow regime up to the viscous flow regime. The EQC model consists of two parallel lines, representing the molecular and the viscous damping mechanism, respectively. The molecular line consists of an R–L circuit, which describes the intrinsic losses and the transfer of kinetic energy from the micro-oscillator to the surrounding gas molecules. The viscous line is formed by a resistor and a newly introduced inductive constant phase element. These elements represent the thermoviscous losses and the collision processes in the viscous flow regime. This EQC model was applied to the first fundamental bending mode of an oscillator vibrating in seven different types of gases (He, Ne, Ar, N₂, CO₂, N₂O, SF₆) as well as to the first five bending modes for another type of oscillator vibrating in nitrogen gas, only. In all cases, variations of an adjustable gap width to a fixed plate in the range of 150–3500 μm were also taken into account. The results from the presented EQC model are found to be in excellent agreement with the experimental data. Additionally, the electronic components of the EQC can be correlated to real physical properties of the setup, i.e. to the viscosity and density of the gas, as well as to the adjusted gap width and to the resonance frequency of the micro-oscillator. This allows the prediction of the quality factor curve of an oscillator over a large pressure range in a simple way for various configurations, concerning gas type, gap width, and bending mode/resonance frequency. Based on these results, an optimization model and design rules for enhancing the quality factor were derived.

Keywords: equivalent circuit model, viscous damping, molecular damping, micro-oscillator, aluminium nitride

(Some figures may appear in colour only in the online journal)

1. Introduction

The quality factor Q of micromechanical oscillators is a critical parameter in a number of applications [1]. This factor is defined by the damping mechanisms which are strongly

influenced by the surrounding medium and varies from ultra-high vacuum to atmospheric pressure in scanning probe microscopy and from pure gases to liquid solutions in biological investigations [2–5]. In many cases, damping is the limiting factor for the resolution as well as for the bandwidth of sensors [6]. The prediction of the attenuation is therefore an important factor in the design of efficient devices based

* Author to whom any correspondence should be addressed.

on micromechanical oscillators [7, 8]. One possibility is the use of numerical finite element methods (FEM) simulations based on the Navier–Stokes equation [9]. The solution of this numerical problem requires a considerable amount of computing power, especially for 3D problems, and is very time consuming for a variation of parameters within an optimization study. A first step to simplify this task is the development of a lumped element model which can be solved with less complex methods (e.g. LTSpice, PSpice, etc) [10–12]. This was successfully done by Veijola *et al* for the squeeze film damping of microelectromechanical systems (MEMS) devices [13–15]. The authors show that the simplified equivalent circuit (EQC) models are in a good agreement with the experimental data for the frequency response of MEMS devices. This significant simplification of the complexity of the problem allows a prediction of the behaviour of MEMS devices in a much more efficient way and with less computational effort.

This paper follows a similar simplification approach based on lumped elements. Thus, we present an EQC model which describes the damping of a micromechanical oscillator for the fundamental mode and for higher bending modes in a much wider perspective, ranging from the molecular to the viscous flow regime. When comparing with experimental data, the maximum deviation we found was 10%. The EQC was applied to six different types of gases for the fundamental mode and, as a result, physical quantities such as viscosity and density of the gas were correlated to model elements.

2. Theory

2.1. Damping

The damping D of micro-oscillators is quantified by the quality factor Q , which is defined as ratio of the stored energy E to the energy loss ΔE per cycle:

$$Q = \frac{1}{2D} = \frac{E}{\Delta E} = \frac{f_{\text{res}}}{\Delta f_{3\text{dB}}} = \frac{\pi f_{\text{res}}}{\ln(2)} \tau, \quad (1)$$

and is either measured by the ratio of the mechanical resonance frequency f_{res} to the 3 dB bandwidth $\Delta f_{3\text{dB}}$, by the decay time τ with the ring down method or by fitting a Lorentzian curve [16].

In general, the overall damping D_{tot} and, thus, the correspondent quality factor Q_{tot} of a micro-oscillator is given by the superposition of several damping mechanism D_i (respectively Q_i), each of them corresponding to a certain physical phenomenon being related to the solid-state oscillator itself (intrinsic damping) or else to the surrounding gas (extrinsic damping). Thus, the total damping D_{tot} (respectively Q_{tot}) can be described by:

$$\begin{aligned} D_{\text{tot}} &= \sum_i D_i = \frac{1}{2Q_{\text{tot}}} = \sum_i \frac{1}{2Q_i} = \frac{1}{2} \left(\frac{1}{Q_{\text{int}}} + \frac{1}{Q_{\text{gas}}} \right) \\ &= \frac{1}{2} \left(\frac{1}{Q_{\text{int}}} + \frac{1}{Q_{\text{mol}}} + \frac{1}{Q_{\text{trans}}} + \frac{1}{Q_{\text{vis}}} \right). \end{aligned} \quad (2)$$

In general, damping models for the individual phenomena and flow regimes have been developed, as well as analytical and empirical models for the most common geometries, such as the cantilever structure [17]. Intrinsic damping Q_{int} can be described by mechanical losses due to thermoelasticity, by anchor losses and by thin film damping [18, 19]. It is pressure independent and therefore provides the limiting factor in the UHV regime. In our case, the mechanical losses are mainly given by thin film damping caused by the piezoelectric aluminium nitride layer. Extrinsic damping Q_{gas} in a gas environment can be subdivided, according to the pressure region, into molecular flow damping Q_{mol} , transitional flow damping Q_{trans} and viscous regime damping Q_{vis} . The classification is based on the Knudsen number Kn which is the ratio of the mean free path to a characteristic length [20]. As an example, a combination of individual damping mechanisms (intrinsic, molecular, transitional, and viscous), fitting the measured quality factor curve, is shown in figure 1(a) [21].

2.2. Equivalent circuit (EQC) model

The EQC model for describing the damping effects of micro-oscillators from molecular flow regime up to the viscous regime can be seen in figure 2(a). The damping effects are covered by a combination of resistive and inductive elements representing dissipative effects and losses via transfer of kinetic energy to surrounding gas molecules, respectively. The functionality of each component of the EQC is listed in table 1. The physical relations of the components to the properties of the gases as well as on the gap width h and resonance frequency f_r will be deduced in the section 4. An analogous approach was presented by Veijola *et al* [12] to describe damping effects in narrow gaps (squeeze film damping). Thereby, a sequence of parallel resistors and inductors was used to describe viscous losses and a spring like behaviour between the oscillator and the enclosed gas volume, respectively. In this context, the quality factor Q (damping ratio D) which is a measure for the lossless (for the dissipative) behaviour is replaced by the admittance Y (impedance Z) of the EQC. The pressure, which indicates the number of collisions between the gas molecules and the micro-oscillator is substituted by the Laplace factor s with angular frequency ω which stands for the number of electric pulses applied to the EQC. The EQC is divided into two lines which represent the molecular flow regime ($\text{Kn} > 1$) and the viscous regime ($\text{Kn} < 0.01$). The transitional regime ($0.01 < \text{Kn} < 1$) is given by the superposition of the two lines. The lines consist of a resistive part representing dissipative effects and an inductive part covering the kinetic energy transfer due to oscillator collisions with the surrounding gas molecules. In the molecular flow regime, the resistor R_{mol} is mainly given by the mechanical intrinsic damping [18, 19]. The molecular inductor is representative for the kinetic energy losses of the micro-oscillator according to the energy transfer onto the gas molecules [22]. In good approximation, the limited number of collisions within a low

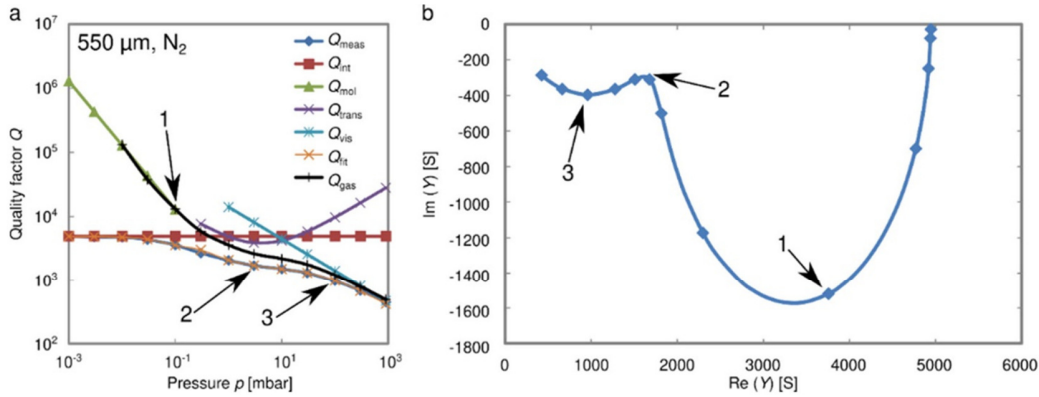


Figure 1. Example for the superposition of the quality factor of micro-oscillator 1 measured in a nitrogen atmosphere with a gap width of 550 μm (a). In (b) the corresponding Nyquist plot determined with the EQC model is shown for the same configuration (see section 4). The markers are indicating the transition from molecular to transitional flow (1), the thermal resonance of the transitional flow regime (2), and the beginning of the viscosity-dominated flow regime (3).

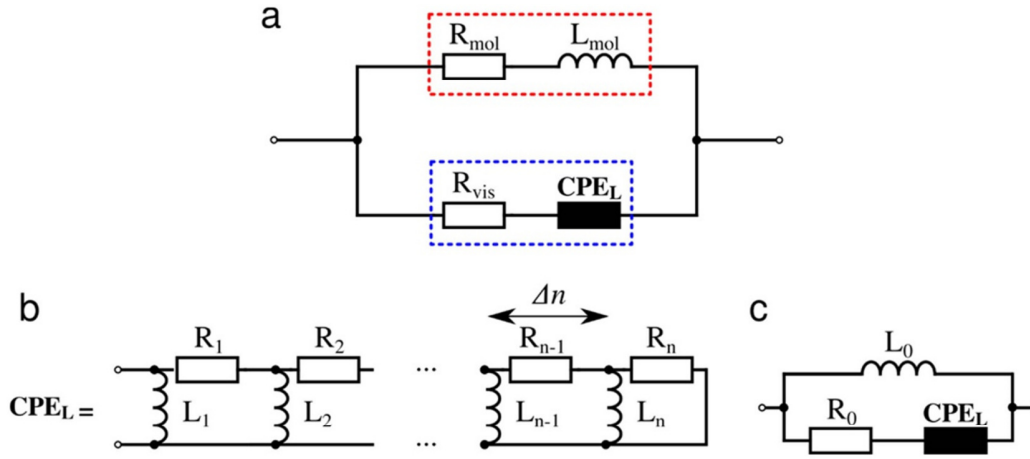


Figure 2. Proposed EQC model for the damping effects of micro-oscillators (a). In the viscous regime a newly developed device, the CPE with inductive behaviour CPE_L , is proposed. Transmission line of the CPE_L (b) and reciprocal description (c).

pressure atmosphere (low molecular density) are combined in one inductive element. In the viscous regime (high molecular density), the kinetic losses due to a series of collisions are represented in a constant phase element (CPE_L) consisting of inductive parts (see figure 2(b)) [23]. In EQC modelling, the CPE built of resistive and capacitive parts has been established for describing diffusion effects [24, 25]. The use of inductive elements instead of capacitive elements is based on the fact that collision processes involve the transfer of kinetic energy. The viscous resistance represents losses due to frictional effects of the oscillator in the viscous fluid and thermal dissipation effects due to thermal resonance effects in the transitional flow regime [26].

The transfer function in the form of the conductance Y and the impedance Z of the CPE_L depending on the Laplace factor s ($= j\omega$, with j imaginary number and ω angular frequency) is derived in the following. The

impedance of the inductive CPE can be derived by a reciprocal approach (compare figure 2(c)). Therefore, the n th part Δn of the admittance, consisting of the inductance L_0 and the resistance R_0 , is connected with the remaining inductive CPE:

$$Z_{\text{CPEL}} = \frac{1}{\frac{1}{sL_0} \Delta n + \frac{1}{R_0 \Delta n + Z_{\text{CPEL}}}}. \quad (3)$$

Consequently, the impedance of the CPE_L results in the first order approximation of Δn to:

$$Z_{\text{CPEL}} = \sqrt{R_0 L_0} s = A_{\text{vis}} \sqrt{s}. \quad (4)$$

The total admittance Y in a parallel circuit can be calculated by the sum of the parallel lines:

$$Y_{\text{tot}} = Y_{\text{mol}} + Y_{\text{vis}} \quad (5)$$

Table 1. Listing of the electric components introduced in the EQC model and their physical proportionalities to properties of the type of gas as well as to the resonance frequency of the micro-oscillators f_r and the gap width h to the boundary geometry (see section 4). δ_{therm} is indicating the thermal penetration depth [9].

Component	Function	Physical relations
R_{mol}	Solid-state damping	$s_{\text{mol}} = \frac{R_{\text{mol}}}{L_{\text{mol}}} \propto \frac{1}{\sqrt{\rho}}$
L_{mol}	Heat dissipation in molecular flow regime Collision processes in the molecular flow regime	
R_{vis}	Dissipation via viscous friction	$\propto \frac{\delta_{\text{vis}}^2}{h} \left\{ \begin{array}{l} \frac{\eta}{\rho} \\ \frac{1}{f_r} \end{array} \right.$
A_{vis}	Collision processes in the viscous flow regime Heat dissipation via thermal resonance effects	$\propto \delta_{\text{therm}} \left\{ \begin{array}{l} \sqrt{\frac{\lambda}{\rho C_p}} \\ \frac{1}{\sqrt{f_r}} \end{array} \right.$

$$Y_{\text{mol}} = \frac{1}{Z_{\text{mol}}} = \frac{1}{R_{\text{mol}} + sL_{\text{mol}}} = \frac{1/R_{\text{mol}}}{1 + s \frac{L_{\text{mol}}}{R_{\text{mol}}}}$$

$$= \frac{1/R_{\text{mol}}}{1 + \frac{s}{s_{\text{mol}}}} \text{ with } s_{\text{mol}} = \frac{R_{\text{mol}}}{L_{\text{mol}}} \quad (6)$$

$$Y_{\text{vis}} = \frac{1}{Z_{\text{vis}}} = \frac{1}{R_{\text{vis}} + A_{\text{vis}}\sqrt{s}} = \frac{1/R_{\text{vis}}}{1 + \frac{A_{\text{vis}}}{R_{\text{vis}}}\sqrt{s}}$$

$$= \frac{1/R_{\text{vis}}}{1 + \sqrt{\frac{s}{s_{\text{vis}}}}} \text{ with } s_{\text{vis}} = \left(\frac{R_{\text{vis}}}{A_{\text{vis}}} \right)^2. \quad (7)$$

By replacing the Laplace factor s , the total admittance can be divided into a real part and into an imaginary part:

$$Y_{\text{tot}} = \left[\frac{R_{\text{mol}}}{R_{\text{mol}}^2 + (\omega L_{\text{mol}})^2} + \frac{R_{\text{vis}} + \frac{A_{\text{vis}}}{\sqrt{2}}\sqrt{\omega}}{\left(R_{\text{vis}} + \frac{A_{\text{vis}}}{\sqrt{2}}\sqrt{\omega} \right)^2 + \frac{A_{\text{vis}}^2}{2}\omega} \right]$$

$$- i \left[\frac{\omega L_{\text{mol}}}{R_{\text{mol}}^2 + (\omega L_{\text{mol}})^2} - \frac{\frac{A_{\text{vis}}}{\sqrt{2}}\sqrt{\omega}}{\left(R_{\text{vis}} + \frac{A_{\text{vis}}}{\sqrt{2}}\sqrt{\omega} \right)^2 + \frac{A_{\text{vis}}^2}{2}\omega} \right]$$

$$= \text{Re}(Y_{\text{tot}}) + \text{Im}(Y_{\text{tot}}). \quad (8)$$

Consequently, the phase, which is a measure for the ratio of kinetic energy transfer to dissipative losses, can be determined as:

$$\tan = \frac{\text{Im}(Y_{\text{tot}})}{\text{Re}(Y_{\text{tot}})}. \quad (9)$$

3. Results

The proposed EQC model was applied to experimental data of two micro-oscillators measured within a pressure range from 10^{-3} to 10^3 mbar for different gap widths (150–3500 μm), various gas atmospheres (He, Ne, Ar, N₂, CO₂, N₂O, SF₆), and higher bending modes (fundamental mode up to the 5th bending mode). Micro-oscillator 1 consist of two beams with a length of 1200 μm , a width of 600 μm and a suspended plate of $2400 \times 1800 \mu\text{m}^2$ resulting in an eigenfrequency of 1.55, 9.25,

25.20, 48.33, and 81.10 kHz for the first five bending modes [27, 28]. Micro-oscillator 2 possess two beams with a length of 350 μm , a width of 400 μm and the suspended plate has a quadratic shape with the dimensions of $1600 \times 1600 \mu\text{m}^2$ leading to an eigenfrequency of 5.05 kHz for the first fundamental mode. The thickness of both micro-oscillators is 20 μm . More details on the experimental setup, the measurement and on the micro-oscillators can be found in previous work [21, 26].

The fitting of the EQC model to the measured data is done by a non-linear curve fitting algorithm using the Levenberg–Marquardt method implemented in a custom-made LabVIEW program [29]. The quality of the fit is represented by the coefficient of determination R^2 . For all fitting processes an R^2 value greater than 0.99 was achieved (R^2 equal to one is indicating a perfect match between experimental data and the fitting model). The deviation between the experimental data and the EQC model is within a range of $\pm 10\%$ for all gap widths (150–3500 μm) and over the whole pressure range from 10^{-3} to 10^3 mbar.

Figure 3 shows the fitting of the EQC model to the experimental data. Excellent agreement between the model and the experimental data was found. Furthermore, the superposition principle of the two rails of the EQC model is illustrated. In figure 4, the correlation of the quality factor Q to admittance Y of the EQC model as well as the damping ratio D to the impedance Z of the EQC model is shown for a wider gap width of 2050 μm .

4. Discussion

4.1. Pole factors

By applying the EQC model presented above, the experimental data are evaluated in a completely new way. This approach to use an EQC model allows for the division of the quality factor, respectively the damping ratio, into a real part and into an imaginary part. Therefore, we are fitting equation (5) to the experimental data for the quality factor of figure 1(a) to obtain the values for the electric components of the EQC. These values are used in equation (8) to distinguish between the real and imaginary part in a so-called

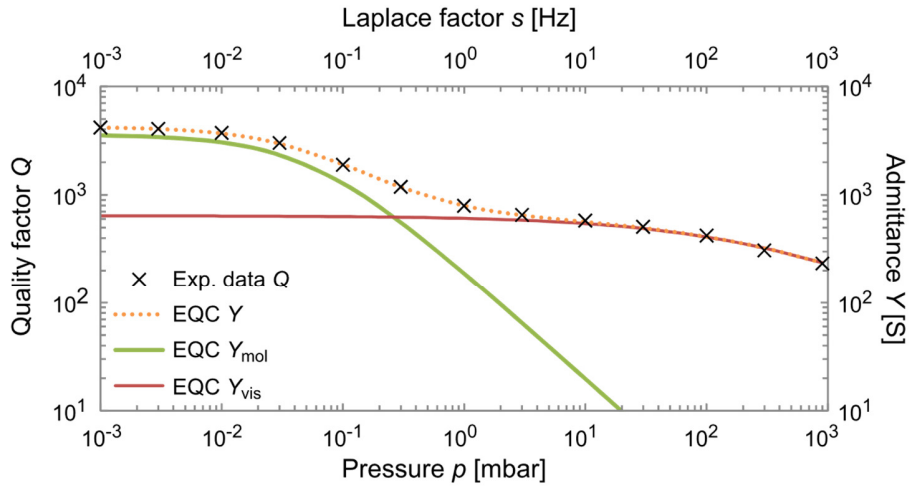


Figure 3. Adaptation of the EQC model to the experimental data of micro-oscillator 1 at a gap width of 550 μm in a N_2 atmosphere measured in the fundamental mode.

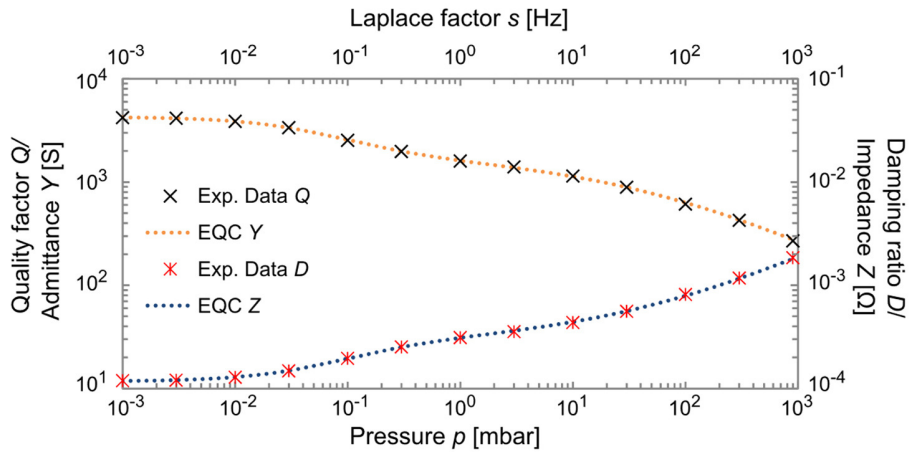


Figure 4. Adaptation of the EQC model to the experimental data of micro-oscillator 1 for a gap width of 2050 μm in a N_2 atmosphere measured in the fundamental mode for the quality factor Q as well as for the damping D .

Nyquist plot (see figure 1(b)). The real losses can be attributed to irreversible mechanical, thermal and viscous losses and the imaginary part to the reversible transfer of kinetic energy between the solid state oscillator and the surrounding gas molecules. This spring behaviour of gas films was introduced previously by Veijola *et al* for describing squeeze film effects [12]. In the Nyquist plots the relation of real to imaginary admittance (respectively quality factor) is displayed and is illustrated in figure 5 for various configurations.

From the Nyquist plots shown in figure 5 various fundamental physical interpretations can be extracted. In general, the Nyquist plots show two semicircles for the two pole factors s_{mol} and s_{vis} (see equations (6) and (7)). The appearance of a single semicircle is based on two effects. Firstly, in the case of squeeze film damping, the molecular range goes directly into the viscous range without the thermodynamic transition

area having a significant influence (see fundamental mode in figure 5(a)) [26]. Secondly, a dominant intrinsic damping masks the molecular flow area, thus, hiding its influence. This effect can be seen at the 5th bending mode in figures 5(a) and (c) and partly at the 4th mode in figure 5(c).

In the case of two semicircles, a transitional flow regime dominated by thermal dissipation effects can be found (point 2 in figure 1(b)). This regime is indicated by a local minimum in the absolute value of the phase ψ (see equation (9)) due to high real dissipative losses and low imaginary losses via kinetic energy transfer to the surrounding gas molecules (see figures 5(b), (d) and (f)). In figures 5(e) and (f), the Nyquist plot and phase diagram are shown for various gas atmospheres. Especially the transition regime between the semicircles depends very strongly on the type of gas, due to the difference in the thermal diffusivity, which is a measure

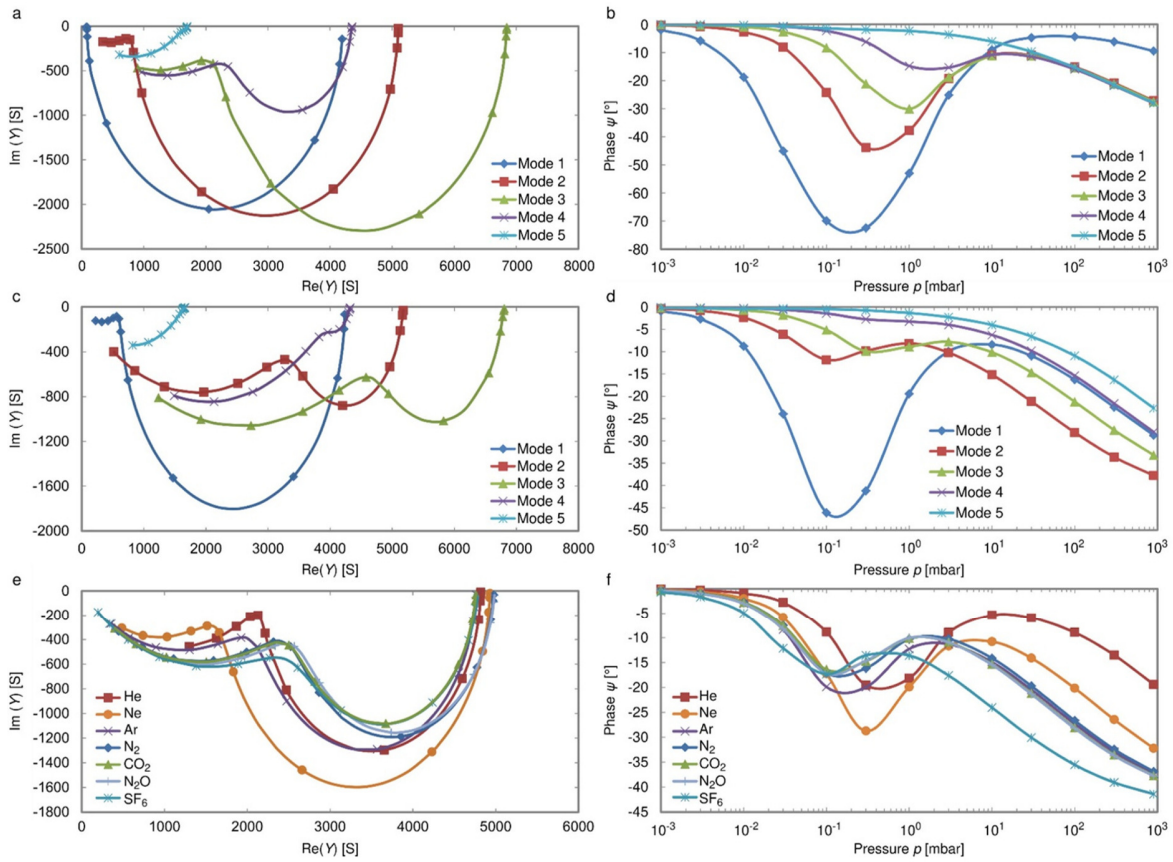


Figure 5. Re–Im-plot and phase plot of micro-oscillator 1 measured in a nitrogen atmosphere for various bending modes for a gap width of $150\ \mu\text{m}$ (a) and (b), and $550\ \mu\text{m}$ (c) and (d). Re–Im-plot and phase plot of sensor micro-oscillator 2 measured in the first bending mode for different gas atmospheres for a gap width of $900\ \mu\text{m}$ (e) and (f).

for thermal transport effects and, thus, for thermal losses. The damping effect of thermal resonance being the dominant loss mechanism in the transitional flow regime was shown previously [26]. The noble gases He and Ne differ significantly in that value from the other measured gases as well as the larger SF_6 molecule.

The molecular semicircle constructed by the molecular pole factor s_{mol} is defined by the molecular mass which can be seen in figure 6. This is in accordance with the theory given for the damping of micro-oscillators in the molecular flow regime [22]. For a larger gap width a deviation from the linear plot versus the reciprocal square root of the molar mass can be seen. This effect can be attributed to the activation process of rotational and vibrational degrees of freedom, leading to an increase of the heat capacity. It was discussed in a previous work [21].

The viscous semicircle is given by the viscous pole factor s_{vis} and is affected by the macroscopic properties of the gas like the density ρ and the viscosity η . For s_{vis} we find a linear dependency to the reciprocal density of the gas (see figure 7). This dependency of the damping in the viscous regime can be found in the literature [30]. It opens up the

possibility for a density measuring instrument which was shown previously [31].

4.2. Viscous resistance

Most applications take place in the viscous flow regime or even at atmospheric pressure. In this case the viscous resistance is the limiting quantity for the quality factor and therefore for the efficiency of the micro-oscillator. The following discussion focuses on the reduction of the viscous resistance, providing some design rules for enhancing the performance of micro-oscillators.

In figure 8(a) the viscous resistance as function of the gap width is illustrated. A reciprocal behaviour can be seen leading to a strong decrease of the viscous resistance by an increasing gap width. In the range of small gap widths the viscous resistance decreases by more than one order of magnitude and approaches a saturation value starting at about $900\ \mu\text{m}$. At narrow gaps the movement of the oscillator creates a pressure gradient which can only escape via the edges [12]. This leads to high viscous friction losses due to compression effects in

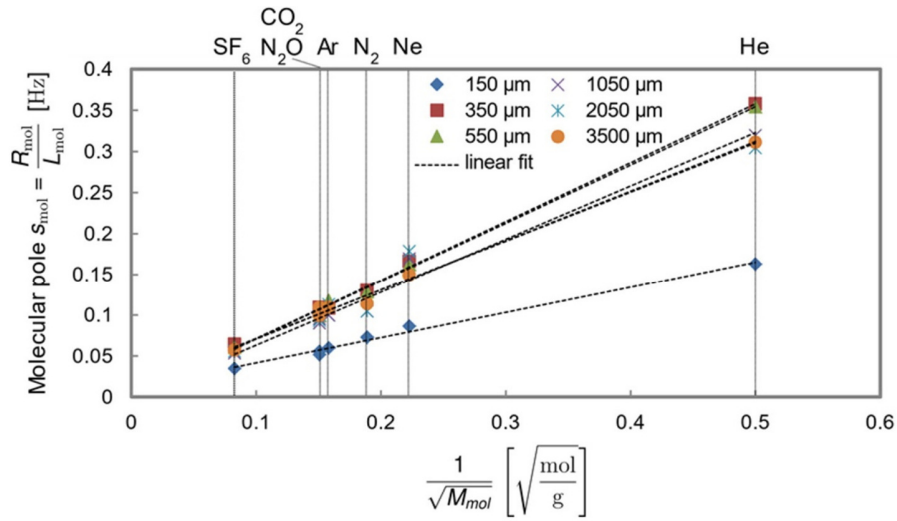


Figure 6. Molecular pole factor s_{mol} as function of the molar mass for various gap widths measured with micro-oscillator 2.

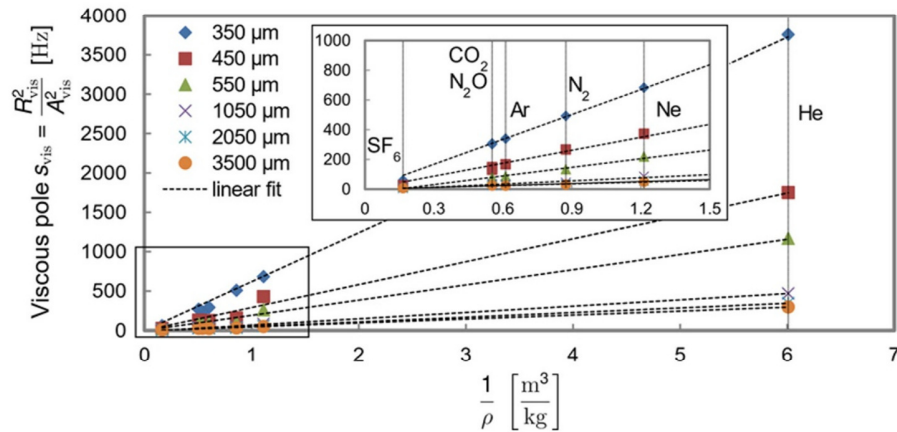


Figure 7. Viscous pole factor s_{vis} as function of the reciprocal density for various gap widths measured with micro-oscillator 2.

the fluid against which the oscillation must work. This effect decreases with increasing gap width, since the positive pressure can also escape to the top over a larger volume and compression effects are decreasing. From this one can deduce that an enlargement of the distance has a great positive influence on the quality factor. At a gap width of $550 \mu\text{m}$ the viscous resistance is decreased by about one decade compared to the narrowest gap width of $150 \mu\text{m}$ (squeeze film area) which leads to an increase in the quality factor by a factor of 4.5.

The influence of the viscosity of the gas type can be seen in figure 8(b). For all gap widths we find a linear behaviour of the viscous resistance to the viscosity of the gas. The slope of the linear trend is decreasing with an increasing gap width. Therefore, the influence of the viscosity and thus of the gas type is most significant especially for small gap widths. The viscous resistance itself can be reduced by a factor of 1.5 by using a He atmosphere instead of a Ne atmosphere, in the

case of narrow gap widths. The influence on the quality factor is given by the viscous pole factor s_{vis} which is additionally depending on the parameter A_{vis} . Therefore, there is an additional dependence on the density, which is depicted in figure 7. The total influence of the gas type on the quality is therefore given by the combination of the density and the viscosity. A change from Ne to He at a gap width of $550 \mu\text{m}$ leads to an increase of the quality factor by a factor of 2.

Figure 9 shows the dependence of the viscous resistance on the resonance frequency or rather the influence of higher bending modes. Hereby, two effects are superimposed. On the one hand, a higher resonance frequency leads to a smaller viscous boundary layers δ_{vis} ($\delta_{vis} = \sqrt{\eta/\pi\rho f}$) [30] and, thus, to less viscous frictional losses. On the other hand, the higher modes lead to the formation of more complex pressure profiles. This results in high-pressure areas being directly adjacent to low-pressure areas, leading to smaller compressional effects

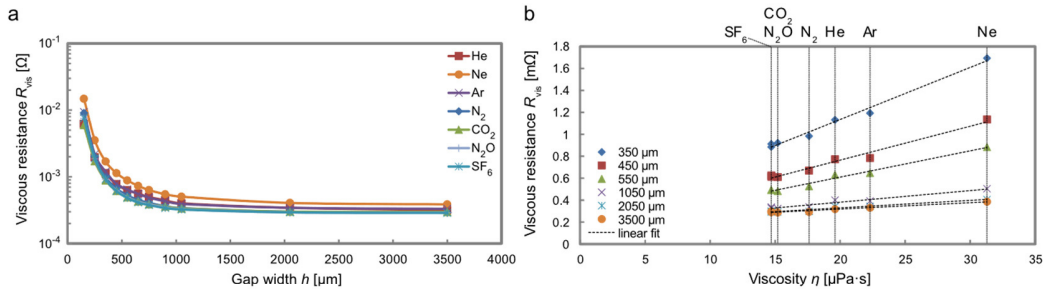


Figure 8. Viscous resistance as function of the adjusted gap width measured in various gas atmospheres with micro-oscillator 2 (a). Dependence of the viscous resistance on the viscosity of the medium for different gap widths measured with micro-oscillator 2 (b).

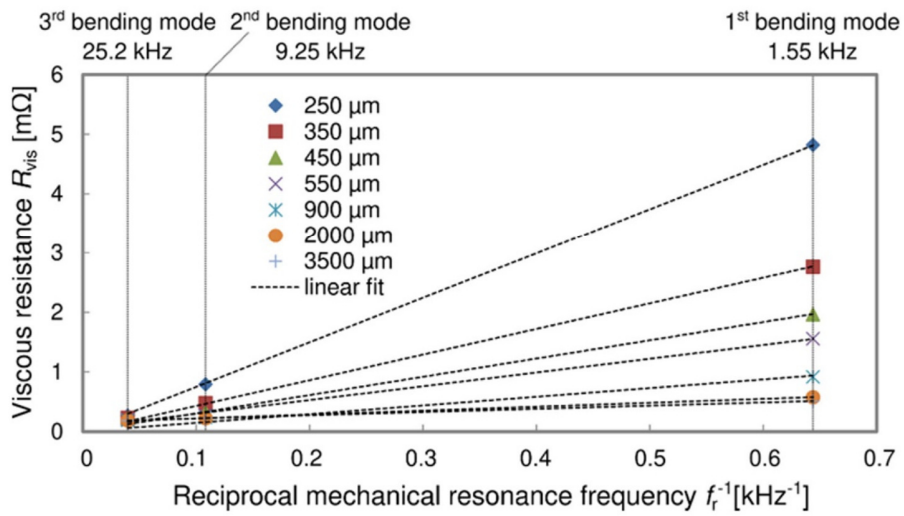


Figure 9. Viscous resistance versus the reciprocal mechanical resonance frequency of the first three bending modes of micro-oscillator 1 for various gap widths measured in a N₂ atmosphere.

by the oscillator movement. Furthermore, the high-pressure areas can partially compensate the pressure gradient by diffusion into the low-pressure areas. This results in lower viscous friction losses and, in case of a gap width of 550 μm, to a reduction of the viscous resistance by a factor of 8 when the fundamental mode (1.55 kHz) is compared to the 3rd bending mode (25.2 kHz). This reduction in the viscous resistance increases the quality factor by a factor of 6. The 4th and 5th modes exhibit even smaller viscous resistances which could not be determined in the presence of a dominating intrinsic damping effect (see figure 5(a)).

All proportionalities found within this study between the electric components and the physical properties of the type of gas (molecular mass M_{mol} , viscosity η , density ρ , heat conductivity λ , and heat capacity C_p) as well as on the resonance frequency f_r (respectively higher bending mode) of the micro-oscillators are summarized in table 1. Additionally, the insights of a previous study on the transitional flow regime with focus on the parameter A_{vis} is included [32].

From these results, design rules can be derived for the optimization of the quality factor of micromechanical oscillators, which are summarized in the following (the design rules

are sorted in the order of decreasing impact, from high influence to low influence on the quality factor):

- Use higher resonance frequencies or higher bending modes.
- Increase the gap width to surrounding boundary surfaces, e.g. to substrate or to packaging.
- Reduction of the density-viscosity-product of the surrounding gas, e.g. using He or N₂ for the encapsulated atmosphere.

5. Conclusion

In this work an EQC model was presented based on two individual branches, the molecular and the viscous branch. In a first step, the EQC model was developed and the transfer function in the form of the conductance was derived. The adaptation of the model to the experimental data shows excellent agreement with a maximum deviation of 10% over the whole pressure range from 10^{-3} to 10^3 mbar. The advantages of the EQC model are, on the one hand, its simplicity and, on the other hand the possibility to divide the damping into real dissipative effects and imaginary parts, resulting from the transfer

of kinetic energy onto the surrounding gas molecules. The values obtained for the electric components of the EQC were investigated as a function of the mode number and the resonance frequency as well as the gap width and different gas properties. The characteristics of these components are reasonable and are consistent with results given for the quality factor in the literature. For most applications there is a particular interest in reducing the viscous resistance which is often the limiting factor for the efficiency of micro-oscillator devices. Finally, based on the results, three design rules are derived for optimizing the performance of micro-oscillators.

Data availability statement

The data that support the findings of this study are available upon reasonable request from the authors.

Acknowledgments

The authors wish to thank the German Research Foundation (DFG) for financial support within the Grant SE 1425/14-1.

Conflict of interest

The authors declare that there is no conflict of interest.

ORCID iDs

T Zengerle  <https://orcid.org/0000-0003-0590-9443>

A Ababneh  <https://orcid.org/0000-0002-3746-7507>

H Seidel  <https://orcid.org/0000-0003-4210-2964>

References

- [1] Kucera M, Manzaneque T, Sanchez-Rojas J L, Bittner A and Schmid U 2013 Q -factor enhancement for self-actuated self-sensing piezoelectric MEMS resonators applying a lock-in driven feedback loop *J. Micromech. Microeng.* **23** 1–8
- [2] Albrecht T, Gruetter P, Horne D and Rugar D 1991 Frequency modulation detection using high- Q cantilevers for enhanced force microscopy sensitivity *J. Appl. Phys.* **69** 668–73
- [3] Aoust G, Levy R, Verlhac B and Le Traon O 2018 Ultra high quality factor resonators operated in fluids *Sens. Actuators A* **269** 569–73
- [4] Basu A K, Basu A and Bhattacharya S 2020 Micro/nano fabricated cantilever based biosensor platform: a review and recent progress *Enzyme Microb. Technol.* **139** 109558
- [5] Manzaneque T, Ruiz-Diez V, Hernando-Garcia J, Wistrela E, Kucera M, Schmid U and Sanchez-Rojas J L 2014 Piezoelectric MEMS resonator-based oscillator for density and viscosity sensing *Sens. Actuators A* **220** 305–15
- [6] Zotov S A, Simon B R, Trusov A A and Shkel A M 2015 High quality factor resonant MEMS accelerometer with continuous thermal compensation *IEEE Sens. J.* **15** 5045–52
- [7] Elfrink R, Renaud M, de Nooijer C, Jambunathan M, Goedbloed M, Hohlfield D, Matova S, Pop V and Caballero L 2010 Vacuum-packaged piezoelectric vibration energy harvesters: damping contributions and autonomy for a wireless sensor system *J. Micromech. Microeng.* **20** 1–7
- [8] Candler R N, Park W T, Li H, Yama G, Partridge A, Lutz M and Kenny T W 2003 Single wafer encapsulation of MEMS devices *IEEE Trans. Adv. Packag.* **26** 227–32
- [9] Qiu H and Seidel H 2018 Hydrodynamic loading on vibrating piezoelectric microresonators *Piezoelectricity—Organic and Inorganic Materials and Applications* (London: IntechOpen Limited) pp 43–64
- [10] Kavitha C and Madhan M G 2013 A PSpice model for the study of thermal effects in capacitive MEMS accelerometers *Proc. Eng.* **64** 292–301
- [11] Vemuri S, Fedder G K and Mukherjee T 2000 Low-order squeeze film model for simulation of MEMS devices *Technical Proc. 2000 Int. Conf. on Modeling and Simulation of Microsystems* pp 205–8
- [12] Veijola T, Kuisma H, Lahdenperä J and Ryhänen T 1995 Equivalent-circuit model of the squeezed gas film in a silicon accelerometer *Sens. Actuators A* **48** 239–48
- [13] Veijola T 1999 *Equivalent Circuit Models for Micromechanical Inertial Sensors* (Espoo, Finland: Helsinki University)
- [14] Westby E and Fjeldly T 2002 Dynamical equivalent-circuit modeling of MEMS with squeezed gas film damping *Phys. Scr.* **2002** 192–5
- [15] Mukhiya R, Garg M, Gaikwad P, Sinha S, Singh A and Gopal R 2020 Electrical equivalent modeling of MEMS differential capacitive accelerometer *Microelectron. J.* **99** 104770
- [16] Petersan P J and Anlage S M 1998 Measurement of resonant frequency and quality factor of microwave resonators: comparison of methods *J. Appl. Phys.* **84** 3392–402
- [17] Pandey A K and Pratap R 2007 Effect of flexural modes on squeeze film damping in MEMS cantilever resonators *J. Micromech. Microeng.* **17** 2475–84
- [18] Zener C 1938 Internal friction in solids: II. General theory of thermoelastic internal friction *Phys. Rev.* **53** 90–9
- [19] Frangi A, Cremonesi M, Jaakkola A and Pensala T 2013 Analysis of anchor and interface losses in piezoelectric MEMS resonators *Sens. Actuators A* **190** 127–35
- [20] Karniadakis G, Beskok A and Aluru N 2006 *Microflows and Nanoflows: Fundamentals and Simulation* (New York: Springer Science & Business Media) pp 16–7
- [21] Zengerle T, Joppich J, Schwarz P, Ababneh A and Seidel H 2019 Polyatomic degrees of freedom and their temporal evolution extracted from the damping of micro-oscillators *Sens. Actuators A* **297** 111460
- [22] Bao M, Yang H, Yin H and Sun Y 2002 Energy transfer model for squeeze-film air damping in low vacuum *J. Micromech. Microeng.* **12** 341–6
- [23] Holm S, Holm T and Martinsen O 2021 Simple circuit equivalents for the constant phase element *PLoS One* **16** e0248786
- [24] Hirschorn B, Orazern M E, Tribollet B, Frateur I and Musiani M 2010 Determination of effective capacitance and film thickness from constant-phase-element parameters *Electrochim. Acta* **55** 6218–27
- [25] Biswas K, Sen S and Dutta P K 2006 Realization of a constant phase element and its performance study in a differentiator circuit *IEEE Trans. Circuits Syst. II* **53** 802–6
- [26] Zengerle T, Joppich J, Schwarz P, Ababneh A and Seidel H 2020 Modeling the damping mechanism of MEMS oscillators in the transitional flow regime with thermal waves *Sens. Actuators A* **311** 112068
- [27] Langer P, Jelich C, Guist C, Peplow A and Marburg S 2021 Simplification of complex structural dynamic models: a case study related to a cantilever beam and a large mass attachment *Appl. Sci.* **11** 1–14
- [28] Li Z, He Y, Lei J, Han S, Guo S and Liu D 2019 Experimental investigation on size-dependent higher-mode

- vibration of cantilever microbeams *Microsyst. Technol.* **25** 3005–15
- [29] Ma C and Lihua J 2007 Some research on Levenberg–Marquardt method for the nonlinear equations *Appl. Math. Comput.* **184** 1032–40
- [30] Blom F R, Bouwstra S, Elwenspoek M and Fluitman J H J 1992 Dependence of the quality factor of micromachined silicon beam resonators on pressure and geometry *J. Vac. Sci. Technol. B* **10** 19–26
- [31] Schwarz P, Feili D, Engel R, Pagel N and Seidel H 2010 Vacuum pressure and gas detection with a silicon based micromechanical squeeze film sensor *Proc. Eurosensors XXIV* vol 5 pp 750–3
- [32] Zengerle T, Joppich J, Lensch H, Ababneh A and Seidel H 2020 A lumped element model for the damping mechanism of micro-oscillators in the transitional flow regime *Int. Conf. on Microelectronics (ICM) (Aqaba, Jordan)* (<https://doi.org/10.1109/ICM50269.2020.9331778>)

6.6 Damping in Liquids (Unpublished Data)

In the following section, the damping behavior of micro-oscillators in a liquid environment is investigated. The high interest in micro-oscillator measurements is due to the fact that the damping can be used to draw valuable information about the properties of the fluid [97]. This allows real-time monitoring of liquids [102], which has led to applications in the observation of wine fermentation process [139], the aging of operating oils [140], or biological investigations [103], among others [141].

6.6.1 Experimental Results in Liquids

The big challenge for measurements in liquids is the low quality factor, which is associated with a low displacement and thus a low measurement signal. For this reason, the following measurements in liquids were evaluated using optical measurement methods. The investigations were carried out in the laboratory of Prof. Sánchez-Rojas at the Universidad de Castilla - La Mancha (UCLM), Ciudad Real, Spain with a laser Doppler vibrometer (MSV-400 from *Polytec*). All presented results are recorded with a beam-oscillator BO (*cf.* Figure 4b) with a plate of $1600 \times 1600 \mu\text{m}^2$ attached to two beams with a length L_B of $350 \mu\text{m}$ and a width B_B of $400 \mu\text{m}$. The thickness was determined to be $20 \mu\text{m}$ from the resonance frequency of 5 kHz of the first fundamental mode with the method presented in Section 6.4.2.

In addition to the higher resolution compared to the electrical signal acquisition, the mode shape can also be identified by scanning the entire structure with a grid pattern. For this purpose, the measurements were performed with a pattern consisting of 100 points covering the whole micro-oscillator surface. After the scan, the individual measurement points are combined and interpolated in-between. Figure 40 shows four different modes as an example for this measurement principle.

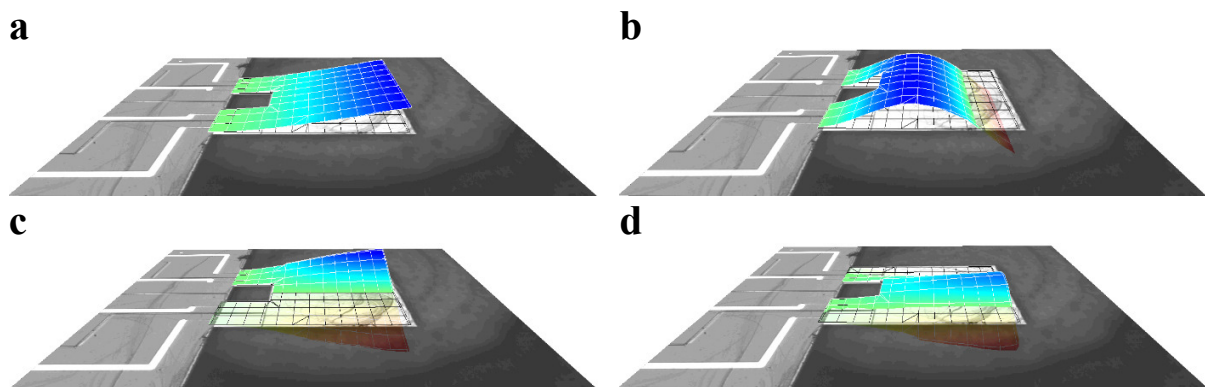


Figure 40. Laser Doppler vibrometer measurement of a micro-oscillator in air. In (a) and (b) the first two bending modes are depicted, in (c) the first torsional mode is illustrated and in (d) the first roof-tile shape mode is shown.

By means of a Fourier transformation, as presented in Section 3.3, the time signal is transferred into the frequency domain and additionally averaged for all measurement points. The averaged results of the out of plane displacement of the micro-oscillator structure as a function of frequency leads to a frequency spectrum. Figure 41 shows the frequency spectra in air and isopropanol. The

bending modes, torsional modes and the first roof-tile shape mode can be identified in both frequency spectra and are labelled with their associated resonance frequency and quality factor. In isopropanol, the averaged displacement signal of the second bending mode is vanishingly small and therefore this mode is not included in Figure 41b.

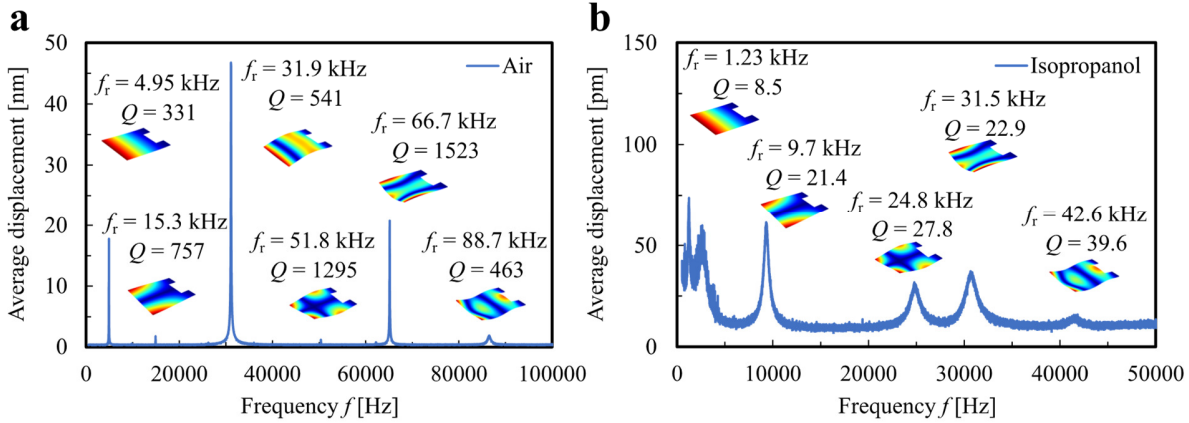


Figure 41. Frequency spectrum of the averaged displacement measured in air (a) and isopropanol (b). The corresponding shape mode, resonance frequency and quality factor are inserted for each resonance peak.

Due to the stronger damping of the micro-oscillator in liquids, such as isopropanol, the signal decreases by about three orders of magnitude. This also results in the fluctuations being more prominent at constant noise due to the lower signal-to-noise ratio. Therefore, the data are evaluated with a modified amplitude function to cover the effect of a non-negligible offset.

The offset is modeled by Petersan *et al.* with three fit parameters representing the constant part (Z_1), the slope (Z_2) and the skew (Z_3) of the offset function [142]:

$$A_{\text{offset}}(f) = Z_1 + Z_2 f + \frac{Z_3 f + A_{\text{max}}}{\sqrt{1 + 4 \left(\frac{f - f_0}{\Delta f} \right)^2}} \quad (6.8)$$

The quality factor Q is calculated as presented in Equation (2.16) with the resonance frequency f_0 and the 3dB bandwidth Δf . The parameter A_{max} represents the height of the maximum amplitude above the offset noise in the resonance case.

As can be seen in Figure 42a-c, a very good agreement between the experimental data and the fit function is achieved. Thus, the resonance peak itself as well as the offset are covered very well by this approach. Additionally, the decreasing signal-to-noise ratio with decreasing quality factor from Isopropanol to N10 can be observed. A qualitative comparison between the experimental fitted resonance peak functions illustrated in Figure 42d and the simulated curves (see Figure 14b) show a very good agreement. The deviation is mainly caused by the underground noise leading to a tilt of the resonance peak function and a constant shift from the zero level. These effects are both covered by the modified amplitude function, so the resulting quality factor and resonance frequency should not be affected by the background noise.

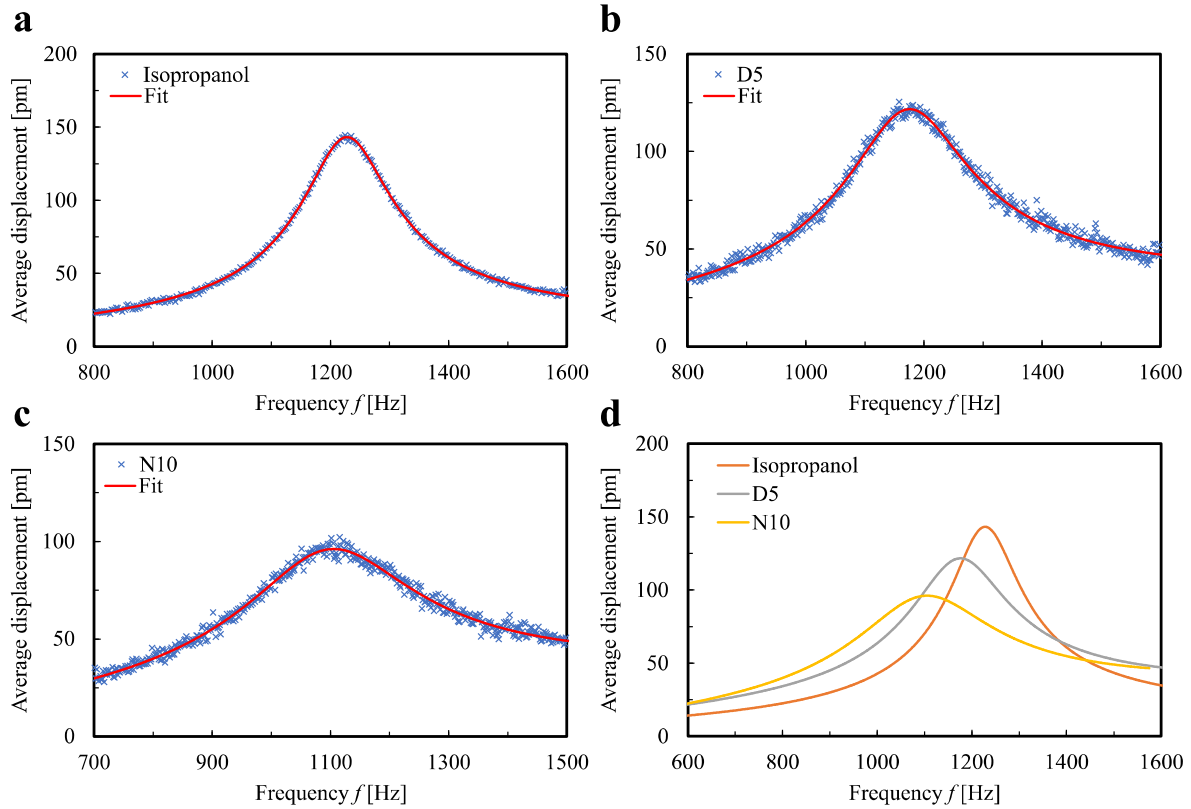


Figure 42. Resonance peak of the first bending mode measured in isopropanol (a) and the standard viscosities D5 (b) and N10 (c). The measurement data are fitted by a modified Lorentzian fit function to evaluate the resonance peaks. In (d) the resulting fitted resonance peaks are summarized for comparison between the liquids.

In Table 10 the results for the quality factor and the resonance frequency are summarized for the first bending mode and compared to the numeric values presented in Section 3.3. The deviation for the resonance frequency is less than a percent and is therefore very well predicted by the numerical fluid-structure interaction approach. The quality factor values are less accurate and a deviation of up to 10 % can be observed. The reason for this may be the neglect of the turbulent flow and associated losses in the gap between the beams, by the numerical laminar flow model [143].

Table 10. Experimentally determined values for the quality factor Q and resonance frequency of a micro-oscillator in different liquids. The results are compared to the numerically simulated values regarding the absolute and relative deviation.

Liquid	Experiment		Simulation		Absolute deviation		Relative deviation	
	f_0 [Hz]	Q_{exp} [1]	f_0 [Hz]	Q_{sim} [1]	Δf [Hz]	ΔQ [1]	Δf [%]	ΔQ [%]
Isopropanol	1228	8.5	1230	8.1	2	0.4	0.16	4.71
D5	1176	5.5	1168	5.9	8	0.4	0.68	7.27
N10	1105	3.8	1108	4.2	3	0.4	0.27	10.53

6.6.2 Comparison between Liquid and Gases

In the following, the results for the other higher modes are analyzed and are compared with the previously presented measurements in different gas atmospheres. In Figure 43, the resonance frequency and quality factor for different modes achieved in different media are illustrated. It can be observed that the resonance frequency increases in the same way as the mode number, with a factor of approximately 2 between the values in liquid and in air. The sorting of the resonance frequency between the liquids follows the density of the medium. Isopropanol has the highest resonance frequency and N10 the lowest within the measurement series. The quality factor plot reveals a significant dependence on the mode number as well as on the mode shape (*cf.* Figure 43b). The torsional modes show relative high quality factors in both media, liquids and air atmosphere. The bending modes are significantly more attenuated than the other modes due to the compression effect of these mode shapes. This effect is very pronounced in the air atmosphere. The highest quality factor in the air atmosphere was achieved with the roof-tile shape mode, which is already known from the literature to be weakly damped [32]. Surprisingly, this phenomenon does not show up in the measured liquids. The reason for this may be the gap between the beam structures of the bending oscillator. The referenced measurements are performed with cantilever structures without such an opening. Basak *et al.* have shown the additional loss effect due to turbulence generated by edges and openings, which lead to a stronger damping [143]. These additional turbulences in the gap between the beam cause losses, which may explain this observation.

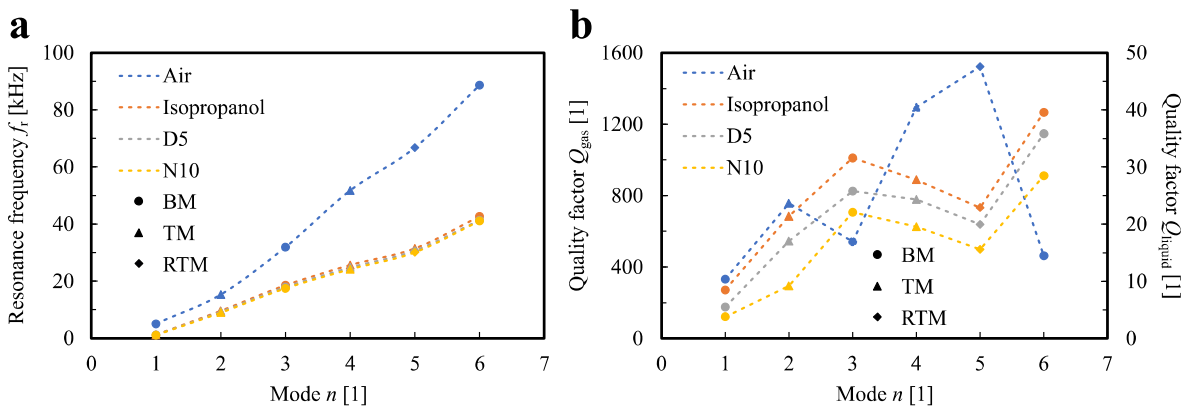


Figure 43. Measured resonance frequency (a) and quality factor (b) of the micro-oscillator versus the mode number. Mode 1, 3 and 6 are indicating the first three bending modes (circle), mode 2, 4 are representing the first two torsional modes (triangle) and mode 5 stands for the roof tile shape mode (diamond).

In Figure 44, the measured quality factors of the first bending mode in various liquid environments (isopropanol, D5, N10) and different gas atmospheres (He, Ne, Ar, CO₂, N₂O, SF₆) are plotted in double logarithmic scale. When the quality factor values are plotted versus the reciprocal square root of the product of density and viscosity, a linear trend appears for both gas and liquid media, which is in accordance with the Equations (2.33) and (2.38). This means that both damping mechanisms have the same dependence of the quality factor on the properties of the medium. A deviation is only visible at small gap widths, since here the squeeze film damping is dominant instead of the viscous damping. Therefore, especially the Ne value deviates from the linear fit due to the high dynamic viscosity, which is more relevant in the squeeze film range. Above a gap width of 350 μm ,

however, the values are almost perfectly on the fit line with a coefficient of determination R^2 of above 0.99 ($R^2 = 1$ indicating a perfect match between measurement values and fit line). A significant difference is noticeable between the locations of the fit lines of the liquid damping and the viscous damping. The gas damping lines are found to the left due to the lower density and dynamic viscosity whereby also a dependence on the gap width is visible. Narrow gap widths increase more slowly with the reciprocal product than larger gap widths and are thus stronger attenuated. When extrapolating the fit lines of the liquid values and the gas fit lines, it is noticeable that the liquid values have a higher quality factor at the same product, which means that normalized to the properties of the medium, the damping in gases is stronger than in liquids. This phenomenon that the liquid damping is relatively weaker than the damping in a gas atmosphere can be explained by the compressibility properties of the media. Liquid media can be considered incompressible when a force due to the oscillatory motion is acting on them. Therefore, the last term in Equation (3.1) can be neglected due to the condition $\nabla \cdot \vec{u} = 0$ (incompressible flow). This leads to no attenuation effects by the bulk viscosity μ_B , which is associated with expansion and compression effects. Compared to gases, the energy losses are therefore reduced by the factor of the compression losses.

Assuming an extrapolation of the fit lines and a continuous transition between the liquid damping and viscous damping lines, the crossing can be modeled by the squeeze film damping mechanism. This means that in the transition between the damping of a liquid medium and a gaseous medium, the squeeze film regime must be overcome. To resolve this, however, further measurements are necessary, especially in the middle range, as well as measurements with different phases of a single medium [144], [99], e.g., liquid and gaseous nitrogen or even within a phase transition [145]. In conclusion, it turns out that the proportionality of the damping mechanism of the liquid damping and the gaseous viscous damping are showing the same proportionality but differ in the slope.

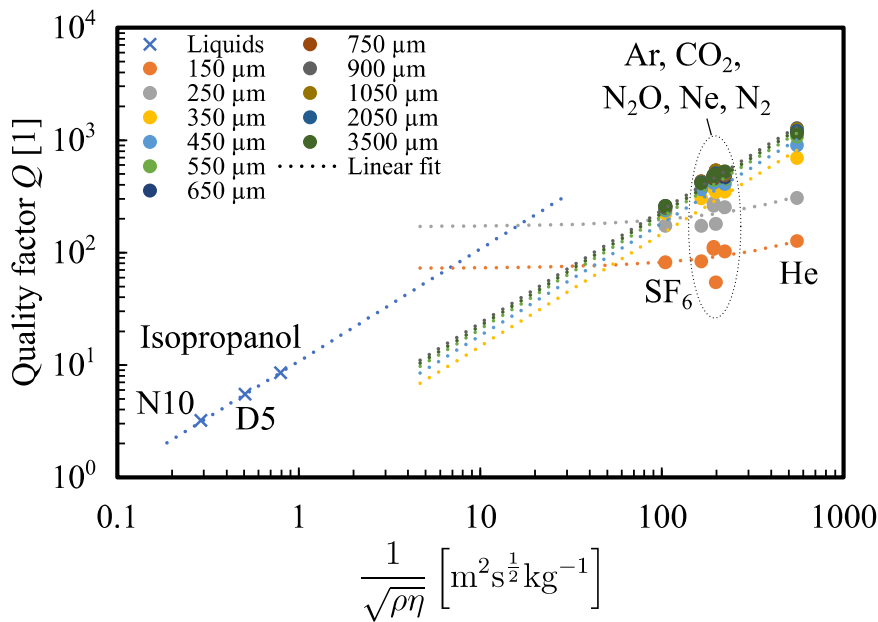


Figure 44. Quality factor as function of the reciprocal square root product of density and dynamic viscosity. The liquids and gases except for the small gap width are showing the same dependency to the product but differ significantly in their location.

6.7 Wide-Range Pressure Sensing Application

6.7.1 Linear Pressure Sensing

The precise measurement of pressure is one of the most important quantities required in many technical applications. The pressure range extends from gas cylinders with an overpressure of several hundred bar, to slight overpressures in tires and slight vacuum in many process chambers in microsystems technology, to the lowest pressures in the range of 10^{-9} bar in scanning electron microscopy. Such a large range cannot be covered by a single sensor or by a single sensor principle [13]. A distinction is made between gas type independent direct measurement methods and gas type dependent indirect measurement methods. The most common principle for slight vacuum atmospheres is the use of mechanical devices, such as capacitive membrane sensors. They measure the deflection of a thin membrane (typically a few μm) due to a pressure gradient between the upper and lower side. The pressure difference to a reference pressure can be measured as well as the absolute pressure. The measurement of the absolute pressure requires a closed bottom side with an enclosed vacuum as high as possible. This measurement method can be used down to a range of about 10^{-4} bar. At lower pressures, the force effect of the pressure gradient is so small that the deflection can no longer be reliably read out.

Therefore, indirect measurement principles are used for the range of lower pressures below 10^{-4} bar. This is achieved by measuring other physical properties of the gas that scale with the pressure. Widespread are Pirani elements, which measure the pressure via the heat conductivity of the gas atmosphere [12]. The disadvantage here is the dependence of the heat losses on the type of gas, as shown in the quality factor measurements of the micro-oscillators in the molecular flow regime (influence of the molecular degrees of freedom) and in the transition regime. This requires the use of calibration curves, which must be adapted to the gas atmosphere and require knowledge of the gas type. A recent approach in MEMS technology has combined two indirect pressure measurement techniques (Pirani and ionization) to limit the influence of the gas species to less than 20% over a pressure range of eight decades [146]. The use of MEMS oscillators for absolute pressure measurement is obvious, since both the quality factor and the resonance frequency are two quantities that scale with the ambient pressure [147]. Since the quality factor is always a measured quantity resulting from a combination of several influences and is subject to greater uncertainty and a stronger dependence on the type of gas, the resonance frequency is selected as variable. The effect of the resonance frequency shift due to the increased damping is illustrated in Figure 45. A correlation between the resonance frequency and the pressure in a range from 10 to 1000 mbar is applicable. In the pressure range below this, the damping effect of the pressure on the resonance frequency is significantly reduced. Only in the range of a small gap width of about $150 \mu\text{m}$ a slight resonance frequency increase at 1 mbar due to squeeze film damping is evident. The overall decrease of the resonance frequency is in the range of up to 1 – 2 % (relative to the vacuum resonance frequency) over the two pressure decades depending on the gap width. The influence of the gap width is shown in Figure 45b and reveals a large influence for small gap widths, which disappears for gaps larger than $900 \mu\text{m}$, showing a saturation behavior. This characteristic was also found in the investigation of the damping behavior of the bending modes (see Section 6.4.2).

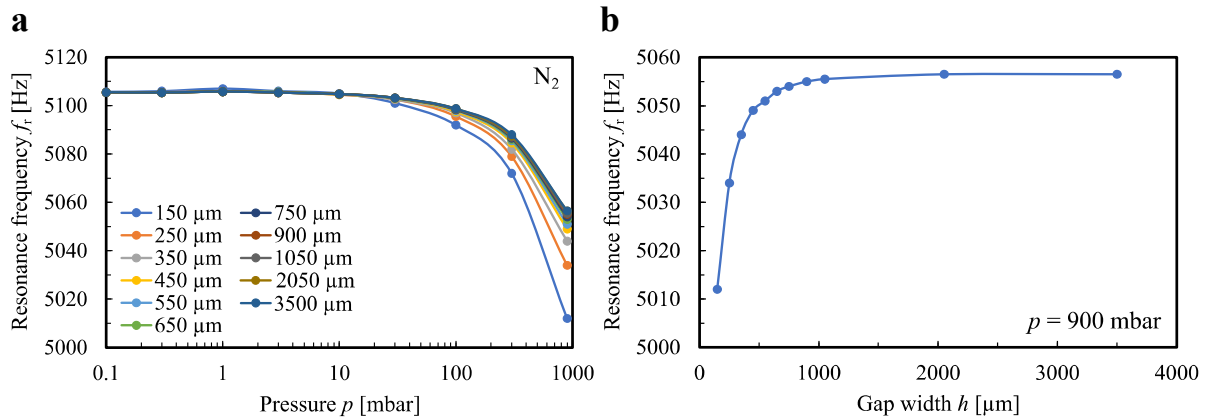


Figure 45. Resonance frequency as function of the ambient pressure of a nitrogen atmosphere for various gap widths (a). The gap width dependency of the resonance frequency is illustrated for a pressure of $p = 900$ mbar revealing a saturation behavior (b).

In addition to the gap width dependence, there is also a dependency on the gas type, which is illustrated in Figure 46. Here, the resonance frequency is sorted according to the density of the gases (see Figure 46b). From this it can be deduced that the resonance frequency as a measurand is subject to the influence of both the gas type and the gap distance. In general, the gap width is a fixed value that is given by the package of the measurement setup and it is not variable. The influence of the gas type can be eliminated by knowledge of the gas atmosphere or can also be used in the other direction to determine the density of the gas atmosphere when the pressure is known. The present results were all obtained in the linear range of the oscillator.

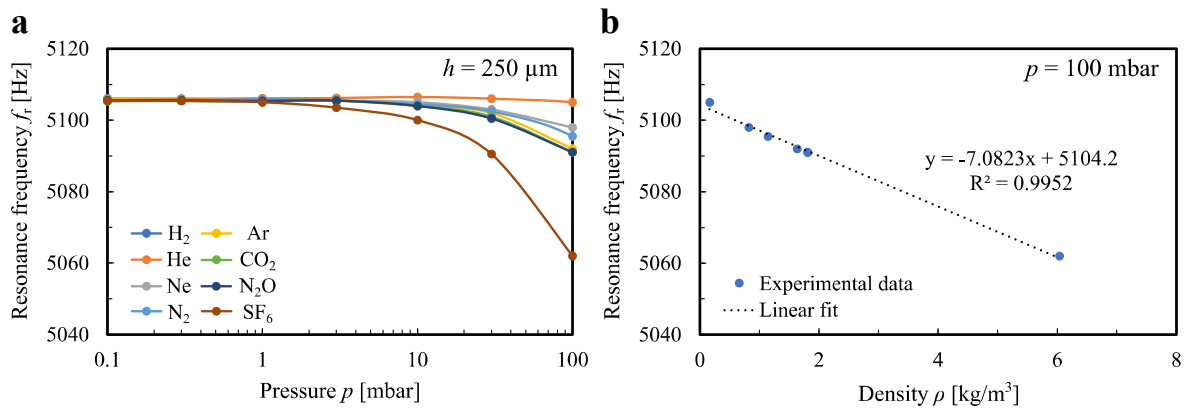


Figure 46. Resonance frequency as function of the ambient pressure for different gas atmospheres at a gap width of $h = 250$ μm (a). In (b), the resonance frequency at a pressure of $p = 100$ mbar is evaluated regarding the density of the gas atmosphere showing a linear correlation.

In the following, the nonlinear range will be investigated. In addition to the resonance frequency, this range offers a hysteresis behavior due to the nonlinearity, which is used for pressure determination. By exploiting the nonlinearity, a significantly larger measuring range of up to six decades was achieved. As a special feature, the strength of the nonlinearity can be adjusted by the actuation voltage and thus the measuring sensitivity can be set in counterplay to the size of the measurement range.

6.7.2 Addendum VI



Article

Using the Nonlinear Duffing Effect of Piezoelectric Micro-Oscillators for Wide-Range Pressure Sensing

Tobias Zengerle ^{1,*}, Michael Stopp ¹, Abdallah Ababneh ^{1,2} and Helmut Seidel ¹

¹ Chair of Micromechanics, Microfluidics and Microactuators, Campus A5.1, Saarland University, 66123 Saarbrücken, Germany; michael.stopp@imm.uni-saarland.de (M.S.); a.ababneh@yu.edu.jo (A.A.); seidel@imm.uni-saarland.de (H.S.)

² Electronic Engineering Department, Hijawi Faculty for Engineering Tech., Yarmouk University, Irbid 21163, Jordan

* Correspondence: t.zengerle@imm.uni-saarland.de

Abstract: This paper investigates the resonant behaviour of silicon-based micro-oscillators with a length of 3600 μm , a width of 1800 μm and a thickness of 10 μm over a wide range of ambient gas (N_2) pressures, extending over six orders of magnitude from 10^{-3} mbar to 900 mbar. The oscillators are actuated piezoelectrically by a thin-film aluminium-nitride (AlN) layer, with the cantilever coverage area being varied from 33% up to 100%. The central focus is on nonlinear Duffing effects, occurring at higher oscillation amplitudes. A theoretical background is provided. All relevant parameters describing a Duffing oscillator, such as stiffness parameters for each coverage size as well as for different bending modes and more complex modes, are extracted from the experimental data. The so-called 2nd roof-tile-shaped mode showed the highest stiffness value of $-97.3 \cdot 10^7 \text{ m}^{-2} \text{ s}^{-2}$. Thus, it was chosen as being optimal for extended range pressure measurements. Interestingly, both a spring softening effect and a spring hardening effect were observed in this mode, depending on the percentage of the AlN coverage area. The Duffing-effect-induced frequency shift was found to be optimal for obtaining the highest pressure sensitivity, while the size of the hysteresis loop is also a very useful parameter because of the possibility of eliminating the temperature influences and long-term drift effects of the resonance frequency. An reasonable application-specific compromise between the sensitivity and the measurement range can be selected by adjusting the excitation voltage, offering much flexibility. This novel approach turns out to be very promising for compact, cost-effective, wide-range pressure measurements in the vacuum range.

Keywords: MEMS oscillator; nonlinearity; pressure sensor; roof-tile-shaped mode; AlN



Citation: Zengerle, T.; Stopp, M.; Ababneh, A.; Seidel, H. Using the Nonlinear Duffing Effect of Piezoelectric Micro-Oscillators for Wide-Range Pressure Sensing. *Actuators* **2021**, *10*, 172. <https://doi.org/10.3390/act10080172>

Academic Editor:
Micky Rakotondrabe

Received: 14 June 2021

Accepted: 22 July 2021

Published: 24 July 2021

Publisher's Note: MDPI stays neutral with regard to jurisdictional claims in published maps and institutional affiliations.



Copyright: © 2021 by the authors. Licensee MDPI, Basel, Switzerland. This article is an open access article distributed under the terms and conditions of the Creative Commons Attribution (CC BY) license (<https://creativecommons.org/licenses/by/4.0/>).

1. Introduction

Micromechanical oscillators enjoy a wide range of applications in many areas. In consumer and automotive electronics, gyroscopes and accelerometers have become omnipresent [1]. Applications that are more specific can be found as microbalances in bio analytics or as sensing elements in scanning probe microscopy (SPM) [2]. In the upcoming field of energy autonomous systems, piezoelectric oscillators are used as vibrational energy harvesters [3]. In some cases and under certain conditions, micro-oscillators may exhibit nonlinear behaviour. Such nonlinearities have been studied and described, e.g., in signal processing and amplification [4,5], or else in pressure sensing [6–8] and gas sensing applications [9], among others. In this context, nonlinearities can strongly affect the frequency response of micro-oscillators regarding their dynamic range and damping behaviour under varying ambient pressure and can therefore significantly increase the sensitivity of oscillator devices [3,4,10]. MEMS oscillators are, e.g., used for leakage detection [11] in autonomous systems which can be accessed via wireless networks [12] (e.g., tire pressure sensors).

This work focusses on the investigation of the nonlinear Duffing effect of micromechanical silicon cantilevers driven by piezoelectric thin film actuators. In order to understand

the theoretical background, the description of electrostatically driven Duffing oscillators known from the literature [13–15] is adapted and expanded to oscillators with piezoelectric actuation. From this theory, the frequency response is derived and the coefficients for linear and nonlinear damping can be determined. The theoretical results are compared with experimentally obtained values for one type of oscillator, where the piezoelectric thin film actuation area is varied, covering 33%, 50%, or 100% of the cantilever. In contrast to previous works on the pressure dependence of nonlinear micro-oscillators [6,7], we use the frequency shift and the frequency hysteresis by the duffing nonlinearity as correlating quantity to the ambient pressure. Therefore, the sensor response is much higher compared to the classical measurement principle based on the frequency shift of linear damped oscillators.

2. Theory

2.1. Nonlinear Duffing Oscillator

The model for a linear damped harmonic oscillator driven by a periodic force $F(t)$ with actuation amplitude F_{piezo} and angular frequency $\omega (=2\pi f)$ is given by the following differential equation:

$$\ddot{A} + \lambda \dot{A} + \omega_0^2 A = \frac{F(t)}{m} = \frac{F_{\text{piezo}}}{m} \cdot \sin(\omega t) \text{ with } \omega_0^2 = \frac{k}{m}, \quad (1)$$

where $A(t)$, λ , ω_0 , $F(t)$, m , k are the oscillation amplitude of the movement, the linear damping coefficient, the mechanical angular resonant frequency, the actuation force, the mass and the linear stiffness parameter of the oscillator, respectively.

Nonlinear behaviour in its simplest form is included by adding a cubic term for the displacement A together with the nonlinear stiffness parameter β , which leads to an additional restoring force (see Figure 1). This results in a displacement depending on the spring constant, leading to a tilting response curve. Thus, we obtain the well-known Duffing equation [14,16]:

$$\ddot{A} + \lambda \dot{A} + \omega_0^2 A + \beta A^3 = \frac{F_{\text{piezo}}}{m} \cdot \sin(\omega t) \quad (2)$$

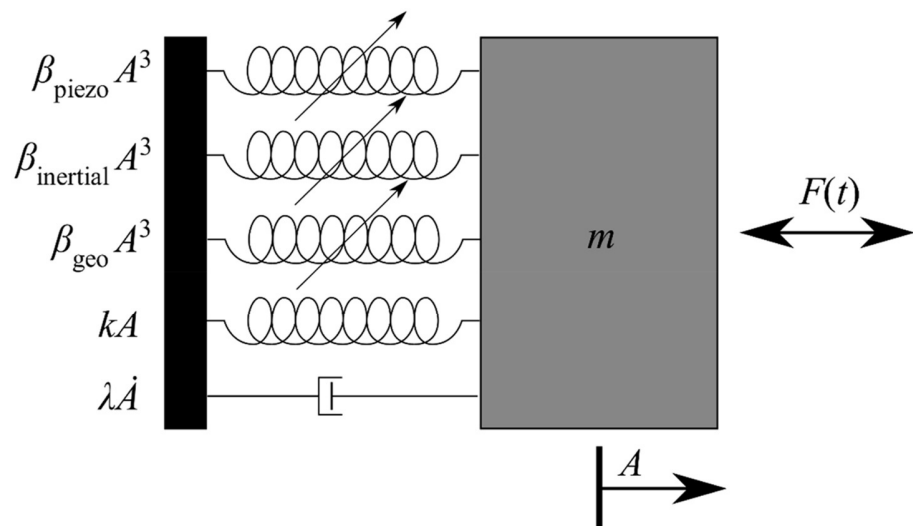


Figure 1. Schematic picture of a piezoelectrically actuated micro-oscillator with force $F(t)$ and mass m . The moving mass is attached to a fixed anchorage via a linear damper and four springs representing the linear and the three nonlinear restoring forces.

This nonlinear differential equation can be solved by the homotopy analysis method (HAM) to derive the frequency response of the oscillating amplitude A [17]:

$$A^2 = \frac{F_{\text{piezo}}^2}{m^2 \left[(\omega^2 - k - \frac{3}{4}\beta A^2)^2 + (\lambda\omega)^2 \right]} \quad (3)$$

Depending on the sign of the nonlinear stiffness parameter β , the resonant curve tilts to the left ($\beta < 0$) or to the right ($\beta > 0$) (see Figure 2a). In terms of a mechanical oscillating system, a spring softening ($\beta < 0$) or else a spring hardening ($\beta > 0$) effect can be observed.

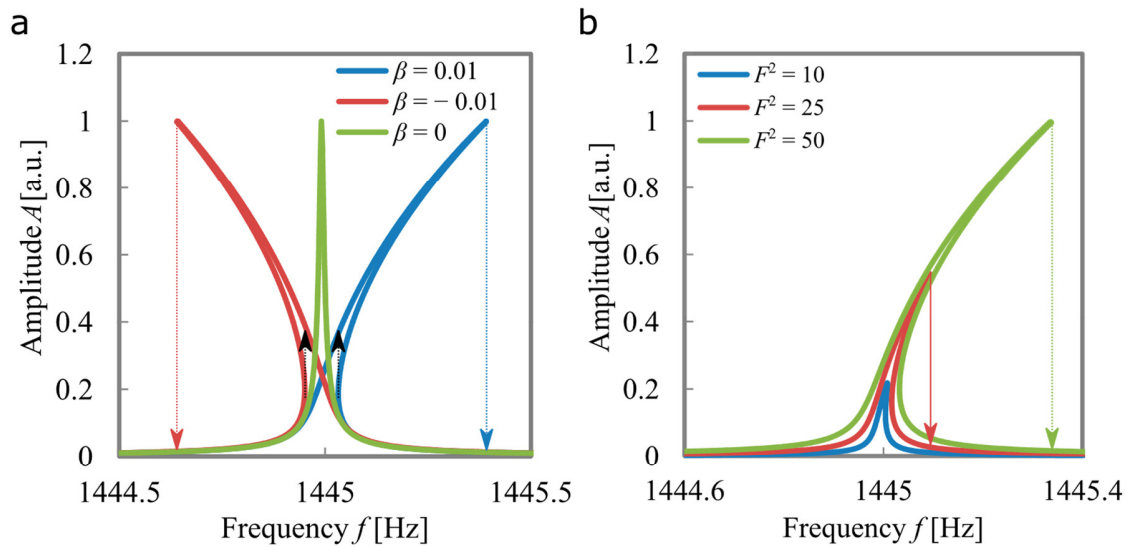


Figure 2. Numerically simulated frequency response of a Duffing oscillator for varying stiffness coefficients (a) and for varying actuation forces (b).

Contributions to the stiffness parameter for piezoelectric oscillators are discussed in the literature and consist of three parts [18–20]: geometric, inertial, and piezoelectric effects. Here, the geometric part β_{geo} has a hardening effect, whereas the inertial component β_{inertial} as well as the piezoelectric influence β_{piezo} have a softening effect:

$$\beta = \beta_{\text{geo}} - \beta_{\text{inertial}} - \beta_{\text{piezo}} \quad (4)$$

The geometrical hardening effect is caused by the rigidity of the solid-state material at large oscillation amplitudes, which leads to a stiffening of the spring. The inertial effects appear predominant at high kinetic energies of the oscillator. The inertial effects are defined by the velocity and the acceleration on the oscillator. These effects are dominating at higher modes, due to the increase of the resonance frequency as well as the decrease of the oscillation amplitude. The piezoelectric effects originate from the nonlinear nature of the deflection of piezoelectric materials when applying high electric fields.

The solution of the Duffing equation for a given frequency is not a single-valued function. When the non-physical negative values for the amplitude are excluded, the equation leads to one (stable region of the resonance curve), two (at the jumping point) or three solutions (unstable region of the resonance curve) for the amplitude response. Within the unstable region, the amplitude exhibits abrupt jumping phenomena, depending on the sweep direction. In Figure 2a, the different sweep directions are indicated by dashed arrows. This leads to a hysteresis behaviour of the amplitude. The strength of the nonlinear effect and therefore the size of the hysteresis loop is strongly dependent on the amplitude of the driving force F_{piezo} , which in turn depends on the actuation voltage. As can be seen

in Figure 2b, the hysteresis gap (frequency difference between the two sweep directions) increases with increasing actuation force.

In the case of piezoelectrically driven oscillators, the actuation force F_{piezo} is given by the electrically induced stress tensor σ of the aluminium nitride (AlN) thin film on the cantilever. Thus, the mechanical stress can be written in the full Voigt matrix and vector notation as:

$$\sigma = d^T E, \quad (5)$$

with the piezoelectric coefficient tensor d^T [21], the electric field E , which is given by the actuation voltage U , and the thickness of the AlN film t ($E = U/t$). In our configuration, the actuation force by the piezoelectric AlN thin film with the actuation area S can be simplified as follows:

$$F_{\text{piezo}} = d_{31} E_3 S = d_{31} \frac{U}{t} S. \quad (6)$$

2.2. Ayela's Model

Due to the fact that the amplitude frequency response of Duffing oscillators is given as an implicit function (see Equation (3)), a higher numerical effort is necessary to extract the information from the resonance curve. Therefore, several approximation models have been established [13,22], to directly evaluate the key parameters out of the resonant behaviour. Important indicators include the shift of the peak frequencies, Δf_{up} , and Δf_{down} , as well as the peak amplitudes of the upward sweep direction A_{up} , and downward sweep direction A_{down} (see Figure 3). Ayela et al. [13] derived an approximation for the Duffing behaviour of electrostatically excited MEMS oscillators, extracting key parameters such as the linear attenuation and the nonlinear stiffness parameter of the oscillator. In the following, the major points of the model are presented and summarised in Table 1.

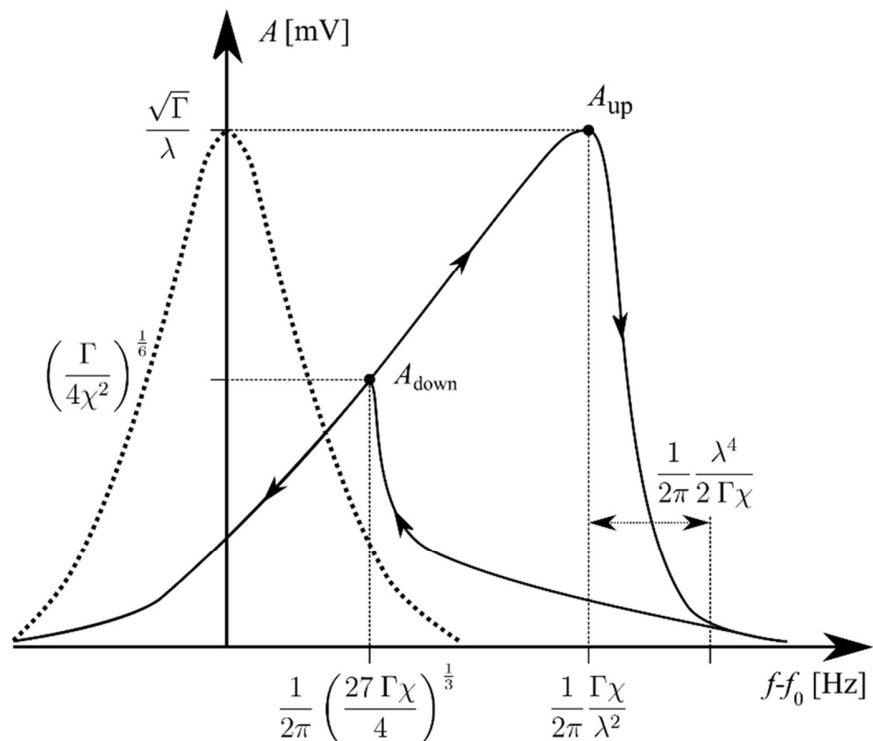


Figure 3. Amplitude versus the frequency shift for a damped harmonic oscillator (dotted line) and Duffing oscillator (solid line). The key parameters according to Ayela's model are included [9].

Table 1. Listing of important parameters for characterising the behaviour of Duffing oscillators.

Ayela's Model [9]	Amplitude [mV]	Frequency [Hz]
Upward Sweep	$A_{\text{up}} = \frac{\sqrt{\Gamma}}{\lambda}$	$\Delta f_{\text{up}} = \frac{1}{2\pi} \frac{\Gamma\chi}{\lambda^2}$
Downward Sweep	$A_{\text{down}} = \left(\frac{\Gamma}{4\chi^2}\right)^{\frac{1}{6}}$	$\Delta f_{\text{down}} = \frac{1}{2\pi} \left(\frac{27\Gamma\chi}{4}\right)^{\frac{1}{3}}$

The frequency shift $\Delta\omega$ caused by the Duffing effect is given by:

$$\omega_{\text{Duff}} = \omega_0 + \Delta\omega = \omega_0 + \frac{3}{8} \frac{\beta}{\omega_0} A^2 = \omega_0 + \chi A^2 \left[\text{s}^{-1} \right]. \quad (7)$$

The gap between A_{up} and $A \approx 0$ is given by:

$$\varepsilon = \frac{1}{2\pi} \frac{\lambda^4}{2\Gamma\chi}, \quad (8)$$

with Γ being the strength of the actuation, which can be calculated via the upward Amplitude A_{up} :

$$\Gamma = (\lambda A_{\text{up}})^2 \left[\text{m}^2 \text{s}^{-2} \right] = \left(\frac{F_{\text{Piezo}}}{2m\omega_0} \right)^2. \quad (9)$$

Combining the equations of the frequency shift in upward and downward directions leads to an expression for the linear damping coefficient λ :

$$\lambda = \sqrt{\frac{2(2\pi\Delta f_{\text{down}})^3}{27\pi\Delta f_{\text{up}}}} = 2.4184 \cdot \sqrt{\frac{(\Delta f_{\text{down}})^3}{\Delta f_{\text{up}}}} \left[\text{s}^{-1} \right]. \quad (10)$$

The nonlinear damping coefficient can either be derived from the downward sweeping amplitude A_{down} or by fitting the slope of the frequency shifts as a function of the associated amplitude Δf_{up} (A_{up}^2) or Δf_{down} (A_{down}^2) (see Equation (7)). The nonlinear damping coefficient χ is given as follows:

$$\chi = \sqrt{\frac{\Gamma}{4A_{\text{down}}^6}} \left[\text{m}^{-2} \text{s}^{-1} \right], \quad (11)$$

This can be related to the stiffness parameter β by using Equation (7), yielding:

$$\beta = \frac{16\pi}{3} \chi f_0 \left[\text{m}^{-2} \text{s}^{-2} \right]. \quad (12)$$

This model is applied to the piezoelectric MEMS oscillator presented in this work to determine the strength of the nonlinearity.

3. Experimental Section

3.1. Manufacturing

The silicon-based micro-oscillators consisted of a single bending beam, also known as a cantilever structure, with a length of 3600 μm , a width of 1800 μm , and a thickness of 10 μm (see Figure 4a). The cantilevers were covered by an AlN thin film layer for actuation and by corresponding gold electrodes for contact. The percentage of coverage of the AlN film was varied from the whole cantilever for C_100, half of the cantilever for C_50 and a third of the cantilever for C_33 (see Figure 4b). The cantilevers were fabricated by standard microtechnology processes, including lithography, sputter deposition and wet/dry etching. A highly doped p-Si wafer ($\rho = 0.01 \Omega\text{cm}$, boron) was chosen as substrate. At first, SiO_2 was grown for electric insulation with a thickness of 120 nm in a thermal oxidation process. The SiO_2 on the bottom side served as an adhesion layer for a 550 nm Si_3N_4 film, which was

deposited by PECVD. The Si_3N_4 film was used as passivation layer for the KOH etching process as part of the releasing step. Both films were structured in a single lithography step using AZ 1518 resist and a subsequent etch process in 6% HF solution. The piezoelectric AlN film with a thickness of 1100 nm was deposited by reactive sputter deposition [21]. After the AlN patterns were lithographically structured, the film was etched with 85% phosphoric acid at 80 °C. The gold electrodes were deposited via DC sputtering and etched using aqua regia at 25 °C. The cantilevers were released in a two-step process. In the first step, a thin membrane was created by time-controlled KOH etching from the backside. Afterwards, the cantilevers were released from the front side using a Bosch dry etching process. In between the two steps, the KOH cavity was filled with AZ 1518 photo resist to stop the dry etching process and prevent the cantilever from suffering mechanical damage. Finally, the cantilevers were diced and cleaned with a solution of acetone, isopropanol, water and ethanol in an ultrasonic bath.

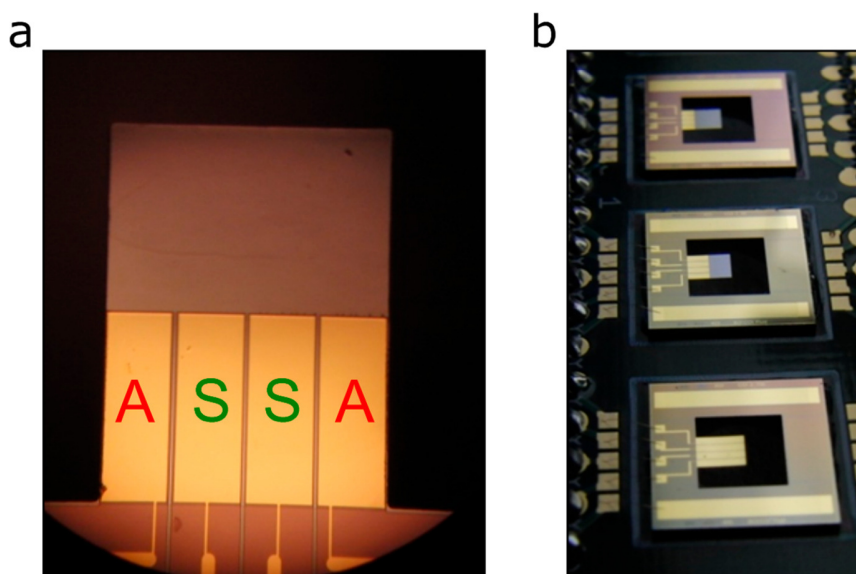


Figure 4. Top view on the cantilever structure C_50 (a) and measurement board with the cantilevers C_33, C_50, and C_100 (from top to the bottom) (b). “A” signifies the actuation electrodes, “S” signifies the sensing electrodes.

3.2. Experimental Setup

The cantilevers were glued on top of a printed circuit board (PCB) and were electrically connected by gold wire bonds. The measurement board (compare Figure 4b) was placed within a custom-built vacuum chamber providing a pressure range from high vacuum (10^{-3} mbar) up to atmospheric pressure (900 mbar). Via a feedback loop, the pressure was adjusted in a dynamic equilibrium by controlling the inlet gas flow with a mass flow controller (MFC). A pure nitrogen atmosphere was chosen to provide a clean and defined measurement environment. The pressure was measured using three pressure sensors from Pfeiffer Vacuum (CMR 261/264/362) with an accuracy of <0.2%. The cantilevers were excited by a function generator decoupled with a buffer amplifier, providing a sinusoidal signal with varying amplitude and frequency. When measuring piezoelectrically driven oscillators, a parasitic crosstalk appears which can be eliminated by a compensation circuit proposed by Qiu et al. [23]. In addition to the compensation circuit, the PCB board was equipped with a charge amplifier and with an inverting amplifier. Subsequently, the resonance curves were measured by recording the compensated and amplified frequency response of the cantilever with a lock-in amplifier (SR 5210) (see Figure 5).

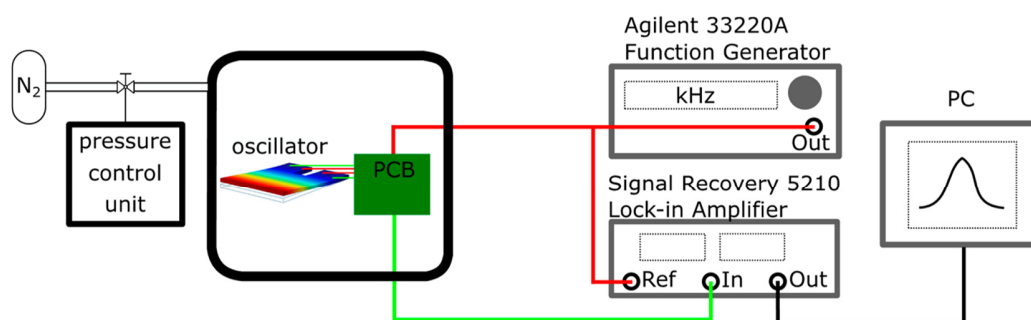


Figure 5. Schematic of the experimental setup. The vacuum chamber ranges from 10^{-3} to 10^3 mbar.

4. Results

In order to investigate the possibility of using nonlinear Duffing MEMS oscillators for pressure sensing applications, the frequency response of the presented cantilever structures was recorded under varying ambient pressure conditions as well as excitation voltages. The hysteresis behaviour of the frequency response was recorded in upward (u) and downward (d) sweep direction around the peak frequency. For all AlN-layer coverage sizes the Duffing behaviour of the cantilevers was investigated up to a frequency of 120 kHz (limitation of the lock-in amplifier). The detected modes were associated with their shape by correlation with FEM eigenfrequency analysis and with recordings of a laser Doppler vibrometer (UHF-120 from Polytec).

The resonance curve of the micro-oscillator operating in the same higher mode can be seen in Figure 6. The results show hysteresis behaviour depending on both excitation voltage and ambient pressure. An increasing ambient pressure p leads to a decreasing hysteresis gap until it finally disappears (see Figure 6a,b). The influence of the ambient pressure on the frequency response is given by the linear damping coefficient λ , which increases with increasing pressure. In addition, the peak amplitude as well as the hysteresis loop become larger with increasing excitation voltage (see Figure 6c). These proportionalities are in accordance with the Duffing theory presented above (see Figure 2b). The dependency of the excitation voltage on the frequency response can be directly derived by taking Equation (6) into account.

The presented results show the frequency response of cantilevers with different AlN-coverage sizes (33 to 100%), operated in the same mode. A difference in the eigenfrequency appears that is mainly caused by fabrication tolerances (cantilever thickness) and, to a lesser extent, by the difference of the coverage sizes of the AlN/Au stack. The presented eigenmode is the so-called second roof-tile-shaped mode, which has been found to be advantageous for operating in heavily damped environments [24] and therefore possesses relatively large oscillation amplitudes, leading to strong Duffing effects.

Interestingly, the results in Figure 6a,b indicate a spring softening effect for 100% AlN coverage, whereas a spring hardening effect occurs for a cantilever with 33% AlN coverage, but otherwise identical geometry and mode (compare Figure 6c). According to Equation (4), the nonlinearity can be divided into a geometric part, an inertial part and a piezoelectric part [18]. The geometric nonlinearity has a spring hardening effect, whereas both inertial and piezoelectric nonlinearities have a spring softening effect. This could explain why a larger coverage area of the AlN film (C_100, Figure 6a,b) can overcome the originally dominant geometric spring hardening nonlinearity (C_33, Figure 6c) and changes it into a spring softening nonlinearity. The fundamentals behind this influence of the piezoelectric coverage area on the softening/hardening behaviour require more detailed investigation, and will be analysed in a future work. Moreover, a mode-matching optimisation of the electrode shape as well as a phase-correct actuation scheme seems promising for enhancing both sensing and actuation [25].

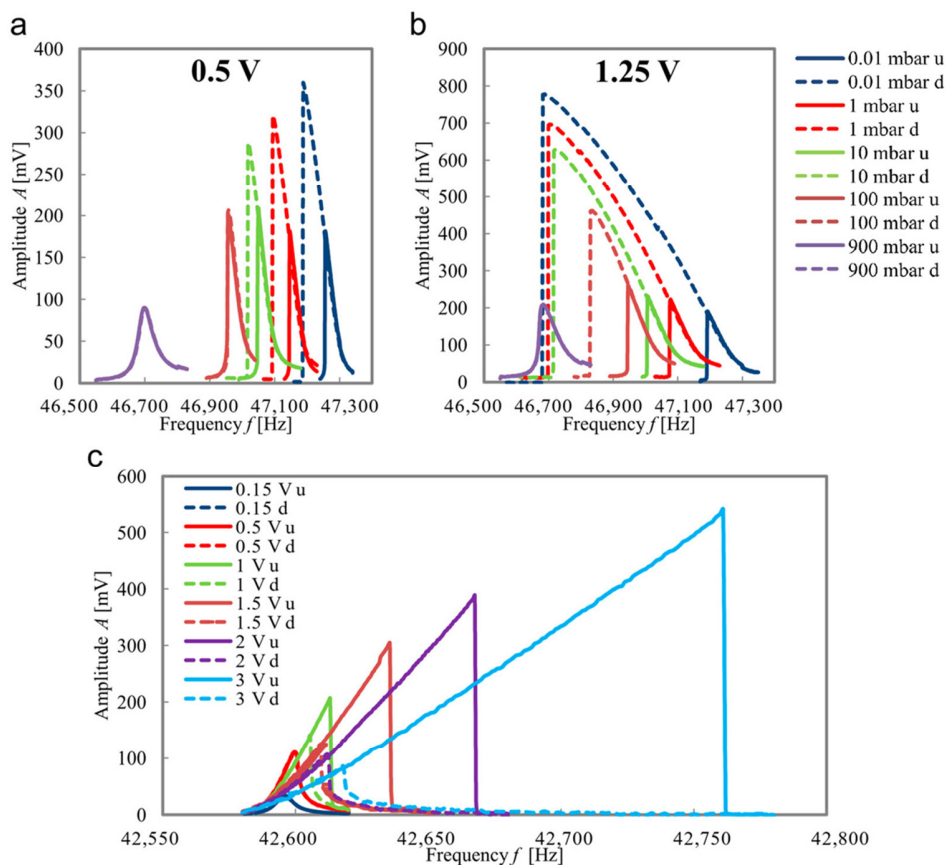


Figure 6. Amplitude frequency response in upward (u, solid) and downward (d, dotted) sweep of the 2nd roof-tile-shaped mode of sensor C₁₀₀ for different ambient pressures and for an excitation voltage of 0.5 V (a) and 1.25 V (b), respectively. Amplitude frequency response in upward (u, solid) and downward (d, dotted) sweep of the 2nd roof-tile-shaped mode of sensor C₃₃ for different excitation voltages at a fixed ambient pressure of 1 mbar (c).

To investigate the strength of the nonlinear Duffing effect, the frequency response was measured for the first four bending modes, and for the 2nd roof-tile-shaped mode. This was done at the best available vacuum level (10^{-3} mbar) to suppress the damping from the surrounding fluid. The stiffness parameter β , and the frequency shifting parameter χ (see Equations (11) and (12)) were analysed to understand the dependency of these parameters with respect to the coverage size and the mode shape. In Figure 7 the frequency shift of the peak amplitude in dependency of the squared measured amplitude is shown for both sweep directions (compare Equation (7)). The first bending mode exhibits the smallest frequency shift and biggest amplitude signal, therefore the frequency shifting parameter χ resulting from the linear fit will be the smallest. For all three coverage sizes, the frequency shifting parameter is on the same order of magnitude. The higher modes show a significantly higher frequency shift at smaller amplitudes and therefore possess a much higher value for the frequency shifting parameter. In particular, the 2nd roof-tile-shaped mode exhibits very high values, indicating a strong nonlinear Duffing effect. All results are summarised in Table 2.

The 2nd roof-tile-shaped mode (see Figure 7d,f) shows the highest value for χ within these experiments, and therefore has been chosen for further investigations under varying ambient pressure. Additionally, the spring softening behaviour of sensor C₁₀₀ operating in this mode is an interesting aspect.

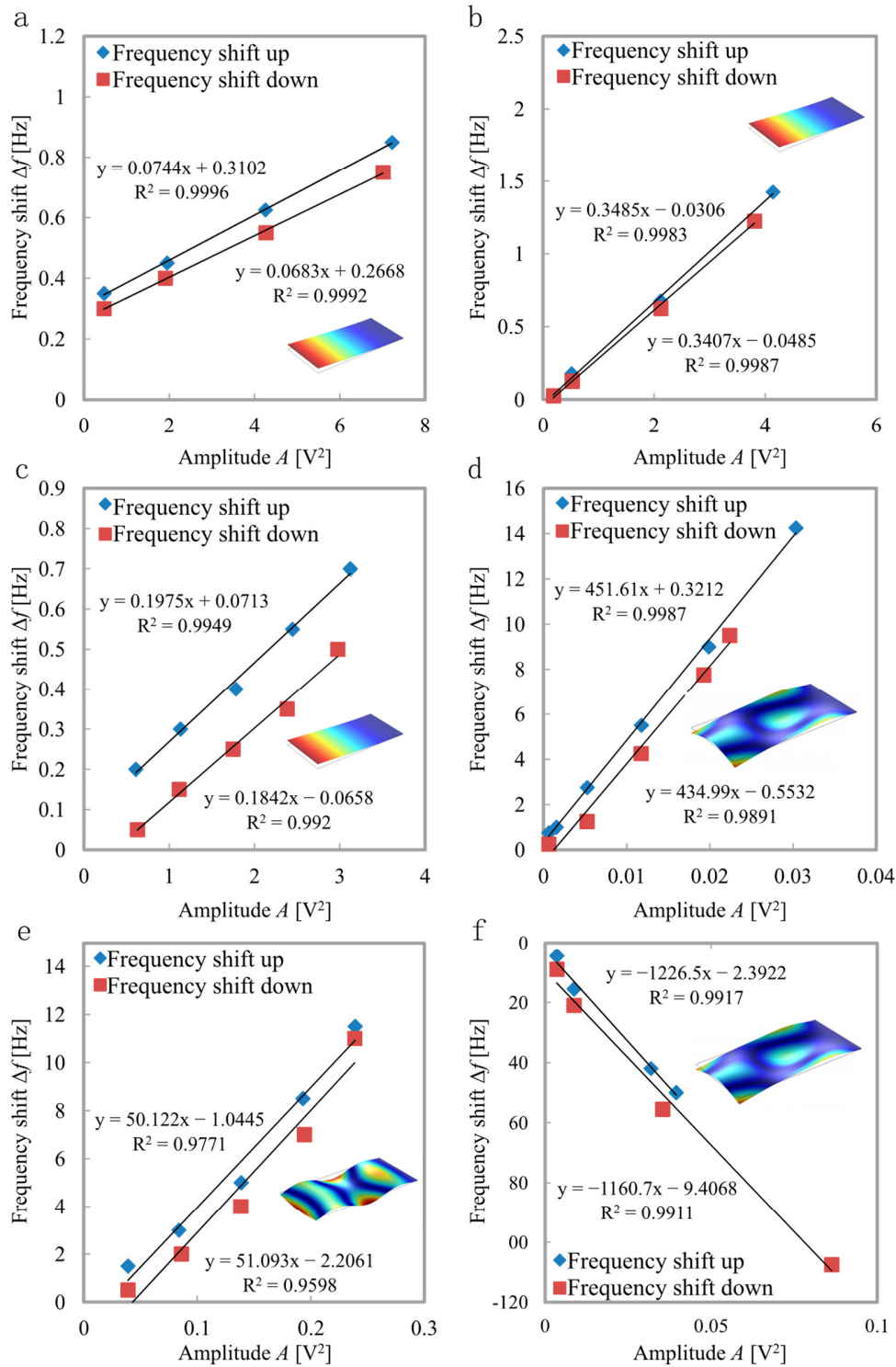


Figure 7. Frequency shift vs. squared measured amplitude for C_33 (a), C_50 (b), and C_100 (c) in the first bending mode, C_33 in the second roof-tile-shaped mode (d), C_100 in the fourth bending mode (e) and in the second roof-tile-shaped mode (f) at 0.001 mbar. The shape of the respective eigenmodes is shown in the inserts.

Table 2. Listing of determined key parameters for the presented sensors and mode shapes of Figure 7.

Sensor	Mode	Resonance Frequency f_r [Hz]	Sweep Direction	χ [$\text{m}^{-2}\text{s}^{-1}$]	β [$\text{m}^{-2}\text{s}^{-2}$]
C33	1st bending	1396.6	up	0.0744	1741
			down	0.0683	1598
C50	1st bending	1448.3	up	0.3485	8457
			down	0.3307	8025
C100	1st bending	967.9	up	0.1975	3203
			down	0.1842	2987
C100	4th bending	35543	up	50.122	29.8×10^6
			down	51.093	30.4×10^6
C33	2nd roof-tile-shape	42704.5	up	435.61	31.2×10^7
			down	434.99	31.1×10^7
C100	2nd roof-tile-shape	47355.5	up	-1226.5	-97.3×10^7
			down	-1160.7	-92.1×10^7

The possibility of cantilever structures exploiting Duffing effects for pressure sensing purposes was investigated by recording the frequency response under a defined pressure (see Figure 6). The amplitude was measured in both sweep directions for different excitation voltages. In the following, the resonance curves are analysed regarding their peak amplitudes and peak frequencies in upward and downward sweep directions. It turned out that the best correlation between measurement and ambient pressure could be achieved by the shift of the peak frequencies in upward direction in the case of hardening effects, and shift of the peak frequencies in downward direction in the case of softening effects, respectively (see Figure 8a,c). Thereby, the shift is related to the resonance frequency of the linear oscillator, which can be measured by applying a lower excitation voltage where no nonlinear effects occur.

The best results in the sense of maximum sensitivity were obtained by cantilever C_100, with an excitation voltage of $1.5 V_{pp}$. A linear frequency shift of 648 Hz was measured over three pressure decades, resulting in a sensitivity of 216 Hz/decade. Normalised to the resonant frequency of 47.4 kHz, this means a frequency shift of 0.46%/decade in linear approximation. By decreasing the excitation voltage, the saturation effect can be delayed. Thus, the measurement range increases at the expense of sensitivity. Depending on the application, a reasonable compromise between sensitivity and measurement range can be adjusted by choosing an appropriate excitation voltage. Furthermore, the size of the hysteresis loop, given by the difference of the peak frequencies in both directions, is strongly affected by the ambient pressure (see Figure 8b,d). Qualitatively, this measurement shows the same behaviour as the peak frequency. The absolute values are smaller because the shift in the other sweep direction is subtracted, and therefore the sensitivity (change of measurement value with pressure) is slightly smaller. An advantage of this measurement principle could be that environmental factors such as temperature effects or long-term drift effects influencing the resonance frequency can be cancelled out more easily [26–29]. Other parameters, such as, e.g., peak amplitudes, are also affected by the ambient pressure [8], but the absolute change is relatively small and more difficult to detect. For this reason, the frequency measurement is preferable. A measurement series investigating the stability of the frequencies results in a standard deviation of 2.6 Hz (corresponding to 56 ppm), and therefore provides a reliable measure for detecting the ambient pressure.

A comparison with results obtained in previous works is shown in Table 3, ranking the performance of the presented AlN nonlinear micro-oscillator. Since the plot in Figure 8 is on a logarithmic scale, a nonlinear behaviour to the measured variable, the ambient pressure, can clearly be seen. Thus, it can be deduced that the sensitivity decreases with

increasing pressure, when linearising this value for the individual pressure decades. The results indicate that the sensitivity related to the resonance frequency is exceeding the values obtained in the previous works, for nearly all pressure ranges, or else it is at least comparable. A special feature is the wide measurement range down to the high vacuum regime where most mechanical sensor principles have their limitations. In this low-pressure area, our sensor exhibits its highest sensitivity.

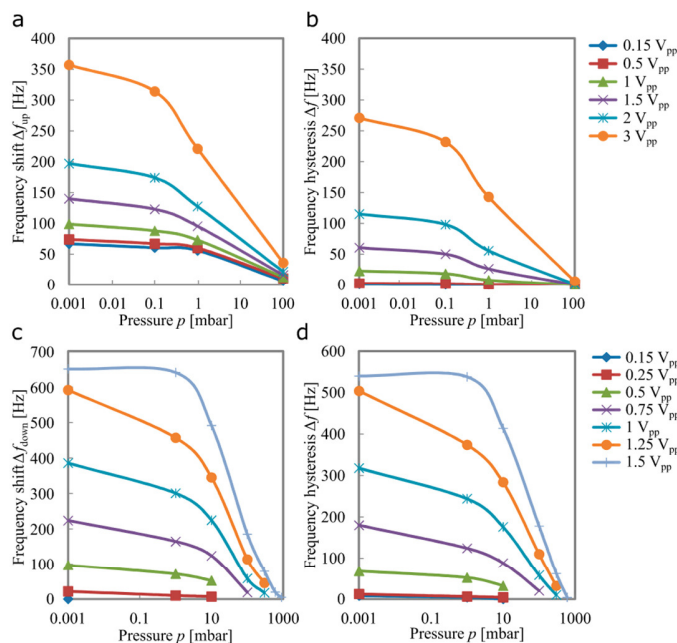


Figure 8. Frequency shift caused by the Duffing effect in dependency of the ambient pressure for the 2nd roof-tile-shaped mode of C_33 (a) and C_100 (c) for varying excitation voltages. Frequency hysteresis between the sweep directions in dependency of the ambient pressure for the 2nd roof-tile-shaped mode of C_33 (b), and C_100 (d) for varying excitation voltages.

Table 3. Comparison of the key parameters for different pressure sensing systems.

Sensor	Measurement Range [mbar]	Sensitivity [Hz/mbar]	Sensitivity [ppm/mbar]	Measurement Principle	Resonance Frequency
Zuo [30]	50–2000	16.5	0.1	AIN Contour mode resonator	140 MHz
Wang [31]	100–4000	221	0.27	AIN Contour mode resonator	820 MHz
Anderas [32]	0.1–500	360	0.4	AIN Contour mode resonator	900 MHz
Rodriguez-Madrid [33]	1000–4000	330	0.03	AIN Surface acoustic wave resonator	10.8 GHz
Han [34]	0.01–2000	1.9	35	Capacitive oscillator with piezoelectric read out	53 kHz
Shi [35]	100–1500	8	94	Capacitive oscillator with piezoelectric read out	85 kHz
This work C_100	1–10	17	362	Duffing nonlinearity	47 kHz
	10–100	3.4	72		
U = 1.5 V _{pp}	100–900	0.23	4.9		
This work C_100	0.001–1	136	2894	Duffing nonlinearity	47 kHz
	1–10	13	277		
	10–100	2.6	55		
U = 1.25 V _{pp}	100–300	0.35	7.4		

In the next steps, the gas type dependence will be investigated by characterising the sensor under different gas atmospheres as well as the temperature influence of the measurement principle. A further work which investigates the nonlinear effect of different geometries and modes to optimise the sensor response can already be found in [36].

5. Conclusions

In this study, we analysed the frequency response of a cantilever structure with different piezoelectric AlN coverage sizes. The resonance behaviour was investigated with a focus on the nonlinear Duffing effect. The strength of the nonlinearity was experimentally identified, and the Duffing parameters were determined for each AlN coverage size and for each eigenmode. Based on these results, the 2nd roof-tile-shaped mode, which was found to be the best mode according to the stiffness parameters, was selected for pressure measurements over a wide range of six decades. The quantity with the strongest correlation to the ambient pressure was found to be the frequency shift of the peak amplitude. For the 2nd roof-tile-shaped mode, a maximum sensitivity of 0.29%/mbar for the high-vacuum regime was experimentally found. In addition, the influence of the excitation voltage was shown, revealing the possibility of adjusting the sensitivity and measurement range depending on the specific application. Compared to the other measurement principles presented in the paper, the frequency shift induced by the Duffing effect of piezoelectrically actuated MEMS oscillators offers a significantly higher sensitivity, exceeding existing work, especially in the high-vacuum range.

The current state of the art for high-dynamic-range pressure sensing in vacuum chamber applications usually requires a combination of several high cost sensors (e.g., Pirani and membrane). The new principle introduced in this work, using the Duffing-effect-induced frequency shift of a micro-oscillator to obtain high-quality pressure measurements, opens up an opportunity for a new class of wide range vacuum sensors, which can be fabricated in a much more cost-effective way. Alternatively, the size of the hysteresis loop can also be exploited with the same type of sensor, giving the advantage of reducing environmental factors such as temperature effects or long-term drift. In future work, the fundamentals behind the strong Duffing effect of the selected mode need to be clarified more precisely, as well as the influence of the actuator coverage size on the spring softening or spring hardening behaviour.

Author Contributions: Investigation, T.Z. and M.S.; Data curation, T.Z.; Project administration A.A. and H.S.; Funding acquisition A.A. and H.S., Writing- original draft T.Z. and H.S.; Writing—review & editing, T.Z. and H.S. All authors have read and agreed to the published version of the manuscript.

Funding: This research was funded by the German Science Foundation (DFG) within the grant SE 1425/14-1.

Institutional Review Board Statement: Not applicable.

Informed Consent Statement: Not applicable.

Data Availability Statement: Data available on request.

Acknowledgments: We thank Frank Tiefensee and Jorge Oevermann from the Fraunhofer Society for providing access to the laser vibrometer.

Conflicts of Interest: The authors declare that there is no conflict of interest.

References

1. Aikele, M.; Bauer, K.; Ficker, W.; Neubauer, F.; Prechtel, U.; Schalk, J.; Seidel, H. Resonant accelerometer with self-test. *Sens. Actuator A Phys.* **2001**, *92*, 161–167. [[CrossRef](#)]
2. Binnig, G.; Quate, C.F.; Gerber, C. Atomic force microscope. *Phys. Rev. Lett.* **1986**, *56*, 930–934. [[CrossRef](#)]
3. Chen, S.T.; Du, S.; Arroyo, E.; Jia, Y.; Seshia, A. Utilising Nonlinear air damping as a soft mechanical stopper for MEMS vibration energy harvesting. *J. Phys. Conf. Ser.* **2016**, *773*, 012098. [[CrossRef](#)]
4. Almog, R.; Zaitsev, S.; Shtempluck, O.; Buks, E. Signal amplification in a nanomechanical Duffing resonator via stochastic resonance. *Appl. Phys. Lett.* **2007**, *90*, 013508. [[CrossRef](#)]

5. Sharma, M.; Sarraf, E.H.; Baskaran, R.; Cretu, E. Parametric resonance: Amplification and damping in MEMS gyroscopes. *Sens. Actuator A Phys.* **2012**, *177*, 79–86. [[CrossRef](#)]
6. Li, Y.; Li, H.; Xiao, Y.; Cao, L.; Guo, Z. A compensation method for nonlinear vibration of silicon-micro resonant sensor. *Sensors* **2021**, *21*, 2545. [[CrossRef](#)]
7. Hasan, M.; Alsaleem, F.; Oukad, H. Novel threshold pressure sensors based on nonlinear dynamics of MEMS resonators. *J. Micromech. Microeng.* **2018**, *28*, 065007. [[CrossRef](#)]
8. Keskar, G.; Elliott, B.; Gaillard, J.; Skove, M.J.; Rao, A.M. Using electric actuation and detection of oscillations in microcantilevers for pressure measurements. *Sens. Actuator A Phys.* **2008**, *147*, 203–209. [[CrossRef](#)]
9. Kacem, N.; Arcamone, J.; Perez-Murano, F.; Hentz, S. Dynamic range enhancement of nonlinear nanomechanical resonant cantilevers for highly sensitive NEMS gas/mass sensor applications. *J. Micromech. Microeng.* **2010**, *20*, 045023. [[CrossRef](#)]
10. Green, P.L.; Worden, K.; Atallah, K.; Sims, N.D. The effect of Duffing-type non-linearities and Coulomb damping on the response of an energy harvester to random excitations. *J. Intell. Mater. Syst. Struct.* **2012**, *23*, 2039–2054. [[CrossRef](#)]
11. Millar, S.; Desmulliez, M. MEMS ultra low leak detection methods: A review. *Sens. Rev.* **2009**, *29*, 339–344. [[CrossRef](#)]
12. Martínez Rojas, J.A.; Fernández, J.L.; Sánchez Montero, R.; López Espí, P.L.; Díez-Jimenez, E. Model-based systems engineering applied to trade-off analysis of wireless power transfer technologies for implanted biomedical microdevices. *Sensors* **2021**, *21*, 3201. [[CrossRef](#)]
13. Ayela, F.; Fournier, T. An experimental study of anharmonic micromachined silicon resonators. *Meas. Sci. Technol.* **1998**, *9*, 1821–1830. [[CrossRef](#)]
14. Nabholz, U.; Heinzlmann, W.; Mehner, J.E.; Degenfeld-Schonburg, P. Amplitude- and gas pressure-dependent nonlinear damping of high-Q oscillatory MEMS micro mirrors. *J. Microelectromech. Syst.* **2018**, *27*, 383–391. [[CrossRef](#)]
15. Lifshitz, R.; Cross, M.C. Nonlinear Dynamics of Nanomechanical and Micromechanical Resonators. In *Review of Nonlinear Dynamics and Complexity*; John Wiley & Sons: Hoboken, NJ, USA, 2008.
16. Duffing, G. *Erzwungene Schwingungen bei Veränderlicher Eigenfrequenz und ihre Technische Bedeutung*; Vieweg & Sohn: Braunschweig, Germany, 1918.
17. Tajaddodianfar, F.; Yazdi, M.R.H.; Pishkenari, H.N. Nonlinear dynamics of MEMS/NEMS resonators: Analytical solution by the homotopy analysis method. *Microsyst. Technol.* **2017**, *23*, 1913–1926. [[CrossRef](#)]
18. Mahmoodi, S.N.; Jalili, N.; Daqaq, M.F. Modeling, nonlinear dynamics, and identification of a piezoelectrically actuated microcantilever sensor. *IEEE ASME Trans. Mechatron.* **2008**, *13*, 58–65. [[CrossRef](#)]
19. McHugh, K.; Dowell, E. Nonlinear responses of inextensible cantilever and free-free beams undergoing large deflections. *J. Appl. Mech.* **2018**, *85*, 051008. [[CrossRef](#)]
20. Villanueva, L.G.; Karabalin, R.B.; Matheny, M.H.; Chi, D.; Sader, J.E.; Roukes, M.L. Nonlinearity in nanomechanical cantilevers. *Phys. Rev. B* **2013**, *87*, 024304. [[CrossRef](#)]
21. Ababneh, A.; Schmid, U.; Hernando, J.; Sánchez-Rojas, J.L.; Seidel, H. The influence of sputter deposition parameters on piezoelectric and mechanical properties of AlN thin films. *Mater. Sci. Eng. B Solid State Mater. Adv. Technol.* **2010**, *172*, 253–258. [[CrossRef](#)]
22. Davis, W.O. Measuring quality factor from a nonlinear frequency response with jump discontinuities. *J. Microelectromech. Syst.* **2011**, *20*, 968–975. [[CrossRef](#)]
23. Qiu, H.; Schwarz, P.; Völm, H.; Feili, D.; Wu, X.; Seidel, H. Electrical crosstalk in two-port piezoelectric resonators and compensation solutions. *J. Micromech. Microeng.* **2013**, *23*, 045007. [[CrossRef](#)]
24. Kucera, M.; Wistrela, E.; Pfusterschmied, G.; Ruiz-Diez, V.; Manzanque, T.; Sánchez-Rojas, J.L.; Schalk, J.; Bittner, A.; Schmid, U. Characterization of a roof tile-shaped out-of-plane vibrational mode in aluminum-nitride-actuated self-sensing micro-resonators for liquid monitoring purposes. *Appl. Phys. Lett.* **2014**, *104*, 233501. [[CrossRef](#)]
25. Sanchez-Rojas, J.L.; Hernando, J.; Donoso, A.; Bellido, J.; Manzanque, T.; Ababneh, A.; Seidel, H.; Schmid, U. Modal optimization and filtering in piezoelectric microplate resonators. *J. Micromech. Microeng.* **2010**, *20*, 055027. [[CrossRef](#)]
26. Kim, B.; Candler, R.N.; Hopcroft, M.A.; Agarwal, M.; Park, W.T.; Kenny, T.W. Frequency stability of wafer-scale encapsulated MEMS resonators. *Sens. Actuator A Phys.* **2007**, *136*, 125–131. [[CrossRef](#)]
27. Prikhodko, I.; Trusov, A.; Shkel, A. Compensation of drifts in high-Q MEMS gyroscopes using temperature self-sensing. *Sens. Actuator A Phys.* **2013**, *201*, 517–524. [[CrossRef](#)]
28. Tanner, D.; Olsson, R., III; Parson, T.; Crouch, S.; Walraven, J.; Ohlhausen, J. Stability experiments on MEMS aluminum nitride RF resonators. *Proc. SPIE* **2010**, *7592*, 759209.
29. Defoort, M.; Taheri-Tehrani, P.; Horsley, D.A. Exploiting nonlinear amplitude-frequency dependence for temperature compensation in silicon micromechanical resonators. *Appl. Phys. Lett.* **2016**, *109*, 153502. [[CrossRef](#)]
30. Zuo, J.; Zhang, H.; Chang, Y.; Liang, J.; Pang, W.; Duan, X. Highly sensitive AlN contour-mode resonator-based pressure sensor for in-line monitoring of chemical reactions. In Proceedings of the 20th International Conference on Solid-State Sensors, Actuators and Microsystems & Eurosensors XXXIII (TRANSDUCERS & EUROSENSORS XXXIII), Berlin, Germany, 23–27 June 2019; pp. 1373–1376.
31. Wang, T.; Tang, Z.; Lin, H.; Zhan, K.; Wan, J.; Wu, S.; Gu, Y.; Luo, W.; Zhang, W. A low temperature drifting acoustic wave pressure sensor with an integrated vacuum cavity for absolute pressure sensing. *Sensors* **2020**, *20*, 1788. [[CrossRef](#)]

32. Anderås, E.; Katardjiev, I.; Yantchev, V. Lamb wave resonant pressure micro-sensor utilizing a thin-film aluminium nitride membrane. *J. Micromech. Microeng.* **2011**, *21*, 085010. [[CrossRef](#)]
33. Rodríguez-Madrid, J.G.; Iriarte, G.F.; Williams, O.A.; Calle, F. High precision pressure sensors based on SAW devices in the GHz range. *Sens. Actuator A Phys.* **2013**, *189*, 364–369. [[CrossRef](#)]
34. Han, X.; Mao, Q.; Zhao, L.; Li, X.; Li, W.; Yang, P.; Wang, Y.; Yan, X.; Wang, S.; Zhu, N.; et al. Novel resonant pressure sensor based on piezoresistive detection and symmetrical in-plane mode vibration. *Microsyst. Nanoeng.* **2020**, *6*, 95. [[CrossRef](#)]
35. Shi, X.; Lu, Y.; Xie, B.; Li, Y.; Wang, J.; Chen, D.; Chen, J. A resonant pressure microsensor based on double-ended tuning fork and electrostatic excitation/piezoresistive detection. *Sensors* **2018**, *18*, 2494. [[CrossRef](#)] [[PubMed](#)]
36. Zengerle, T.; Stopp, M.; Ababneh, A.; Seidel, H. Investigations on nonlinearities of roof-tile shape modes for pressure measurement applications. In Proceedings of the 21th International Conference on Solid-State Sensors, Actuators and Microsystems, TRANSDUCERS 21, Online, 20–25 June 2021.

6.8 Oxygen Concentration Sensor (Unpublished Data)

The precise measurement of the oxygen concentration is an essential component in many applications. These include the monitoring of air quality [148] or within biological and chemical decomposition processes [149], as well as in the (automotive) engine control [150]. Both physical and chemical measurement methods are available and are used according to the specification of the application (accuracy, measuring range, long-term stability, ...).

Among the chemical sensor principles, so-called electrochemical cells are widely used, which are characterized by high accuracy and compactness. Due to the chemical mechanism, however, these sensors exhibit a drift, which must be compensated repeatedly by means of calibration. Much more robust are the lambda sensors, which are used in automotive applications. Here, the oxygen concentration is determined via the O₂ ion current through a heated solid electrolyte (ZrO₂). The only disadvantage here is the heating power required to bring the sensor up to an operating temperature above 350 °C [151]. The most precise and reliable measurement methods are the physical sensing principles using spectroscopy [152] and the paramagnetic effect. For the evaluation of the paramagnetic effect of oxygen, both mechanical [153] and anemometric [19] methods are common which have already been implemented in MEMS designs. The disadvantages of these methods are the relatively high complexity of the sensor design and the sensitivity to mechanical vibrations.

In the following chapter, a novel sensor concept for the detection of oxygen concentration based on MEMS oscillators is presented. First, the magnitude of the measurement effect due to a change of the oxygen concentration is predicted numerically and then it is investigated experimentally. Finally, the paramagnetic effect of oxygen is analyzed by generating a strong magnetic field in the periphery of the MEMS oscillator. For testing, different oxygen concentrations were obtained in the vacuum chamber by mixing dry air containing 20.5 % oxygen with pure nitrogen.

6.8.1 Numerical Investigation

Prior to the experimental investigations, finite element simulations were performed to approximate the effect of a changing oxygen concentration on the characteristic values of the micro-oscillator, resonance frequency f_r and quality factor Q . Therefore, the physical and thermal properties (density, dynamic viscosity and heat conductivity, abbreviated PTP) of the nitrogen-oxygen mixture PTP_{mix} were written according to the superposition principle as function of the oxygen concentration in the following manner:

$$PTP_{mix} = PTP_{O_2} \cdot c_{O_2} + PTP_{N_2} \cdot (1 - c_{N_2}), \quad (6.9)$$

with PTP_{O_2} , PTP_{N_2} , the corresponding physical or thermal property and, c_{O_2} , c_{N_2} the associated concentration of oxygen O₂ and nitrogen N₂, respectively.

In addition to the magnitude of the effect, a parameter study was performed to optimize the sensor geometry. Figure 47a and b show the influence of the oscillator size. In both cases, it can be seen that an increase of the width and the length of the oscillator structure has a positive influence on the sensitivity. The measurement signal is the change of the resonance frequency with respect to the 0 % oxygen value (corresponding to 100 % nitrogen). The magnitude of the change is in the

range of up to 0.15 % with an oscillator placed in the center of the 1 mm gap of the magnetic circuit structure (see Figure 31). The distance to a geometrical boundary is therefore about 500 μm in both directions. When the oscillator is moved away from this center, the measurement effect increases strongly (see Figure 47c). Due to the reduction of the gap width, the damping effect increases and changes in the physical and thermal properties (especially viscosity) appear much stronger [96]. In this case, a slight influence on the quality factor can be observed. All other geometrical changes (length or width of the micro-oscillator), have no significant influence on the quality factor reduction with increasing oxygen concentration. The decrease of the quality factor was always in the range of about 3 % between a pure nitrogen atmosphere with 0 % oxygen and dry air with 20.5 %.

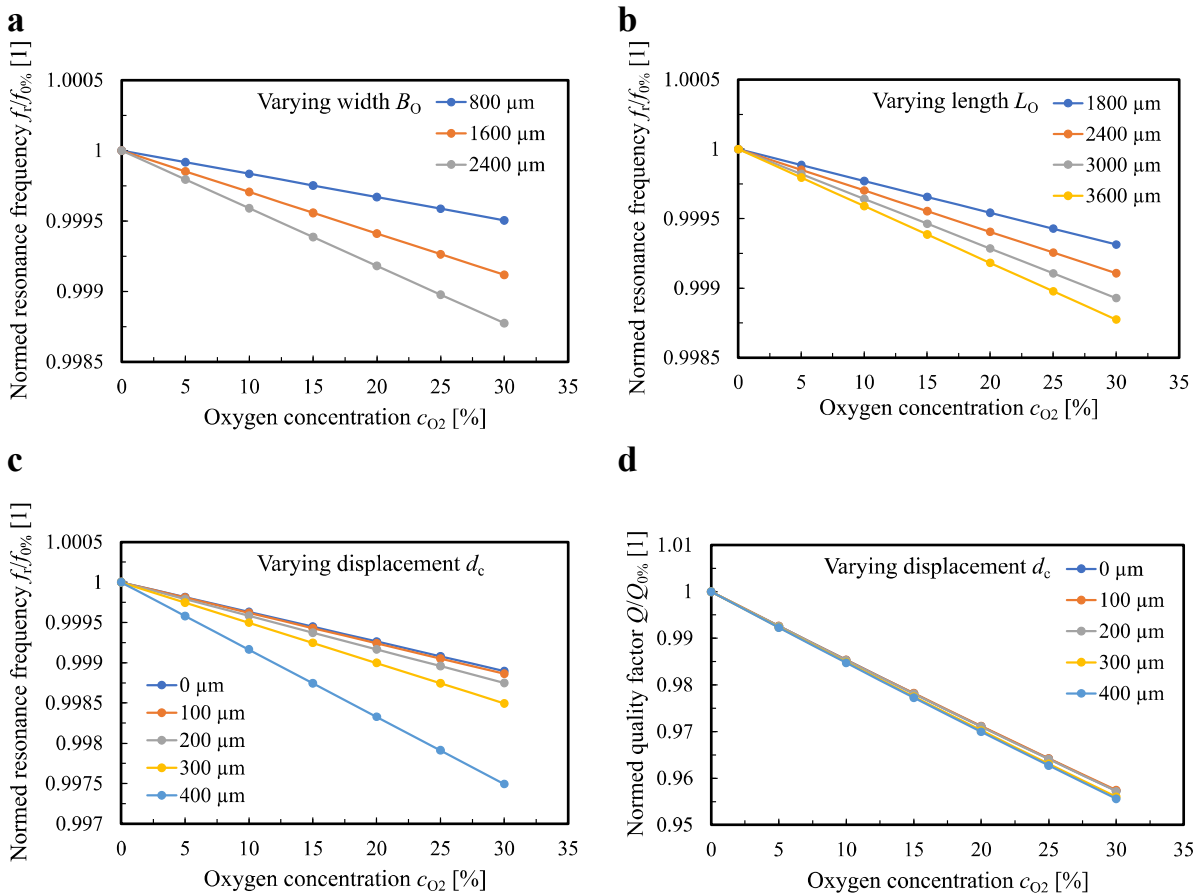


Figure 47. Numerical investigation of the sensor response for varying geometry. The base structure is a cantilever with a length of 3600 μm and a width of 2400 μm . In (a) and (b), the change of the resonance frequency is shown as function of the oxygen concentration for varying width and length, respectively. In (c) and (d), the influence on the resonance frequency and the quality factor by a varying sensor displacement from the center of the gap is illustrated.

In a next step, the influence of the paramagnetic oxygen enrichment in the periphery of the micro-oscillator was estimated. Therefore, the whole volume of the strong magnetic field in-between the flattened pyramid structure ($2.5 \times 2.5 \times 1 \text{ mm}^3$) was assumed to enrich with an additional oxygen concentration c_{para} , exceeding the ambient oxygen concentration c_{O_2} . In the literature, comparable

paramagnetic oxygen enrichment experiments with a product of magnetic field and magnetic field gradient of $563 \text{ T}^2/\text{m}$ were performed by Cai *et al.* [154]. In these experiments, an absolute enrichment of oxygen of 0.62 % was reported. Our coils are capable to produce a magnetic field in the strength of 1.02 T with gap width of 1 mm leading to a product of $1040 \text{ T}^2/\text{m}$ (*cf.* Figure 34). Therefore, an enrichment of up to 1 % can be assumed for the simulations.

In Figure 48, the change of the characteristic value due to an increase of the oxygen concentration in the previously mentioned volume around the micro-oscillator is depicted. Due to the reason that the increase of oxygen concentration is much smaller than in the previous investigations, the decrease is in the range of just a few ppm for the resonance frequency and about one permille for the quality factor, respectively. For both cases, the influence of the background oxygen concentration was additionally investigated regarding a possible use of the enrichment for determining the oxygen concentration. The resonance frequency clearly possesses no dependency on the ambient oxygen concentration. The quality factor on the other hand shows a small dependence, which is however below the standard deviation of the measurement value and therefore below the detectability limit of the micro-oscillator.

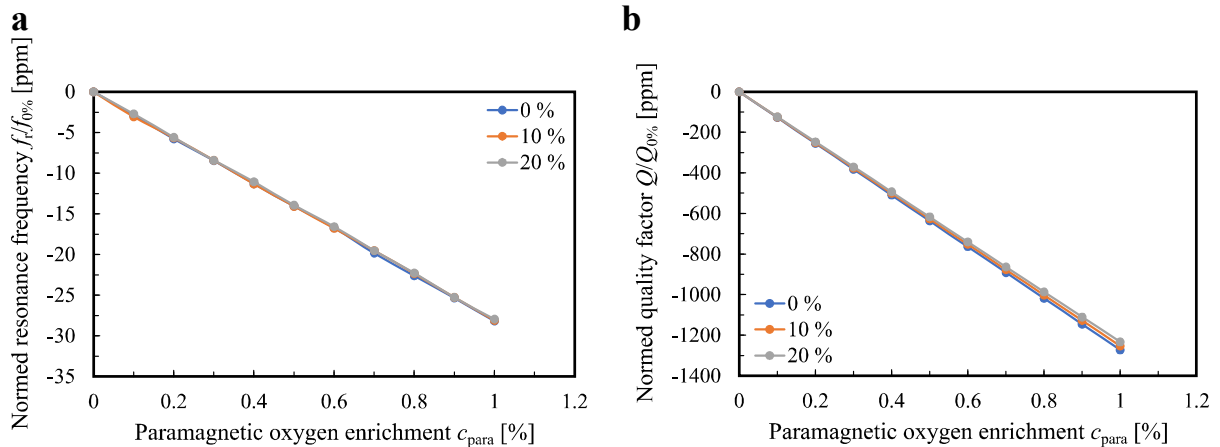


Figure 48. Change of the resonance frequency and quality factor due to a paramagnetic oxygen enrichment in the vicinity of the micro-oscillator for different background oxygen concentrations.

6.8.2 Oxygen Concentration Detection

The measurements focusing on the oxygen concentration were performed in the vacuum chamber with defined oxygen concentrations in the range from 0 % up to 20.5 %. The different concentrations were produced by a dry air-nitrogen -mixture and controlled by an electrochemical oxygen sensor (ME2-O2- Φ 20 from *Winsen Electronics Technology*). This sensor is only applicable at a pressure range around the normal atmosphere ($1013 \text{ mbar} \pm 10 \%$) and was therefore used at a pressure level of 900 mbar to check the oxygen concentration of the gas mixture. The accuracy of the sensor is given by the manufacturer to be 2 % of the output value [155].

For these measurements, two micro-oscillators with a cantilever shape structure and geometrical dimension as listed in Table 11 were chosen. Besides the fundamental bending mode, the next three higher bending modes were investigated. The resonance behavior of these micro-oscillators was characterized in the viscous damping regime in a pressure range from 100 mbar up to 900 mbar.

Table 11. List of the measured micro-oscillators for the oxygen concentration detection and their geometric parameters as well as the resonance frequency and the associated bending modes.

Name	L_0 [μm]	B_0 [μm]	T [μm]	α [1]	Mode	f_r [kHz]
O1	3600	2400	15	0.83	1. BM	1.71
					2. BM	10.7
					3. BM	29.9
					4. BM	58.5
O2	2400	1200	10	1	1. BM	2.47
					2. BM	13.6
					3. BM	36.2
					4. BM	71.6

In Figure 49, the resonance frequency and the quality factor plot are shown as function of the ambient pressure of the gas mixture with various oxygen concentrations. The resonance frequency reveals a linear trend which slightly distinguish between the oxygen concentrations with increasing pressure. The quality factor plot indicates a reciprocal behavior to the square root of the pressure up to 700 mbar. This is consistent with the previous investigations in the viscous flow regime (see Section 6.4.2). For a higher pressure, the damping is dominated by the squeeze film effect indicated by the plateau in the quality factor plot (*cf.* Section 2.3.5).

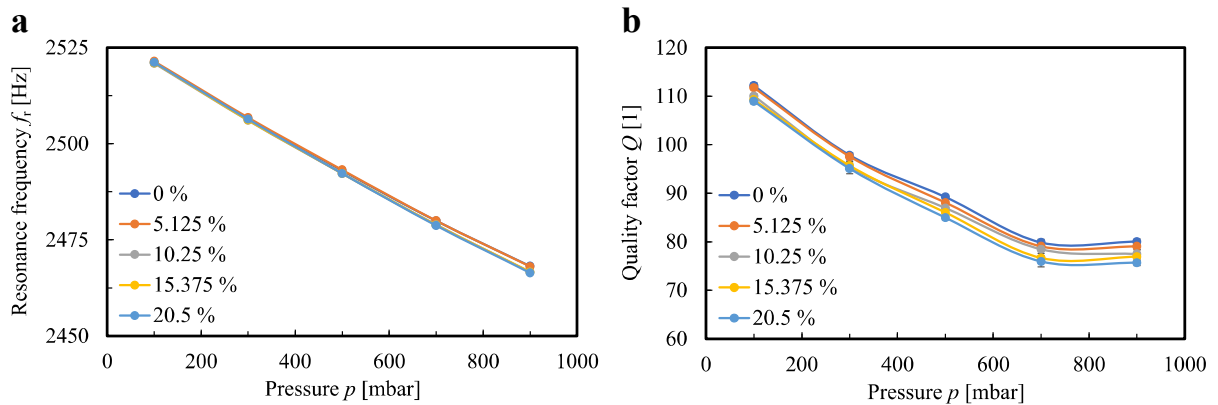


Figure 49. Resonance frequency and quality factor plot of sensor O2 versus the ambient pressure for various oxygen concentrations.

In the following, the small deviations between the resonance frequency and quality factor plots of the different oxygen concentrations are evaluated. In order to compare the decrease between different pressure levels and bending modes, the values are presented normalized to the pure nitrogen atmosphere with no oxygen components. In Figure 50, the experimental results for the decrease of the resonance frequency and of the quality factor with an increasing oxygen concentration are shown for micro-oscillator O1. The reduction of the resonance frequency is in the range of up to 700 ppm for the first bending mode at a pressure level of 900 mbar. This leads to a linearized sensitivity of 34 ppm/% oxygen. Taking the standard deviation of 42 ppm of the resonance frequency into account, this means a resolution of the oxygen concentration of 1.2 %. At lower pres-

sures the damping effects are reduced and therefore the effect of the increasing oxygen concentration is decreasing. The same can be observed for the higher bending modes. Due to the lower damping losses, the relative reduction of the resonance frequency is also lower.

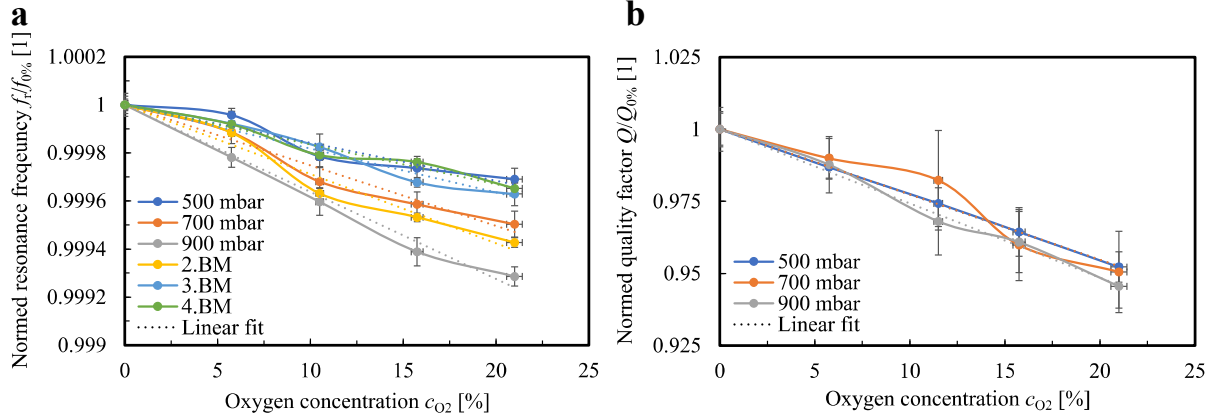


Figure 50. Experimental results for the change of the resonance frequency (a) and the quality factor (b) regarding the zero percent oxygen value as function of the oxygen concentration for sensor O1.

The evaluation of the quality factor shows comparable results for the different pressure levels. This is in accordance with the numerical results, which predict a decrease of about 3 % (related to the zero percent oxygen value $Q_{0\%}$) regardless of the pressure level and geometry (*cf.* Figure 47d). The sensitivity can be calculated from the reduction of the quality factor of about 5 % to be 0.25 %/% oxygen. A disadvantage is the significantly higher standard deviation of 1 %, which leads to a resolution of just 4 % oxygen concentration.

Additionally, a second micro-oscillator was investigated to confirm the results and to gain knowledge about the performance of an altered geometry (see Figure 51). As predicted by the numerical results, a smaller oscillator structure leads to a smaller sensitivity of the sensor. The results reveal a decrease of the resonance frequency by 400 ppm over the entire measurement range, which means 19.5 ppm/% oxygen. The decrease of the quality factor is in the same range as micro-oscillator O2. This confirms the numerical results, which predicted no significant influence of the geometry on the reduction of the quality factor with the oxygen concentration.

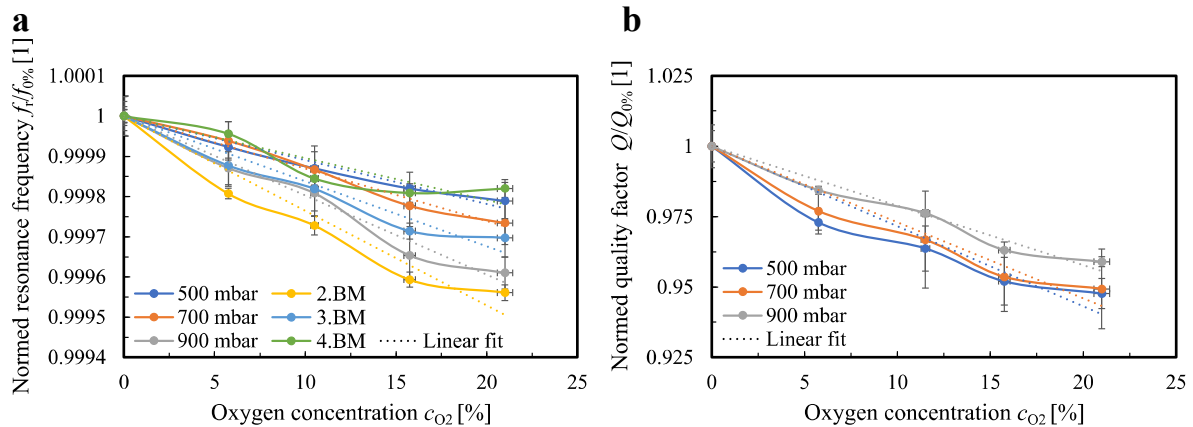


Figure 51. Experimentally determined change of the resonance frequency (a) and quality factor (b) with regard to the zero percent oxygen value as function of the oxygen concentration for sensor O2.

6.8.3 Paramagnetic Effect

In the last section, the measurement concerning the paramagnetic effect of oxygen will be discussed. Therefore, micro-oscillator O1 was chosen for this measurement because of the higher sensitivity. According to the literature and to the numerical simulations, an enrichment of less than 1 % is to be expected leading to a shift of the resonance frequency in the range of a few ppm and one permille for the quality factor (*cf.* Figure 48). This is slightly under the resolution limit determined in the previous chapter, regarding the detection of the oxygen concentration. Nevertheless, the measurements reveal a significant effect by the magnetic field surrounding the micro-oscillator.

In Figure 52, the resonance curves of sensor O1 recorded in a dry air atmosphere are depicted, indicating a clear effect on the damping behavior. The resonance curves are on the one hand shifting to higher frequencies and on the other hand increasing in the peak amplitude with increasing magnetic flux density. Both effects representing a decrease of the damping or an increase of the quality factor, respectively. This is at first contradictory to the assumption of an enrichment of oxygen and a subsequent increase of damping. Therefore, an additional measurement with a pure nitrogen atmosphere was performed. Here, no effect was expected because of the absence of paramagnetic gas molecules.

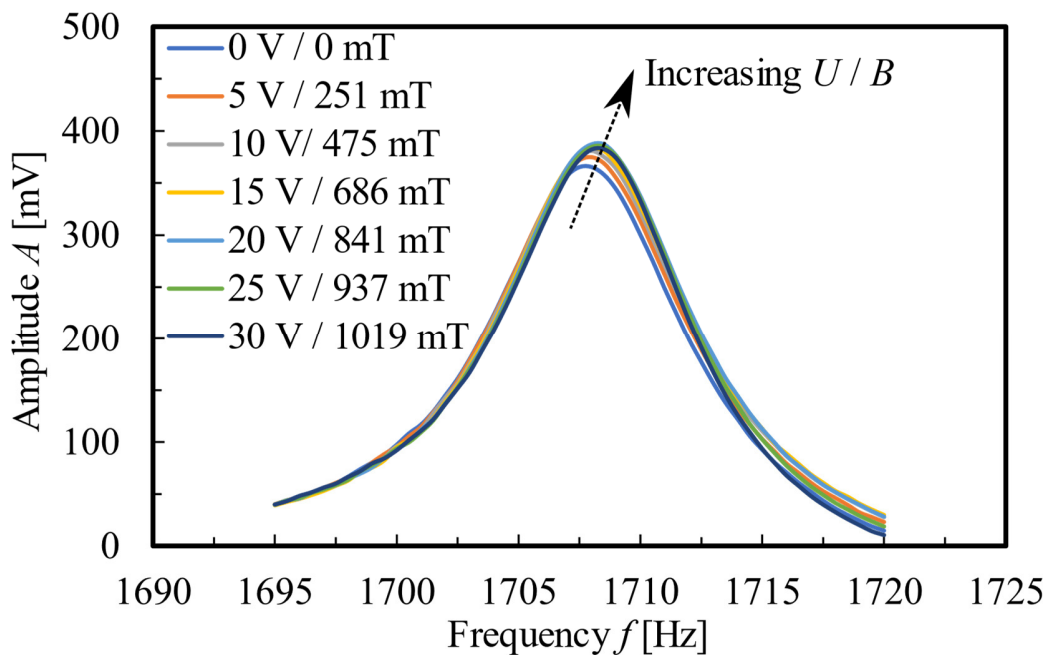


Figure 52. Recorded resonance curve of the 1st bending of micro-oscillator O1 in air for different operating voltages of the coils, respectively magnetic flux densities. The peak of the resonance curve is shifting to the top and right for increasing magnetic flux density.

Figure 53 shows the measurement results for the resonance frequency and of the quality factor of sensor O1 for both dry air and for a pure nitrogen atmosphere. Unexpectedly, the same effect is also found in the nitrogen atmosphere. In both cases, an increase of the resonant frequency and the quality factor with the magnetic field is shown.

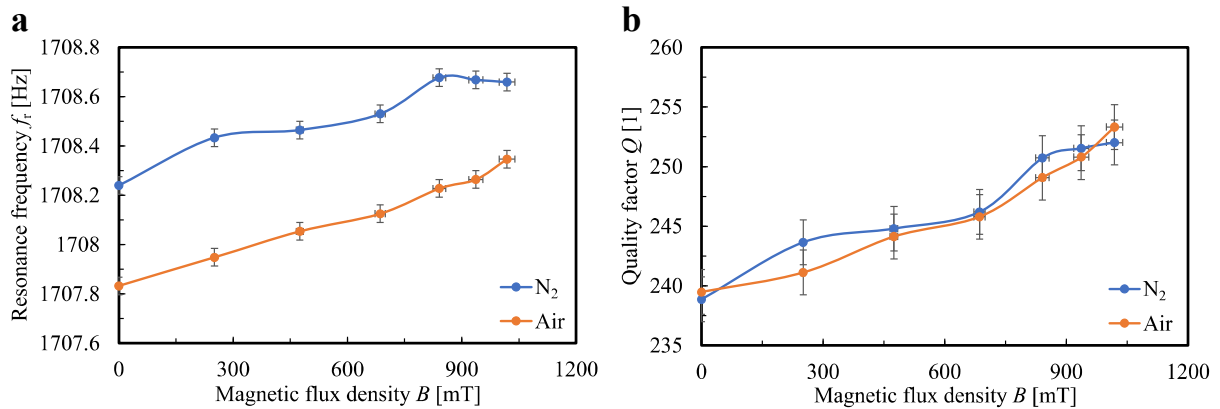


Figure 53. Measured shift of the resonance frequency (a) and quality factor (b) of micro-oscillator O1 as function of the magnetic flux density for two different gas atmospheres.

Since none of the materials used in the sensor exhibit any magnetic interaction, a direct influence by the magnetic field can be excluded. To confirm this, the measurements were repeated under slight negative pressure and revealed no significant shift of the resonance frequency and quality factor below 700 mbar within the limits of measurement accuracy (see Figure 54). One explanation is therefore that the opposite effect, the magnetic repulsion of the nitrogen components, predominates. Nitrogen as a diamagnetic gas molecule is displaced from the magnetic field by the force. This displacement results in a local gas medium with less dissipative effect due to fewer gas molecules to interact with the micro-oscillator. The magnetic effect of displacement of nitrogen thus completely masks the enrichment effect of oxygen. In order to fully resolve this, measurements with a higher oxygen content than 21% are required, which was not possible within the experimental setup for safety reasons.

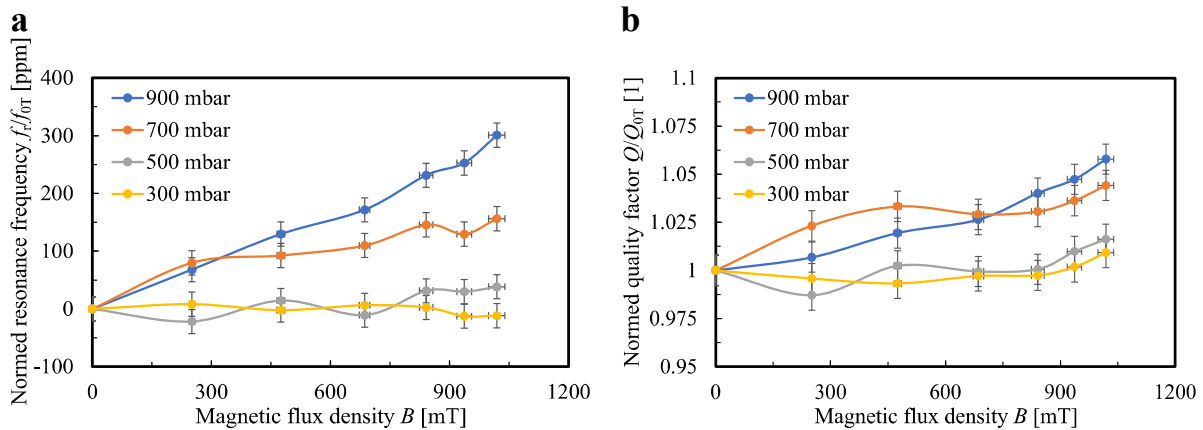


Figure 54. Normed change (relative to the 0 T value) of the resonance frequency (a) and quality factor (b) under the effect of an external magnetic field for various pressure levels.

7 Summary

In the presented thesis, piezoelectric oscillating microstructures and their dissipation mechanisms to the surrounding medium were systematically examined. Therefore, three different micro-oscillator structures, paddle, bending and cantilever, with different geometric parameters were investigated in nine different gas atmospheres. Additionally, the influence of a neighboring wall in spatial distance of 150 μm up to 3500 μm was examined. The ambient pressure of the different gas atmospheres ranged from high vacuum ($p = 0.001$ mbar) up to 900 mbar. Besides the fundamental bending mode, which was mainly explored, higher bending modes and more complex eigenmodes such as the roof-tile modes were studied. Based on the results, the thesis offers analytical approaches for the description of micro-oscillators, numerical calculations on the damping phenomena and new models for the description of individual effects. The results of each are briefly summarized in the following.

Analytical Modelling

At first, the basic properties of the gas atmospheres were presented and a brief review on the state of the art of the analytical expressions for the damping mechanism was given. Based on the model of a linear harmonic oscillator and fundamental mechanics, an analytical approach was introduced describing the three different shapes of oscillating structures. Moreover, the model was expanded for the nonlinear case and the three different effects causing the nonlinearity were discussed.

Numerical Simulations

Next, the analytical formalism for the calculation of the resonance frequency was proofed by numerical finite element simulations. Subsequently, the damping phenomena of the viscous flow regime were added by taking a solid-fluid interaction into account. The behavior of the micro-oscillator in a gas atmosphere was calculated using a linearized Navier-Stokes equations in an eigenfrequency step. In the case of a liquid environment, the full equation set was taken and solved in the time domain. Thus, the damping of the sensor could also be considered in the design stage, besides the eigenfrequency of the eigenmodes. Finally, numerical calculations were performed on the design of a magnetic field concentrator to generate a high magnetic flux density above 1 T in a spatially confined space in-between a gap of 1 mm.

Sensor Manufacturing

The micro-oscillators were fabricated in a cleanroom environment simultaneously in a large number within a batch process on a 4" silicon wafer. Therefore, standard microtechnology processes were used and the piezoelectric material AlN was deposited with a reactive sputter deposition. All steps of the manufacturing chain were presented and classified in terms of their relevance to the entire process. The most critical steps with influence on the eigenfrequency and the damping behavior (thickness and residual/initial bending) were especially highlighted and investigated with different measuring methods.

Experimental Details

The characterization of the damping behavior of the micro-oscillators were performed in a custom-build vacuum chamber. As gas atmosphere, the four noble gases He, Ne, Ar and Kr and the polyatomic gases H₂, N₂, N₂O, CO₂ and SF₆ were selected. In addition, dry air was used for proof measurements on the applicability of the micro-oscillators as oxygen sensors. This set of gases represents a wide range of physical and thermal properties that can be obtained from gases. The measurements were carried out in two different setups which were implemented within the chamber. One setup is a construction for setting a defined gap width in the range of 150 μm up to 3500 μm between the micro-oscillator and a geometrical boundary given by an Al plate. The other is a magnetic circuit with a magnetic concentrator which generates a very strong magnetic field in a volume of 2.5 × 2.5 × 1 mm³ around the micro-oscillator. The magnetic field can either be generated by FeNdB permanent magnets or by coils. Furthermore, the electronic circuit for recording the resonance curves, from which the damping is calculated, is also presented.

Measurement Results

The measurement results are further subdivided and cover different aspects of the dissertation. First, the results for the molecular flow regime are discussed, followed by the findings in the transitional flow regime. Subsequently, two sections are presented that deal with the modeling of the total damping over the entire pressure range. Finally, the results are compared to the investigations in liquids and, moreover, two possible applications for the micro-oscillators as pressure sensors and oxygens detector are proposed.

Molecular Flow Regime

The experimental results of the measurements focusing on the molecular flow regime revealed an interesting behavior of polyatomic gas molecules. In dependence of the gap width, the data points of the polyatomic gas molecules deviated significantly from the linear trend of the molecular quality factor versus the reciprocal square root of the molecular mass. As was shown, this deviation could be attributed to the number of active and thus available degrees of freedom. A higher number of degrees of freedom leads to an increase in the heat capacity, which is associated with a lower thermal dissipation flux. The quality factor of polyatomic gases thus exceeds the linear curve defined by the noble gases. By investigating the deviation as a function of the gap width and including the thermal velocity of flight, the temporal evolution of the polyatomic degrees of freedom was determined. The results obtained for the time constants of the rotational degrees of freedom showed very good agreement with values available in the literature. By extending the molecular damping model with this phenomenon, it was possible to represent the molecular damping of all gases from the squeeze film damping range up to 3500 μm. Thus, the gap between the theories of Bao *et al.* for small distances and Christian for a free oscillator was closed.

Transitional Flow Regime

For the transitional flow regime, a new model working with thermal resonance effects within the gap was proposed. This approach is adapted in analogy to the solid-state model of Zener for intrinsic friction losses based on thermal resonances. The resonance frequency was adapted for the case of a gas atmosphere and derived on the principle of a constructive standing wave. Thus, a good agreement between the analytical approach and the experimental data was achieved. A further evaluation of the obtained fit parameters showed some clear correlations with the thermal properties of the gases and led to a physically well-founded justification of the approach. Especially at the resonance point where maximum dissipation into the surrounding medium occur, many thermal properties could be revealed. A dependence of the minimum of the quality factor on the thermal diffusivity as well as a dependence of the resonance pressure on the adiabatic index was found. For that reason, noble gases exhibit a significantly higher dissipative effect in the transition region than polyatomic gases due to the fewer degrees of freedom and associated lower heat capacity. The polyatomic gases are in general heavier and therefore slower as well as have a higher heat capacity due to additional rotational and vibrational degrees of freedom, which means that heat is better stored in the medium than transported away.

Generalized Model

A generalization by applying the model to quality factor plots of different oscillators and higher bending modes was achieved. The fitting of the model showed a good agreement for all plots and allowed a further analysis of the frequency behavior and mode dependency of the individual damping mechanism. The evolution of thermal and viscous damping with an increasing gap width could be described by a saturation function whose characteristic value correlates with the thickness of the viscous and the thermal boundary layer. The viscous effects show a range of influence in the order of 8 to 15 times of the thickness of the viscous boundary layer. An important measure for the strength of the damping is given by the interaction area and thus the oscillator surface. The thermal losses have a longer range of influence in the order of 20 to 30 times the thickness of the thermal boundary layer. Furthermore, a strong decrease of the thermal losses with an increasing resonance frequency was observed, whereby higher modes are subject to fewer losses due to thermal resonance effects.

Equivalent Circuit Model

Further simplification of the damping model was achieved by introducing an equivalent circuit. Analogies as typical in lumped element modeling were made and a complete representation of the damping effects by electrical components was accomplished. For the transition regime, an inductive constant phase element consisting of a series of resistors and coils was designed and derived in an analytical expression using a recursive approach. The fit shows very good agreement for all data and allows a completely new perspective on the analysis of the damping losses. By splitting the data into real and imaginary parts, it was thus possible to distinguish between dissipative and kinetic losses, for example.

Measurement in Liquids

In addition, the damping of the fundamental bending mode in gases and liquids was compared for one micro-oscillator structure. The results showed that the damping phenomena both, in liquids and gases, scale with the same dependence on the properties of the media. However, the interesting finding is that the damping in liquids is relatively lower than in gases assuming the same values for the properties. Adding the values for small gaps, the squeeze film damping, a continuous curve could be obtained between the media. This suggests that at the phase transition between liquid and gases, a regime of the squeeze film damping must be overcome.

Wide-Range Pressure Sensor

A novel sensor concept for the measurement of the ambient pressure exploiting the nonlinear range of the micro-oscillator was presented. For this purpose, the effect of the tilt of the resonance curve was investigated in detail as a function of the pressure. By recording the resonance curves in both frequency sweep directions, a hysteresis behavior became visible which clearly scales with the strength of the damping due to the ambient pressure. With the nonlinear frequency shift and the frequency hysteresis, two measurement quantities were presented which scale sensitively with the ambient pressure. The measuring principle is applicable over a wide-range up to six pressure decades and shows, unlike conventional mechanical measuring principles, its highest sensitivity in the high-vacuum range. In addition, the sensitivity can be adjusted in tradeoff with the measurement range via the actuation voltage.

Oxygen Concentration Sensor

Finally, a measurement methodology for the detection of oxygen concentration was presented. The sensing principle uses the increase of the damping due to a higher oxygen content. The measurements show a shift of the resonance frequency in the order of a few ppm, which in relation to the frequency stability leads to a measurement resolution of about 1 % oxygen. The evaluation of the decrease of the quality factor resulted in a clearly larger sensitivity of some percent. However, this measurand is subject to a larger fluctuation, thus only a resolution of about 4 % oxygen could be achieved. A subsequent investigation of the paramagnetic effect of oxygen showed a reversed behavior than expected. Due to the significantly higher nitrogen content in the gas atmosphere, an increase in the resonance frequency and the quality factor for an increasing magnetic flux density was observed. This is related to the displacement of the diamagnetic nitrogen, which means that fewer gas molecules are available to damp the oscillator via collisions.

8 Outlook

Research is always an ongoing process and despite many presented results not completely finished. In the following, aspects are listed which were not feasible within the scope of the thesis, but which contain further interesting questions that are worth more detailed investigations.

The damping effects were mainly investigated in pure and dry gas atmospheres. Only the measurements concerning the oxygen sensor technology included a gas mixture of nitrogen and oxygen. Since in many technical applications gas mixtures are present, this is an interesting point which still needs to be investigated. Furthermore, the influence of humidity and temperature of the gas should be included. This could answer the question of how great the influence of the ambient parameters (background gas, humidity, temperature) is on the response of the sensor.

Equally interesting is the study of the damping of different states of matter of a substance, such as liquid and gaseous nitrogen. For this purpose, measurements were carried out in both media, but only with different substances. For the completeness of the theory and verification of the assumption of a transition from liquid to gas form over a squeeze film regime, these measurements are required. In addition, the mixture of different states of matter such as aerosols (smoke, particles) or emulsions (milk) is feasible. This opens the possibility to realize many other sensors based on the damping effects of micro-oscillators for safety and monitoring applications, as well as for air quality measurements. For example, particle detection of smoke has already been demonstrated [156].

The measurements of liquids could be extended by two further aspects. On the one hand, the investigation of non-Newtonian liquids which could show interesting effects in the interaction with the oscillator motion. And on the other hand, the investigation of the temperature influence especially in comparison to the gases. For the damping in liquids mainly the dynamic viscosity is responsible which has a completely different temperature dependency for gases and liquids. The dynamic viscosity of gases is increasing nearly linear with temperature whereas in liquids the dynamic viscosity is exponentially dropping with an increasing temperature.

The presented equivalent circuit requires further investigation for a more precise description of the individual components. For this purpose, some proportionalities have already been deduced from the results. However, the description is not complete and still needs a geometry study to derive the dependencies of the lumped elements on the oscillator geometry.

Finally, an extension of the electronics with a phase-locked loop (PLL) is required so that real-time measurements of the resonance frequency as well as the quality factor are possible.

In the scope of this dissertation, some open questions in the wide field of the damping of micro-oscillators have been addressed and answered. Although there are still some open points, this work contributes to the description of the fundamental effects of the different damping mechanisms and gives some approaches for the development of novel gas sensors based on a physical mechanism of action.

Bibliography

- [1] G. Binning, C. Quate and C. Gerber, "Atomic force microscope," *Physical Review Letters*, vol. 56, no. 9, pp. 930 - 934, 1986.
- [2] H. Lang, M. Hegner and C. Gerber, "Microfabricated cantilever array sensors for (bio-) chemical detection," in *Applied Scanning Probe Methods IV. NanoScience and Technology*, Berlin, Springer, 2006, pp. 183 - 213.
- [3] V. Mortet, "Wide range pressure sensor based on a piezoelectric bimorph microcantilever," *Applied Physics Letters*, vol. 88, no. 133511, pp. 1 - 3, 2006.
- [4] X. Zhao, Z. Shang, G. Luo and L. Deng, "A vibration energy harvester using AlN piezoelectric cantilever array," *Microelectronic Engineering*, vol. 142, pp. 47 - 51, 2015.
- [5] J. van Beek and R. Puers, "A review of MEMS oscillators for frequency reference and timing applications," *Journal of Micromechanics and Microengineering*, vol. 22, no. 013001, pp. 1 - 35, 2011.
- [6] B. Kim, R. Candler, M. Hopcroft, M. Agarwal, W. Park and T. Kenny, "Frequency stability of wafer-scale film encapsulated silicon based MEMS resonators," *Sensors and Actuators A: Physical*, vol. 136, no. 1, pp. 125 - 131, 2007.
- [7] R. Elfrink, M. Renaud, T. Kamel, C. de Nooijer, M. Jambunathan, M. Goedbloed, D. Hohlfeld, S. Matova, V. Pop and L. Caballero, "Vacuum-packaged piezoelectric vibration energy harvesters: damping contributions and autonomy for a wireless sensor system," *Journal of Micromechanics and Microengineering*, vol. 20, no. 10, pp. 1 - 7, 2010.
- [8] A. Ababneh, U. Schmid, J. Hernando, J. Sanchez-Rojas and H. Seidel, "The influence of sputter deposition parameters on piezoelectric and mechanical properties of AlN thin films," *Materials Science and Engineering: B*, vol. 172, no. 3, pp. 253 - 258, 2010.
- [9] J. Toledo, T. Manzaneque, V. Ruiz-Diez, F. Jimenez-Marquez, M. Kucera, G. Pfusterschmied, E. Wistrela, U. Schmid and J. Sanchez-Rojas, "Comparison of in-plane and out-of-plane piezoelectric microresonators for real-time monitoring of engine oil contamination with diesel," *Microsystem Technologies*, vol. 22, pp. 1781 - 1790, 2016.
- [10] G. Karniadakis, A. Beskok and N. Aluru, *Microflows and Nanoflows: Fundamentals and Simulation*, New York, USA: Springer, 2005.

- [11] B. Rapp, "Chapter 9 - Fluids," in *Microfluidics: Modeling, Mechanics and Mathematics*, Amsterdam, Netherlands, Elsevier, 2017, pp. 243 - 263.
- [12] M. Wiemer and M. Bender, "Vacuum Technology," in *The Vacuum Technology Book*, Asslar, Germany, Pfeiffer Vacuum , 2008, pp. 26 - 183.
- [13] K. Jousten, *Wutz Handbuch Vakuumtechnik*, Wiesbaden, Germany: Springer Vieweg, 2018.
- [14] E. Lemmon, M. McLinden and D. Friend, "Thermophysical properties of fluid systems," NIST, [Online]. Available: <https://webbook.nist.gov/chemistry/fluid/>. [Accessed 01 September 2021].
- [15] N. W. Tschoegl, "Equilibrium thermodynamics," in *Fundamentals of Equilibrium and Steady-State Thermodynamics*, Pasadena, USA, Elsevier, 2000, pp. 83-88.
- [16] W. Demtröder, "Mechanik und Wärme," in *Experimentalphysik 1*, Kaiserslautern, Germany, Springer Spektrum, 2014, pp. 186-208.
- [17] L. Pauling, "Apparatus for determining the partial pressure of oxygen in a mixture of gases". Us Patent 2,416,344, 25 February 1947.
- [18] P. Krippner, M. Wetzko, P. Szasz, B. Andres and T. Bauer, "MEMS based paramagnetic oxygen measurement," *TRANSDUCERS 2007 - 2007 International Solid-State Sensors, Actuators and Microsystems Conference*, pp. 2393-2396, 2007.
- [19] S. Vonderschmidt and J. Müller, "A fluidic bridge based MEMS paramagnetic oxygen sensor," *Sensors and Actuators B: Chemical*, vol. 188, pp. 20-30, 2013.
- [20] A. C. Manning, R. F. Keeling and J. Severinghaus, "Precise atmospheric oxygen measurements with a paramagnetic oxygen analyzer," *Global Biogeochemical Cycles*, vol. 13, no. 4, pp. 1107-1115, 1999.
- [21] W. M. Haynes, *CRC Handbook of Chemistry and Physics*, 95. ed., CRC Press, 2014.
- [22] H. Shaftel, R. Jackson, S. Callery and D. Bailey, "Carbon dioxide - NASA: climate change," NASA's Jet Propulsion Laboratory, [Online]. Available: <https://climate.nasa.gov/vital-signs/carbon-dioxide/>. [Accessed 22 Mai 2020].
- [23] K. Song, T. Tagawa, L. Wang and H. Ozoe, "Numerical investigation for the modeling of the magnetic buoyancy force during the natural convection of air in a square enclosure," *Advances in Mechanical Engineering*, pp. 1 -11, 2014.

- [24] S. Ueno and M. Iwasaka, "Properties of magnetic curtain produced by magnetic fields," *Journal of Applied Physics*, vol. 67, no. 9, pp. 5901 - 5903, 1990.
- [25] N. Wakayama, "Behavior of gas flow under gradient magnetic fields," *Journal of Applied Physics*, vol. 69, no. 4, pp. 2734 - 2736, 1991.
- [26] S. Alrasheed, "Oscillatory motion," in *Principles of Mechanics: Fundamental University Physics*, Jeddah, Saudi Arabia, Springer, 2019, pp. 155-171.
- [27] A. F. J. Levi, "Transient dynamics of driven oscillation," in *Essential Classical Mechanics for Device Physics*, California, USA, Morgan & Claypool Publishers, 2016.
- [28] Z. Qiu, T. Qu, Y. Pan, Y. Jia, Z. Fan, K. Yang, J. Yuan and H. Luo, "Optical and electrical method characterizing the dynamic behavior of the fused silica cylindrical resonator," *Sensors*, vol. 19, no. 2928, 2019.
- [29] R. Blevins, "Formulas for natural frequency and mode shape," Florida, USA, Krieger Publishing Company, 1995, pp. 101-113.
- [30] W. Young and R. Budynas, "Roark's formulas for stress and strain," New York, USA, McGraw-Hill Education, 2001, pp. 799-812.
- [31] A. Boisen, S. Dohn, S. Keller, S. Schmid and M. Tenje, "Cantilever-like micromechanical sensors," *Reports on Progress in Physics*, vol. 74, no. 3, 2011.
- [32] V. Ruiz-Diez, J. Toledo, J. Hernando-Garcia, A. Ababneh, H. Seidel and J. Sanchez-Rojas, "A geometrical study on the roof tile-shaped modes in AlN-based piezoelectric microcantilevers as viscosity–density sensors," *Sensors*, vol. 19, no. 3, 2019.
- [33] S. Timoshenko, *Vibration problems In engineering*, Wolfenden Press, 2008.
- [34] A. Labuschagne, N. van Rensburg and A. van der Merwe, "Comparison of linear beam theories," *Mathematical and Computer Modelling*, vol. 49, no. 1-2, pp. 20-30, 2009.
- [35] G. Duffing, "Erzwungene Schwingungen bei veränderlicher Eigenfrequenz und ihre technische Bedeutung," *Sammlung Vieweg*, vol. 41/42, 1918.
- [36] L. Cveticanin, "Analysis techniques for the various forms of the Duffing equation," in *The Duffing Equation: Nonlinear Oscillators and their Behaviour*, Southampton, UK, John Wiley & Sons, 2011, pp. 81-138.

- [37] F. Tajaddodianfar, M. Yazdi and H. Pishkenari, "Nonlinear dynamics of MEMS/NEMS resonators: analytical solution by the homotopy analysis method," *Microsystem Technologies*, vol. 23, pp. 1913-1926, 2017.
- [38] T. Kalmar-Nagy and B. Balachandran, "Forced harmonic vibration of a Duffing oscillator with linear viscous damping," in *The Duffing Equation: Nonlinear Oscillators and their Behaviour*, Southampton, UK, John Wiley & Sons, 2011, pp. 139-174.
- [39] K. McHugh and E. Dowell, "Nonlinear responses of inextensible cantilever and free-free beams undergoing large deflections," *Journal of Applied Mechanics*, vol. 85, no. 5, 2018.
- [40] L. Villanueva, R. Karabalin, M. Matheny, D. Chi, J. Sader and M. Roukes, "Nonlinearity in nanomechanical cantilevers," *PHYSICAL REVIEW B*, vol. 87, no. 1/2, 2013.
- [41] H. Cho, B. Jeong, M. Yu, F. Vakakis, D. McFarland and L. Bergman, "Nonlinear hardening and softening resonances in micromechanical cantilever-nanotube systems originated from nanoscale geometric nonlinearities," *International Journal of Solids and Structures*, vol. 49, no. 15/16, pp. 2059-2065, 2012.
- [42] S. Mahmoodi, N. Jalili and M. Daqaq, "Modeling, nonlinear dynamics, and identification of a piezoelectrically actuated microcantilever sensor," *IEEE/ASME Transactions on Mechatronics*, vol. 13, no. 1, pp. 58-65, 2008.
- [43] A. Kulygin, C. Kirsch, P. Schwarz, U. Schmid and H. Seidel, "Decoupled surface micromachined gyroscope with single-point suspension," *Journal of Microelectromechanical Systems*, vol. 21, no. 1, pp. 206 - 216, 2012.
- [44] U. Nabholz, W. Heinzlmann, J. Mehner and P. Degenfeld-Schonburg, "Amplitude- and gas pressure-dependent nonlinear damping of high-Q oscillatory MEMS micro mirrors," *Journal of Microelectromechanical Systems*, vol. 27, no. 3, pp. 383-391, 218.
- [45] J. Rodriguez, S. Chandorkar, G. Glaze, D. Gerrard, Y. Chen, D. Heinz, I. Flader and T. Kenny, "Direct detection of anchor damping in MEMS tuning fork resonators," *Journal of Microelectromechanical Systems*, vol. 27, no. 5, pp. 800-809, 2018.
- [46] L. Villanueva and S. Schmid, "Evidence of surface loss as ubiquitous limiting damping mechanism in SiN micro- and nanomechanical resonators," *Physical Review Letters*, vol. 113, no. 227201, 2014.
- [47] J. Rodriguez, S. Chandorkar, C. Watson, G. Glaze, C. Ahn, E. Hg, Y. Yang and T. Kenny, "Direct detection of Akhiezer damping in a silicon MEMS resonator," *Scientific Reports*, vol. 9, no. 2244, 2019.

- [48] R. Candler, A. Duwel, M. Varghese, S. Chandorkar, M. Hopcroft, W. Park, B. Kim, G. Yama, A. Partridge, M. Lutz and T. Kenny, "Impact of geometry on thermoelastic dissipation in micromechanical resonant beams," *Journal of Microelectromechanical Systems*, vol. 15, no. 4, pp. 927-934, 2006.
- [49] H. Qiu, A. Ababneh, D. Feili, X. Wu and H. Seidel, "Analysis of intrinsic damping in vibrating piezoelectric microcantilevers," *Microsystem Technologies*, vol. 22, pp. 2017-2025, 2016.
- [50] C. Zener, "Internal friction in solids: I. Theory of internal friction in reeds," *Physical Review*, vol. 52, no. 3, pp. 230-235, 1937.
- [51] C. Zener, "Internal friction in solids: II. General theory of thermoelastic internal friction," *Physical Review*, vol. 53, no. 1, pp. 90-99, 1937.
- [52] R. Lifshitz and M. Roukes, "Thermoelastic damping in micro- and nanomechanical systems," *Physical Review B*, vol. 61, no. 8, pp. 5600-5609, 2000.
- [53] R. Christian, "The theory of oscillating-vane vacuum gauges," *Vacuum*, vol. 16, no. 4, pp. 175-178, 1966.
- [54] S. Bianco, M. Cocuzza, S. Ferrero, E. Giuri, G. Piacenza, C. Pirri, A. Ricci, L. Scaltrito, D. Bich, A. Meriardo, P. Schina and R. Correale, "Silicon resonant microcantilevers for absolute pressure measurement," *Journal of Vacuum Science & Technology B*, vol. 24, no. 4, pp. 1803-1809, 2006.
- [55] M. Martin, B. Houston, J. Baldwin and M. Zalalutdinov, "Damping models for microcantilevers, bridges, and torsional resonators in the free-molecular-flow regime," *Journal of Microelectromechanical Systems*, vol. 17, no. 2, pp. 503-511, 2008.
- [56] G. Tang and X. Gu, "Lattice Boltzmann simulation of nonequilibrium effects in oscillatory gas flow," *Physical Review E*, vol. 78, no. 8, 2008.
- [57] B. Boom, A. Bertolini, E. Hennes and J. van den Brand, "Gas damping in capacitive MEMS transducers in the free molecular flow regime," *Sensors*, vol. 21, no. 7, 2021.
- [58] W. Newell, "Miniaturization of tuning forks," *Science*, vol. 167, no. 3848, pp. 1320-1326, 1968.
- [59] K. Kokubun, M. Hirata, M. Ono, H. Murakami and Y. Toda, "Unified formula describing the impedance dependence of a quartz oscillator on gas pressure," *Journal of Vacuum Science & Technology A*, vol. 5, pp. 2450-2453, 1987.

- [60] F. Blom, S. Bouwstra, M. Elwenspoek and J. Fluitman, "Dependence of the quality factor of micromachined silicon beam," *Journal of Vacuum Science & Technology B*, vol. 10, pp. 19-26, 1992.
- [61] M. Bao, H. Yang, H. Yin and Y. Sun, "Energy transfer model for squeeze-film air damping in low vacuum," *Journal of Micromechanics and Microengineering*, vol. 12, no. 3, pp. 341-346, 2002.
- [62] J. Lee, S. Lee, C. Yao and W. Fang, "Comments on the size effect on the microcantilever quality factor in free air space," *Journal of Micromechanics and Microengineering*, vol. 17, no. 1, pp. 139-146, 2006.
- [63] H. Hosaka, K. Itao and S. Kuroda, "Damping characteristics of beam-shaped micro-oscillators," *Sensors and Actuators A: Physical*, vol. 49, no. 1-2, pp. 87-95, 1995.
- [64] W. Zhang and K. Turner, "Frequency dependent fluid damping of micro/nano flexural resonators: Experiment, model and analysis," *Sensors and Actuators A: Physical*, vol. 134, no. 2, pp. 594-599, 2007.
- [65] J. Vignola, J. Judge, J. Jarzynski, M. Zalalutdinov, B. Houston and J. Baldwin, "Effect of viscous loss on mechanical resonators designed for mass detection," *Applied Physics Letters*, vol. 88, no. 4, 2006.
- [66] J. Judge, J. Vignola and J. Jarzynski, "Dissipation from microscale and nanoscale beam resonators into a surrounding fluid," *Applied Physics Letters*, vol. 92, no. 12, 2008.
- [67] J. Sader, "Frequency response of cantilever beams immersed in viscous fluids with applications to the atomic force microscope," *Journal of Applied Physics*, vol. 84, no. 1, pp. 64 - 76, 1998.
- [68] I. Dufour, E. Lemaire, B. Caillard, H. Debeda, C. Lucat, S. Heinrich, F. Josse and O. Brand, "Effect of hydrodynamic force on microcantilever vibrations: Applications to liquid-phase chemical sensing," *Sensors and Actuators B: Chemical*, vol. 192, pp. 664-672, 2014.
- [69] G. Aoust, R. Levy, B. Bourgeteau and O. Le Traon, "Acoustic damping on flexural mechanical resonators," *Sensors and Actuators A: Physical*, vol. 238, pp. 158-166, 2016.
- [70] R. Agarwal and K. Yun, "Burnett equations for simulation of transitional flows," *Applied Mechanics Review*, vol. 55, no. 3, pp. 219 - 240, 2002.
- [71] Z. Guo, B. Shi and C. Zheng, "An extended Navier-Stokes formulation for gas flows in the Knudsen layer near a wall," *Europhysics Letters*, vol. 80, no. 2, 2007.

- [72] A. Pandey, R. Pratap and F. Chau, "Effect of pressure on fluid damping in MEMS torsional resonators with flow ranging from continuum to molecular regime," *Experimental Mechanics*, vol. 48, pp. 91 - 106, 2008.
- [73] D. Ladiges and J. Sader, "Frequency-domain deviational Monte Carlo method for linear oscillatory gas flows," *Physics of Fluids*, vol. 27, no. 10, 2015.
- [74] J. Park, P. Bahukudumbi and A. Beskok, "Rarefaction effects on shear driven oscillatory gas flows: A direct simulation Monte Carlo study in the entire Knudsen regime," *Physics of Fluids*, vol. 16, no. 2, 2004.
- [75] R. Barber and D. Emerson, "Challenges in modeling gas-phase flow in microchannels: From slip to transition," *Heat Transfer Engineering*, vol. 27, no. 4, pp. 3 - 12, 2006.
- [76] H. Weng and C. Chen, "A challenge in Navier–Stokes-based continuum modeling: Maxwell–Burnett slip law," *Physics of Fluids*, vol. 20, no. 10, 2008.
- [77] F. Bao, J. Lin and X. Shi, "Burnett simulation of flow and heat transfer in micro Couette flow using second-order slip conditions," *Heat Mass Transfer*, vol. 43, pp. 559 - 566, 2007.
- [78] X. Gu and D. Emerson, "Modeling oscillatory flows in the transition regime using a high-order moment method," *Microfluidics and Nanofluidics*, vol. 10, pp. 389 - 401, 2010.
- [79] J. Lee, T. Wright, M. Abel and E. Sunden, "Thermal conduction from microcantilever heaters in partial vacuum," *Journal of Applied Physics*, vol. 101, no. 1, 2007.
- [80] C. Cai, "Heat transfer in vacuum packaged microelectromechanical system devices," *Physics of Fluids*, vol. 20, no. 1, 2008.
- [81] E. Salazar, "Energy propagation of thermal waves," *European Journal of Physics*, vol. 27, no. 6, pp. 1349 - 1355, 2006.
- [82] E. Marin, "On thermal waves," *European Journal of Physics*, vol. 34, no. 5, pp. 83 - 85, 2013.
- [83] E. Marin, L. Vaca-Oyola and O. Delgado-Vasallo, "On thermal waves' velocity: some open questions in thermal waves' physics," *Revista Mexicana De Fisica E*, vol. 62, no. 1, pp. 1 - 4, 2016.
- [84] R. Clausius, "Über eine veränderte Form des zweiten Hauptsatzes der mechanischen Wärmetheorie," *Annalen der Physik*, vol. 169, no. 12, pp. 481 - 506, 1854.

- [85] J. Shen and A. Mandelis, "Thermal-wave resonator cavity," *Review of Scientific Instruments*, vol. 66, no. 10, pp. 4999 - 5005, 1995.
- [86] J. Shen, A. Mandelis and T. Ashe, "Pyroelectric thermal-wave resonant cavity: A precision thermal diffusivity sensor for gases and vapors," *International Journal of Thermophysics*, vol. 19, no. 2, pp. 579 - 593, 1998.
- [87] M. Bao and H. Yang, "Squeeze film air damping in MEMS," *Sensors and Actuators A: Physical*, vol. 136, no. 1, pp. 3 - 27, 2007.
- [88] T. Veijola, H. Kuisma, J. Lahdenperä and T. Ryhänen, "Equivalent-circuit model of the squeezed gas film in a silicon accelerometer," *Sensors and Actuators A: Physical*, vol. 48, no. 3, pp. 239 - 248, 1995.
- [89] M. Bao, H. Yang, Y. Sun and P. French, "Modified Reynolds' equation and analytical analysis of squeeze-film air damping of perforated structures," *Journal of Micromechanics and Microengineering*, vol. 13, no. 6, pp. 795 - 800, 2003.
- [90] A. Pandey and R. Pratap, "Effect of flexural modes on squeeze film damping in MEMS cantilever resonators," *Journal of Micromechanics and Microengineering*, vol. 17, no. 12, pp. 2475 - 2484, 2007.
- [91] H. Qiu, P. Schwarz, D. Feili, X. Wu and H. Seidel, "Air damping of micro bridge resonator vibrating close to a surface with a moderate distance," *Journal of Micromechanics and Microengineering*, vol. 25, no. 5, pp. 1 - 9, 2015.
- [92] M. Lutz, A. Partridge, P. Gupta, N. Buchan, E. Klaassen, J. McDonald and K. Petersen, "MEMS oscillators for high volume commercial applications," in *TRANSDUCERS 2007 - 2007 International Solid-State Sensors, Actuators and Microsystems Conference*, Lyon, France, 2007.
- [93] D. Shaeffer, "MEMS inertial sensors: A tutorial overview," *IEEE Communications Magazine*, vol. 51, no. 4, pp. 100 - 109, 2013.
- [94] A. Frangi, P. Fedeli, G. Laghi, G. Langfelder and G. Gattere, "Near vacuum gas damping in MEMS: Numerical modeling and experimental validation," *Journal of Microelectromechanical Systems*, vol. 25, no. 5, pp. 890 - 899, 2016.
- [95] P. Fedeli, A. Frangi, G. Laghi, G. Langfelder and G. Gattere, "Near vacuum gas damping in MEMS: Simplified modeling," *Journal of Microelectromechanical Systems*, vol. 26, no. 3, pp. 632 - 642, 2017.

- [96] P. Schwarz, D. Feili, R. Engel, N. Pagel and H. Seidel, "Vacuum pressure and gas detection with a silicon based micromechanical squeeze film sensor," *Procedia Engineering*, vol. 5, pp. 750 - 753, 2010.
- [97] T. Manzaneque, V. Ruiz-Diez, J. Hernando-Garcia, E. Wistrela, M. Kucera, U. Schmid and J. Sanchez-Rojas, "Piezoelectric MEMS resonator-based oscillator for density and viscosity sensing," *Sensors and Actuators A: Physical*, vol. 220, pp. 305 - 315, 2014.
- [98] A. Maali, C. Hurth, R. Boisgard, C. Jai, T. Cohen-Bouhacina and J. Aime, "Hydrodynamics of oscillating atomic force microscopy cantilevers in viscous fluids," *Journal of Applied Physics*, vol. 97, no. 7, pp. 1 - 6, 2005.
- [99] O. Svitelskiy, V. Sauer, N. Liu, K. Cheng, E. Finley, M. Freeman and W. Hiebert, "Pressurized fluid damping of nanoelectromechanical systems," *Physical Review Letters*, vol. 103, no. 24, pp. 1 - 4, 2009.
- [100] J. Toledo, F. Jimenez-Marquez, J. Ubeda, V. Ruiz-Diez, G. Pfusterschmied, U. Schmid and J. Sanchez-Rojas, "Piezoelectric MEMS resonators for monitoring grape must fermentation," *Journal of Physics: Conference Series*, vol. 757, pp. 1 - 8, 2016.
- [101] O. Cakmak, E. Ermek, N. Kilinc, G. Yaralioglu and H. Urey, "Precision density and viscosity measurement using two cantilevers with different widths," *Sensors and Actuators A: Physical*, vol. 232, pp. 141 - 147, 2015.
- [102] Y. Tao, X. Li, T. Xu, H. Yu, P. Xu, B. Xiong and C. Wei, "Resonant cantilever sensors operated in a high-Q in-plane mode for real-time bio/chemical detection in liquids," *Sensors and Actuators B: Chemical*, vol. 157, no. 2, pp. 606 - 614, 2011.
- [103] O. Cakmak, C. Elbuken, E. Ermek, A. Mostafazadeh, I. Baris, B. Alaca, I. Kavakli and H. Urey, "Microcantilever based disposable viscosity sensor for serum and blood plasma measurements," *Methods*, vol. 63, no. 3, pp. 225 - 232, 2013.
- [104] A. Ali and J. Lee, "Piezoelectric-on-silicon square wine-glass mode resonator for enhanced electrical characterization in water," *IEEE Transactions on Electron Devices*, vol. 65, no. 5, pp. 1925 - 1931, 2018.
- [105] N. Khan and M. Ahamed, "Design and development of a MEMS butterfly resonator using synchronizing beam and out of plane actuation," *Microsystem Technologies*, vol. 26, pp. 1643 - 1652, 2020.
- [106] J. Zhang, F. Josse, S. Heinrich, N. Nigro, I. Dufour and O. Brand, "Resonant characteristics of rectangular hammerhead microcantilevers vibrating laterally in viscous liquid media,"

- European Frequency and Time Forum & International Frequency Control Symposium (EFTF/IFC)*, pp. 624 - 627, 2013 .
- [107] J. Anderson, "Governing equations of fluid dynamics," in *Computational fluid dynamics - An introduction*, Berlin, Springer-Verlag, 2009, pp. 15 - 51.
- [108] COMSOL Multiphysics, *Acoustics module user's guide*, Burlington, USA: COMSOL Inc..
- [109] COMSOL Multiphysics, *Vibrating micromirror with viscous and thermal damping*, Burlington, USA: COMSOL Inc..
- [110] D. Lide, G. Baysinger, L. Berger, R. Goldberg, H. Kehiaian, K. Kuchitsu, G. Rosenblatt , D. Roth and D. Zwillinger, *CRC Handbook of Chemistry and Physics*, Boca Raton, USA: Taylor & Francis Ltd, 2018.
- [111] Paragon Scientific Ltd., "General purpose viscosity reference standards," [Online]. Available: <https://www.paragon-sci.com/products-and-services/products/calibration-standards/viscosity-standards/general-purpose-viscosity-reference-standards.html>. [Accessed 18 August 2021].
- [112] AK Steel International, "ARMCO Telar 57 magnetic iron product data bulletin," 2019.
- [113] U. Schmid, A. Ababneh, H. Seidel, R. Wagner and K. Bauer, "Characterization of aluminium nitride and aluminium oxide thin films sputter-deposited on organic substrates," *Microsystem Technologies*, vol. 14, pp. 483 - 490, 2008.
- [114] H. Seidel, L. Csepregi, A. Heuberger and H. Baumgärtel, "Anisotropic etching of crystalline silicon in alkaline solutions: I. Orientation dependence and behavior of passivation layers," *Journal of The Electrochemical Society*, vol. 137, no. 11, pp. 3612 - 3626, 1990.
- [115] H. Seidel, L. Csepregi, A. Heuberger and H. Baumgärtel, "Anisotropic etching of crystalline silicon in alkaline solutions: II. Influence of dopants," *Journal of The Electrochemical Society*, vol. 137, no. 11, pp. 3626 - 2632, 1990.
- [116] H. Nazeer, H. Bhaskaran, L. Woldering and L. Abelmann, "Young's modulus and residual stress of GeSbTe phase-change thin films," *Thin Solid Films*, vol. 592, pp. 69 - 75, 2015.
- [117] G. Ross, H. Dong, C. Karuthedath, A. Sebastian, T. Pensala and M. Paulasto-Kröckel, "The impact of residual stress on resonating piezoelectric devices," *Materials & Design*, vol. 196, pp. 1 - 8, 2020.

- [118] A. Bale, S. Reddy and S. Tiwari, "Effect of residual stress on resonant frequency in nitinol based thin film resonator," in *Conference on Materials Science and Manufacturing Technology*, India, 2020.
- [119] T. Zengerle, A. Ababneh and H. Seidel, "Generalized damping model for MEMS oscillators from molecular to viscous flow regime," *Eng*, vol. 3, no. 1, pp. 124 - 141, 2022.
- [120] H. Qiu, P. Schwarz, H. Völlm, D. Feili and H. Seidel, "Electrical crosstalk in two-port piezoelectric resonators and compensation solutions," *Journal of Micromechanics and Microengineering*, vol. 23, no. 4, pp. 1 - 8, 2013.
- [121] S. Murad, Aufbau eines integrierten Lock-in Verstärker zur Messung gedämpfter Oszillationen, Saarbrücken: Universität des Saarlandes, 2019.
- [122] I. Djuemo, Bestimmung von Viskosität und Dichte mittels Messungen von AlN Resonatoren in Flüssigkeiten, Saarbrücken: Universität des Saarlandes, 2020.
- [123] J. Joppich, Untersuchung thermischer Resonanzeffekte und der Wärmediffusivität von Gasen im Bereich der Knudsenströmung, Saarbrücken: Universität des Saarlandes, 2018.
- [124] L. Landau and E. Lifshitz, "Statistical Physics," in *Course of Theoretical Physics*, Oxford, Pergamon Press, 1970, pp. 106 - 143.
- [125] T. Fließbach, "Statistische Physik," in *Lehrbuch zur Theoretischen Physik IV*, Heidelberg, Spektrum Akademischer Verlag, 2010, pp. 225 - 234.
- [126] L. Sutton, Tables of Interatomic Distances and Configuration in Molecules & Ions, London: The Chemical Society, 1965.
- [127] S. Alrasheed, "Principles of mechanics," in *Fundamental University Physics*, Cham, Springer, 2019, pp. 109 - 110.
- [128] J. Nash, "Vibrational modes of small molecules," Purdue University, 2013. [Online]. Available: <https://www.chem.purdue.edu/jmol/vibs/index.html>. [Accessed 02 November 2021].
- [129] I. Jobard and A. Chedin, "Critical analysis of the series expansion of the potential energy function of CO₂," *Journal of Molecular Spectroscopy*, vol. 57, no. 3, pp. 464 - 479, 1975.
- [130] J. Zúñiga, A. Bastida and A. Requena, "Theoretical calculations of vibrational frequencies and rotational constants of the N₂O isotopomers," *Journal of Molecular Spectroscopy*, vol. 217, no. 1, pp. 43 - 58, 2003.

- [131] C. Chapados and G. Birnbaum, "Infrared absorption of SF₆ from 32 to 3000 cm⁻¹ in the gaseous and liquid states," *Journal of Molecular Spectroscopy*, vol. 132, no. 2, pp. 323 - 351, 1988.
- [132] H. Kneser, "Schallabsorption in mehratomigen Gasen," *Annalen der Physik*, vol. 408, no. 3, pp. 337 - 349, 1933.
- [133] J. Opsal, "Fundamentals of thermal wave physics," in *Review of Progress in Quantitative Nondestructive Evaluation*, Boston, Springer, 1987, pp. 217 - 225.
- [134] T. Bechtold, G. Schrag and L. Feng, System-level modeling of MEMS, Weinheim, Germany: Wiley-VCH Verlag GmbH & Co. KGaA, 2013.
- [135] G. Schrag and G. Wachutka, "Physically based modeling of squeeze film damping by mixed-level system simulation," *Sensors and Actuators A: Physical*, Vols. 97 - 98, pp. 193 - 200, 2002.
- [136] K. Tao, L. Tang, J. Wu, S. Lye, H. Chang and J. Miao, "Investigation of multimodal electret-based MEMS energy harvester with impact-induced nonlinearity," *Journal of Micromechanics and Microengineering*, vol. 27, no. 2, pp. 276 - 288, 2018.
- [137] J. Jean, "The phasance concept: A review," *Current Topics in Electrochemistry*, vol. 4, pp. 127 - 136, 1997.
- [138] S. Holm, T. Holm and O. Martinsen, "Simple circuit equivalents for the constant phase element," *PLoS One*, vol. 16, no. 3, pp. 1 -12, 2021.
- [139] J. Toledo, V. Ruiz-Diez, G. Pfusterschmied, U. Schmid and J. Sanchez-Rojas, "Flow-through sensor based on piezoelectric MEMS resonator for the in-line monitoring of wine fermentation," *Sensors and Actuators B: Chemical*, vol. 254, pp. 291 - 298, 2018.
- [140] F. Patocka, C. Schneidhofer, N. Dörr, M. Schneider and U. Schmid, "Novel resonant MEMS sensor for the detection of particles with dielectric properties in aged lubricating oils," *Sensors and Actuators A: Physical*, vol. 315, no. 112290, pp. 1 - 13, 2020.
- [141] W. Xu, X. Zhang, S. Choi and J. Chae, "A high-quality-factor film bulk acoustic resonator in liquid for biosensing applications," *Journal of Microelectromechanical Systems*, vol. 20, no. 1, pp. 213 - 220, 2011.
- [142] P. Petersan and M. Anlage, "Measurement of resonant frequency and quality factor of microwave resonators: Comparison of methods," *Journal of Applied Physics*, vol. 84, no. 6, pp. 3392 - 3402, 1998.

- [143] S. Basak, A. Raman and S. Garimella, "Hydrodynamic loading of microcantilevers vibrating in viscous fluids," *Journal of Applied Physics*, vol. 99, no. 114906, pp. 1 - 10, 2006.
- [144] O. Svitelskiy, V. Sauer, D. Vick, K. Cheng, N. Liu, M. Freeman and W. Hiebert, "Nanoelectromechanical devices in a fluidic environment," *Physical Review E*, vol. 85, no. 056313, pp. 1 - 12, 2012.
- [145] L. Nguyen, P. Larsen, T. Larsen, S. Goswami, L. Villanueva, A. Boisen and S. Keller, "Pyrolytic carbon resonators for micromechanical thermal analysis," *Microsystems & Nanoengineering*, vol. 5, no. 58, pp. 1- 10, 2019.
- [146] F. Dams, Mikrotechnologische Strukturen zur Bestimmung druckabhängiger Gaseigenschaften für Anwendungen in der Vakuummesstechnik, Kiel: TU Kiel, 2015.
- [147] J. Rodríguez-Madrid, G. Iriarte, O. Williams and F. Calle, "High precision pressure sensors based on SAW devices in the GHz range," *Sensors and Actuators A: Physical*, vol. 189, pp. 364 - 369, 2013.
- [148] R. Ramamoorthy, P. Dutta and S. Akbar, "Oxygen sensors: Materials, methods, designs and applications," *Journal of Materials Science*, vol. 38, pp. 4271 - 4282, 2003.
- [149] S. Sachse, A. Bockisch, U. Enseleit, F. Gerlach, K. Ahlborn, T. Kuhnke, U. Rother, E. Kielhorn, P. Neubauer, S. Junne and W. Vonau, "On the use of electrochemical multi-sensors in biologically charged media," *Journal of Sensors and Sensor Systems*, vol. 4, pp. 295 - 303, 2015.
- [150] S. Fischer, R. Pohle, B. Farber, R. Proch, J. Kaniuk, M. Fleischer and R. Moos, "Method for detection of NO_x in exhaust gases by pulsed discharge measurements using standard zirconia-based lambda sensors," *Sensors and Actuators B: Chemical*, vol. 147, no. 2, pp. 780 - 785, 2010.
- [151] J. Riegel, H. Neumann and H. Wiedenmann, "Exhaust gas sensors for automotive emission control," *Solid State Ionics*, Vols. 152 - 153, pp. 783 - 800, 2002.
- [152] T. Berhanu, J. Hoffnagle, C. Rella, D. Kimhak, P. Nyfeler and M. Leuenberger, "High-precision atmospheric oxygen measurement comparisons between a newly built CRDS analyzer and existing measurement techniques," *Atmospheric Measurement Techniques*, vol. 12, no. 12, pp. 6803 - 6826, 2019.
- [153] P. Krippner, M. Wetzko, P. Szasz, B. Andres and T. Bauer, "MEMS based paramagnetic oxygen measurement," *TRANSDUCERS 2007 - 2007 International Solid-State Sensors, Actuators and Microsystems Conference*, pp. 2393 - 2396, 2007.

-
- [154] J. Cai, L. Wang, P. Wu, L. Tong and S. Sun, "Experimental investigation on possibility of oxygen enrichment by using gradient magnetic fields," *Frontiers of Chemical Engineering in China*, vol. 1, no. 3, pp. 271 - 276, 2007.
- [155] Winsen Electronics Technology, "ME2-O2-Φ20 Electrochemical oxygen sensor: Manual," [Online]. Available: <https://www.winsen-sensor.com/sensors/o2-sensor/me2-o2.html>. [Accessed 15 December 2021].
- [156] J. Toledo, V. Ruiz-Diez, M. Bertke, H. Wasisto, E. Peiner and J. Sánchez-Rojas, "Piezoelectric MEMS resonators for cigarette particle detection," *Micromachines*, vol. 10, no. 2, pp. 1 - 13, 2019.

Publications

Journal Publications

- [1] T. Zengerle, J. Joppich, P. Schwarz, A. Ababneh, and H. Seidel, „Polyatomic degrees of freedom and their temporal evolution extracted from the damping of micro-oscillators”, *Sensors and Actuators A: Physical*, vol. 297, 111460, 2019.
- [2] T. Zengerle, J. Joppich, P. Schwarz, A. Ababneh, and H. Seidel, „Modeling the damping mechanism of MEMS oscillators in the transitional flow regime with thermal waves”, *Sensors and Actuators A: Physical*, vol. 311, 112068, 2020.
- [3] A. Ababneh, Z. Albataineh, A. Dagamseh, I. Al-Kofahi, B. Schäfer, T. Zengerle, K. Bauer, and H. Seidel, “Optical characterization of sputtered aluminum nitride thin films – correlating refractive index with degree of c-axis orientation“, *Thin Solid Films*, vol. 693, 137701, 2020.
- [4] A. Ababneh, A. Dagamseh, Z. Albataineh, M. Tantawi, Q. Al-Bataineh, M. Telfah, T. Zengerle, and H. Seidel, „Optical and structural properties of aluminium nitride thin-films synthesized by DC-magnetron sputtering technique at different sputtering pressures”, *Microsystem Technologies*, vol. 27, pp. 3149 - 3159, 2021.
- [5] T. Zengerle, M. Stopp, A. Ababneh, and H. Seidel, „Using the nonlinear Duffing effect of piezoelectric micro-oscillators for wide-range pressure sensing”, *Actuators*, vol. 10, no. 8, 2021.
- [6] T. Zengerle, J. Joppich, H. Lensch, A. Ababneh, and H. Seidel, “Equivalent circuit model for the damping of micro-oscillators from molecular to viscous flow regime”, *Journal of Micromechanics and Microengineering*, vol. 31, 095010, 2021.
- [7] T. Zengerle, A. Ababneh, and H. Seidel, „Generalized damping model for MEMS oscillators from molecular to viscous flow regime”, *Eng*, vol. 3, no. 1, pp. 124 – 141, 2022.
- [8] T. Zengerle, A. Ababneh, and H. Seidel, „Thermal resonance model for micro-oscillators in the vicinity of a geometric boundary”, *Sensors and Actuators A: Physical*, vol. 341, 113614, 2022.

Conference Publications

- [1] T. Zengerle, J. Joppich, P. Schwarz, A. Ababneh, and H. Seidel, „Influence of molecular degrees of freedom on the gas damping behavior of micro-oscillators in the molecular flow regime”, *Proceedings of Transducers 2019 & Eurosensors XXXIII*, pp. 2118 - 2121, 2019.
- [2] T. Zengerle, J. Joppich, P. Schwarz, A. Ababneh, and H. Seidel, „Einfluss molekularer Freiheitsgrade auf das Dämpfungsverhalten von Mikrooszillatoren im molekularen Strömungsbereich“, *Proceedings of Mikrosystemtechnik Kongress*, pp. 522 - 525, 2019.
- [3] T. Zengerle, J. Joppich, H. Lensch, A. Ababneh, and H. Seidel, „A lumped element model for the damping mechanism of micro-oscillators in the transitional flow regime”, *Proceedings of 32nd International Conference on Microelectronics (ICM)*, pp. 1 - 4, 2020.
- [4] T. Zengerle, M. Stopp, A. Ababneh, and H. Seidel, “Investigations on nonlinearities of roof tile-shape modes for pressure measurement applications”, *Proceedings of Transducers 2021 Virtual Conference*, pp. 1343 - 1346, 2021.

List of Figures

Figure 1. Knudsen number as a function of ambient pressure for various characteristic lengths. The Knudsen number divides the flow into the three schematically drawn regimes.....	12
Figure 2. Normalized amplitude function (a) and phase shift (b) in the resonance case shown for different quality factor values Q	18
Figure 3. Normalized amplitude of an oscillator during transition (blue), stationary, (red) and decay (green) process.	20
Figure 4. 3D illustration of the investigated micro-oscillators including the geometric sizes for the variation of the eigenfrequency for a paddle-oscillator (a), beam-oscillator (b) and cantilever-oscillator (c).....	20
Figure 5. Resonance frequency of different geometric shapes of micro-oscillators versus the squared eigenvalue of the higher bending modes.	21
Figure 6. Frequency response of a nonlinear oscillator for various nonlinear stiffness parameters: Amplitude (a) and phase (b).....	23
Figure 7. Plot of the molecular quality factor Q_{mol} as function of the ambient pressure. The experimental results (points) of the maximum and minimum gap width used in our investigations enclose the presented theories (solid lines) listed in Table 4.	26
Figure 8. Plot of the viscous quality factor Q_{vis} as function of the ambient pressure. The experimental results (points) of the maximum and minimum gap width enclose the presented theories (solid lines). The blue line (Hosaka) is masked by the green line (Kokubun), due to the equality of the equations.	27
Figure 9. Quality factor plots of the squeeze film damping for a BO with $1600 \times 1600 \mu\text{m}^2$ plate. In (a) the quality factor plot for different gap widths within a nitrogen atmosphere is shown and in (b) for different gas atmospheres for a gap width of $100 \mu\text{m}$. In (c) and (d) the evaluated proportionalities according to Equation (2.36) are depicted. For gap widths larger than $150 \mu\text{m}$, a clear deviation from the squeeze film theory is observed.....	30
Figure 10. Simulated shape of the complex eigenmodes specially designed for measurement in liquids. In (a) the 1 st roof tile-shape mode, in (b) the butterfly mode and in (c) the corresponding eigenmode of a hammerhead resonator is illustrated.....	31
Figure 11. Simulated resonance frequency in dependency of the geometry. The base of the simulations is a cantilever CO with the length $L_O = 3600 \mu\text{m}$, width $B_O = 2400 \mu\text{m}$ and thickness $H = 20 \mu\text{m}$. The bending oscillator BO and paddle oscillator PO possess a length $L_O = 1200 \mu\text{m}$, width $B_O = 2400 \mu\text{m}$ and thickness $H = 20 \mu\text{m}$ attached to the substrate by two beams with length $L_B = 2400 \mu\text{m}$ and width $B_B = 600 \mu\text{m}$. In (a) and (b) all geometrical influences on the resonance frequency of the CO structure are shown. In (c) and (d) the geometric influence of the beam structures is illustrated. In (a), (e) and (f) the proportionalities of the resonance frequency of BO and PO to the size and the thickness of the oscillating plate is displayed.....	33
Figure 12. Simulated quality factor plots and shift of the resonance frequency as function of the ambient pressure for the first bending mode for various gap widths (a) and (b) as well for different eigenmodes for a gap width of $550 \mu\text{m}$ (c) and (d).....	37

Figure 13. Decay curves of a micro-oscillator in water (a), isopropanol (b), D5 (c) and N10 (d) (blue solid line). The maxima and minima of the oscillation movement are marked with crosses and fitted using an exponential fit (dotted line).	38
Figure 14. Fourier analysis of the decay plot of micro-oscillator in water (a). The corresponding eigenmodes as well as the associated quality factor and resonance frequency are included. In (b) the resonance peaks resulting from the Fourier analysis of the first bending mode for various liquids are shown.....	39
Figure 15. Schematic diagram of the magnetic circuit including all dimensions. In grey, the magnetic noble material for transporting the magnetic field is highlighted. The magnetic field generators are colored in black and the focusing unit is marked in red.	40
Figure 16. Magnitude of the magnetic field strength in the x - z -plane side view (a) and in the top view on the x - y -plane (b). In (c) the calculated magnetic force in the x -direction is depicted and in (d) the magnitude of the magnetic force as well as the vectorial representation of the force direction is shown.....	41
Figure 17. Schematic overview of the process flow, which includes the key manufacturing steps. On the left side in cross-section and on the right side in top view. The thickness ratios in the side view are not to scale.	42
Figure 18. Back side view showing the refilled KOH cavities with photoresist AZ 1518 (a) and top view on a processed wafer covered with the DRIE photomask before the DRIE process (b). ..	43
Figure 19. Microscopic image of the fabricated micro-oscillators: PO (a), PO fully covered (b), CO (c) and BO (d).	44
Figure 20. Lithographic masks for DRIE process (a) and Au electrode structuring after the chrome etching.	44
Figure 21. Alignment structures to adjust the masks to the wafer (a) and test structures to control the resolution of the lithography step as well as the etching process (b).	45
Figure 22. Microscopic image of the photomask of an AlN piezo element after the phosphoric acid etching (a) and after the Au structuring (b). SEM image of a micro-oscillator showing the edge in a side view. The scalloped sidewall of the DRIE process can be observed (c), as well as the piezo element composed of an AlN and Au stack (d). In (e) the stylus profilometer measurement of a KOH etched profile is shown as well as a 3D microscopic image (f).	47
Figure 23. Height measurement of a stylus profilometer over the test structures to determine the layer thicknesses of SiO ₂ (blue), AlN (green) and Au (gold).	48
Figure 24. Thickness distribution for two wafers with the targeted thickness of 30 μm (a) and 15 μm (b).....	49
Figure 25. Measurement of the initial displacement with a Dektak profilometer on two beam side of a BO sensor (a), for different geometries (b) and varying coverage sizes of the AlN thin films as well as additional Al ₂ O ₃ passivation layers (c).	51
Figure 26. Schematic of the measurement circuit for the compensation of the electrical crosstalk as well as the signal amplification of the sensing element.....	53
Figure 27. Measurement of resonance curves under varying ambient pressures with the proposed charge amplification circuit. In (a, c, e) the amplitude, phase and bode plot are depicted without capacitive feedthrough compensation and in (b, d, f) with this compensation.	54

- Figure 28.** PCB with the measurement electronics consisting of an amplification circuit, a compensation part and a chip scale lock-in amplifier. The total dimensions are $104.5 \times 50 \text{ mm}^2$ 55
- Figure 29.** PCB for connecting the micro-oscillators and place them within the experimental setup. In (a), the board for the measurements in dependence of the adjusted gap width under varying ambient pressure is shown and in (b), the board for the investigation as oxygen sensor in the magnetic field construction can be seen..... 55
- Figure 30.** Construction to place the micro-oscillators in a defined gap width to a geometrical boundary. In (a), the cross-section for mounting the board is shown and in (b), the entire construction including the linear motor for controlling the gap width by regulating the height of the Al plate can be seen [122]. 56
- Figure 31.** Picture of the mounted magnetic circuit. The distance can be adjusted precisely via the adjusting wheel by means of a plastic screw and two countered nuts (a). In (b) a detailed view on the gap where the sensor is placed can be seen..... 57
- Figure 32.** Measurement of the magnetic field within the gap (blue points) showing the convolution of the actual magnetic field and the sensor geometry. The points are fitted with the convolution using Equation (5.3) (orange line) to reconstruct the real magnetic field (grey line). From this result the gradient of the magnetic field (yellow line) is calculated. 58
- Figure 33.** Magnetic field circuit with the coils as active field generating component (a) to create a high magnetic field gradient between the two flattened pyramid structures (b). Two different wire diameters are used, indicated by different colors ($280 \mu\text{m}$ red and $315 \mu\text{m}$ copper)..... 59
- Figure 34.** Magnetic flux density measured within the gap between the flattened pyramid structure as function of the operating voltage applied to the coils..... 59
- Figure 35.** Schematic drawing of the molecular structure of the polyatomic gas molecules. In (a) the diatomic N_2 is shown, in (b) and (c) the triatomic gases CO_2 and N_2O are depicted and in (d) the gas molecule SF_6 is illustrated..... 64
- Figure 36.** Schematic plot of the heat capacity of a diatomic gas molecule as function of the ambient temperature. The total heat capacity is divided into three storage mechanism (translation, rotation, vibration) for accumulating thermal energy in the gas molecule. 66
- Figure 37.** Simulated temperature distribution within the gap (a). Due to the upwards movement of the micro-oscillator (not to scale), a compression of the gas atmosphere arises and a corresponding temperature increase. The temperature and pressure plots are shown for the cut line through the maximum temperature value from the micro-oscillator surface to the top plate for the compression (solid) and expansion (dotted) case (b). 76
- Figure 38.** Quality factor of the fundamental bending mode and higher bending modes as function of the resonance frequency for different ambient pressure levels. The experimental data of micro-oscillator BO3 mentioned in the attached study is shown. 91
- Figure 39.** Measure of the damping obtained from the ratio of the quality factor to the resonance frequency is shown as a function of ambient pressure for the first five bending modes. The fundamental bending mode shows the biggest increase of damping for higher pressures. The experimental data of micro-oscillator CO1_33 mentioned in the attached study is shown. 92

- Figure 40.** Laser Doppler vibrometer measurement of a micro-oscillator in air. In (a) and (b) the first two bending modes are depicted, in (c) the first torsional mode is illustrated and in (d) the first roof-tile shape mode is shown. 122
- Figure 41.** Frequency spectrum of the averaged displacement measured in air (a) and isopropanol (b). The corresponding shape mode, resonance frequency and quality factor are inserted for each resonance peak. 123
- Figure 42.** Resonance peak of the first bending mode measured in isopropanol (a) and the standard viscosities D5 (b) and N10 (c). The measurement data are fitted by a modified Lorentzian fit function to evaluate the resonance peaks. In (d) the resulting fitted resonance peaks are summarized for comparison between the liquids. 124
- Figure 43.** Measured resonance frequency (a) and quality factor (b) of the micro-oscillator versus the mode number. Mode 1, 3 and 6 are indicating the first three bending modes (circle), mode 2, 4 are representing the first two torsional modes (triangle) and mode 5 stands for the roof tile shape mode (diamond). 125
- Figure 44.** Quality factor as function of the reciprocal square root product of density and dynamic viscosity. The liquids and gases except for the small gap width are showing the same dependency to the product but differ significantly in their location. 126
- Figure 45.** Resonance frequency as function of the ambient pressure of a nitrogen atmosphere for various gap widths (a). The gap width dependency of the resonance frequency is illustrated for a pressure of $p = 900$ mbar revealing a saturation behavior (b). 128
- Figure 46.** Resonance frequency as function of the ambient pressure for different gas atmospheres at a gap width of $h = 250$ μm (a). In (b), the resonance frequency at a pressure of $p = 100$ mbar is evaluated regarding the density of the gas atmosphere showing a linear correlation. 128
- Figure 47.** Numerical investigation of the sensor response for varying geometry. The base structure is a cantilever with a length of 3600 μm and a width of 2400 μm . In (a) and (b), the change of the resonance frequency is shown as function of the oxygen concentration for varying width and length, respectively. In (c) and (d), the influence on the resonance frequency and the quality factor by a varying sensor displacement from the center of the gap is illustrated. 144
- Figure 48.** Change of the resonance frequency and quality factor due to a paramagnetic oxygen enrichment in the vicinity of the micro-oscillator for different background oxygen concentrations. 145
- Figure 49.** Resonance frequency and quality factor plot of sensor O2 versus the ambient pressure for various oxygen concentrations. 146
- Figure 50.** Experimental results for the change of the resonance frequency (a) and the quality factor (b) regarding the zero percent oxygen value as function of the oxygen concentration for sensor O1. 147
- Figure 51.** Experimentally determined change of the resonance frequency (a) and quality factor (b) with regard to the zero percent oxygen value as function of the oxygen concentration for sensor O2. 147
- Figure 52.** Recorded resonance curve of the 1st bending of micro-oscillator O1 in air for different operating voltages of the coils, respectively magnetic flux densities. The peak of the resonance curve is shifting to the top and right for increasing magnetic flux density. 148

-
- Figure 53.** Measured shift of the resonance frequency (a) and quality factor (b) of micro-oscillator O1 as function of the magnetic flux density for two different gas atmospheres..... 149
- Figure 54.** Normed change (relative to the 0 T value) of the resonance frequency (a) and quality factor (b) under the effect of an external magnetic field for various pressure levels..... 149

List of Tables

Table 1. Listing of the main physical properties of the gas atmospheres investigated in this thesis for SATP conditions including the speed of sound c_{gas} and the number of atoms of the gas molecule N_{gas} [14].	13
Table 2. Thermal properties of the gases measured in this work [14]. The adiabatic index κ , the number of degrees of freedom (DOF) f_{DOF} and the thermal diffusivity a are calculated from the material properties according to the given equations.	14
Table 3. Listing of the essential components of air and their volume fraction ϕ_V as well as the molar χ_{mol} and volume magnetic susceptibility χ_{vol} .	16
Table 4. Comparison of theories for the quality factor of micro-oscillators in the molecular flow regime.	26
Table 5. Overview of the FEM simulated displacement, temperature and pressure distribution for the first three bending modes (BM). The temperature and pressure distribution are shown from the side (top) and front (bottom) view. In the mode column, the color is indicating the displacement from low (blue) to high (red). In the case of the temperature and pressure distribution the color is indicating the variation from the ambient values (green). Red is indicating a region with higher temperature/pressure and blue representing lower temperature/pressure relative to the ambient value. The displacement is magnified for visualization and is not to scale.	35
Table 6. Listing of the fluid properties investigated numerically regarding their damping behavior. A measure of the strength of the damping is given by the reciprocal square root of the density viscosity product. The properties of water and isopropanol are taken from [110]. The properties of the standard viscosities are taken from the producer <i>Paragon Scientific Ltd.</i> [111].	38
Table 7. Listing of the investigated gas molecules and their corresponding bond length and bond angle [125]. With these informations and with the masses from Table 1, the moment of inertia is calculated according to Steiner's theorem [126]. The rotational temperature and the corresponding rotational energy were calculated using Equation (6.4). The number of moments of inertia is given by #.	64
Table 8. Listing of all investigated gas molecules and their vibrational frequencies and eigenmodes. From the vibrational frequencies, the associated vibrational temperature and corresponding vibrational energy is calculated according to Equation (6.5). In the last column, the number of the individual eigenmodes and the total number of the vibrational modes is given.	65
Table 9. List of the electro-mechanical analogies applied for the representation of the individual dissipation mechanisms with electrical components and networks.	111
Table 10. Experimentally determined values for the quality factor Q and resonance frequency of a micro-oscillator in different liquids. The results are compared to the numerically simulated values regarding the absolute and relative deviation.	124
Table 11. List of the measured micro-oscillators for the oxygen concentration detection and their geometric parameters as well as the resonance frequency and the associated bending modes.	146

List of Symbols

Symbols

Symbol	Description	Unit
A	Oscillation amplitude	m
A_{Gauss}	Amplitude of Gaussian fit function	T
A_{max}	Maximum amplitude in the resonance case	m
A_{offset}	Modified amplitude function with offset	m
A_{trans}	Transitional fitting parameter	-
a	Thermal diffusivity	$\text{m}\cdot\text{s}^{-2}$
B	Width	m
\vec{B}	Magnetic flux density	T
B_{trans}	Thermal resonance frequency fit parameter	$\text{Hz}\cdot\text{mbar}^{-0.5}$
C	Capacity	F
C_p	Heat capacity at constant pressure	$\text{J}\cdot\text{kg}^{-1}\cdot\text{K}^{-1}$
C_V	Heat capacity at constant volume	$\text{J}\cdot\text{kg}^{-1}\cdot\text{K}^{-1}$
c	Concentration	-
c_{gas}	Speed of sound	$\text{m}\cdot\text{s}^{-1}$
D	Damping ratio	-
d	Damping rate	s^{-1}
d_{ij}	Piezoelectric coefficient	$\text{C}\cdot\text{m}^{-2}$
E	Young's modulus	$\text{N}\cdot\text{m}^{-2}$
E_O	Total energy of the oscillator	J
E_{rot}	Energy of rotational degrees of freedom	J
E_{trans}	Energy of translational degrees of freedom	J
E_{vib}	Energy of vibrational degrees of freedom	J
F	Force	N
\vec{F}_{magn}	(Para-)Magnetic force	N
f	Actuation frequency	Hz
f_c	Complex natural frequency	Hz
f_{cut}	Cut off frequency	Hz
f_{DOF}	Number of molecular degrees of freedom (DOF)	-
f_{liquid}	Liquid damped resonance frequency	Hz
f_n	Resonance frequency of the n^{th} eigenmode	Hz
f_{r}	Resonance frequency of the fundamental mode	Hz
$f_{T,\text{gas}}$	Thermal resonance frequency of gas	Hz
f_{th}	Zener's bulk thermal resonance frequency	Hz
g_1	1 st Hydrodynamic force function	$\text{kg}\cdot\text{m}^{-1}\cdot\text{s}^{-1}$
g_2	2 nd Hydrodynamic force function	$\text{kg}\cdot\text{m}^{-1}$
H	Thickness	m
\vec{H}	Magnetic field	$\text{A}\cdot\text{m}^{-1}$
h	Gap width	m
I	Moment of inertia	m^4
J	Heat flux	$\text{W}\cdot\text{m}^{-1}$
j	Rotational quantum number	-
Kn	Knudsen number	-

k	Spring constant	$\text{N}\cdot\text{m}^{-1}$
L	Length	m
l_{mfp}	Mean free path	m
l^*	Characteristic length	m
\vec{M}	Magnetization	$\text{A}\cdot\text{m}^{-1}$
M_{mol}	Molecular mass	$\text{kg}\cdot\text{mol}^{-1}$
m	Mass	kg
N_{gas}	Number of atoms	-
n	Mode number	-
n_{mol}	Amount of substance	mol
o	Occupation number of vibrational degrees of freedom	-
p	Pressure	mbar
p_{mol}	Molecular moment of a gas molecule	$\text{kg}\cdot\text{m}\cdot\text{s}^{-1}$
Q	Quality factor	-
Q_{ext}	Extrinsic quality factor	-
Q_{int}	Intrinsic quality factor	-
Q_{heat}	Heat source	J
Q_{liquid}	Liquid quality factor	-
Q_{mol}	Molecular quality factor	-
Q_{sim}	Simulated quality factor	-
Q_{sqf}	Squeeze film quality factor	-
Q_{trans}	Transitional quality factor	-
Q_{vis}	Viscous quality factor	-
q	Wave vector	m^{-1}
R	Resistor	Ω
S	Surface	m^2
T	Absolute temperature	K
t	Time	s
U	Voltage	V
U_0	Oscillator perimeter	m
\vec{u}	Velocity field	$\text{m}\cdot\text{s}^{-1}$
V	Volume	m^3
\bar{v}	Mean thermal velocity	$\text{m}\cdot\text{s}^{-1}$
x	Displacement	m
Z_1	Constant part of the offset function	m
Z_2	Slope of the offset function	$\text{m}\cdot\text{Hz}^{-1}$
Z_3	Skew of the offset function	$\text{m}\cdot\text{Hz}^{-1}$
α	Coefficient of thermal expansion	K^{-1}
α_{eff}	Effective mass scale factor	-
β	Nonlinear stiffness parameter	$\text{m}^{-2}\cdot\text{s}^{-2}$
β_{geo}	Geometrical nonlinear stiffness parameter	$\text{m}^{-2}\cdot\text{s}^{-2}$
β_{inertial}	Inertial nonlinear stiffness parameter	$\text{m}^{-2}\cdot\text{s}^{-2}$
β_{piezo}	Piezoelectric nonlinear stiffness parameter	$\text{m}^{-2}\cdot\text{s}^{-2}$
δ	Initial displacement due residual stress	m
δ_{therm}	Thermal boundary layer	m
δ_{vis}	Viscous boundary layer	m

$\varepsilon_{\text{trans}}$	Exponential fitting parameter	-
$\Theta(x)$	Heaviside step function	-
Θ_{rot}	Rotational temperature	K
Θ_{vib}	Vibrational temperature	K
κ	Adiabatic index	-
λ	Thermal conductivity	$\text{W}\cdot\text{m}^{-1}\cdot\text{K}^{-1}$
λ_n	Eigenvalue of the n^{th} eigenmode	-
μ	Dynamic viscosity	$\text{Pa}\cdot\text{s}$
μ_{B}	Bulk viscosity	$\text{Pa}\cdot\text{s}$
μ_{r}	Magnetic permeability	$\text{H}\cdot\text{m}^{-1}$
ρ	Density	$\text{kg}\cdot\text{m}^{-3}$
σ	Mechanical stress	$\text{N}\cdot\text{m}^{-2}$
σ_{gas}	Diameter of gas molecule	m
σ_{gauss}	Variance of the Gaussian fit function	-
τ	Exponential decay time	s
φ	Phase between displacement and actuation	°
φ_V	Volume fraction	%
χ_{mol}	Molar magnetic Susceptibility	$\text{m}^3\cdot\text{mol}^{-1}$
χ_{r}	Magnetic Susceptibility	-
χ_{vol}	Volume magnetic Susceptibility	-
ω	Actuation angular frequency	Hz
ω_{D}	Damped angular resonance frequency	Hz
ω_n	Resonance angular frequency of the n^{th} eigenmode	Hz
ω_{r}	Resonance angular frequency of the fundamental mode	Hz
ω_{vib}	Oscillation frequency of the molecular vibration	Hz

Numeric Constants

Symbol	Description	Value	Unit
h	Planck's constant	$6.63\cdot 10^{-34}$	J·s
i	Imaginary Unit	$\sqrt{-1}$	-
I	Identity matrix	$\begin{pmatrix} 1 & 0 & 0 \\ 0 & 1 & 0 \\ 0 & 0 & 1 \end{pmatrix}$	-
k_{B}	Boltzmann constant	$1.38\cdot 10^{-23}$	$\text{m}^2\cdot\text{kg}\cdot\text{s}^{-2}\cdot\text{K}^{-1}$
N_{A}	Avogadro constant	$6.02\cdot 10^{23}$	mol
R_{gas}	Universal gas constant	8.31	$\text{kg}\cdot\text{m}^2\cdot\text{s}^{-2}\cdot\text{mol}^{-1}\cdot\text{K}^{-1}$
V_{mol}	Molar Volume	$24.47\cdot 10^{-3}$	$\text{m}^3\cdot\text{mol}^{-1}$
μ_0	Vacuum permeability	$1.26\cdot 10^{-6}$	$\text{kg}\cdot\text{m}\cdot\text{A}^{-2}\cdot\text{s}^{-2}$
π	Pi	3.14	-

Acknowledgement

First of all, I would like to thank my supervisor, Prof. Dr. Helmut Seidel for his patient guidance throughout the entire PhD work. He inspired me as a young student in micromechanics for the topic and was decisive for my orientation in my later studies. His scientific supervision and his suggestions as well as his friendly support have significantly contributed to the completion of this thesis.

I would also like to thank Prof. Dr. Jose-Luis Sánchez de Rojas for kindly providing the second review.

Very special thanks go to my former colleagues at the Chair of Micromechanics, Microfluidics and Microactuators, Christian Kiefer and Michael Stopp, for the countless discussions both of a technical nature and away from the actual topics. This intellectual stimulation and the open willingness to help contributed to the success of the work. Special thanks go to my pioneer Dr.-Ing. Patrick Schwarz who has supervised me in the context of my master thesis and whose dissertation forms the basis of his thesis.

A big thanks goes to the two institutions of the chair, Ute Flieger and Günther "Günni" Marchand. Ute has already taken care of all administrative tasks before they actually occurred and thus kept my back free for the scientific work. Günni, as the master of the clean room, always ensured very good laboratory conditions and kept all the equipment in top condition, so that I was able to carry out all the processes without any problems.

Many thanks to my co-authors who have contributed to the excellent articles. These are Prof. Abdallah Ababneh from the Yarmouk University in Jordan as well as Julian Joppich and Henrik Lensch from the laboratory of Measurement Technology of the Saarland University. Furthermore, I thank Prof. M. Nienhaus, S. Kleen and R. Schwartz from the Laboratory of Actuation Technology of the Saarland University for the support with the design of the magnetic field construction and the coil manufacturing.

I would like to thank all the students who contributed to the success of the work in the context of a thesis or a HiWi activity. Working with you was always a lot of fun and very refreshing.

Also, I thank the German Research Foundation (DFG) for the financial support within the project SE 1425/14-1.

Finally, I would like to thank my family and friends for their support over the years. Here I have been able to gather a lot of strength and perseverance for the PhD work.